

AD-A253 903

(2)

MIT

PHYSICAL MECHANISMS CONTROLLING
THE STRENGTH-DEFORMATION
BEHAVIOR OF FROZEN SAND: I

FINAL REPORT

by

Glen R. Andersen
John T. Germaine
Charles C. Ladd
and
Chris W. Swan

DTIC
ELECTED
AUG 4 1992

DEPARTMENT
OF
CIVIL
ENGINEERING

April 1992

SCHOOL OF ENGINEERING

MASSACHUSETTS INSTITUTE OF TECHNOLOGY

Cambridge Massachusetts 02139

U.S. ARMY RESEARCH OFFICE
Contract Number
DAAL03-89-K0023

Constructed Facilities Division
Research Report No. R92-15

APPROVED FOR PUBLIC RELEASE;
DISTRIBUTION UNLIMITED

92-20880



92 7 31 165

**THE VIEW, OPINIONS, AND/OR FINDINGS CONTAINED IN THIS REPORT ARE
THOSE OF THE AUTHORS AND SHOULD NOT BE CONSTRUED AS AN OFFICIAL
DEPARTMENT OF THE ARMY POSITION, POLICY, OR DECISION, UNLESS SO
DESIGNATED BY OTHER DOCUMENTATION.**

REPORT DOCUMENTATION PAGE

Form Approved
OMB No. 0704-0188

Public reporting burden for this collection of information is estimated to average 1 hour per response, including the time for reviewing instructions, searching existing data sources, gathering and maintaining the data needed, and completing and reviewing the collection of information. Send comments regarding this burden estimate or any other aspect of this collection of information, including suggestions for reducing this burden, to Washington Headquarters Services, Directorate for Information Operations and Reports, 1215 Jefferson Davis Highway, Suite 1202, Arlington, VA 22202-4302, and to the Office of Management and Budget, Paperwork Reduction Project (0704-0188), Washington, DC 20503.

1. AGENCY USE ONLY (Leave blank)	2. REPORT DATE	3. REPORT TYPE AND DATES COVERED		
	April 1992	Final Report: Jan. 1989-Dec. 1991		
4. TITLE AND SUBTITLE		5. FUNDING NUMBERS		
Physical Mechanisms Controlling the Strength-Deformation Behavior of Frozen Sand: I		DAAL 03-89-15-0023		
6. AUTHOR(S)				
Glen R. Andersen, John T. Germaine, Charles C. Ladd and Chris W. Swan				
7. PERFORMING ORGANIZATION NAME(S) AND ADDRESS(ES)		8. PERFORMING ORGANIZATION REPORT NUMBER		
Department of Civil Engineering Massachusetts Institute of Technology 77 Massachusetts Avenue Cambridge, MA 02139				
9. SPONSORING / MONITORING AGENCY NAME(S) AND ADDRESS(ES)		10. SPONSORING / MONITORING AGENCY REPORT NUMBER		
U. S. Army Research Office P. O. Box 12211 Research Triangle Park, NC 27709-2211		AR 26 260.2-G-5		
11. SUPPLEMENTARY NOTES				
The view, opinions and/or findings contained in this report are those of the author(s) and should not be construed as an official Department of the Army position, policy, or decision, unless so designated by other documentation.				
12a. DISTRIBUTION / AVAILABILITY STATEMENT		12b. DISTRIBUTION CODE		
Approved for public release; distribution unlimited.				
13. ABSTRACT (Maximum 200 words)				
<p>A high-pressure low-temperature triaxial compression testing system with on specimen axial strain measurements and lubricated end plattens was developed in order to measure the stress-strain-volume change behavior of frozen Manchester Fine Sand (MFS) from very small (0.01%) to very large (25%) axial strains. The main testing program was conducted at a temperature of $T = -9.5^{\circ}\text{C}$ and varied the relative density from 20 to 100%, the confining pressure from 0.1 to 10 MPa, and the strain rate from $3 \times 10^{-6}/\text{sec}$ (slow) to $4 \times 10^{-4}/\text{sec}$ (fast). These data: show a constant Young's modulus that can be explained in terms of a composite materials model; provide the first detailed evaluation of the upper yield stress, which is essentially independent of sand density and confining pressure, and has a rate sensitivity similar to that of granular ice; and show that the peak strength generally increases linearly with sand density, increases nonlinearly with confinement, and has a rate sensitivity much less than granular ice. Initial tests at different temperatures indicate a larger temperature sensitivity than predicted for granular ice.</p> <p>A similar triaxial system was used to measure the stress-strain behavior of unfrozen MFS as a function of relative density and confining pressure. These data are used to evaluate Ladanyi's dilatancy-hardening model developed to predict the strength of frozen sand.</p>				
14. SUBJECT TERMS		15. NUMBER OF PAGES		
Cold regions, confining pressure, deformation, dilatancy, frozen soil, modulus, sand, shear strength, strain rate, temperature, triaxial tests, yield stress		166		
17. SECURITY CLASSIFICATION OF REPORT		18. SECURITY CLASSIFICATION OF THIS PAGE	19. SECURITY CLASSIFICATION OF ABSTRACT	20. LIMITATION OF ABSTRACT
UNCLASSIFIED		UNCLASSIFIED	UNCLASSIFIED	UL

TABLE OF CONTENTS

	<u>Page</u>
TITLE PAGE & DISCLAIMER CLAUSE	
REPORT DOCUMENT PAGE (Form 298)	i
TABLE OF CONTENTS	ii
LIST OF TABLES	iv
LIST OF FIGURES	v
1. INTRODUCTION	1
1.1 Background	1
1.2 Objectives of Research	2
1.2.1 Rational and original objectives	3
1.2.2 Actual scope and objectives	5
1.3 Organization of Report	7
1.4 Publications and Reports	8
1.5 Staff	8
1.6 Acknowledgments	10
2. EXPERIMENTAL PROCEDURES	14
2.1 Introduction	14
2.2 Description of Manchester Fine Sand	14
2.3 Cold Room Facility	15
2.4 Triaxial Testing Equipment	18
2.5 Frozen Manchester Fine Sand Test Procedures	21
2.5.1 Specimen preparation	21
2.5.2 Specimen set-up	23
2.5.3 Specimen shearing	24
2.5.4 Precision of Stress-strain parameters	25
2.6 Unfrozen Manchester Fine Sand Test Procedures	26
3. BEHAVIOR OF FROZEN MANCHESTER FINE SAND IN TRIAXIAL COMPRESSION	39
3.1 Scope of Testing Program	40
3.2 Definition of Parameters and General Overview of Stress-Strain Behavior	40
3.2.1 Definition of parameters	40
3.2.2 Types of stress-strain curves	41
3.3 Small Strain Behavior	42
3.3.1 Young's modulus	42

	<u>Page</u>
3.3.2 Application of composite material model	43
3.3.3 Proportional limit	44
3.3.4 Yield offset at 10^{-4} strain	44
3.4 Large Strain Behavior	45
3.4.1 Overview of large strain behavior	45
3.4.2 Upper yield behavior	45
3.4.3 Peak strength behavior	47
3.4.4 Volumetric behavior	49
3.4.5 Summary of effects of relative density, confining pressure and strain rate	50
3.5 Effect of Temperature on the Behavior of Frozen Manchester Fine Sand	51
3.6 Effect of Confinement During Freezing on Frozen Sand Behavior	55
4. BEHAVIOR OF UNFROZEN MANCHESTER FINE SAND IN TRIAXIAL COMPRESSION	95
4.1 Scope of Testing	95
4.1.1 Series A tests	95
4.1.2 Series B tests	96
4.2 Undrained Stress–Strain and Effective Stress Path Behavior	97
4.3 Behavior in Terms of Steady State Line and State Parameter ψ	98
4.4 Drained Stress–Strain and Volumetric Behavior	100
5. APPLICATION OF DILATANCY–HARDENING MODEL	114
5.1 Ladanyi's Model	114
5.2 Application of Ladanyi's Model to Frozen MFS	117
5.3 Discussion	118
6. SUMMARY, CONCLUSIONS AND RECOMMENDATIONS	126
6.1 Summary and Conclusions	126
6.2 Recommendations	130
7. REFERENCES	132
APPENDIX A: TABULATED DATA FROM TEST PROGRAM ON FROZEN MFS	135
APPENDIX B: TABULATED DATA FROM TEST PROGRAM ON UNFROZEN MFS	154

LIST OF TABLES

		<u>Page</u>
Table 1.1	Mechanisms of Strength for Frozen Sand	11
Table 1.2	Tentative Scope of Triaxial Strength Testing Programs in 1988 ARO Proposal	12
Table 3.1	Scope of Testing Program on the Triaxial Compression Behavior of Frozen Manchester Fine Sand	58
Table 3.2	Tentative Scope of Triaxial Testing on MFS at Different Temperatures ("Conventional" tests, i.e., frozen before applying confining pressures)	59
Table 4.1	Scope of Testing Programs on Unfrozen Manchester Fine Sand in Triaxial Compression	101

DTIC QUALITY INSPECTED 5

Accession For	
NTIS	<input checked="" type="checkbox"/>
DTIC FAR	<input type="checkbox"/>
Unannounced	<input type="checkbox"/>
Justification _____	
By _____	
Distribution/ _____	
Availability Codes _____	
Dist	Avail and/or Special
A-1	

LIST OF FIGURES

	<u>Page</u>
Fig. 1.1: Proposed Structure and Strength Mechanisms for Frozen Sand from Ting et al. (1983)	13
Fig. 2.1: Mechanical Sieve Analysis on MFS (Results from 4 Tests)	29
Fig. 2.2: Unfrozen Water Content Versus Temperature for MFS	30
Fig. 2.3: Plan View of MIT Cold Room Facility	31
Fig. 2.4: Schematic View of Environmental Chamber and Triaxial Cell (Before Addition of Second Heat Source)	32
Fig. 2.5: Details of the Modified High Pressure Triaxial Cell for Testing Frozen Soil	33
Fig. 2.6: Schematic Drawing of Mechanical Portion of Pressure/Volume Controller	34
Fig. 2.7: Details of On-Specimen Axial Strain Yoke	35
Fig. 2.8: Schematic Drawing of Specimen Preparation Molds (after Martin et al. 1981)	36
Fig. 2.9: Schematic Diagram of Multiple Sieve Pluviation Frame for Frozen MFS Specimen Preparation	37
Fig. 2.10: Unfrozen MFS Specimen Preparation Using Membrane Expander/Sample Former and Multiple Sieve Pluviation	38
Fig. 3.1: Idealized Stress–Strain Behavior and Graphical Construction Techniques	60
Fig. 3.2: Overview of Types of Stress–Strain Curves	61
Fig. 3.3: Young's Modulus Versus Relative Density for Frozen MFS	62
Fig. 3.4(a): Proportional Limit Versus Relative Density for Frozen MFS	63
Fig. 3.4(b): Effect of Confining Pressure On Proportional Limit for Frozen MFS	64
Fig. 3.4(c): Effect of Strain Rate on Proportional Limit for Frozen MFS	65
Fig. 3.5(a): Yield Offset Stress at 10^{-4} Strain Versus Relative Density for Frozen MFS	66

	<u>Page</u>
Fig. 3.5(b): Effect of Confining Pressure on Yield Offset Stress for Frozen MFS	67
Fig. 3.5(c): Effect of Strain Rate on Yield Offset Stress for Frozen MFS	68
Fig. 3.6(a): Normalized Stress–Strain Curves Showing the Effect of Relative Density for Moderate Strain Rate and Low Confining Pressure for Frozen MFS	69
Fig. 3.6(b): Normalized Stress–Strain Curves Showing the Effect of Relative Density for Moderate Strain Rate and High Confining Pressure for Frozen MFS	70
Fig. 3.7(a): Normalized Stress–Strain Curves Showing the Effect of Confining Pressure for Moderate Strain Rate and Low Relative Density for Frozen MFS	71
Fig. 3.7(b): Normalized Stress–Strain Curves Showing the Effect of Confining Pressure for Moderate Strain Rate and High Relative Density for Frozen MFS	72
Fig. 3.8(a): Stress–Strain Curves Showing the Effect of Strain Rate for Low Relative Density and Low Confining Pressure on Frozen MFS	73
Fig. 3.8(b): Stress–Strain Curves Showing the Effect of Strain Rate for High Relative Density and High Confining Pressure on Frozen MFS	74
Fig. 3.8(c): Stress–Strain Curves Showing the Effect of Strain Rate for Low Relative Density and High Confining Pressure on Frozen MFS	75
Fig. 3.9(a): Stress–Strain Curves Showing Upper Yield Behavior of Frozen MFS at Varying Relative Density	76
Fig. 3.9(b): Stress–Strain Curves Showing Upper Yield Behavior of Frozen MFS at Varying Confining Pressure	77
Fig. 3.9(c): Stress–Strain Curves Showing Upper Yield Behavior of Frozen MFS at Varying Strain Rate	78
Fig. 3.10: Corrected Upper Yield Stress Versus Relative Density for Frozen MFS	79
Fig. 3.11: Effect of Confining Pressure on Corrected Upper Yield Stress for Frozen MFS	80
Fig. 3.12: Effect of Strain Rate on Upper Yield Stess for Frozen MFS	81

	<u>Page</u>
Fig. 3.13(a): Axial Strain at Upper Yield Stress Versus Relative Density for Frozen MFS	82
Fig. 3.13(b): Effect of Strain Rate on the Axial Strain at the Upper Yield Stress for Frozen MFS	83
Fig. 3.14: Comparison of Rate Sensitivity of Upper Yield Stress of Frozen MFS to that of Peak Strength of Polycrystalline Ice	84
Fig. 3.15(a): Peak Deviator Stress Versus Relative Density at Moderate Strain Rate for Frozen MFS	85
Fig. 3.15(b): Peak Deviator Stress Versus Relative Density for Range in Strain Rates and Confining Pressures for Frozen MFS	86
Fig. 3.16(a): Axial Strain at Peak Deviator Stress Versus Relative Density for Moderate Strain Rate and Range in Confining Pressures for Frozen MFS	87
Fig. 3.16(b): Axial Strain at Peak Deviator Stress Versus Relative Density for Range in Strain Rates and Confining Pressures for Frozen MFS	88
Fig. 3.17: Effect of Confining Pressure on Peak Deviator Stress for Moderate Strain Rate for Frozen MFS	89
Fig. 3.18: Effect of Strain Rate on Peak Deviator Stress for Range in Relative Densities and Confining Pressures for Frozen MFS	90
Fig. 3.19: Stress–Strain Curves Showing the Effect of Temperature at Moderate Strain Rate for Low Relative Density and Low Confining Pressure for Frozen MFS	91
Fig. 3.20: Effect of Temperature on the Upper Yield Stress and Peak Strength of Frozen MFS at Moderate Strain Rate	92
Fig. 3.21: Comparison Between Measured Upper Yield Stress and Peak Strength of Frozen MFS and Calculated Peak Strength of Ice at Moderate Strain Rate	93
Fig. 3.22: Stress–Strain Curves to Show the Effect of Specimen Preparation Technique on Frozen MFS	94
Fig. 4.1: Effective Stress Failure Envelope of MFS at Maximum Obliquity from Unfrozen Triaxial Compression Results	102
Fig. 4.2: Effect of Confining Stress on Stress–Strain Behavior of Unfrozen Dense MFS from CIUC Tests	103

	<u>Page</u>
Fig. 4.3: Effect of Confining Pressure on Effective Stress Paths of Unfrozen Dense MFS for CIUC Tests	104
Fig. 4.4: Effect of Density on Stress–Strain Behavior of CIUC Tests on Unfrozen MFS with $\sigma'_{c} = 2.0$ MPa	105
Fig. 4.5: Effect of Density on Effective Stress Paths for CIUC Tests on Unfrozen MFS with $\sigma'_{c} = 2.0$ MPa	106
Fig. 4.6: Definition of State Parameter, Ψ (after Been and Jefferies 1985)	107
Fig. 4.7: Steady State Line for 16 CIUC Tests on Unfrozen MFS	108
Fig. 4.8: A_f vs. Ψ Parameter from CIUC Tests on Unfrozen MFS	109
Fig. 4.9: Normalized Undrained Shear Ratio Versus Ψ Parameter from CIUC Tests on Unfrozen MFS	110
Fig. 4.10: Stress–Strain and Volumetric Strain Response for CIDC Tests on Dense Unfrozen MFS	111
Fig. 4.11: Effective Stress Paths of CIDC Test Results on Dense Unfrozen MFS	112
Fig. 4.12: Steady State Line and CIDC Test Result for Unfrozen MFS	113
Fig. 5.1: MIT q–p Plot for Ladanyi's Dilatancy Hardening Model	122
Fig. 5.2: Critical Confining Pressure Line of Unfrozen MFS from CIUC Tests	123
Fig. 5.3: Application of Ladanyi's Model to Dense Frozen MFS ($D_r = 95\%$, $T = -9.5^\circ C$)	124
Fig. 5.4: Force Equilibrium of Sand Particle In Frozen Sand	125

1. INTRODUCTION

1.1 BACKGROUND

Frozen soils exist in Arctic regions as perennially frozen soil (permafrost) that underlies nearly 20% of the land surface of the earth. In addition, artificial freezing is widely used as a construction aid to enhance ground support and for control of water during excavations of tunnels, shafts, etc. Projects involving construction in or on frozen earth pose unique design problems because the time-dependent strength-deformation behavior of frozen soil is probably the most variable and difficult of all "geomaterials" to understand and model. Even the simplest system, such as a saturated frozen sand, represents a highly complex interaction between the *solid soil skeleton* and the *pore matrix*, composed of ice and unfrozen water, that changes continuously with time as a function of temperature, state of stress and/or strain level.

In order to develop solutions to design problems involving frozen soils, engineers have generally relied on empirically based behavioral models as a means of predicting material response. These have been based on correlations between various parameters such as temperature, strain rate and peak strength, or creep stress and minimum creep rate or time to minimum creep rate. Unconfined compression tests have been used most often as a means of calibrating these behavioral models. These tests are performed in the laboratory where the time scale is generally much shorter than the field. Accordingly, extrapolation of the measured laboratory behavior to the field can introduce a considerable amount of uncertainty in the predicted response.

Unconfined compression tests also apply a relatively simple state of stress to the specimen. In the field, where the actual states of stress and deformational constraints are very complex, behavior extrapolated from such simple element tests may lead to unconservative predictions unless a large factor of safety (factor of ignorance) is used. In order to model complex field conditions, it would be necessary to conduct sophisticated laboratory testing programs where principal stress directions could be controlled and

widely varying deformational constraints could be imposed. Such testing procedures are extremely costly and have not been developed for frozen soil applications.

Most experimental data on frozen soils comes from laboratory tests wherein the specimens have been prepared with "zero" effective (intergranular) stress acting on the soil skeleton prior to freezing. In triaxial compression tests, a confining pressure is subsequently applied to the frozen soil and, if it is completely saturated, this confinement is initially carried primarily by the pore ice. In contrast, both natural and artificial freezing occurs in soils that already have significant effective stresses acting on the soil skeleton prior to freezing. No data exist to predict how differences in the pre-freezing effective stresses may affect laboratory versus field behavior.

Therefore, empirically based behavioral models, while certainly necessary for solving immediate engineering design problems, are liable to involve significant uncertainty in their ability to predict actual behavior in the field. The eventual development of more rationally based design procedures, which presumably can lead to safer and more cost efficient designs, requires a far better understanding of the physical mechanisms that control the time-dependent behavior of frozen soils.

1.2 OBJECTIVES OF RESEARCH

The long term objective of MIT frozen soil research is to develop physically based constitutive relations for frozen soil behavior, for which an understanding of the fundamental behavior of frozen soils is essential. The near term research objective is the identification of the principal mechanisms which control the behavior of frozen soils and a quantitative assessment of their relative importance.

These mechanisms can be broadly classified into those which are associated with the soil skeleton, those associated with the pore ice, and those which are due to the interaction between the soil particles and the pore ice. Ideally frozen soils could be studied on the micro-level. Direct measurements of the behavior of the soil skeleton independent of the

ice matrix and visa versa would go a long way towards understanding the complex interaction between these two components. But such measurements are not currently possible. An alternative approach is to study frozen soils at a *macro-level*. This involves observing the overall behavior of the frozen soil system under a wide variety of conditions and comparing it to predicted behavior using simplified models aimed at describing the various physical mechanisms. The relative importance of these mechanisms can then be addressed. The primary thrust of MIT's current research has taken this macro-level approach.

1.2.1 Rational and Original Objectives

Ting et al. (1983) proposed and attempted to evaluate various physical mechanisms controlling the strength of frozen sand, concluding that the principal components are (see Table 1.1): ice strength and strengthening; soil strength; and soil skeleton–ice matrix interaction through dilatancy effects and structural hindrance. Figure 1.1(a) shows their proposed structure for frozen sand and Fig. 1.1(b) illustrates their attempt to quantify the relative importance of these different strength mechanisms as a function of the volume fraction of sand from unconfined compression data obtained by Goughnour and Andersland (1968) on frozen Ottawa sand. A major objective of our 1988 ARO proposal was to extend the Ting et al. conceptual picture to obtain a quantitative assessment of the physical components of strength for a range of frozen soils and testing conditions. Specifically, the research would make, for the first time, a direct comparison of the total stress versus strain behavior of representative frozen soils with the undrained total and effective stress versus strain behavior of the same systems in an unfrozen state. By varying the testing conditions (i.e., specimen density, confining stress, strain rate, etc.) for each system, the research hoped to quantify the factors affecting the various physical mechanisms and their relative importance. The results would also be compared to predictions by Ladanyi's "dilatancy–hardening" theory (e.g., Ladanyi and Morel 1990). This theory is further described in Section 5 and assumes that the strength of frozen dense

sand has two components: 1) one due to the undrained strength of the soil skeleton, which is controlled by its friction angle and the tensile strength of ice (at low confining stresses); and 2) the other due to the compressive strength of the ice matrix (equated to that of regular granular ice at the same temperature, strain rate and confining pressure).

Limited, but consistent, volumetric strain data in the literature indicated that shear of frozen soils in triaxial compression occurred at almost constant volume up to the *peak strength*. This formed the basis for Ladanyi's hypothesis that the undrained ($\Delta V = 0$) effective stress-strain behavior of the same soil in an unfrozen state could provide an estimate of the contribution of the soil skeleton strength (components 2 and 3bi in Table 1.1) to the overall strength of the frozen soil. Consequently, the experimental program would conduct isotropically consolidated-undrained triaxial compression (CIUC) tests with pore pressure measurements on *unfrozen* soil in order to compare its effective stress and total stress behavior with the total stress behavior of the same soil in a *frozen* state. Table 1.2 shows the proposed scope of a three year strength testing program. Some explanations follow:

- 1) The program would start with Manchester Fine Sand since its behavior is typical of frozen sands and prior ARO sponsored research (Martin et al. 1981; Ting et al. 1983) had developed extensive unconfined creep data at varying densities and degrees of ice saturation.
- 2) The confining stresses for all test series would vary over a wide range (0.1 to 10 MPa), since this is an important variable for both unfrozen and frozen soil. All tests would be conducted with measurements of *volumetric strain* and would incorporate lubricated end caps.
- 3) The U Series would represent conventional CIUC (isotropically consolidated-undrained compression) tests on unfrozen soil systems.
- 4) The F Series would represent conventional UUC tests on frozen soil (i.e., specimens are sheared immediately after application of the cell pressure, σ_c); the FC Series

would involve very prolonged application of confining stress in order to consolidate the frozen soil (i.e., allow ice to flow out of the specimen until the soil skeleton carries the confining stress).

- 5) The F1 Series would evaluate the influence of confining stress at a typical temperature and strain rate. The F2 Series would evaluate the influence of higher and lower values of temperature and $\dot{\epsilon}$ at low and high confining pressures.
- 6) The frozen Boston Blue Clay would represent a soil having a strength approximately equal to that of granular ice and frozen Fairbanks Silt would represent a soil having a strength significantly less than granular ice.
- 7) The program on Glass Beads was included for comparison with Ting et al. (1983) creep data.

1.2.2 Actual Scope and Objectives

The actual scope of the triaxial testing program has been restricted to the U and F Series on Manchester Fine Sand (MFS) and hence has far less breadth than originally proposed. Some explanations are needed to understand the reasons for this substantial change.

Development of New Experimental Capabilities

The time and effort required to design, construct and evaluate two new triaxial systems (especially that for frozen soil) were greater than expected in large part due to changes in measurement and experimental techniques as follows:

- The addition of on-specimen measurements of axial strain (which required a new design since suitable devices were not commercially available). This proved to be both essential and highly successful.
- The subsequent need to develop a complex technique to measure volumetric strains via changes in cell volume rather than radial strain gages as originally proposed.

- The change from "wet tamping" to "multiple sieve pluviation" to achieve more uniform specimen densities.

Consequently it took about one year of full time effort by one student (Glen Andersen) to produce the first "reported" test on frozen sand. A second student (Chris Swan) devoted a similar effort for the unfrozen sand testing system.

Results from Testing Frozen MFS

The improved measurement techniques led to the acquisition of unique stress-strain-strength data compared to that reported in the literature, particularly regarding behavior at small strains. The addition of on-specimen axial strain devices allowed for the measurement of strains down to less than 0.01%. Consequently, the decision was made to obtain for the first time the complete characterization of the stress-strain behavior of a frozen sand in triaxial compression as a function of relative density (D_r), confining stress (σ_c), strain rate ($\dot{\epsilon}$) and temperature (T).

Research Objectives

The main objective of the research was to use the new experimental system in order to obtain detailed measurements of the behavior of frozen Manchester Fine Sand (MFS) as a function of the above four variables (i.e., density, confinement, strain rate and temperature). An extensive literature review revealed that information of this type had not been published for any frozen soil. The authors feel that this complete characterization represents the most significant contribution of the research and is a necessary and important step towards the eventual development of physically based constitutive models for frozen soils.

The second objective of the research was to evaluate the measured behavior of frozen Manchester Fine Sand (MFS) in terms of Ladanyi's (1985) dilatancy-hardening model. His model attempts to quantify the relative contributions of the frictional resistance of the soil skeleton and of the tensile and compressive strength of the ice matrix. The evaluation process required detailed measurements of the stress-strain-strength

behavior of unfrozen MFS over the same range of densities and confining pressures as used for the test series on frozen sand. This effort also constitutes a significant contribution and the first data set comparing undrained—unfrozen sand and frozen sand behavior over a wide range of densities, strain rates and confining pressures.

The third and final objective evolved during the research and involved the use of a behavioral model from the field of composite materials in an effort to understand the interaction between the sand skeleton and pore ice at *small* strains. In particular, predictions from Counto's (1964) composite material model for concrete are compared to measured behavior.

1.3 ORGANIZATION OF REPORT

Section 2 describes the laboratory facilities and equipment and triaxial testing procedures used in both frozen and unfrozen tests. It also contains a description of Manchester Fine Sand and specimen preparation techniques.

Section 3 presents the measured behavior of frozen Manchester Fine Sand in triaxial compression. It gives an overview of the scope of the testing program and then shows the effects of the relative density, confining pressure and strain rate on the stress-strain behavior and is based on data contained in the doctoral thesis by Andersen (1991). These tests were conducted at one temperature (-9.5°C). Summary plots of parameters taken directly from the stress-strain curves are presented and form the basis of discussion. These plots are supplemented by typical stress and volumetric strain versus axial strain curves. Parameters are tabulated in Appendix A. The effect of temperature, which is still being studied, and the influence of different specimen preparation techniques on the behavior of frozen MFS are also presented. In addition, the measured behavior at very small strains is analyzed in terms of the composite materials model presented by Counto (1964).

The results of triaxial tests on unfrozen MFS are presented in Section 4. After outlining the scope of the testing, the effects of relative density and effective confining

pressure on undrained stress-strain behavior are presented. Tabulated test results are presented in Appendix B. The unfrozen test results are analyzed using the "state parameter" concept developed by Been and Jefferies (1985).

Section 5 presents the dilatancy-hardening model developed by Ladanyi (1985). Predicted results from this model are compared to those measured in this research.

Section 6 summarizes the principal conclusions and presents recommendations for continued research.

1.4 PUBLICATIONS AND REPORTS

Progress Reports were submitted to ARO for the six month periods ending in June and December of 1989, 1990 and 1991. A copy of the doctoral thesis that was completed in June, 1991 by Glen R. Andersen entitled "Physical Mechanisms Controlling the Strength and Deformation Behavior of Frozen Sand" was sent to ARO. Dr. Andersen is currently preparing drafts of two co-authored papers for submittal to the Canadian Geotechnical Journal. The first will present the effects of density, confining pressure and strain rate (and maybe temperature) on the behavior of frozen MFS. The second will analyze the data (e.g., use of composite and Ladanyi's models) and compare these data with prior results. (Note: the papers will be too long for acceptance by ASCE, whereas the CGJ has no page limitations and has contained many excellent papers on ice and frozen soils).

1.5 STAFF

Dr. Charles C. Ladd, Professor of Civil Engineering, and Dr. John T. Germaine, Principal Research Associate, served as co-principal investigators for the three year project. In simplified terms, Dr. Germaine was mainly responsible for development of the new testing capabilities and supervision of the experimental work, whereas Professor Ladd administered the contract and was mainly responsible for supervision of the project and the writing of reports and the thesis.

Glen R. Andersen worked on the project for two and one-half years either as a full-time graduate Research Assistant or a part-time Instructor, made an extensive review of the literature on the behavior of ice and frozen sands, and conducted or supervised most of the tests on frozen MFS involving the effects of density, confining pressure and strain rate. After receiving his ScD degree in June 1991, Dr. Andersen joined the Chevron Oil Field Research Company in La Habra, California.

Chris W. Swan worked on the project through the last two years, first as a recipient of a Department of Civil Engineering Fellowship and then as a full-time graduate Research Assistant. He developed the capability for conducting high pressure triaxial tests on unfrozen MFS that produced the results presented in Section 4 and then assumed responsibility for testing frozen MFS, primarily on the effects of temperature. Mr. Swan plans to continue research in this area for his doctoral thesis, with emphasis on comparison of the influence of the magnitude of the *pre-freezing* effective stress on the measured behavior of frozen MFS.

Other involvement by students included:

- 1) Patrick Kinnicut as a half-time graduate Research Assistant during the Spring semester of 1989 who developed improved techniques for preparation of specimens of MFS;
- 2) Peter Kukielski as a Summer Intern Fellowship Student from the University of Rhode Island who performed a significant number of high quality tests on frozen MFS under Mr. Andersen's supervision;
- 3) Victor Salvador as a Summer Intern Fellowship Student from Columbia University who assisted Mr. Swan in conducting tests on frozen MFS at varying temperatures.

Mr. David M. Cole of the Cold Regions Research and Engineering Laboratory (CRREL) in Hanover, NH served as technical liaison for the project. He also served as a member of Andersen's doctoral thesis committee along with Professor Ladd and Dr. Germaine.

1.6 ACKNOWLEDGMENTS

The authors are indebted to the late Dr. Steven J. Mock, Program Manager of Terrestrial Sciences in the ARO Geosciences Division at Research Triangle Park, NC. During preparation of this report, Professor Ladd studied the outside reviews of our 1988 proposal to ARO. Some were highly unfavorable and all contained valid criticisms, yet Dr. Mock decided to fund the proposal. We feel that our results support his decision, which we attribute to a combination of his confidence in MIT and insight. His support and guidance will certainly be missed among the many researchers in the terrestrial sciences.

Mr. David M. Cole of CRREL did an outstanding job as technical liaison for the project. Besides providing close cooperation with allied research at CRREL, he spent numerous hours in helping MIT staff (and particularly Glen Andersen) understand the intricacies of ice and frozen soil behavior, made several visits to MIT to help improve our experimental techniques and guide our research directions (most notably the testing program at different temperatures), spent many hours on the phone in technical consultation, and served as a very active member of Andersen's doctoral thesis committee.

Mr. Peter Kukielski deserves special recognition for his outstanding experimental capabilities and productivity while serving as a fellowship student during the summer of 1990. He produced nearly half of the tests on frozen MFS that are contained in Andersen's doctoral thesis.

The authors, plus Mr. Kukielski, met with Messrs. David Cole and Francis H. Sayles of CRREL and Professor Branko Ladanyi of Ecole Polytechnique, Montreal on January 21, 1991 in Hanover, NH for an indepth review and discussion of MIT's data on frozen MFS. Mr. Andersen also presented a seminar the next day at CRREL.

Besides attending the above meeting, Professor Ladanyi provided technical assistance via correspondence and copies of papers and theses from Ecole Polytechnique.

Finally, Pat Black of CRREL kindly provided NMR unfrozen water content data on frozen MFS.

Table 1.1 Mechanisms of Strength for Frozen Sand

Possible Mechanisms from Ting et al. (1983)	Conclusions from Ting et al. (1983)
(1) Ice Strength Function of ϵ , T, σ_c , grain fabric	<ul style="list-style-type: none"> Thought to dominate at low strains.
(2) Soil Strength	<ul style="list-style-type: none"> Thought to dominate at large strains.
	Cited Rowe (1962) for drained strength of cohesionless soil having three components: <ul style="list-style-type: none"> Sliding between grains Particle inference Dilatancy (volume increase against $\sigma' c$)
(3) Interaction Between Ice and Soil	<ul style="list-style-type: none"> Thought to dominate at low strains.
(a) Ice strengthening—due to altered	<ul style="list-style-type: none"> Thought to dominate at large strains.
i) Structure	<ul style="list-style-type: none"> Increase σ' due to strong tensile adhesional soil–ice interface forces resisting expansion of soil skeleton.
ii) State of stress & deformational constraints	<ul style="list-style-type: none"> Synergistic mechanical interaction due to strong bonding between the ice matrix and soil skeleton.
iii) Strain rate (higher)	<ul style="list-style-type: none"> Probably not very significant (e.g., decreasing ice saturation leads to much lower strength).
(b) Soil strengthening	<ul style="list-style-type: none"> Structural hindrance
i) Increased dilatancy	
ii) Structural hindrance	
(c) Tension in unfrozen water film	

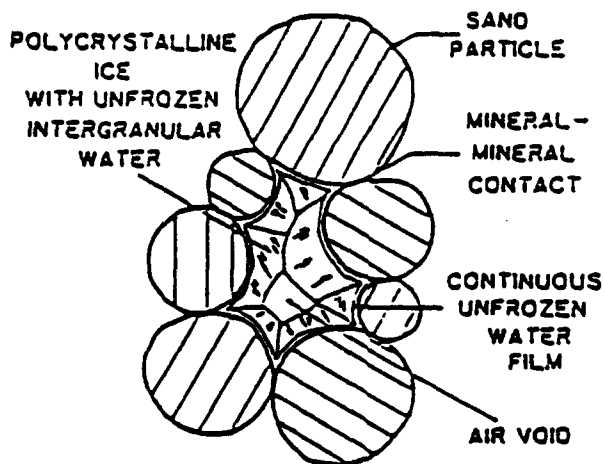
Table 1.2 Tentative Scope of Triaxial Strength Testing Program in 1988 ARO Proposal

A. TEST SERIES (Stresses in MPa and $\dot{\epsilon}$ per second)

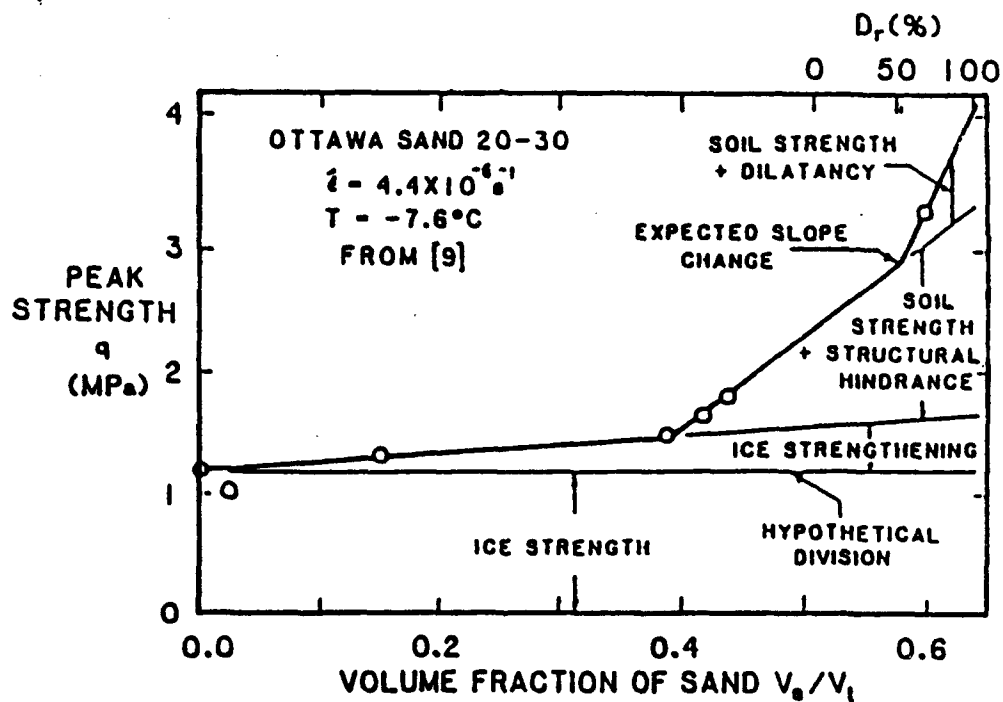
<u>Designation and Description</u>	<u>Confining Pressure, σ_c</u>	<u>Strain Rate, $\dot{\epsilon}$</u>	<u>Temperature</u>
U = Unfrozen CIUC	0.1, 2, 5 and 10	3×10^{-5} (moderate)	Room
F1 = Frozen UUC	As above	As above	-10°C
F2 = Frozen UUC	0.1 & 5	10^{-6} (slow) 10^{-3} (fast)	-5°C -20°C
FC = Frozen CIUC	2 & 10	3×10^{-5}	-10°C

B. TEST SYSTEMS

- 1) Manchester Fine Sand (MFS) at 55 & 95% relative density, plus three ice-sand mixtures.
- 2) Boston Blue Clay at overconsolidation ratio = 4.0.
- 3) Fairbanks Silt at natural water content.
- 4) Glass Beads at 95% relative density, coarse and fine silt size, plus one non-wetting.



(a) Two Dimensional Schematic of the Proposed Structure of Frozen Sand



(b) Proposed Mechanism Map for Unconfined Compressive Strength of Frozen Ottawa Sand 20-30 (Goughnour and Andersland, 1968) at -7.6°C and Applied Strain Rate of $4.4 \times 10^{-4} \text{ s}^{-1}$

Figure 1.1:

Proposed Structure and Strength Mechanisms for Frozen Sand from Ting et al. (1983)

2. EXPERIMENTAL PROCEDURES

2.1 INTRODUCTION

A significant effort (approximately one year) went into development of high pressure triaxial testing equipment for both the frozen and unfrozen testing programs. Principal attributes of the frozen testing include: lubricated end platens (via ice caps); on-specimen axial strain measurements (precision of about 0.002%); volumetric strains (precision of $\pm 0.2\%$) from volume of cell fluid; internal load cell to measure axial force; and good temperature control (top of specimen at -9.4°C , bottom at -9.7°C and fluctuations of $\pm 0.05^{\circ}\text{C}$ for majority of frozen tests). In addition, high pressure triaxial testing capabilities (including lubricated end platens and on-specimen axial strain measurements) were developed for characterizing the unfrozen behavior of MFS as a function of density and consolidation (confining) pressure. This section describes the test material and the laboratory facilities, testing equipment and experimental procedures used in testing frozen and unfrozen Manchester Fine Sand.

2.2 DESCRIPTION OF MANCHESTER FINE SAND

The sand used in this testing program, known as Manchester Fine Sand (MFS), was collected at the Plourde Sand and Gravel Company located in Hooksett, NH approximately 10 miles north of Manchester along the banks of the Merrimack River. This sand is a river bed deposit with nearly horizontal bedding planes. The gradation can vary widely between adjacent bedding planes and the sand for this testing series was collected from several of these with an effort to obtain representative material.

An initial mechanical sieve analysis of the collected material showed that the fines content, i.e., the material finer than 0.074mm, was approximately 20%. The sand was subsequently processed by dry sieving with a #200 sieve to remove a portion of the fines. The processed batch was thoroughly remixed and subsequent sieve analyses indicated that

the fines content averaged approximately 7% (see Fig. 2.1). The coefficient of uniformity for this sand is approximately 2.4 and the coefficient of concavity is approximately 1.1, based on the average of four sieves. The material passing the No. 200 sieve (fines) is nonplastic. The Manchester Fine Sand tested in this research is classified as SP-SM, a poorly graded fine sand with 7% nonplastic silt size particles according to the Unified Soil Classification System.

Other pertinent characteristics of Manchester Fine Sand are:

- Mainly quartz and feldspar (with some mica flakes) having sub-angular particles (Martin et al. 1981).
- Specific gravity = 2.688 ± 0.003 .
- Minimum dry density = 1408 kgf/m^3 ; maximum dry density = 1701 kgf/m^3 .
- See Fig. 2.2 for unfrozen water content versus temperature.
- Although MFS is significantly more compressible than Standard Ottawa Sand, it shows little evidence of particle crushing at $\sigma'_c = 10 \text{ MPa}$ (from grain size distribution and SEM analyses).

2.3 COLD ROOM FACILITY

The Low-Temperature Testing Facility was completed in 1988 with a combination of grants from NSF and two MIT projects, ARO/PACT and the Center for Scientific Excellence in Offshore Engineering. Constructed and located inside a regular room-temperature laboratory, the facility has three separate rooms with independent temperature control: the vestibule; the growth room; and the testing room (Fig. 2.3). The vestibule is used as a temperature buffer between the outside laboratory and the inner cold rooms. It cuts down on the amount of humidity that reaches the two inner rooms and also serves as a staging area for preparing and trimming frozen soil specimens. It normally has a temperature of -4 to -5°C . The growth room, located to the rear of the vestibule and maintained at a temperature of 0°C , is used for specimen freezing. The testing room

contains the triaxial apparatus, loading frame and the environmental chamber. It can be regulated to -40°C , and is normally maintained at a temperature a few degrees colder than the desired set point temperature for a particular test. Temperature control of the triaxial cell is accomplished by heating a small environmental chamber (Fig. 2.3) located inside the testing room.

Each room is composed of sheet metal walls with styrofoam insulation. The testing room has a double-paned glass window to allow for observation of the testing equipment from the outside, room-temperature laboratory. This window is heated to prevent icing. The testing and growth rooms are fitted with feed-through ports to allow for the passage of instrumentation cables and power lines. These are used to connect a thermoregulator system, load cell, displacement transducers, pressure transducer and temperature sensors to the controller circuits, power supplies and data acquisition system located outside the harsh environment of the testing room. See Andersen (1991) for a comprehensive description of these systems and devices. Only the actual sensing devices, the circulating fan and heat source of the thermoregulator system and the pressure/volume controller system are located inside the cold room.

The temperature inside the testing room fluctuates about a control point. The air temperature fluctuates by $\pm 1.5^{\circ}\text{C}$ about the desired set point and has a typical period of 400 to 600 seconds. The testing room has programmable defrost cycles which are required for continuous operation. These defrost cycles produce temperature spikes of about 3°C above the normal cyclic oscillation and can last as long as 20 minutes.

Testing is performed inside an environmental chamber located within the testing room. The environmental chamber is a double-walled container composed of sheets of styrofoam mounted on a wooden frame. Figure 2.4 shows a schematic of this chamber and the location of all the devices within it. The front door of the chamber is constructed of two sheets of plexiglas mounted on an aluminum frame to allow for direct observation of the testing equipment during operation. The chamber is mounted on top of the loading

frame and completely encloses the triaxial cell, the loading platen, the crosshead of the loading frame and the oil reservoir for the pressure/volume controller.

The temperature inside of the environmental chamber is controlled by a thermoregulator system composed of a continuously circulating fan (flow rate = 45cfm), a heat source mounted inside of a metal box and a mercury contact switch preset at the desired testing temperature. The system operates by adding increments of heat to the chamber as heat is lost to the colder testing room. The temperature in the chamber fluctuates around the desired set point by $\pm 0.15^{\circ}\text{C}$ and has a slight gradient of about 0.2°C (warmer near the base).

A new environmental chamber was constructed during the summer of 1991; however, most of the aforementioned characteristics were retained. The main purpose for the new chamber was to create a more stable temperature of the air surrounding the triaxial cell. For example, a second heat source was added to improve temperature stability. A similiar environmental chamber was also constructed for the unfrozen soil testing that occurs in the regular room-temperature laboratory.

Digital data acquisition is an integral part of the Low Temperature Testing Facility. Output voltages from transducers and thermistors from the frozen and unfrozen testing apparati are connected to the Geotechnical Laboratory's Central Control Acquisition System. The system has a 140 channel capability and connects to every room in the laboratory complex. The system is designed around the Hewlett Packard 3477A data acquisition/control unit. This is a very low noise integrating analog to digital converter. It has 17 bit precision and auto ranging capability resulting in one micro volt sensitivity and a 100 volt range. Any type of direct current transducer can be connected to this network without the uncertainty of additional signal conditioners. The Low Temperature Testing Facility currently uses 25 data acquisition channels.

2.4 TRIAXIAL TESTING EQUIPMENT

The triaxial cells used for the testing program were manufactured by Wykeham Farrance Engineering Ltd. of Slough, England. They were first used at MIT 25 years ago for investigating the strength-deformation properties of stabilized soils (sponsored by the Army Material Command). The cells were modified to accommodate lubricated end platens, internal force measurement, on-specimen axial strain measurement and internal temperature measurement.

Figure 2.5 is a side view of the triaxial cell. As part of the cells' modification, the bottom pedestal and top cap were replaced by enlarged "lubricated" platens that could accommodate radial deformation of the soil specimen during shear. The specimens initially measure 1.4 inch diameter and the end platens are 1.6 inch diameter. The modified top cap is a floating top cap, meaning that it is not rigidly connected to the loading piston. The cylinder wall of the triaxial cell has been replaced with a much longer one to accommodate the length of the new top cap and internal load cell. The modified triaxial cell used for unfrozen tests is essentially identical, except drainage connections have been provided to both the bottom and top of the specimen.

Silicone 510 oil manufactured by the Dow-Corning Company is used in the triaxial cell as the pressurizing medium. It was selected for its low viscosity at low temperatures, its nonconducting properties (necessary for internal force and temperature measurements with electronic devices) and its compatibility with the prophylactic membranes used to surround the frozen and unfrozen sand specimens. The manufacturer recommended its use for temperatures down to -51°C . Temperature measurements inside the triaxial cell during frozen tests indicate that the silicone oil acts as an efficient temperature buffer. Data taken during individual tests show a temperature variation of $\pm 0.05^{\circ}\text{C}$ at any individual location. While there is no obvious cyclic component to the variation, there is a 0.3°C temperature gradient within the cell. This gradient is opposite (warmer near the top) to the temperature gradient measured in the environmental chamber. It is most likely

caused by heat generated by the internal instrumentation. We are currently exploring methods for internal circulation of the silicone oil to eliminate the temperature gradient.

The cell pressure (and the back pressure in the unfrozen tests) is applied using a DC-servomotor based pressure/volume control system which is capable of continuously sensing and adjusting the fluid pressure to maintain a target value. A DC-servomotor is attached to a ball-screw actuator which drives a piston into a reservoir of silicon oil (Fig. 2.6). The motion of the piston then serves to increase or decrease the fluid pressure. A closed loop analog circuit is used to control the motor for the frozen tests. This analog system was also initially used to control the cell pressure in the unfrozen tests but now a digital closed loop circuit is employed. This newer circuit system provides for complete computer automation of three axes (axial, cell and pore pressures) during the testing process (see next paragraph).

The current frozen soil testing system uses a Wykeham Farrance T-57 screw driven loading frame having a nominal capacity of 10,000 pounds. An AC motor and gear box advance the loading platen at a constant rate of deformation. Due to the flexibility of the loading frame and the use of lubricated end platens, the actual rate of deformation experienced by the specimen is not constant, but increases slowly and reaches its maximum at about 0.5% strain. The initial strain rate is roughly one order of magnitude less than the maximum or nominal strain rate. Thus the tests are not really sheared at a constant strain rate until reaching the "large strain" region. (Note: a new two axis computer control system will be implemented to decrease the strain rate variability in future tests). The unfrozen soil test system initially used a Wykeham Farrance screw driven loading frame. This mechanical system was replaced by a hydraulic loading jack capable of loads exceeding 8000 pounds. The new hydraulic system, along with the aforementioned DC-servomotor based, pressure control system, allows for complete computer automation of the unfrozen testing program.

The deviator force applied to the specimen is measured by a load cell located inside the triaxial chamber at the end of the loading piston. This avoids measurement errors due to friction between the loading piston and its brass bushing guide. The load cell contacts the floating top cap with a cylindrical seating piece. This piece is in contact with the entire flat end of the cylindrical top cap and has a small circular lip with an inside taper to provide a guide during set up when the load cell and piston must be lowered onto the top cap. This lip also restricts lateral motion of the top cap during shear.

Axial strains are measured by two Alternating Current Differential Transformers (ACDT's) mounted in diametrically opposite positions around the circumference of the sand specimen on a specially designed yoke (Fig. 2.7). The upper piece holds the barrels of the displacement transducers and the cores rest on the lower yoke. Each yoke is spring-loaded and contacts the specimen at third points around the circumference. The face of each contact foot is a flat rectangle approximately 0.125 inches wide and 0.25 inches long. During set up, three alignment rods run between the upper and lower yoke. These are held in position with 0.063 inch diameter hardened steel pins. The function of these rods is to aid in the placement of the yoke on the specimen and to fix the appropriate gage length. After placing the yoke on the specimen, these small pins are removed and the alignment rods drop freely away from the yoke allowing it to be free floating and move unimpeded as the specimen deforms.

Interchangeable cell pressure (and pore pressure for the unfrozen tests) transducers are mounted directly on the triaxial cell. These have capacities of 200 psi, 2000 psi or 5000 psi depending on the particular test requirements.

Volume changes of the frozen sand specimens during shear were computed from the motions of the cell pressure/volume controller piston and the triaxial cell loading piston. Displacements of these are measured by DC-DC type Linear Variable Differential Transformers (LVDT's) mounted on each piston. The corresponding volume changes are computed from the cross-sectional area of each piston. Various "corrections" were then

applied to these measurements in order to account for leakage of the cell fluid, compressibility of the cell fluid and triaxial chamber and flexure of the base of the triaxial cell (Chapter 3 of Andersen 1991). This method of measurement results in a maximum volumetric strain error of $\pm 0.20\%$. The error increases with the test duration (i.e., the slow tests are subject to the largest error).

Volume changes during drained shear tests on unfrozen sand are measured from motions of the back pressure controller piston. This is a direct measure of the fluid passing into or out of the specimen and is not subject to the same complications as for the frozen tests.

2.5 FROZEN MANCHESTER FINE SAND TEST PROCEDURES

2.5.1 Specimen Preparation

The molds used for the preparation and freezing of the Manchester Fine Sand specimens were obtained from CRREL and were the same molds used previously by Martin et al. (1981). Figure 2.8 presents a series of schematic drawings of one of these molds in different stages of operation. Figure 2.8(a) is the mold prepared for the wet tamping procedure, Fig. 2.8(b) is the mold prepared for multiple sieve pluviation, Fig. 2.8(c) is the mold prepared for saturation and Fig. 2.8(d) is the mold prepared for freezing.

The vast majority of the specimens were prepared using multiple sieve pluviation (MSP) as outlined by Miura and Toki (1982). This produced specimens of uniform density with relative densities ranging from 20 to 100%. In this procedure (set-up shown in Fig. 2.9), oven dried sand is poured into a funnel mounted in a frame above the mold. The sand falls out of the funnel, through a vertical plexiglas tube and across four 3 inch diameter sieves (two with No. 20 mesh sizes and two with No. 10 mesh sizes). The sieves act to disperse the raining cloud of sand. The sand then falls across a knife edge guide and into the mold.

After pluviation, the dry sand specimens are taken into the growth room maintained at 0°C. The upper side of each mold is connected to one reservoir and the lower side is connected to another reservoir. A 28-inch Hg (95 kPa) vacuum is drawn on the specimens and deaired, deionized, distilled water is passed through the molds from the base to the top by gravity feed under an initial head of approximately five feet of water. After several pore volumes of water pass through the specimens, the upper and lower reservoirs are raised to the same elevation above the specimens. This is maintained under vacuum over night.

The following morning, the vacuum is slowly removed, the upper reservoir is disconnected and the lower reservoir is placed at the elevation of the top of the specimens. The brass top caps of the specimen preparation molds are removed and replaced with freezing caps. The filter papers are retained on the top of each specimen. The freezing caps are placed in direct contact with the filter paper. Refer to Figure 2.8(d). Antifreeze fluid at -15°C is circulated through the freezing caps and the specimens are frozen from the top down, while allowing for drainage through the base of the molds and into the lower reservoir. The entire freezing process lasts approximately four hours. After freezing, the specimen (with surrounding plexiglas split sleeve) is removed from the mold and stored in a freezer until trimmed for testing.

The actual trimming of the specimen takes place in the vestibule room of the cold room facility. This room is maintained at -4 to -5°C. The specimens are taken from the testing room at -15°C to the vestibule for a maximum of 5 minutes for trimming. This prevents melting due to handling. One end of the specimen is extruded approximately 0.25 inches out of the split sleeve and a hose clamp is placed on the split sleeve to hold the specimen firmly in position. The trimming is done by hand with sharpened steel knives. After trimming one end, the specimen is partially extruded from the other end and the process is repeated. In order to measure the parallelism of the ends, the specimen is taken out of the split sleeve and placed on a metal stand with a spring loaded depth gage

sensitive to 0.0001 inch. The height is selectively trimmed to within a 0.001 inch tolerance across the diameter of the specimen.

The diameter of the specimen is measured with a hand held micrometer with a direct readout to 0.001 in. at eight locations along the length (at each end and third points, two measurements at 90° to each other at each point). The height of the specimen is measured at four locations spaced at roughly 90° around the circumference. The averages of the diameter and height measures are used subsequently to compute the specimen volume. The entire trimmed specimen is then weighed on an electronic scale sensitive to ±0.01 g.

2.5.2 Specimen Set-Up

For those specimens tested with "lubricated" ends, an ice cap was frozen onto each end and subsequently trimmed in the same manner as the frozen sand. In order to properly align the frozen sand specimen between the base pedestal and floating top cap of the triaxial cell, 0.063 in. diameter holes are drilled through the center of each ice cap and into the frozen sand using a drill bit mounted in a plexiglas boring tool which fits around the outside of the plexiglas split sleeve. These holes are bored approximately 0.125 in. deep and mate with 0.063 in. diameter hardened steel pins mounted in the center of the base pedestal and top cap.

Prior to placement of the trimmed frozen sand specimen in the triaxial cell, the base pedestal and top cap are covered with high-vacuum silicone grease and a prophylactic membrane is placed on the base pedestal with two O-rings. The specimen is placed on the base pedestal (bottom end down) and the top cap is lowered onto the upper surface of the specimen using a specially designed alignment jig mounted directly on the base of the triaxial cell. An axial force is applied by hand to the specimen through the alignment jig in order to force the excess grease from between the specimen and the brass surfaces of the base pedestal and top cap and to bring the frozen sand specimen into vertical alignment. The grease also acts to hold the specimen and top cap on the base pedestal during the set

up procedure. The extruded grease is wiped off and the rubber membrane is stretched from the base pedestal over the specimen and onto the top cap. One of the O-rings on the base pedestal is raised to the top cap to secure the membrane in place.

The axial displacement yoke is placed on the outside of the membrane at roughly the third points along the specimen so that the active gage length includes the central portion of the specimen. After placement of the yoke on the specimen and removal of the alignment posts, the gage length is measured using an optical scope with a veneer that has a direct read out of 0.001 of an inch.

With the axial displacement yoke in position, the top of the triaxial cell is lowered onto the base using a guide stand to prevent accidental disturbance of the axial displacement yokes. The load cell is gently lowered onto the top cap and the top and base of the triaxial cell are bolted together. The loading piston is then locked into position and the entire triaxial cell is placed in the loading frame. Each of the electronic devices are connected to the power supplies and data acquisition system and the output level of each device is checked to verify that it was within the normal range.

A slight preload (0.1 to 0.3 MPa) is applied to the specimen through a manual crank on the loading frame. It is reapplied at various times throughout the preshear stage of the test because it gradually reduces over time due to squeezing out of the grease and creep of the ice cap and frozen sand.

2.5.3 Specimen Shearing

The triaxial cell is filled with silicone oil using a diaphragm pressure reservoir located inside the cold room. The cell pressure is applied and the specimen is allowed to sit in the triaxial cell under pressure with the preload until both the temperature and the leakage rate of oil out of the triaxial cell stabilize. This preshear pressurization phase lasts longer than the expected shearing time of each test.

After the preshear period, the compressibility of the cell fluid is measured by cycling the cell pressure and measuring the corresponding volume change. Just prior to

shearing, the small preload is removed and the zero of the load cell is recorded. The deviator stress is applied to the specimen with the screw driven loading frame. In general, the specimens are sheared to axial strains in excess of 20%. After shearing, the cell pressure is relieved and the triaxial cell is removed from the loading frame and disassembled. The specimen is photographed and then removed from the base pedestal. The final diameter is measured near the ends and at third points along the length.

Calculation of the dry density of the test specimen is based on the volume of the trimmed specimen before shear and dry weights measured after pluviation (minus the weight of trimmings), after shearing (which may contain small amounts of silicone grease or oil), and after washing to remove any silicone (which may also lose some soil particles). The estimated standard deviation in the reported values of relative density is $\pm 2\%$. Table A.1 presents the physical properties of the specimens.

2.5.4 Precision of Stress-Strain Parameters

Chapter 4 of Andersen (1991) presents an "error analysis" of results from nine pairs of tests in order to estimate the likely precision of the reported test data. The following summarizes the principal conclusions, where COV is the coefficient of variation and SD is the standard deviation.

- 1) For Young's modulus wherein the two ACDT's showed "good" or "fair" (as opposed to "poor") agreement:

$$\text{COV} = 9.5\% \text{ with } \text{SD} = \pm 4.5\%.$$

- 2) For the upper yield stress and the corresponding axial strain:

$$\text{COV} = 7\% \text{ with } \text{SD} = \pm 3.5\% \text{ for stress}$$

$$\text{COV} = 8\% \text{ with } \text{SD} = \pm 7\% \text{ for strain.}$$

- 3) For the peak strength and the corresponding axial strain from tests having "good", "fair" and "poor" (as opposed to "very poor") stability. These qualifiers regard the lateral sliding stability at large strains due to the lubricated end conditions:

COV = 3.5% with SD = $\pm 2.5\%$ for stress

COV = 13% with SD = $\pm 9\%$ for strain.

Andersen (1991) also describes the procedure used to compute the instantaneous cross-sectional area of the specimens during shear. This made it possible to correct for the effects of bulging within the central portion or flaring at the ends that occurred in many of the tests.

2.6 UNFROZEN MANCHESTER FINE SAND TEST PROCEDURES

Many of the same procedures used in setting-up frozen specimens are also used on unfrozen specimens. The major difference from frozen test specimens is that unfrozen specimens are formed directly on the pedestal of the triaxial cell base. It is important to set-up the specimen on a clean, dry system. The base pedestal and top cap are prepared by first flushing all drainage lines and ports with water to remove any debris (sand, silicon oil, etc.) in the lines. The lines are then flushed with pressurized air to remove the water from the lines and dry the drainage system. Porous stones are placed in the drainage ports in the pedestal and top cap. Lubricated ends, ranging from greased latex rubber to a silicone coating, are then applied to the pedestal and top cap. A thick (0.014-inch) rubber membrane is attached to the pedestal using O-rings and vacuum grease. A membrane expander is then placed over the pedestal, and a slight vacuum (8-inch Hg) is placed on the membrane to create a cylindrical (1.4 inch diameter) volume that forms the specimen. Multiple sieve pluviation is used to form specimens (see Fig. 2.10 and Section 2.5.1), after which excess sand is removed from the top of the newly-formed specimen and the top cap is placed on the specimen using the alignment jig.

An internal drainage line is attached to the top cap to create a closed system. The small vacuum being maintained on the outside of the membrane (to keep it open during sand placement) is now transferred to the specimen and increased to 15-inch Hg. This vacuum will be maintained until the specimen is placed under an equivalent cell pressure.

The membrane expander/sample former is removed, and sample dimensions (height and diameter) are measured using the optical scope. Two ACDTs are placed on the specimen using an axial displacement yoke assembly similar to that used in frozen MFS tests. The gage length is then measured using the optical scope.

The top of the triaxial cell is lowered onto the base and load cell is gently lowered onto the specimen. The top and base of the cell are then bolted together and the piston is locked in place. The entire cell is moved over to the loading frame, and electronic devices are connected and checked. The cell is raised so that the piston is in contact with the loading point of the load frame. The cell is then filled with oil.

The following testing procedures are those used with the computer automated system. Note that prior to computer automation, the raising and lowering of cell and back pressures was performed using an analog circuit loop and manual control techniques. Computer automation has allowed for better control of the cell and back pressure during the test. A cell pressure, equivalent to the applied vacuum on the specimen, is placed on the specimen to provide support. As the cell pressure increases, the vacuum is slowly released so that the effective stress on the sample remains approximately the same. When the cell pressure is reached and the vacuum has been totally removed from the specimen, the specimen is flushed with carbon dioxide for approximately 15 minutes to remove as much air as possible from the pore voids. At least three pore volumes of deaired, de-ionized water are then passed through the specimen (flowing bottom to top) to displace the carbon dioxide.

The specimen is saturated by increasing the cell pressure and back pressure, in equal increments to maintain the same effective stress, until a cell pressure of 1.1 MPa and backpressure of 1.0 MPa are obtained. The specimen is allowed to saturate overnight under these conditions. The change in volume of the specimen during overnight saturation is then inferred from overnight volume measurement as well as a leakage rate from the back pressuring system under constant pressure conditions.

The following day, successful saturation is confirmed by measuring the B-value ($=\Delta u/\Delta \sigma_c$) using computer control. With a successful B-value obtained (i.e., at least 95% within 2 minutes), the specimen is hydrostatically consolidated by incrementally raising the cell pressure to obtain the desired preshear effective stress (Note: specimens sheared at an effective confining pressure of 0.1 MPa do not undergo this consolidation process). The changes in pore volume are used to compute the volumetric strain during consolidation.

The specimen is sheared after allowing some time for secondary compression (usually two or more hours). In undrained shear, the backpressure drainage lines are closed and pore pressures developed during shear are measured. In drained shear tests, the back pressure drainage lines remain open and volume changes are measured as the controller's piston moves in or out to maintain the constant back pressure. The specimen is usually sheared to axial strains in excess of 20 percent.

After shearing, the cell and back pressures are relieved, oil is removed from the cell, and the cell removed from the loading frame and disassembled. The specimen is photographed and specimen form is noted. The specimen is frozen while still on the pedestal, then the frozen specimen is removed from the cell base for measurements of soil weights before and after oven drying. These data are used to compute the preshear void ratio and relative density (after accounting for volume changes for drained shear tests). Similar variations in specimen properties exist for the unfrozen MFS specimens as noted for frozen MFS specimens.

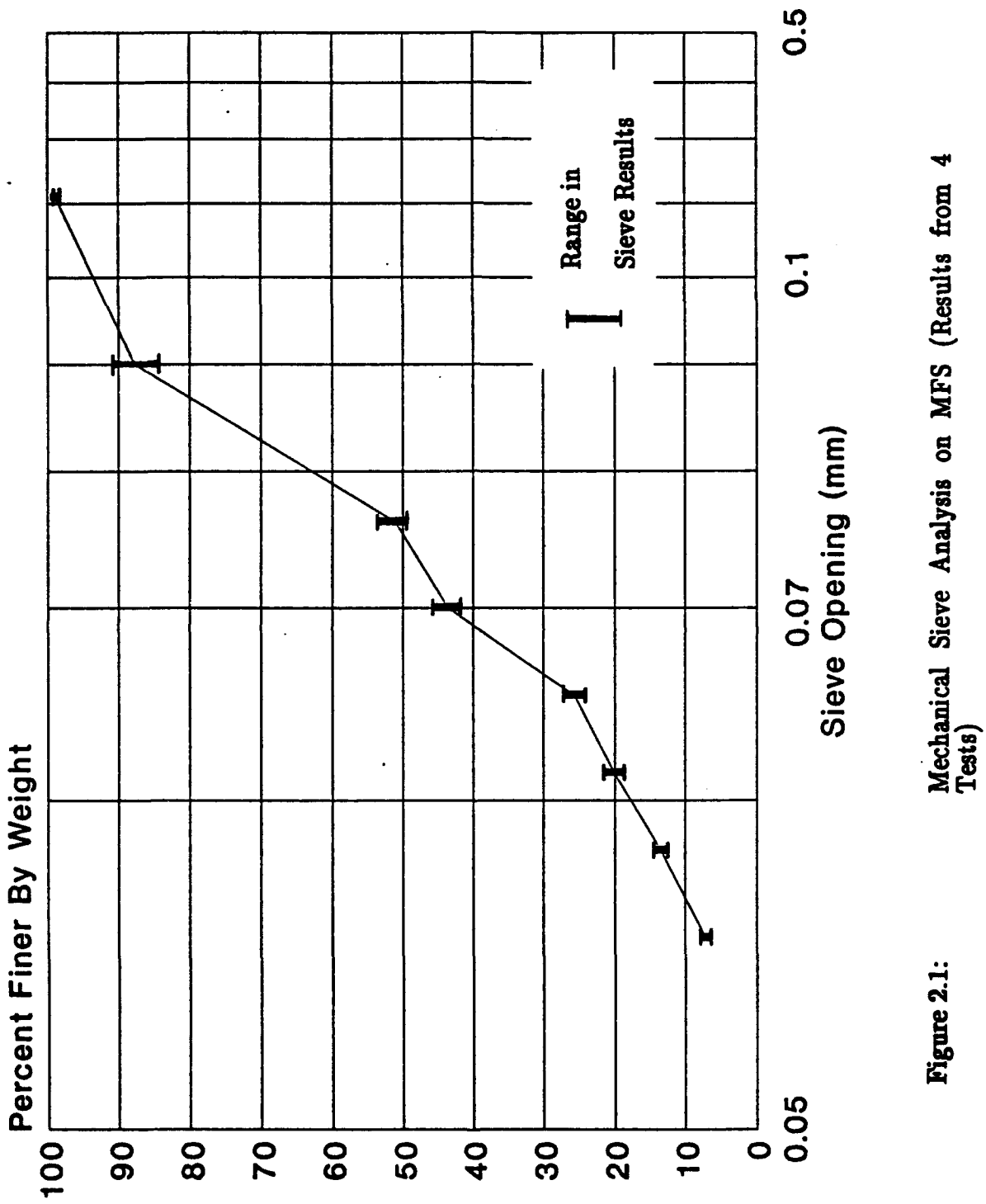
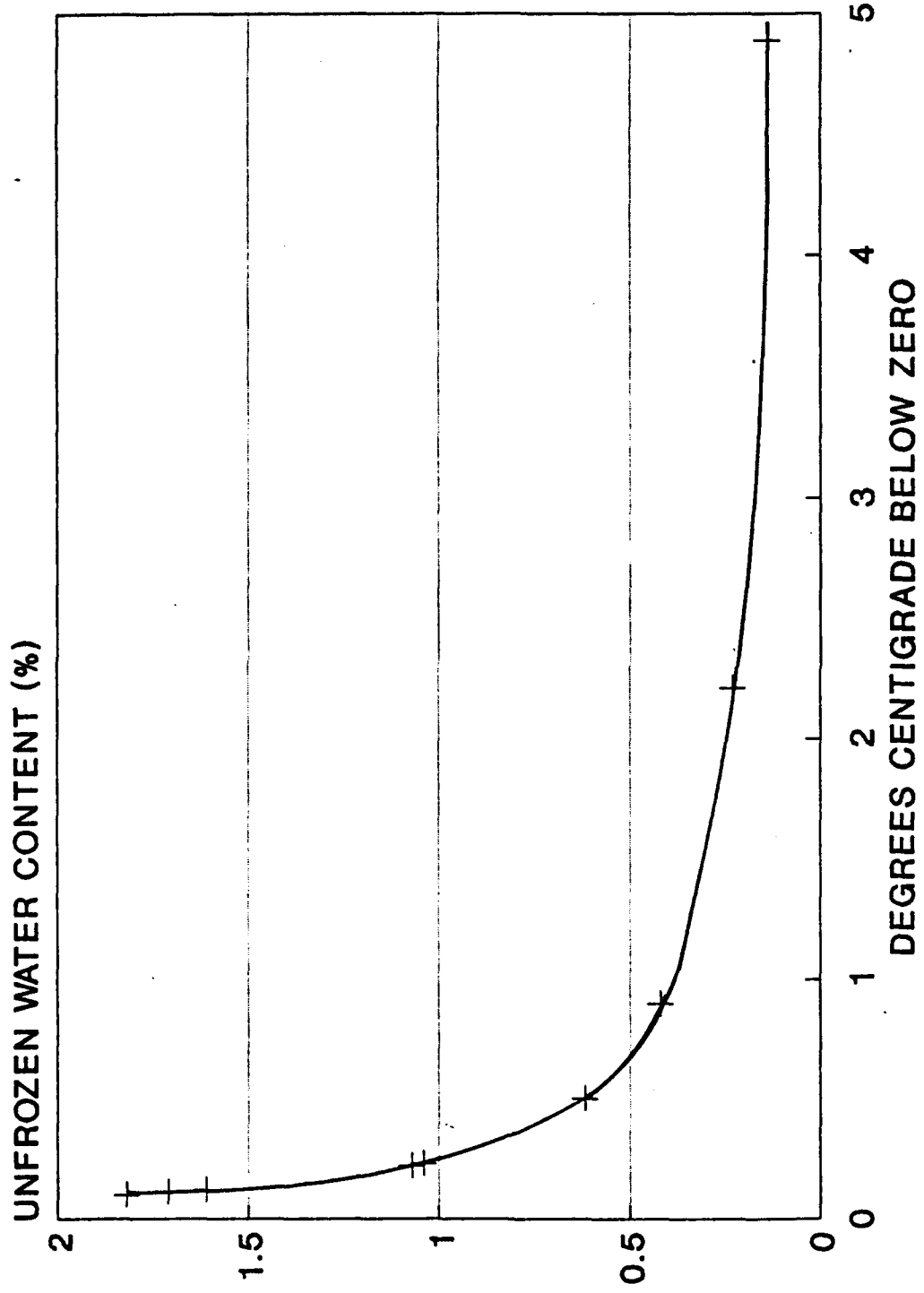


Figure 2.1:

Mechanical Sieve Analysis on MFS (Results from 4 Tests)



Tested by Pat Black 8/2/90

Figure 2.2: Unfrozen Water Content Versus Temperature for MFS

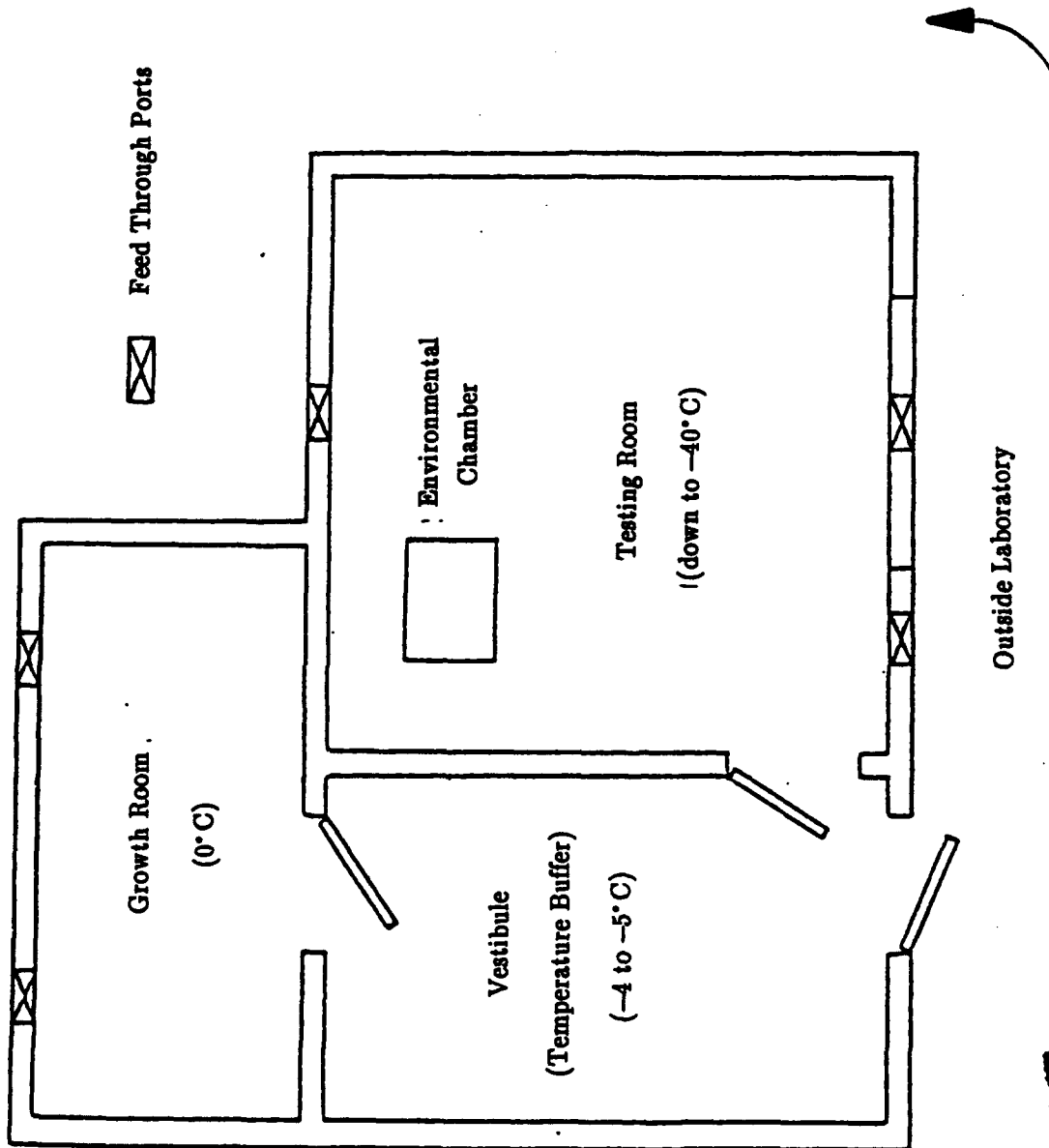


Figure 2.3: Plan View of MIT Cold Room Facility

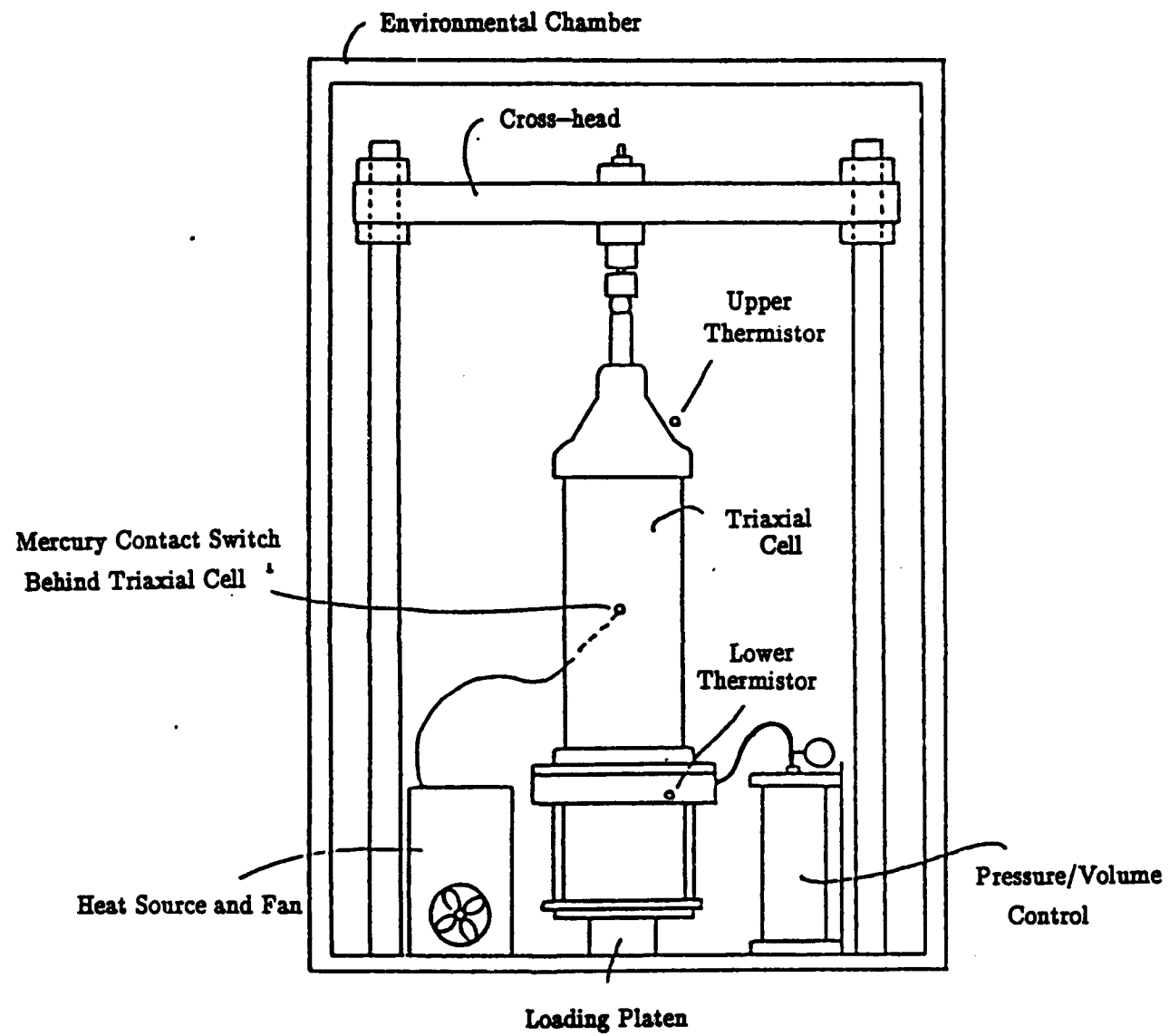


Figure 2.4: Schematic View of Environmental Chamber and Triaxial Cell (Before Addition of Second Heat Source)

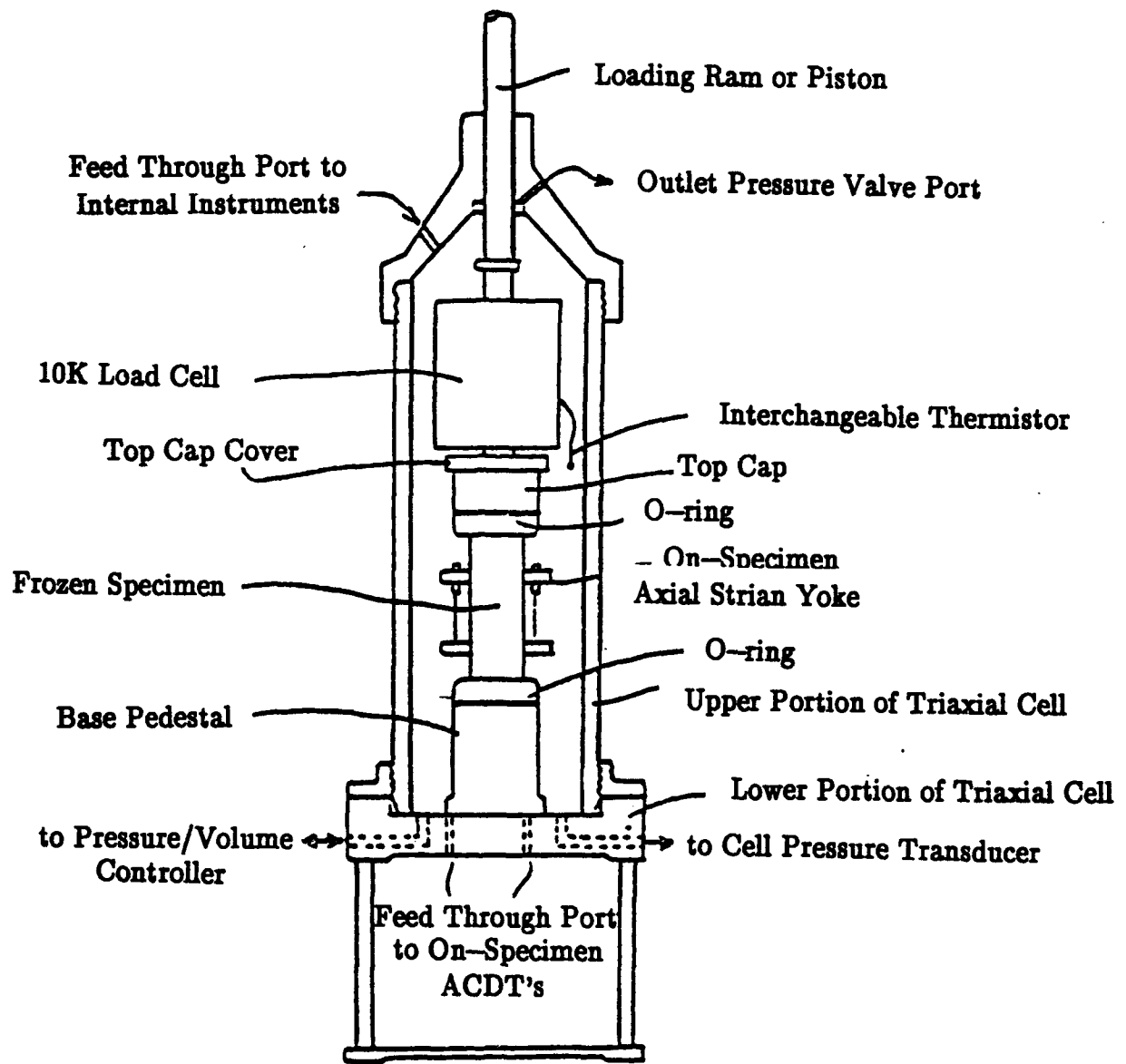
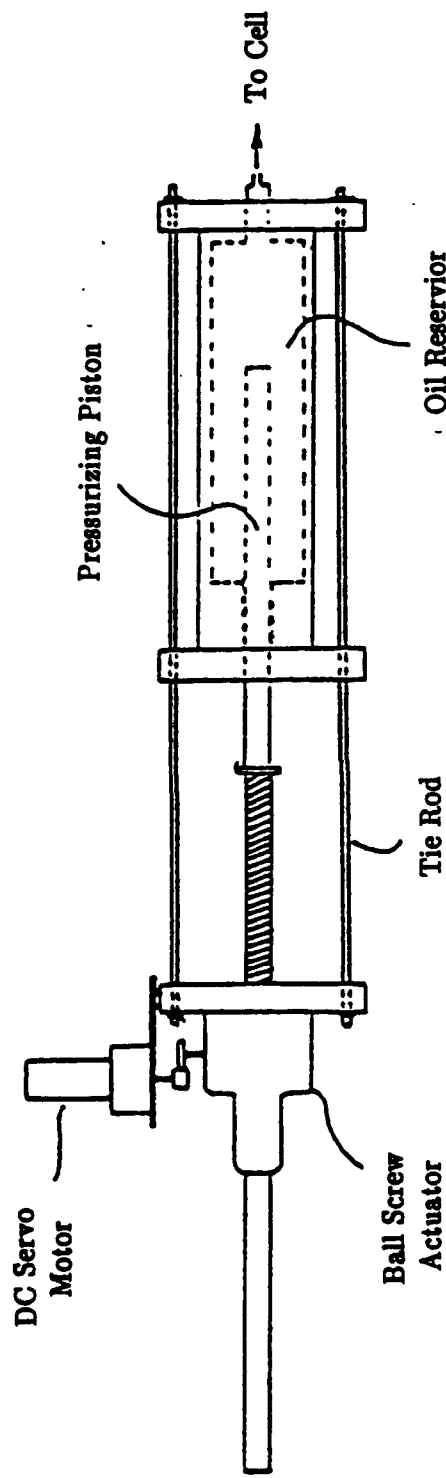


Figure 2.5: Details of the Modified High Pressure Triaxial Cell for Testing Frozen Soil

TOP VIEW



PLAN VIEW

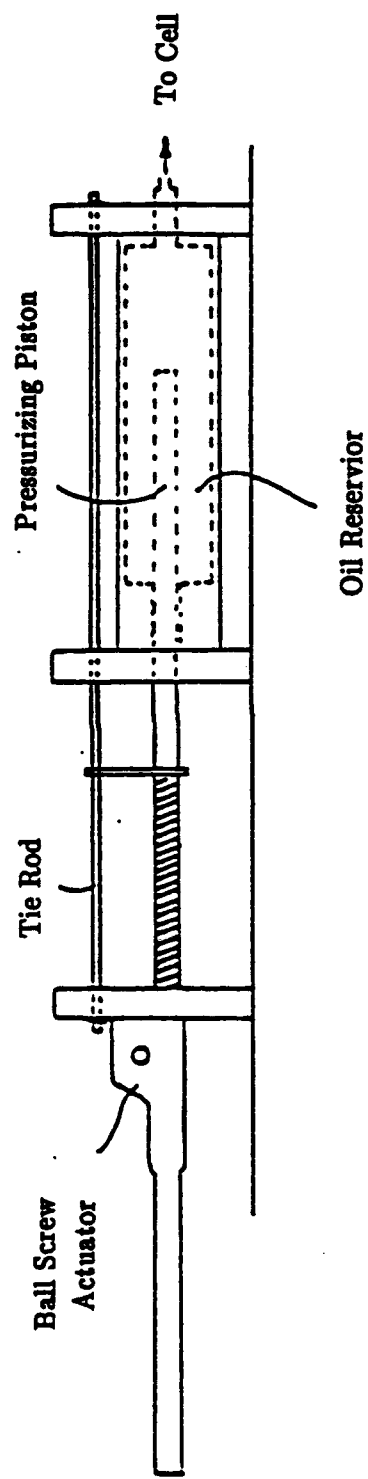
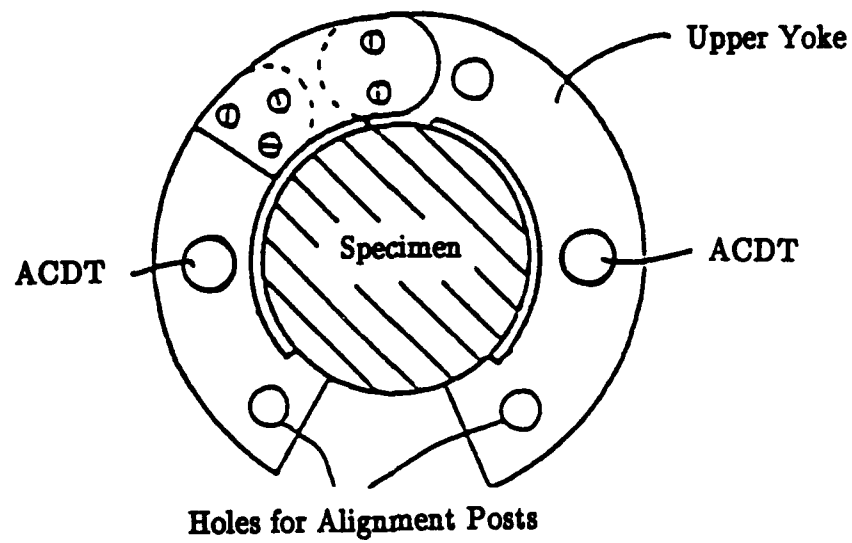


Figure 2.6:

Schematic Drawing of Mechanical Portion of Pressure/Volume Controller

TOP VIEW



SIDE VIEW

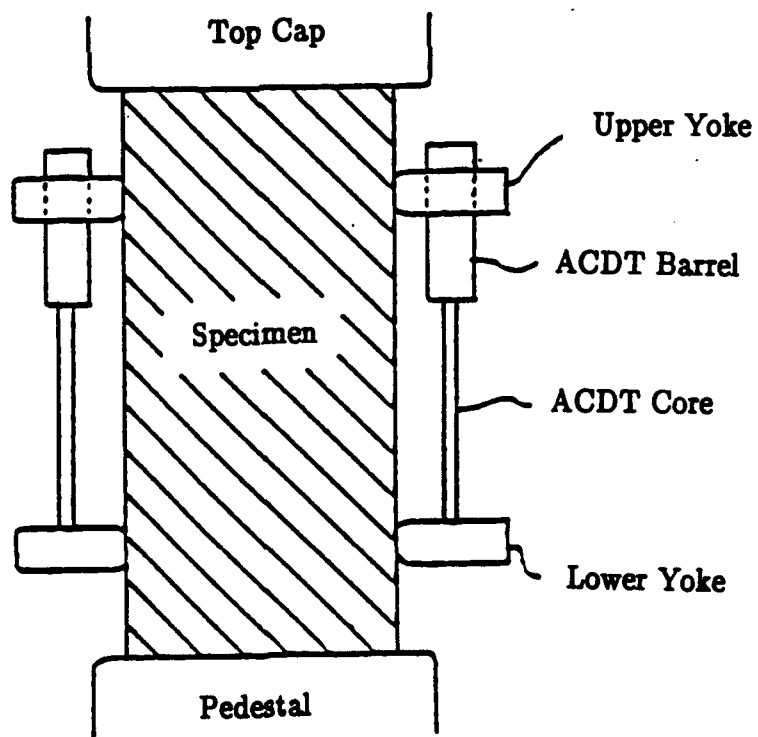


Figure 2.7: Details of On-Specimen Axial Strain Yoke

LEGEND

- 1 Plexiglas Split Sleeve
- 2 Plexiglas Hollow Cylinder
- 3 Porous Stone
- 4 Filter Paper
- 5 Drainage Lines
- 6 Brass Collar
- 7 Knife Edged Aluminum Guide
- 8 Compaction Collar
- 9 Brass Base
- 10 Bolt
- 11 Freezing Cap
- 12 Inlet for Freezing Fluid
- O-rings

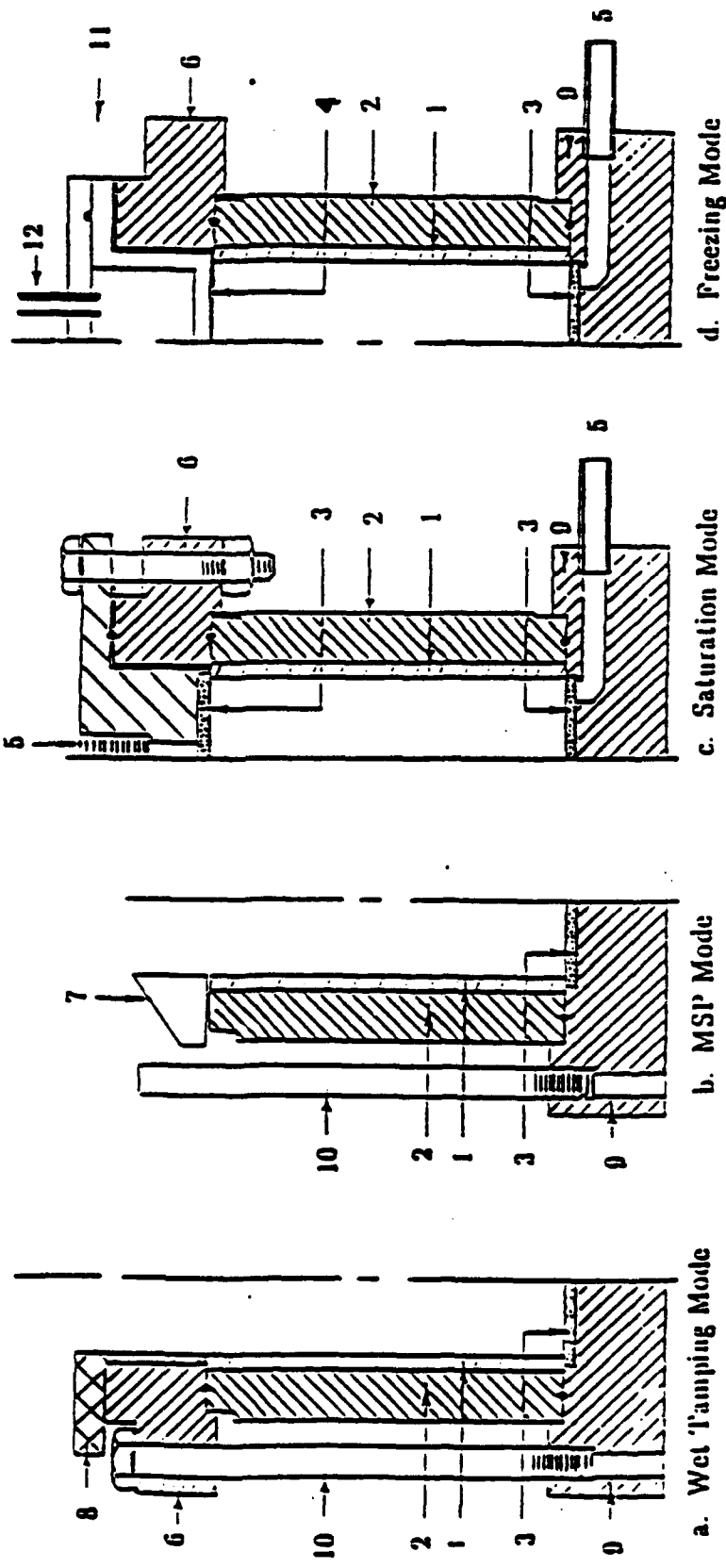


Figure 2.8:
Schematic Drawing of Specimen Preparation Molds
(after Martin et al. 1981)

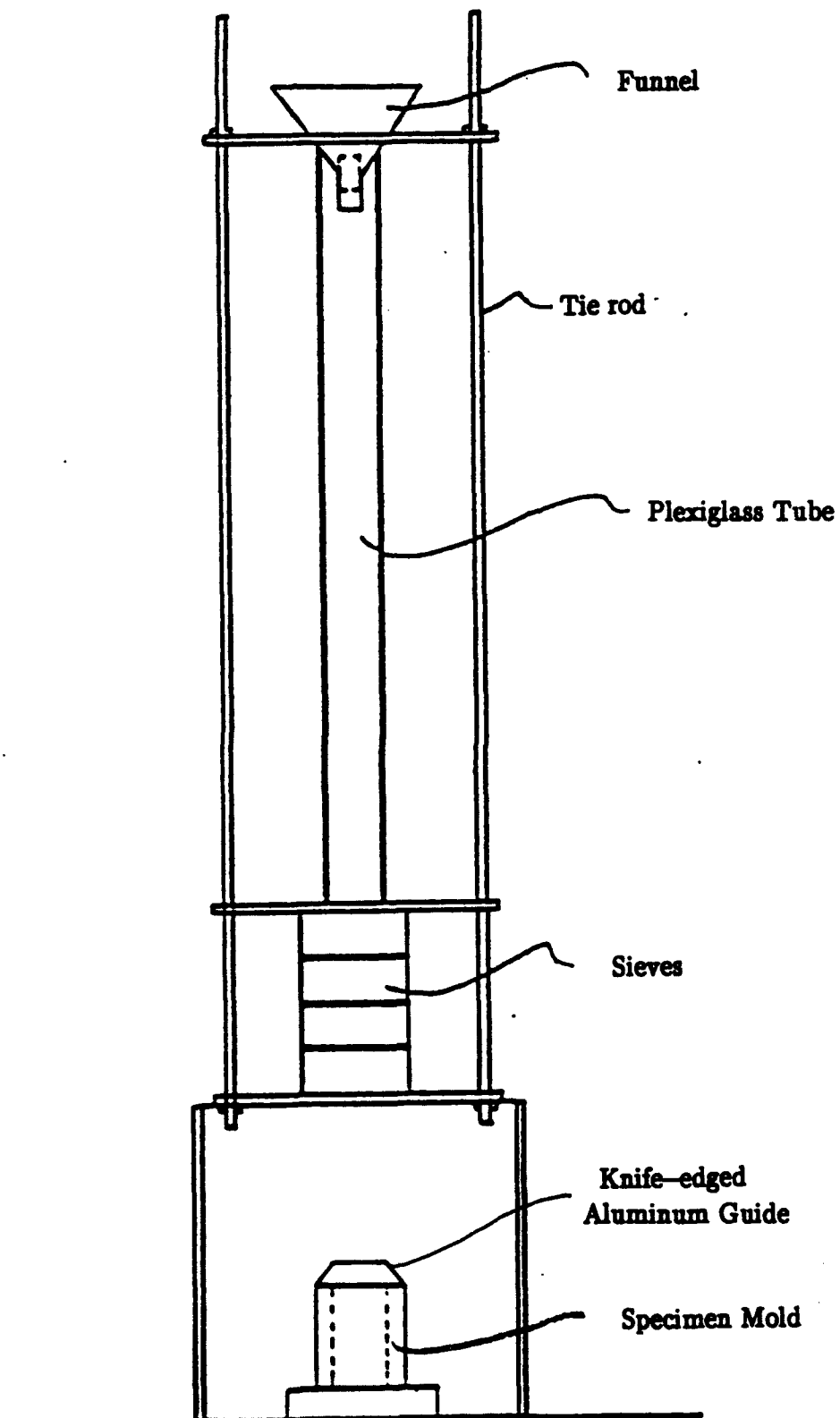


Figure 2.9: Schematic Diagram of Multiple Sieve Pluviation Frame for Frozen MFS Specimen Preparation

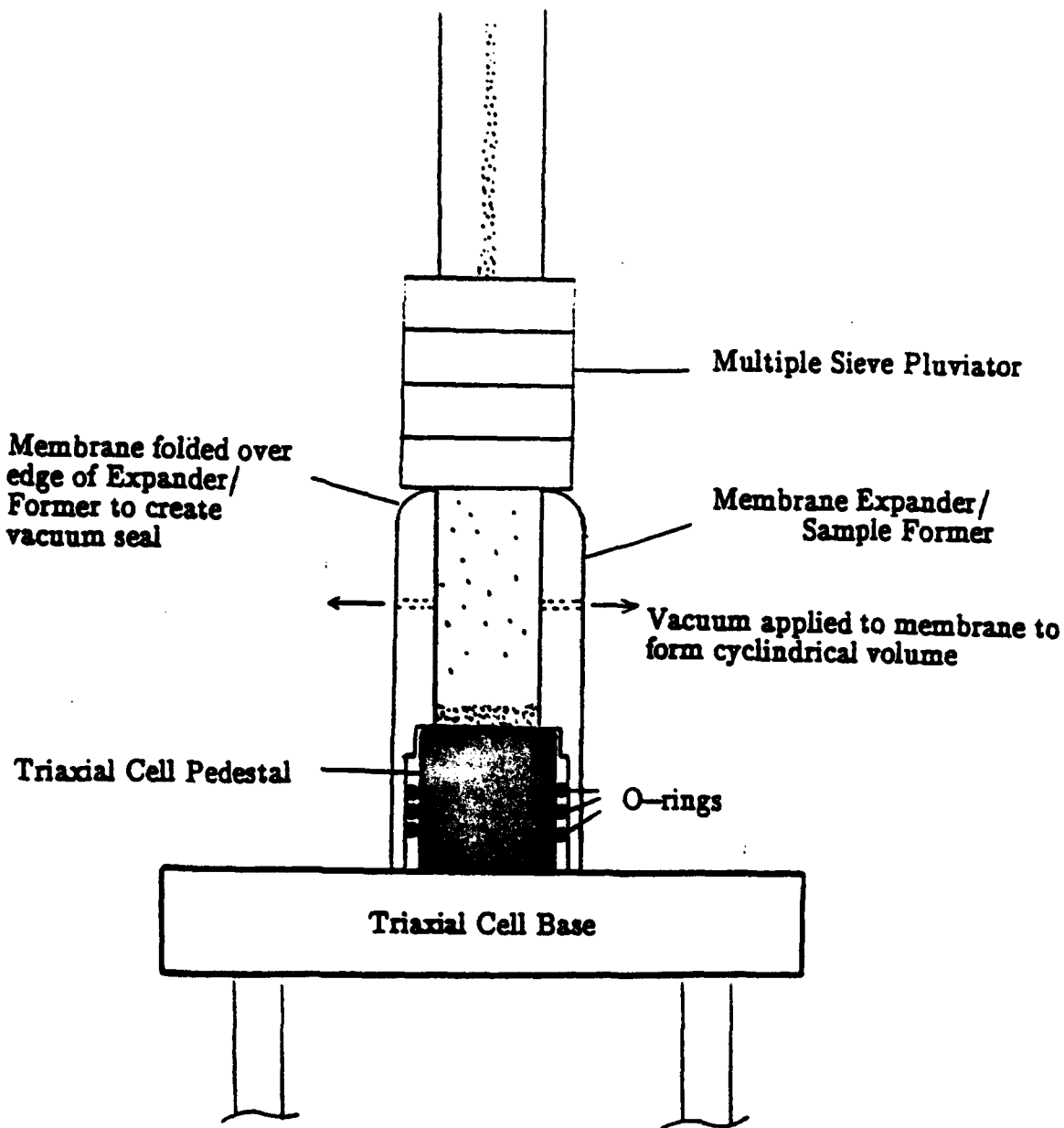


Figure 2.10: Unfrozen MFS Specimen Preparation Using Membrane Expander/Sample Former and Multiple Sieve Pluviation

3. BEHAVIOR OF FROZEN MANCHESTER FINE SAND IN TRIAXIAL COMPRESSION

This section presents the results of the triaxial compression tests conducted on frozen Manchester Fine Sand. Most of this presentation is abstracted from Andersen's (1991) doctoral thesis that focused on a comprehensive evaluation of the effects of relative density (D_r), strain rate ($\dot{\epsilon}$) and confining pressure (σ_c) on stress-strain behavior at one temperature (-9.5°C). After outlining the scope of the testing program, which includes subsequent tests at varying temperature, a qualitative overview of the stress-strain behavior and definitions of the parameters used to describe the stress-strain response follow. A quantitative treatment of the stress-strain behavior at -9.5°C is then presented in two major sections, small strain behavior and large strain behavior. The small strain behavior is considered in terms of the Young's modulus, the proportional limit and the yield offset stress at 10^{-4} strain. The large strain behavior is considered in terms of the upper yield region, the strain hardening or strain softening region, the peak strength region and the volumetric behavior.

Section 3 also presents results from tests conducted at different temperatures. These data and their evaluation are incomplete. Section 3 concludes with recommendations for further research, namely: completion of testing at varying temperatures; and development of new experimental techniques in order to conduct tests on sand that is frozen after application of the confining pressure rather than vice versa. This will allow for the evaluation of how the magnitude of the pre-freezing effective stress acting on the sand skeleton affects strength-deformation properties.

Appendix A contains the tabulated data used to construct the summary plots presented in Section 3 (See the cover page of Appendix A for a listing of these tables).

3.1 SCOPE OF TESTING PROGRAM

Table 3.1 summarizes the scope of the testing program. The "principal" program consists of tests at various relative densities, confining pressures and strain rates. The relative density (D_r) varied from 20 to 100% and the confining pressure (σ_c) varied from 0.1 to 10.0 MPa. Three nominal strain rates ($\dot{\epsilon}$) were used: $3 \times 10^{-6}/\text{sec}$, $3 \times 10^{-5}/\text{sec}$ and $4 \times 10^{-4}/\text{sec}$, referred to as "slow", "moderate" and "fast" tests, respectively. One specimen was tested at a strain rate of $1.2 \times 10^{-4}/\text{sec}$ (referred to as "intermediate"). The testing temperature was $-9.55 \pm 0.3^\circ \text{C}$, except for one test having a temperature of about -15°C .

Six tests are presented to show initial results from the new temperature testing program. Temperatures for these moderate strain rate tests range from -5 to -28°C . A confining pressure of 0.1 MPa was used and relative densities range from 41 to 48%.

3.2 DEFINITION OF PARAMETERS AND GENERAL OVERVIEW OF STRESS-STRAIN BEHAVIOR

3.2.1 Definition of Parameters

Figure 3.1 shows the graphical construction techniques used by Andersen (1991) to obtain various stress-strain parameters from the triaxial compression test program. The figure plots engineering axial strain ($\epsilon_a = \Delta L/L_0$) versus deviator stress ($Q = \sigma_1 - \sigma_3$) and volumetric strain ($\epsilon_v = \Delta V/V_0$, positive for dilation = expansion). The presentation will focus on the following parameters and behavioral features:

- 1) Values of Young's modulus (initial slope of the stress-strain curve), the proportional limit (point on the stress-strain curve where the response departs significantly from linear), and the yield offset stress at 10^{-4} strain (intersection point of the stress-strain curve and a line with a slope of the Young's modulus translated by 10^{-4} strain). See Fig. 3.1(a), plotted to $\epsilon_a = 0.1\%$, for graphical definitions.
- 2) Values of the upper yield stress (Q_{uy}), the knee of the stress-strain curve, and its corresponding strain (ϵ_y) obtained from Fig. 3.1(b) for stress-strain curves plotted

to $\epsilon_a = 2.6\%$. (Note: although plastic strains start at the proportional limit, Fig. 3.1(a), they only become really significant in the "upper yield" region).

- 3) The nature of the post upper yield behavior, i.e., the degree of strain hardening or strain softening after the knee as per Fig. 3.1(b). Most curves exhibited a distinct double yield behavior similar to that of fine-grained polycrystalline ice (e.g., Mellor and Cole 1982; Cole 1987) as further described in Section 3.2.2.
- 4) Values of the peak stress (Q_p) and corresponding strain (ϵ_p) as per Fig. 3.1(c). In general, specimens tested at low confining pressures experienced post peak strain softening, wherein those at the highest confining pressures did not (see Section 3.2.2).
- 5) The volumetric behavior, including the rate of dilation = $d\epsilon_v/d\epsilon_a$, as per Fig. 3.1(d).

3.2.2 Types of Stress-Strain Curves

The general shape of the stress-strain curves as a function of the relative density, confining pressure and strain rate can be classified into seven different types. Figure 3.2 presents several normalized (i.e., deviator stress divided by the upper yield stress, Q/Q_{uy}) stress-strain curves that serve to illustrate visually these different types of behavior.

A qualitative description of each type of stress-strain behavior follows.

Low Confining Pressure

Type I	The peak strength occurs at the upper yield point. This is followed by pronounced strain softening.
Type II	The upper yield stress (knee in the stress-strain curve) is followed by a yield drop. A slight amount of strain hardening occurs after this yield drop to a second peak having a strength similar to the upper yield stress. Some strain softening occurs at very large strains.
Type III	The upper yield stress is followed by a plateau in the stress-strain curve. After this plateau, there is a significant amount of strain hardening to the peak strength, followed by strain softening.

Type IV The upper yield stress is followed by immediate strain hardening to the peak strength. After the peak, there is a considerable amount of strain softening.

For the low confining pressure Type I-IV curves, strain softening causes the large strain post peak resistance to be generally less than the upper yield stress.

High Confining Pressure

Type V The upper yield stress is followed by a yield drop. After the yield drop, there is a slight amount of strain hardening. The deviator stress is almost constant to very large strains.

Type VI The upper yield stress is followed by a small plateau. After the plateau, there is continuous strain hardening to a peak strength at very large strains.

Type VII The upper yield stress is followed by an immediate and significant amount of strain hardening to the peak strength at very large strains.

For the high confining pressure Type V-VII curves, the large strain resistance will generally be larger than the upper yield stress.

The presentation first summarizes Young's modulus, etc. to represent small strain behavior, and then various aspects of large strain behavior (upper yield stress, peak stress, volumetric strains, etc.) as a function of sand density, confining pressure and strain rate.

3.3 SMALL STRAIN BEHAVIOR

The small strain behavior can be described in terms of the measured Young's modulus, the proportional limit, and the yield offset stress at 10^{-4} strain.

3.3.1 Young's Modulus

Figure 3.3 plots Young's modulus (E) versus relative density (D_r) for all confining pressures and strain rates from tests having "good to fair" agreement between the two ACDTs used to measure the on-specimen axial strains. Due to compliance in the triaxial equipment, the *initial* strain rates were about one-tenth of the values listed in Table 3.1 (See Table A.2). Evaluation of the data and comparison with prior results for

frozen sand show the following trends as a function of relative density (D_r), confining pressure (σ_c) and strain rate ($\dot{\epsilon}$).

<u>Variable</u>	<u>Trend in Young's Modulus</u>	
	<u>This Program</u>	<u>Prior Results</u>
$D_r = 25 \text{ to } 95\%$	No clear trend	Baker and Durfurst (1985): Increase of 20% from wave velocity data on Ottawa sand
$\sigma_c = 0.1 \text{ to } 10 \text{ MPa}$	15% decrease	No reliable data
$\dot{\epsilon} = 3 \times 10^{-6} \text{ to } 4 \times 10^{-4}/\text{s}$	No effect	No data

3.3.2 Application of Composite Material Model

Andersen (1991) used the isostrain model proposed by Counto (1964), which was developed to predict the modulus of concrete, in order to model the small strain behavior of frozen MFS. In this model, the composite material is idealized as a cube of aggregate (sand grains) embedded in a cube of matrix material (ice).

An axial force is applied to a composite cube having three horizontal sections (i.e., two pure ice ends and a central section having an isostrain condition imposed between the entire volume of a silicate sand prism and the surrounding ice) and the corresponding deformation of each section is computed from the "known" elastic moduli of the pore ice and the sand particles. The resulting equation for the composite Young's modulus (E_c) using the height to area assumption of Counto (1964) is

$$\frac{1}{E_c} = \frac{1 - \sqrt{V_s}}{E_i} = \frac{1}{\left[\frac{1 - \sqrt{V_s}}{\sqrt{V_s}} \right] E_i + E_s} \quad \dots \dots \dots \quad (3.1)$$

where V_s is the volume fraction of the sand particles, E_i is the Young's modulus for ice and E_s is the Young's modulus of the sand particles (not the sand skeleton). If the geometry of the silicate prism in the central section is that of a perfect cube, a similar relationship predicts values of E_c about 20% higher than Eq. 3.1.

Selecting $E_s = 90$ GPa and $E_i = 7.5$ GPa for sand grains and ice, respectively, Andersen computed $E_c = 25 \pm 2.5$ GPa at $D_r = 35\%$ and $E_c = 29 \pm 3$ GPa at $D_r = 100\%$. These predictions agree very well with the data for MFS which give $E = 26.6$ GPa ± 4.5 SD and hence illustrate the value of considering a frozen sand system as a composite material. It should be emphasized that the much higher modulus of frozen sand compared to pure ice does not result from the stiffness of the sand *skeleton*, which is much less than that of ice, but rather from the very high modulus of sand grains embedded in an ice matrix.

3.3.3 Proportional Limit

Figure 3.4(a) plots the proportional limit as a function of relative density. The magnitude of the proportional limit ranges from 1 MPa to 3.1 MPa over all the testing conditions and has no consistent trend as a function of relative density. A plot of the proportional limit as a function of confining pressure for all tests conducted at moderate strain rate clearly indicates a decrease with increasing confining pressure [Fig. 3.4(b)]. This trend is consistent for all strain rates investigated. Figure 3.4(c) shows the effect of strain rate on the proportional limit for tests conducted at $\sigma_c = 0.1$ and 10 MPa. There is a tendency for the proportional limit to increase with strain rate.

3.3.4 Yield Offset at 10^{-4} Strain

Figure 3.5(a) plots the deviator stress at the 10^{-4} yield offset as a function of relative density. Over all testing conditions, the yield point ranges from 2.7 MPa to 5.2 MPa with no apparent trend as a function of relative density. There is a clear trend for the offset stress to decrease with increasing confining pressure [Fig. 3.5(b)]. This trend is uniform for all strain rates investigated. As a function of strain rate, there is a definite trend for the yield offset to increase with strain rate with a power law coefficient of approximately 11 [Fig. 3.5(c)].

3.4 LARGE STRAIN BEHAVIOR

This section discusses the large strain behavior of frozen Manchester Fine Sand as described by the upper yield stress and corresponding strain, the rate of post upper yield strain hardening or softening, the peak deviator stress and corresponding strain, and the volumetric behavior.

3.4.1 Overview of Large Strain Behavior

The influence of the testing variables (D_r , σ_c and $\dot{\epsilon}$) on the nature of the large strain behavior may be summarized as follows.

1) Change in Relative Density (D_r) at Moderate Strain Rate

As illustrated in Fig. 3.6 (a) and (b), increasing D_r causes a large increase in the rate of post upper yield strain hardening and hence peak strength. The volumetric expansion also increases. Note that the deviator stress has been normalized to Q_{uy} since D_r does not affect the upper yield stress (see Section 3.4.2).

2) Change in Confining Pressure (σ_c) at Moderate Strain Rate

Figures 3.7 (a) and (b) show that increasing σ_c also causes a general increase in the amount of strain hardening and hence peak strength, with the effect being more pronounced at high densities. The amount of dilation is greatly suppressed with higher levels of confinement. Note that in these figures the deviator stress has also been normalized since σ_c has a minor effect on Q_{uy} .

3) Change in Strain Rate ($\dot{\epsilon}$) at varying Density and Confinement

Increasing $\dot{\epsilon}$ causes a large increase in the upper yield stress, the peak strength and increased in the amount of dilation [Fig. 3.8 (a), (b) and (c)]. The fastest strain rate causes the least amount of post yield strain hardening or even strain softening.

3.4.2 Upper Yield Behavior

The upper yield region represents the knee of the stress-strain curve where very significant amounts of plastic deformation begin to occur. This region is emphasized in these data because the use of accurate on-specimen axial strain measurements and the

wide range of testing variables provide the first comprehensive evaluation of the upper yield behavior for frozen soil. Figure 3.9 illustrates the nature of the stress-strain data (plotted up to axial strain levels of about one percent) that enabled reliable determinations of the upper yield stress (Q_{uy}) and corresponding strain (ϵ_y) as a function of: (a) relative density; (b) confining pressure and (c) strain rate. (Note: Section 5.4.1 of Andersen (1991) describes the technique used to obtain values of Q_{uy} corrected to a standard initial specimen height of 7.5 cm; Table A.2 reports both the measured and corrected values).

Figure 3.10 shows that the magnitude of the upper yield stress is independent of relative density and Fig. 3.11 indicates that increasing confining pressure causes a consistent, but relatively small, decrease in Q_{uy} . However, increasing strain rate causes a very significant increase in upper yield stress as shown by the results in Fig. 3.10 (Q_{uy} versus relative density for all tests) and in Fig. 3.12 (Q_{uy} versus strain rate for tests with $\sigma_c = 0.1$ and 10 MPa). The power law coefficient was 4.6 to 4.7 for these strain rates. The influence of testing variables on the magnitude of the axial strain at upper yield follows the same basic pattern: that is, the data in Fig. 3.13(a) show no effect of relative density, whereas the data in Fig. 3.13(b) show significantly larger strains with increasing strain rate. In fact, the magnitude of ϵ_y varies almost linearly with the value of Q_{uy} .

Figure 3.14 compares the strain rate sensitivity of frozen MFS with that of isotropic fine-grained (0.7mm) granular ice tested at $-7 \pm 1^\circ\text{C}$ (Hawkes and Mellor 1972) over roughly the same range in strain rates. Although the upper yield stress of the frozen sand is about double the strength of ice, both systems have the same power law coefficient ($n = 4.7$) defined by the slope of the line in the $\log \dot{\epsilon} - \log Q$ plot. This significant observation suggests that the physical mechanisms controlling the yield behavior of frozen sand (at least for MFS) might be similar to those controlling the strength of polycrystalline ice. In any case, the "strength" of the sand skeleton must not contribute significantly to the upper yield stress since sand density did not influence the upper yield behavior and confining pressure had a minor effect. Further research is warranted to determine if

approaches used to predict the behavior of composite materials, which were successful regarding initial modulus, might be extended into the upper yield region.

3.4.3 Peak Strength Behavior

Since both relative density and confining pressure affect the post upper yield behavior of frozen MFS, the "strength" of the sand skeleton becomes important at large strains.

Effect of Relative Density

The results in Fig. 3.15(a) show that the peak strength (Q_p) increases linearly with relative density for shearing at the moderate strain rate. The data also show that the slope increases with confining pressure. Since the upper yield stress remains constant ($Q_{uy} = 8.1 \pm 0.5$ MPa as per Fig. 3.10), the strength increase is due to higher rates of post yield strain hardening (e.g., Fig. 3.6). Increasing density produces a similar trend at slow strain rates as seen in Fig. 3.15(b). Most prior data also show a linear Q_p vs. D_r relationship, e.g., Goughnour and Andersland (1968); Jones and Parameswaran (1983). But if shearing at low density has a Type I curve, such as test FRS36 in Fig. 3.8(a), increasing density may only lead to less post yield strain softening. Such behavior explains the bilinear Q_p vs. D_r relationship reported by Baker and Kurfurst (1985).

Figures 3.16(a) and (b) plot the axial strain (ϵ_p) at the peak strength versus relative density for tests run at the moderate strain rate and for tests run at the slow and fast strain rates, respectively. Increases in relative density either have little effect on ϵ_p (generally true at low levels of confinement) or cause a relatively modest decrease in ϵ_p (always true at high confining pressures).

Effect of Confining Pressure

Figure 3.17 plots peak strength versus confining pressure at three relative densities. This plot was developed from linear regression on the moderate rate test data in Fig. 3.15(a). As shown in the figure, strengthening due to confinement is less for loose sand than for dense sand and tends to decrease at higher stresses. This strengthening is always

accompanied by an increase in the axial strain at peak strength (Fig. 3.16). As with relative density, confinement increases the amount of post yield strain hardening, especially for dense sand (Fig. 3.7). The strengthening effect is similar for shearing at the slow rate [Fig. 3.15(b)]. However, confinement did not increase the strength for fast shearing of loose sand since it is controlled by the pressure independent upper yield stress; e.g., tests FRS36 and FRS40 in Figs. 3.8(a) and 3.8(c). Hence the total stress friction angle ϕ of frozen MFS ranges from zero (when peak = upper yield stress) to about 15° (for failure at large strains). (Note: $\sin \phi = S/(2 + S)$ where $S = dQ_p/d\sigma_c$).

Data on other sands also show large variations in ϕ at similar confining stresses. The friction angle of some dense frozen sands even exceeds 20 to 25° , e.g., Chamberlain et al. (1972), Alkire and Andersland (1973) and Shibata et al. (1985). Thus ϕ of frozen sand can be much larger than measured for granular ice (say $\phi = 10 \pm 5^\circ$ at moderate to fast strain rates) or from consolidated-undrained tests on unfrozen sand ($\phi = 5$ to 10°).

Effect of Strain Rate

Figure 3.18 summarizes the effect of strain rate on the peak strength of loose and dense MFS at low and high confining pressures. This log-log plot presents the most complete picture of the influence of relative density and confinement on the rate sensitivity of a frozen soil. The corresponding power law coefficients (n) that denote the change in log $\dot{\epsilon}$ per change in log Q_p range from about 6 to 17 (Note: increases in n reflect decreases in the rate sensitivity.) Although these values compare well with prior results at about -10°C , this program did not measure a rate insensitive region (i.e., $n = \infty$) such as observed by Bragg and Andersland (1980) (for unconfined compression tests at $\dot{\epsilon} > 10^{-5}/\text{sec}$ on medium-dense sand) and by Yuanlin et al. (1988) (for unconfined compression tests at $\dot{\epsilon} > 3 \times 10^{-4}/\text{sec}$ on dense sand).

Figure 3.18 shows a consistent trend for the power law coefficient to increase with both increasing relative density and increasing confining stress. The low density-low confinement condition has the highest rate sensitivity ($n = 6.1$), which begins to approach

that for granular ice for the same range of strain rates (e.g., $n = 4.7$ from Fig. 3.14). From the stress-strain curves in Fig. 3.8(a), one sees that the peak strength of these tests either equals or only modestly exceeds the upper yield stress. In turn, Section 3.4.2 suggests that the physical mechanisms controlling the yield stress of frozen MFS might be similar to those controlling the strength of polycrystalline ice.

The high density-high confinement condition has the lowest rate sensitivity ($n = 16.7$) and Fig. 3.8(b) shows that the peak strength for these tests occurs at stress and strain levels much larger than those at the upper yield stress. The very significant post-yield strain hardening probably reflects a substantial contribution from the frictional strength of the sand skeleton, which should be strain rate insensitive. If the upper yield stress inherits its rate sensitivity from the pore ice, and the gain in strength above the upper yield point is much less rate sensitive because of sand skeleton friction, it follows logically that the peak strength of frozen dense sand with high confinement should exhibit less strain rate dependence.

3.4.4 Volumetric Behavior

The volumetric strain data in Figs. 3.6, 3.7 and 3.8 show some aspects that are consistent with the drained shearing of unfrozen sand, i.e., less dilation (expansion) with lower density and higher confinement. But the overall behavior is very different from unfrozen sand in several respects:

- 1) High confinement does not cause significant contraction, since this is prevented by the ice matrix in the pores.
- 2) The peak strength does not occur at the maximum rate of dilation, $d\epsilon_v/d\epsilon_a$.
- 3) The amount of dilation at large strains is much larger than can be explained by behavior of the unfrozen sand skeleton. In other words, the ice matrix causes additional expansion. Continuous dilation in some tests at low density and low confinement caused final densities less than the minimum density, i.e., $D_r < 0\%$.

3.4.5 Summary of Effects of Relative Density, Confining Pressure and Strain Rate

The test program on MFS has generated the most complete study of the effects of relative density, confining pressure and strain rate on the strength-deformation properties of a frozen soil that is available in the literature. Accurate measurements of behavior from very small to very large strains at -9.5°C has produced some unique results, especially regarding definition of the upper yield stress, Q_{uy} . The magnitude of Q_{uy} is independent of sand density (Fig. 3.10) and decreases only slightly with confining pressure (Fig. 3.11). This suggests that the upper yield stress is not affected by the frictional character of the sand skeleton. Although Q_{uy} is about double the unconfined peak strength of fine-grained polycrystalline ice, both systems exhibit similar sensitivities to strain rate (Fig. 3.14). This suggests that the physical mechanisms controlling the upper yield behavior of frozen sand might be similar to those controlling the strength of ice. Section 3.3.2 shows that the initial modulus of frozen MFS can be reasonably predicted by treating the system as a composite material, i.e., "stiff" sand grains embedded in a "soft" ice matrix.

In contrast to the above findings, the stress-strain behavior of frozen MFS at large strains is greatly affected by the frictional resistance of the soil skeleton, except for fast shearing of loose MFS at low confinement, where failure occurs at a low strain and the peak strength equals the upper yield stress [i.e., test FRS36 in Fig. 3.8(a)]. All other conditions (lower $\dot{\epsilon}$, higher D_r and/or higher σ_c) lead to post yield strain hardening and failure at larger strains (Fig. 3.2). Under these conditions, the peak strength was shown to:

- 1) Increase linearly with relative density, with the rate being larger with confinement (Fig. 3.15).
- 2) Increase nonlinearly with confinement, with the rate being larger at higher density (Fig. 3.17).

These strengthening effects are less strain rate sensitive than granular ice (Fig. 3.18) and presumably reflect a greater contribution of the frictional resistance of the sand skeleton to the peak strength.

3.5 EFFECT OF TEMPERATURE ON THE BEHAVIOR OF FROZEN MANCHESTER FINE SAND

All but one of Andersen's (1991) tests in the "principal" program were conducted at one temperature (-9.5°C). Since Ashby and Duval (1985) showed that the "normalized" primary creep behavior of ice (within the ductile deformation regime) was the same for changes in applied stress (equivalent to changes in $\dot{\epsilon}$) and changes in temperature, the principal program focused on changes in strain rate. However, at the suggestion of David Cole, tests at different temperatures were started last summer (1991) after first improving our temperature control and measurement capabilities. The program to date has been restricted to six moderate strain rate tests on loose sand at low confinement for comparison with the effects of changing strain rate.

Figure 3.19 plots deviator stress versus axial strain for the "new" tests (FRS 75 to 80) having temperatures ranging from -5.3°C to -28°C , plus FRS44 as being representative of tests sheared at -9.5°C . Five of the new tests exhibited erratic behavior at large strains for unknown reasons; the dotted curves denote these questionable data. In addition, FRS80 sheared at -28°C appears to have failed prematurely, again for unexplained reasons.

The expanded scale plot in Fig. 3.19(b) indicates that temperature has very little effect on small strain behavior. Moreover, the values of Young's modulus presented in Table A.11 for FRS75 to 80 give $E = 26.2 \pm 3.8 \text{ MPa}$, compared to $26.6 \pm 4.5 \text{ MPa}$ quoted in Table A.4 from the principal program. This close agreement should be expected since: Section 3.3.1 shows that modulus is independent of strain rate; and Sinha (1989) shows

that the modulus of granular ice increases by only about 3% as the temperature decreases from -5 to -30°C.

As expected, Fig. 3.19(a) shows a significant increase in both the upper yield stress and the peak strength with decreasing temperature. There is also a change in the type of curve from type III for shearing at $T = -10 \pm 5^\circ\text{C}$ to types II or I for shearing at lower temperatures. This trend is very similar to that observed for the influence of increasing strain rate on the behavior of frozen MFS at low density and low confining pressure as shown in Fig. 3.8(a).

Figure 3.20 plots the (corrected) upper yield stress (Q_{uy}) and the peak strength (Q_p) as a function of temperature for: loose sand at low confinement from the six new tests and the mean values from three tests run at -9.5°C ; and dense sand at high confinement from tests in the principal program. It should be emphasized that the temperature in test FRS50 was not controlled and that $T = -15^\circ\text{C}$ represents an approximate value. The low D_r - low σ_c tests show an approximately linear increase in both Q_{uy} and Q_p with decreasing temperature (excluding test at -28°C), with slopes of 0.7 and 0.6, respectively. A summary of test results from previous programs (Bourbonnais and Ladanyi 1985) also shows an approximately linear relationship of similar slope ($dQ/dT = 0.7 \pm 0.3$) for the peak strength of various frozen sands sheared at $\dot{\epsilon} = 3 \pm 2 \times 10^{-4}/\text{sec}$ over the same temperature range. The "low" value of Q_{uy} for the test FRS50 at -15°C may reflect uncertainty in the actual temperature because the results in Section 3.4.2 suggest that density and confinement should not affect dQ_{uy}/dT (i.e., these variables did not affect the rate of increase in Q_{uy} with increasing strain rate). The smaller dQ/dT slope for the peak strength at high D_r - high σ_c also needs verification.

As noted earlier in Section 3.5, one objective of testing at different temperatures is to compare its effects with those observed for changes in the strain rate. An important part of this comparison should include an evaluation of how these two variables influence the behavior of frozen MFS vis-a-vis that of granular ice. In Section 3.4, the rate

sensitivity of frozen MFS was directly compared to the rate sensitivity of ice using experimental data at a similar temperature (i.e., at near -10°C). However, the authors did not find ice data to enable a direct comparison of its temperature sensitivity to that of frozen MFS at the moderate strain rate of $\dot{\epsilon} = 3 \times 10^{-5}/\text{sec}$. For example, Jacka (1984) presents extensive creep data at temperatures ranging from -5°C to -32.5°C , but only for strain rates slower than 10^{-6} to $10^{-7}/\text{sec}$, i.e., well within the ductile (flow) deformational regime. Consequently, the temperature sensitivity of ice was estimated using the relation between strain rate, stress and temperature presented in Glenn (1955). Dr. Shyam Sunder at MIT suggested the procedure described below for determining the "constants" in Glenn's equations.

Glen's (1955) power law creep equation can be expressed as (e.g., Shyam Sunder and Wu, 1989)

where Q_p is the measured peak strength (MPa), $\dot{\epsilon}$ is the strain rate (1/sec), n is the power law coefficient determined from the experimental data, and V is the derived temperature dependent reference stress (MPa) at a reference strain rate of unity. In turn, the Arrhenius equation was used to predict the temperature dependence of the reference stress

where T is the temperature ($^{\circ}\text{K}$), Q is the activation energy (assumed equal to 67 kJ/mol), R is the universal gas constant (8.31 J/mol $^{-\circ}\text{K}$), and V_0 is a temperature independent constant that was backcalculated from the experimental data.

Three sets of unconfined compression, constant strain rate test data were evaluated.

<u>Data Set</u>	<u>Reference</u>	<u>Temp(°C)</u>	<u>ε Range</u>	<u>Grain Dia.</u>
A	Hawkes and Mellor (1972)	-7	10^{-5} to 10^{-3}	0.7mm
B	Jones (1982)	-11.7	1.4×10^{-6} to 5.4×10^{-4}	1mm
C	Cole (1987)	-5	10^{-5} to 10^{-3}	1.2mm

Equation 3.2 was first used to determine the values of V and n and then Eq. 3.3 was used to obtain the value of V_0 , with the following results:

<u>Data Set</u>	<u>Temp(°C)</u>	<u>V(MPa)</u>	<u>n</u>	<u>V_0(kPa)</u>	<u>r^2</u>
A	-7	39.7	4.67	60.5	0.96
B	-11.7	21.3	6.48	181	0.95
C	-5	60.9	3.83	23.4	—

The above values of n and V_0 were used with Eq. 3.3 to compute the values of V at different temperatures, and then Eq. 3.2 to calculate Q_p at $\dot{\epsilon} = 3 \times 10^{-5}/\text{sec}$, the moderate strain rate used for the frozen MFS tests. It is recognized that this approach is approximate since: the experimental data lie within the ductile to brittle transition zone (hence n may vary with temperature); and the Arrhenius equation may not be valid at temperatures above -10°C (hence Q may not be constant). Hence the approach was applied to three data sets in order to obtain a range in the predicted temperature sensitivity of ice.

Figure 3.21 compares the calculated strength of ice to the measured upper yield stress (Q_{uy}) and peak strength (Q_p) of frozen MFS at various temperatures. The figure plots log stress versus $1/T$ ($^\circ\text{K}$) since this format produces a linear relationship for ice based on Eqs. 3.2 and 3.3. The results clearly indicate that the temperature sensitivity of frozen MFS is very different from that predicted for ice: the log stress vs. $1/T$ relationship for frozen MFS is highly non-linear and has a much larger sensitivity at temperatures ranging from -5°C to -15°C .

Thus the initial "assumption" that the effects of varying temperature and of varying strain rate on the behavior of frozen sand would be similar is certainly not true. For example, Fig. 3.14 showed that the rate sensitivity of Q_{uy} for frozen MFS and of Q_p for ice (data set A) were the same. This led to the suggestion in Section 3.4.2 that the physical mechanisms controlling the yield behavior of frozen MFS might be similar to those controlling the strength of granular ice. That hypothesis needs further experimental

evaluation, such as by varying the strain rate at different temperatures. Table 3.2 presents the tentative scope of further studies as contained in the Ladd and Germaine (1991) proposal to ARO, which also includes testing at conditions of high density and high confinement.

3.6 EFFECT OF CONFINEMENT DURING FREEZING ON FROZEN SAND BEHAVIOR

The 1988 proposal for this research included some triaxial tests wherein the confining stress would be applied for a long period in order to consolidate the frozen soil and thereby increase the preshear effective stress acting on the sand skeleton (freeze-consolidate series FC in Table 1.2). There are two problems with this type of testing:

- 1) It would require very long times (as predicted by Ladanyi 1985) and thus was not feasible with only one high pressure-low temperature triaxial system;
- 2) It does not simulate in situ conditions wherein effective stresses act on the soil skeleton before freezing occurs.

However, the concept of studying the influence of the pre-freezing effective stress on frozen soil behavior remains valid. But rather than first freezing and then consolidating the soil (FC test), the process will be reversed, i.e., first consolidate and then freeze the soil (consolidate-freeze = CF test). As noted in Section 4, increasing the preshear effective stress should cause a very significant increase in the stiffness of the soil skeleton. For example, stress-strain data for unfrozen dense MFS in Fig. 4.2 at $\epsilon_a = 2\%$ show Q increasing dramatically from 0.7 to 5.5 MPa as σ'_c increases from 0.1 to 10 MPa. This large increase in sand skeleton stiffness will presumably have a significant affect on the strength-deformation behavior of frozen sand at strains near and beyond the upper yield region.

Our review of the literature indicates that no tests have been run to compare the behavior of frozen soil as measured in regular "frozen-unconsolidated" triaxial compression tests compared to tests run on soil that was frozen after application of confinement. Singh et al. (1982) did subject a specimen of uniform sand ($D_{50} = 0.4\text{mm}$) to one-dimensional freezing in a triaxial cell (consolidation stress = 0.56 kg/cm^2 and backpressure = 2.5 kg/cm^2) with measurements of the change in pore volume during freezing and subsequent thawing. But no tests were run on frozen sand since the objective was to show that freezing-thawing did not effect the cyclic behavior of unfrozen sand. Goodman (1975) measured the "viscoelastic response" and yield stress of a 20-40 quartz sand that was frozen one-dimensionally ($T = -7 \pm 1^\circ\text{C}$) after first applying confining pressures of 125, 250 and 500 psi with the objective of simulating deep permafrost. The specimens were enclosed in plasticized PVC tubing during application of the confining pressure and then subjected to axial loading creep tests. However, since the yield stress was shown to be the same for both frozen and unfrozen sand, the writers infer that the loading conditions may have been closer to confined (1-D) compression than triaxial compression. Sego et al. (1982) used a triaxial cell for one-dimensional freezing of mortar sand under a consolidation stress $\sigma'_c = 0.08 \text{ MPa}$ in order to study the influence of pore fluid salinity on strength-deformation behavior at varying strain rates ($T = -7^\circ\text{C}$). But all frozen specimens were transferred to another cell for triaxial compression tests at essentially zero confinement. Thus, the program did not provide information regarding the effect of the pre-freezing effective stress on the behavior of frozen sand.

Test results from the current program may indicate how the pre-freezing effective stress affects the stress-strain behavior of frozen MFS. Andersen (1991) compared the stress-strain behavior of dense frozen MFS prepared by wet tamping (compaction) rather than by multiple sieve pluviation (MSP). A comparison of dense ($D_r = 90\%$) tests under 2 MPa confinement is presented in Fig. 3.22. This figure shows that compaction caused a significant increase in the rate of post upper yield strain hardening. One possible

explanation for this behavior is that the compaction process "locked in" higher effective stresses and that these stresses were preserved during freezing and hence caused higher preshear effective stresses than for pluviated specimens (Note: other comparisons at $\sigma_c = 5$ and 10 MPa also showed higher post upper yield stiffnesses, but little change in the peak strength). If this hypothesis is true, even rather modest changes in the pre-freezing effective stress can represent an extremely important issue about which no information currently exists.

Table 3.1 Scope of Testing Program on the Triaxial Compression Behavior of Frozen Manchester Fine Sand

RANGE IN RELATIVE DENSITY (%)	CONFINING PRESSURE (MPa)											
	0.1			2			5			10		
	Fast	Mod.	Slow	Fast	Mod.	Slow	Fast	Mod.	Slow	Fast	Mod.	Slow
20- 40	•	•	•		•			•		•	•	•
40- 60		•			•			•			•	•
60- 80		•						•			•	
80-100	•	•	•		•			•		•	•	•

STRAIN RATES TESTED

Fast $\approx 4 \times 10^{-4}$ /sec

Moderate $\approx 3 \times 10^{-5}$ /sec

Slow $\approx 3 \times 10^{-6}$ /sec

One specimen tested at 1.2×10^{-4} /sec

TESTING TEMPERATURE

Principal Program

-9.55 \pm 0.3°C

New Program (to date)

Six tests at temperatures ranging
from -5 to -28°C

(Loose sand at moderate strain rate and low confinement)

SPECIMEN PREPARATION TECHNIQUES

Most tests prepared by Multiple Sieve Pluviation

Seven tests prepared by Wet Tamping

SPECIMEN END CONDITIONS

Most tests had ice cap and grease ends (low friction)

Six tests had frozen sand and grease (higher friction)

One test had emery cloth

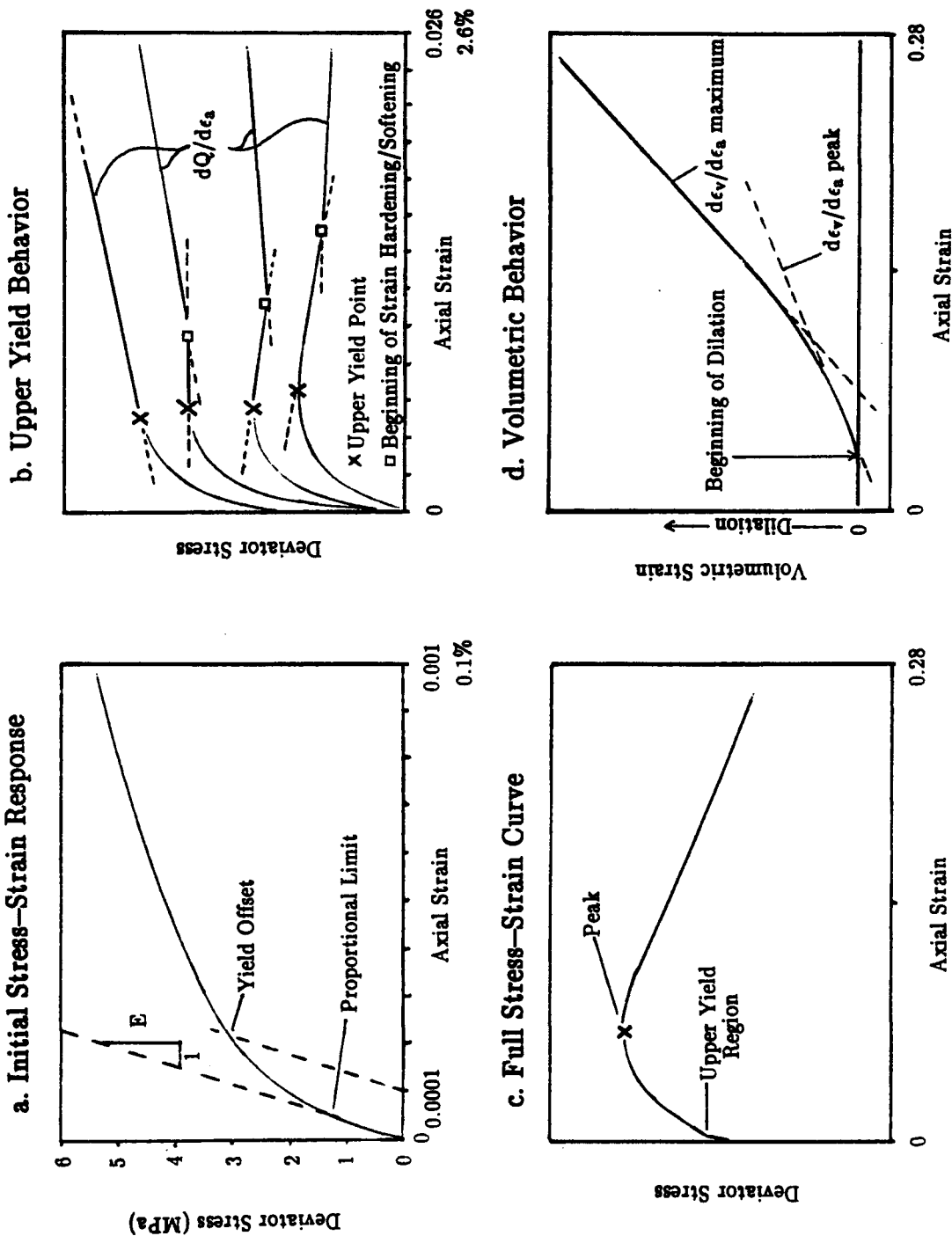
Table 3.2 Tentative Scope of Triaxial Testing on IFS at Different Temperatures ("Conventional" tests, i.e., frozen before applying confining pressure)

Nominal Temp. (°C)	Confining Pressure σ_c (MPa)	SLOW ($3 \times 10^{-6}/\text{s}$)			MODERATE ($3 \times 10^{-5}/\text{s}$)			FAST ($4 \times 10^{-4}/\text{s}$)		
		$D_r = 35\%$	$D_r = 95\%$	$D_r = 35\%$	$D_r = 95\%$	$D_r = 35\%$	$D_r = 95\%$	$D_r = 35\%$	$D_r = 95\%$	
- 5	0.1	0	0	x	•	•	•	•	•	
	10	0	0	•	•	•	•	•	•	
- 10	0.1	x	x	x	x	x	x	x	x	
	10	x	x	x	x	x	x	x	x	
- 15	0.1	•	•	x	•	•	0	0	0	
	10	•	•	•	x	0	0	0	0	
- 20	0.1	•	•	x	0	0	0	0	0	
	10	•	•	•	x	0	0	0	0	
- 25	0.1	0	0	x	0	0	0	0	0	
	10	0	0	0	0	0	0	0	0	

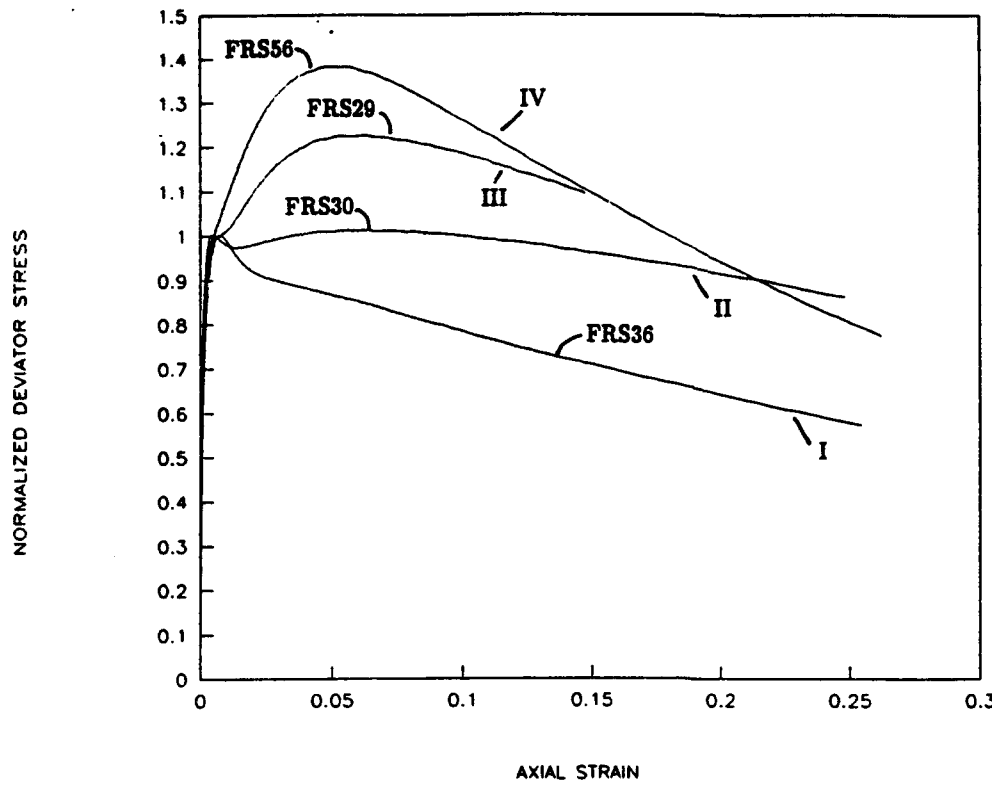
Notation: x = Test Completed • = First Series 0 = Second Series

Idealized Stress–Strain Behavior and Graphical Construction Techniques

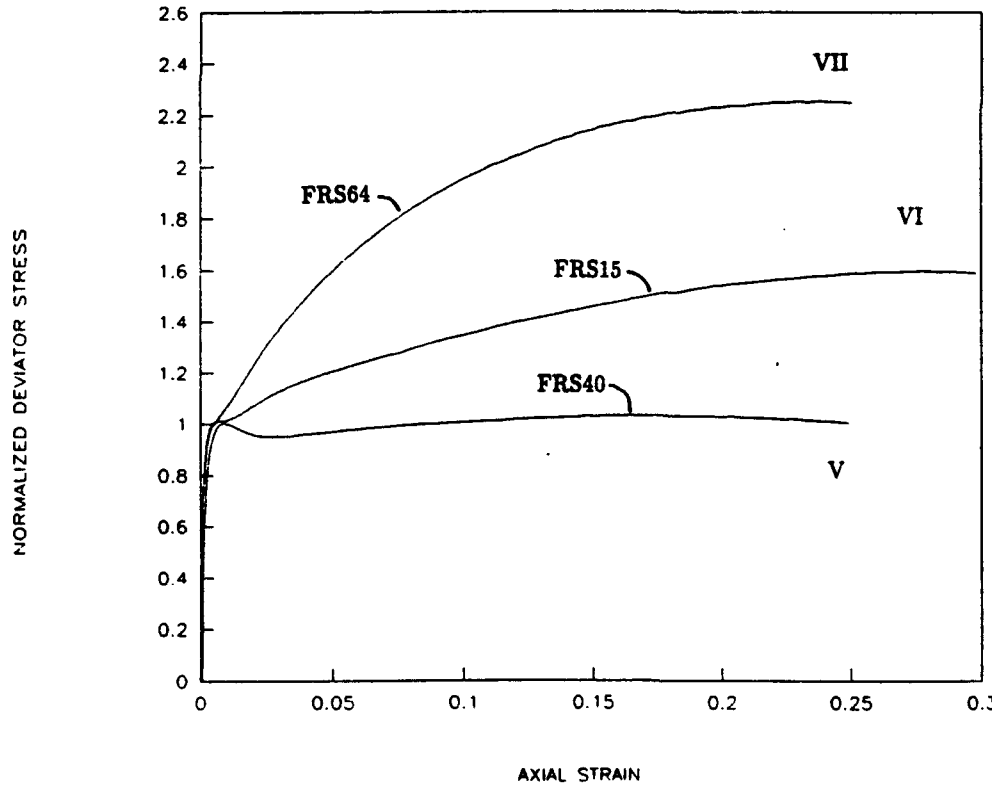
Figure 3.1:



a. Low Confining Pressure



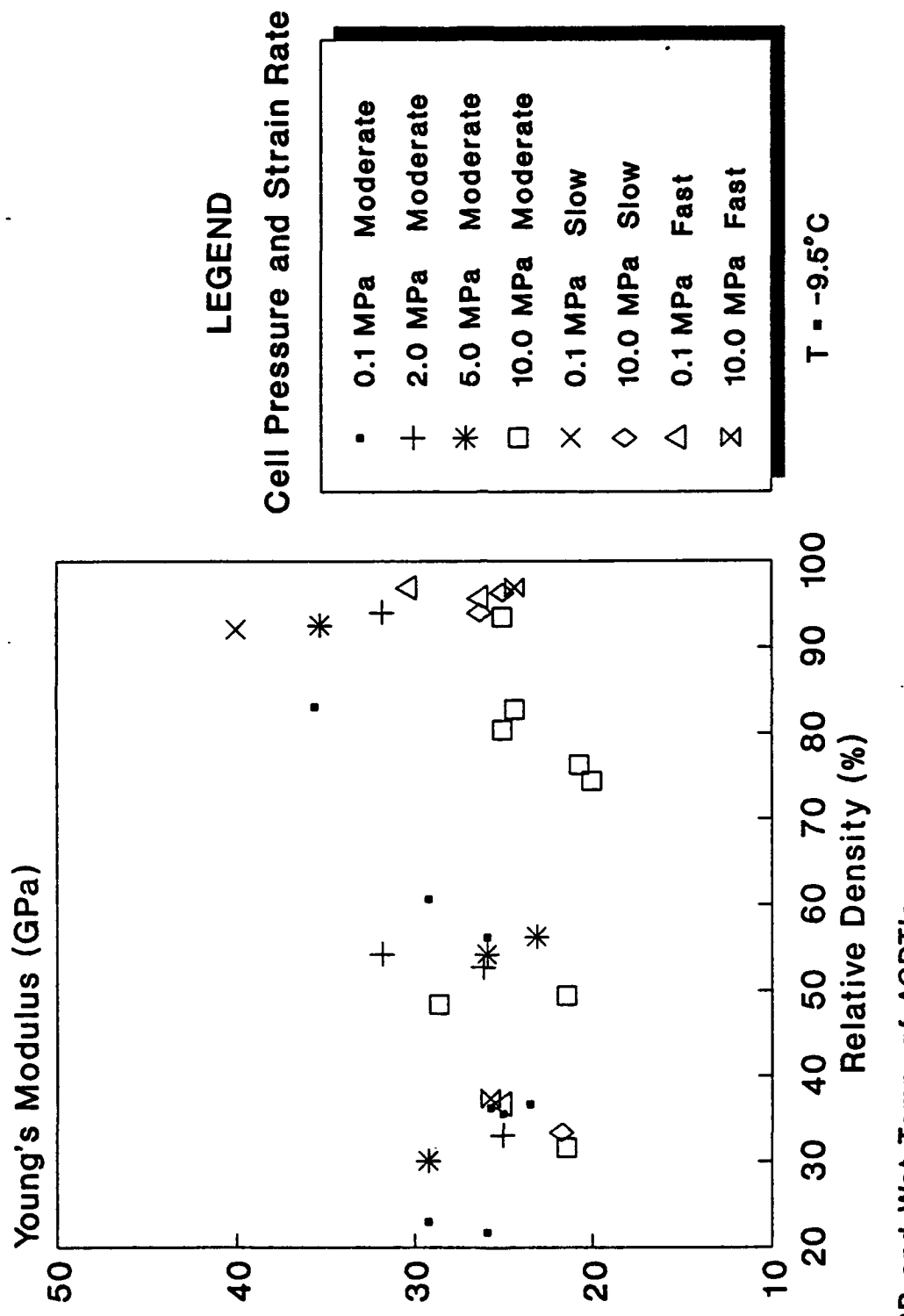
b. High Confining Pressure



Note: Curves have been normalized by the magnitude of the upper yield stress

Figure 3.2:

Overview of Types of Stress-Strain Curves



MSP and Wet Tamp, of ACDT's
lub and fric ends

Figure 3.3: Young's Modulus Versus Relative Density for Frozen MFS

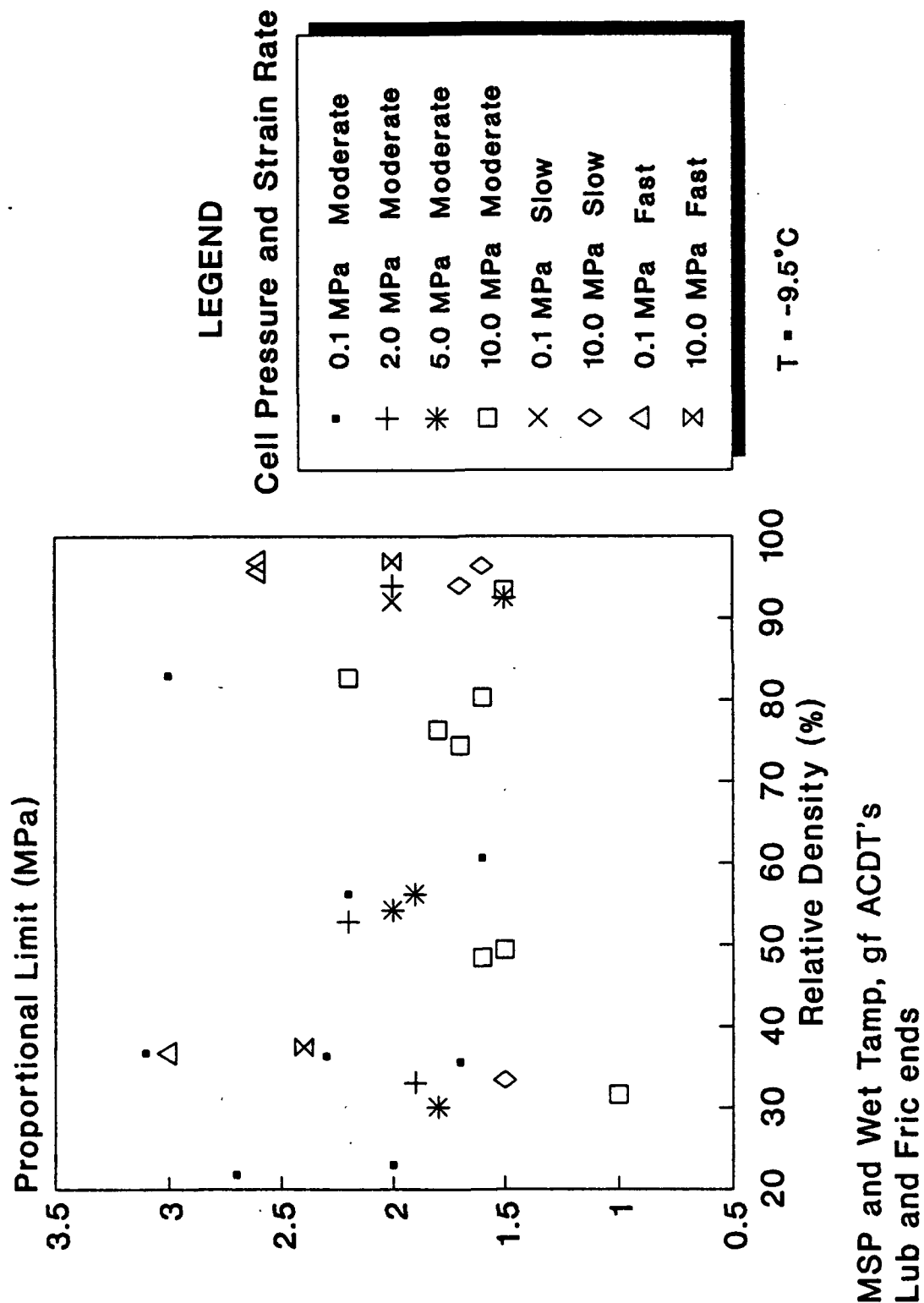
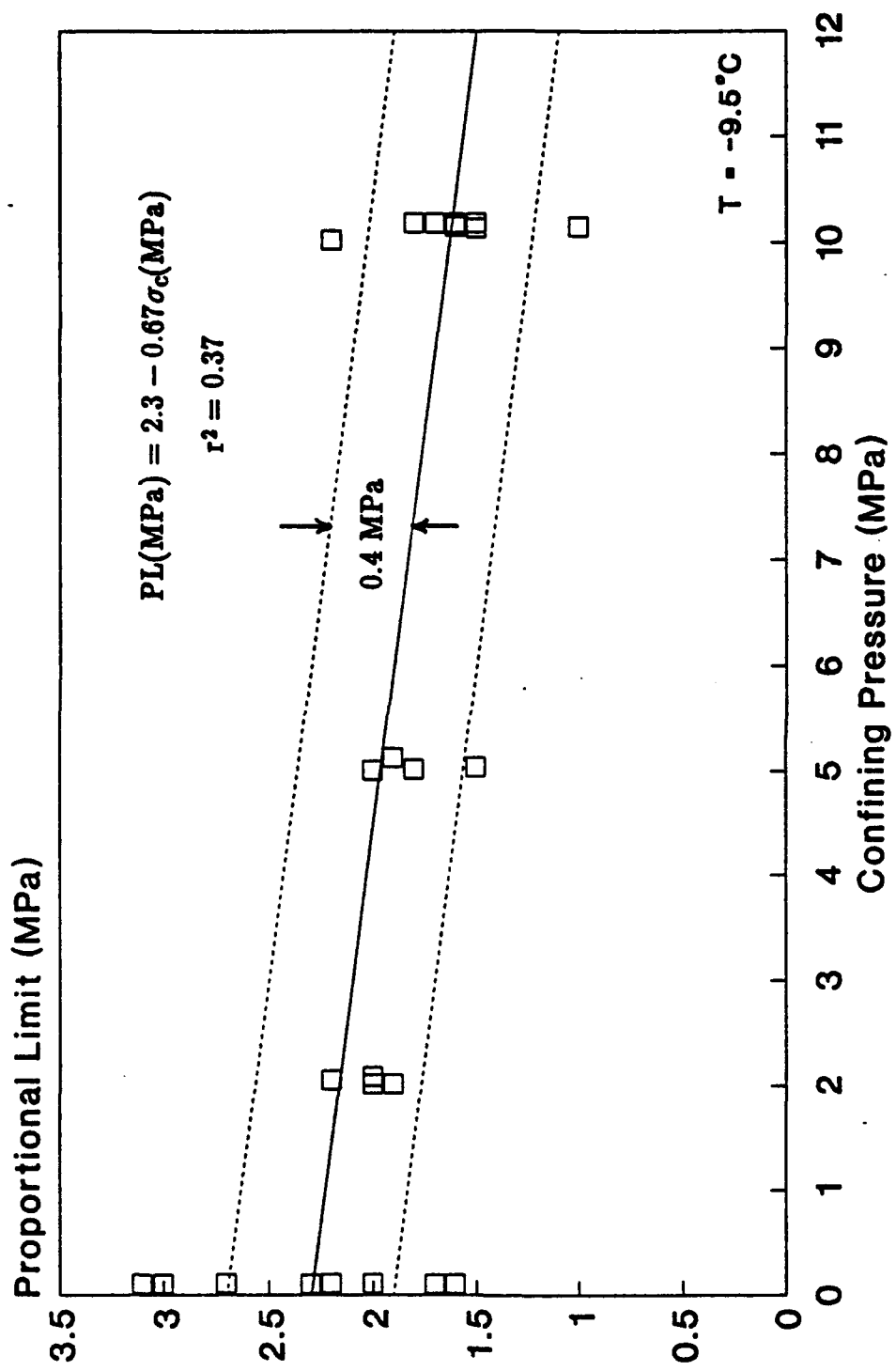


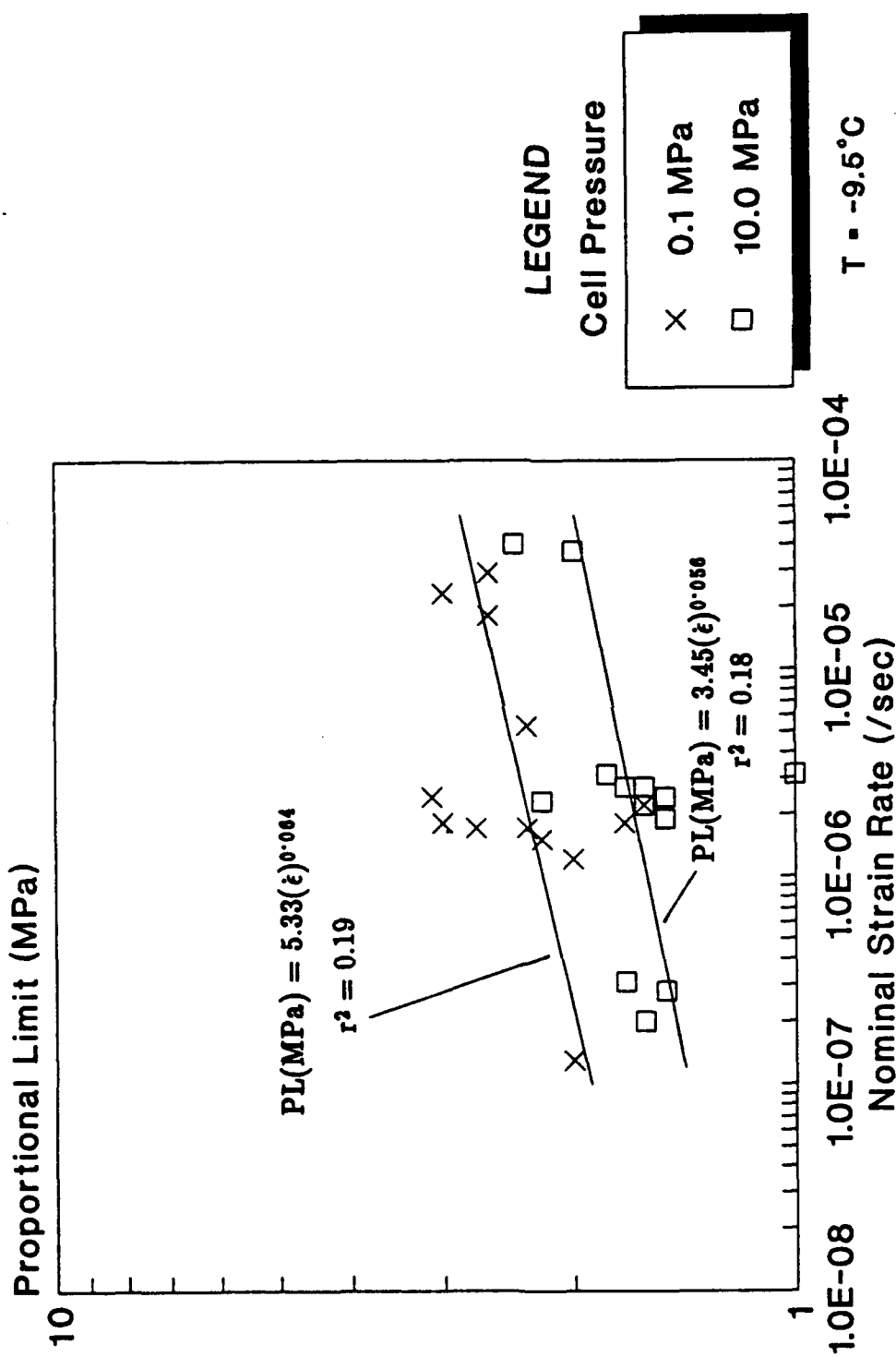
Figure 3.4(a):

Proportional Limit Versus Relative Density for Frozen MFS



Moderate Strain Rate
MSP and Wet Tamp, gf ACDT's
Lub and Fric Ends

Figure 3.4(b):
Effect of Confining Pressure On Proportional Limit for
Frozen MFS



MSP and Wet Tamp, gf ACDT's
Lub and Fric Ends

Figure 3.4(c):

Effect of Strain Rate on Proportional Limit for Frozen
MFS

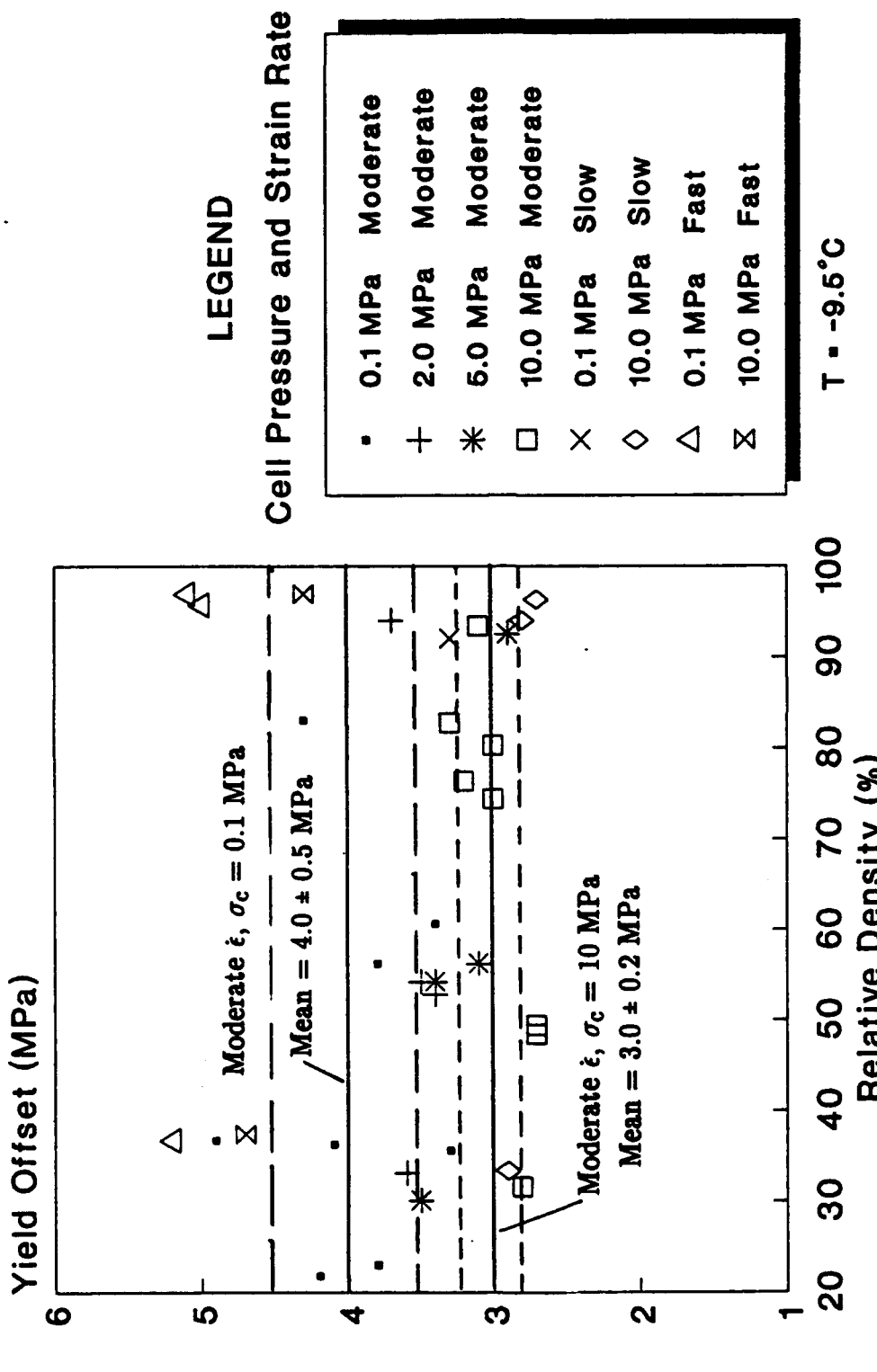
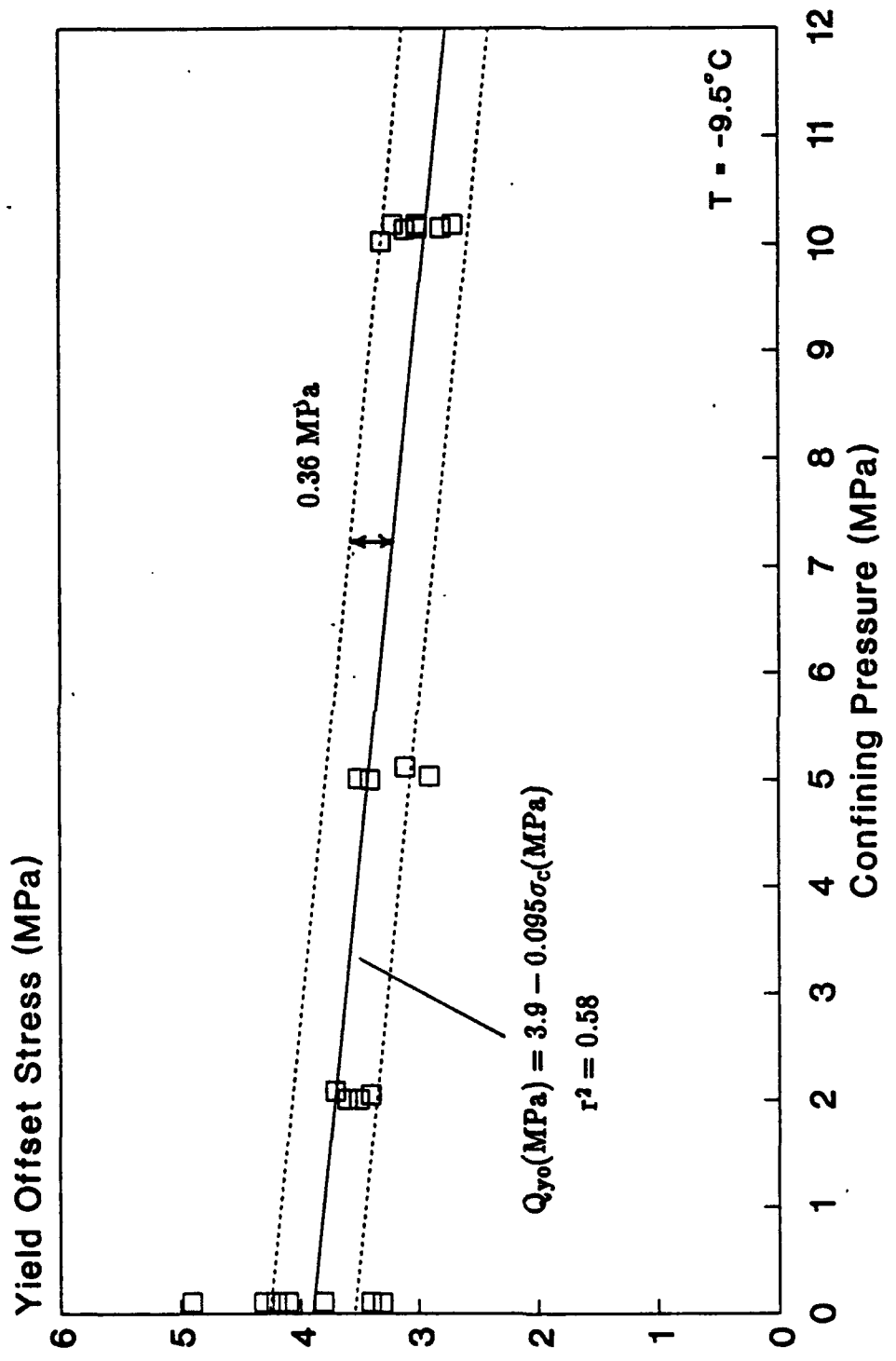
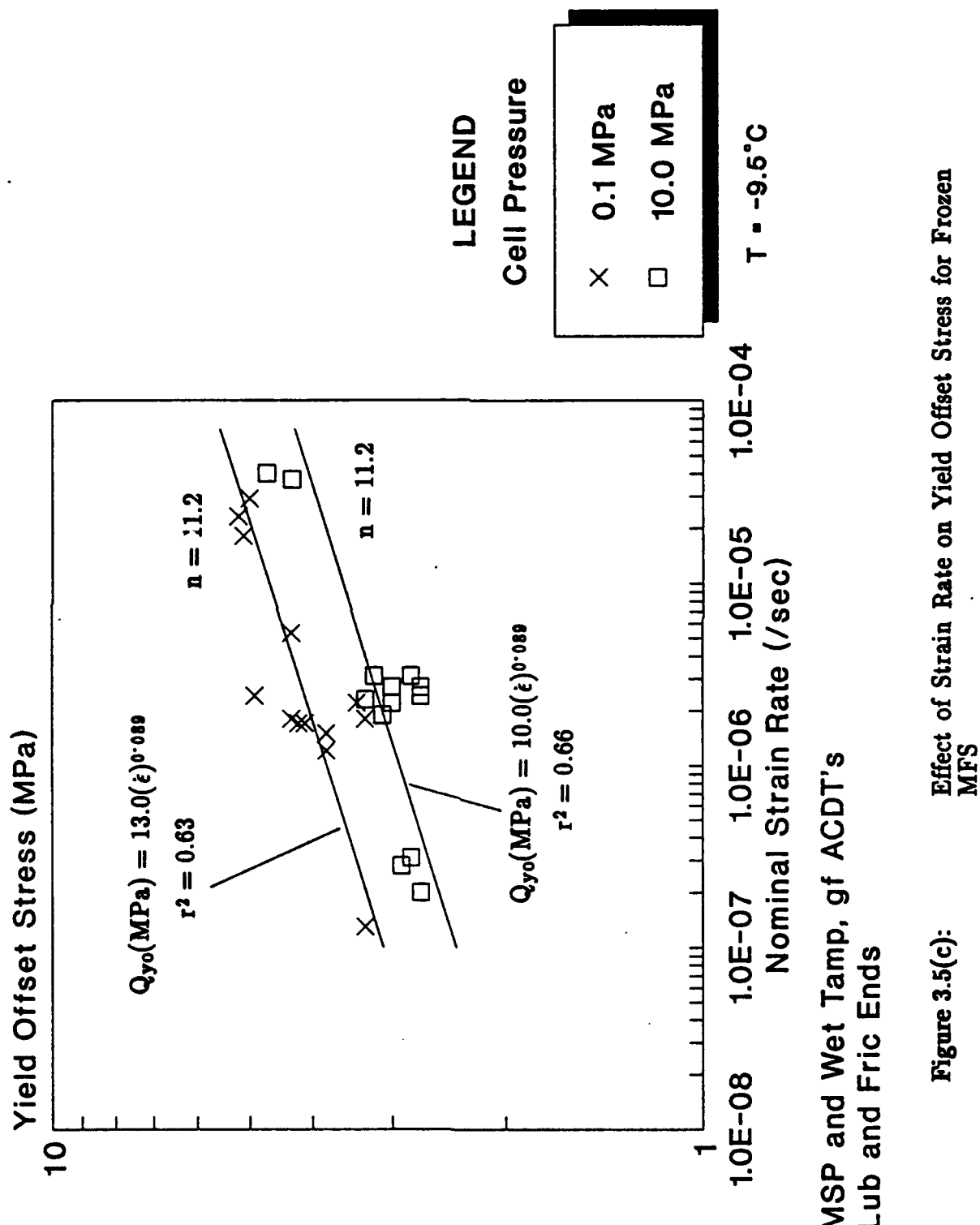


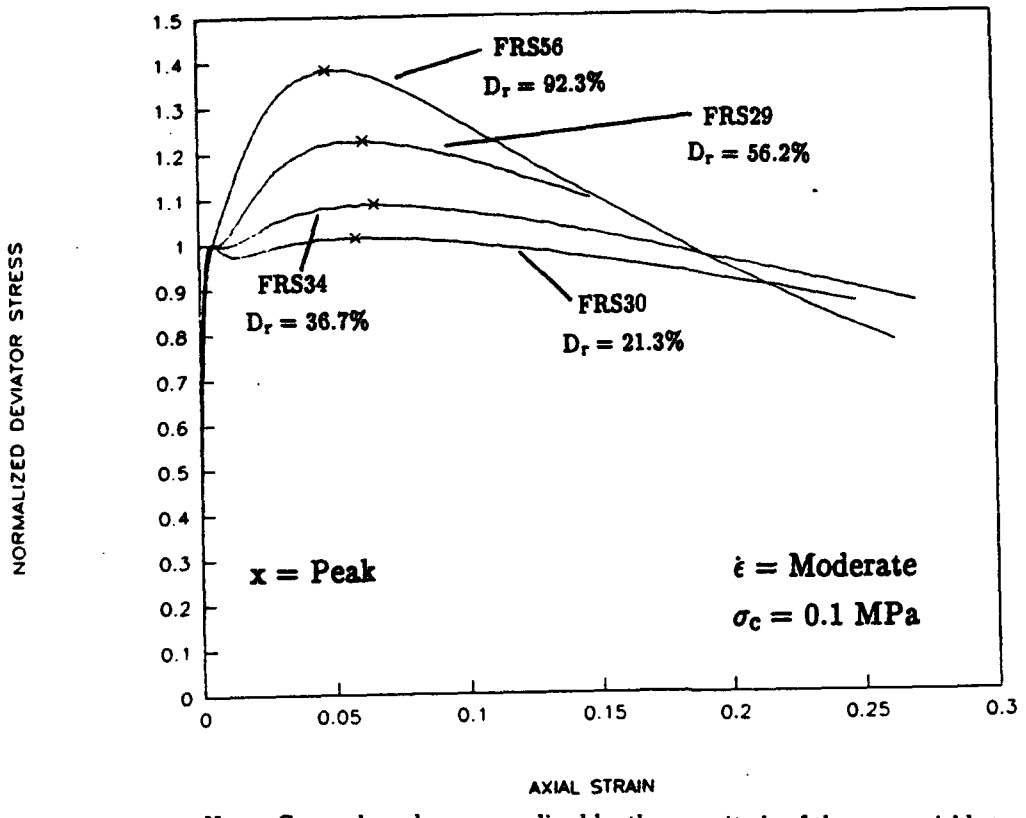
Figure 3.5(a): Yield Offset Stress at 10^{-4} Strain Versus Relative Density for Frozen MFS



Moderate Strain Rate
MSP and Wet Tamp, gf ACDT's
Lub and Fric Ends

Figure 3.5(b):
 Effect of Confining Pressure on Yield Offset Stress for
 Frozen MFS





Note: Curves have been normalized by the magnitude of the upper yield stress

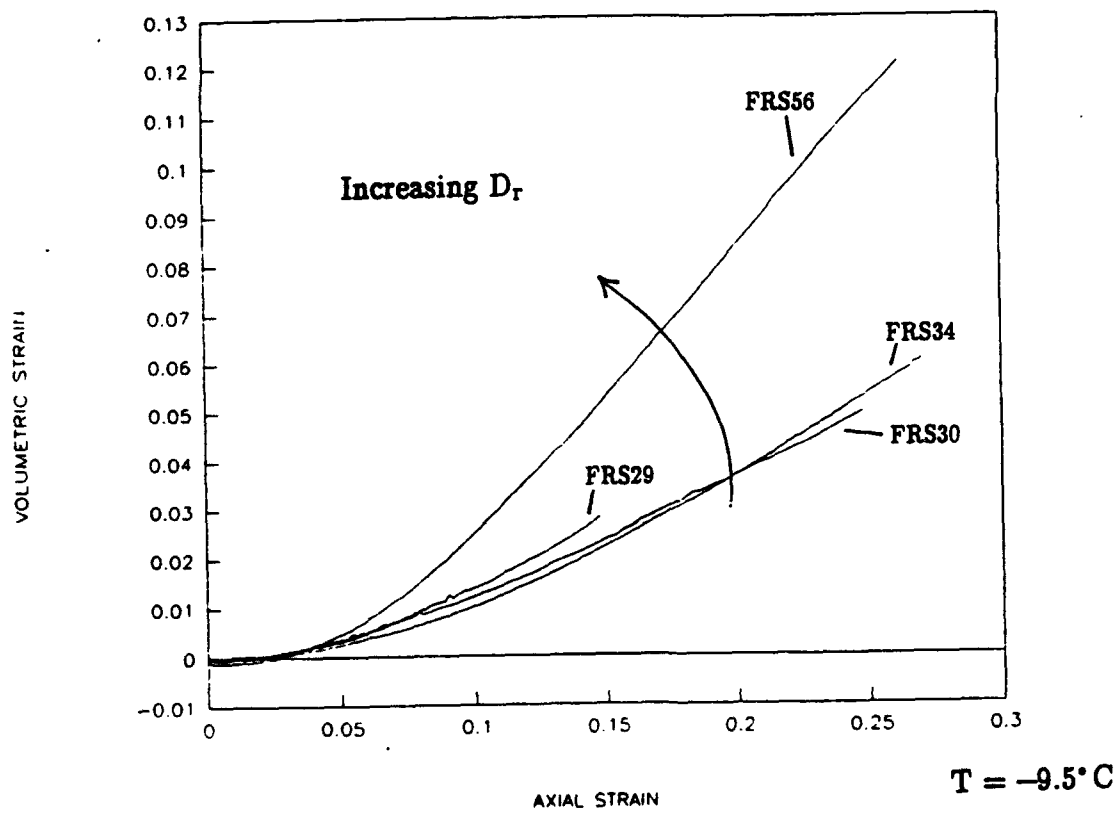


Figure 3.6(a):

Normalized Stress-Strain Curves Showing the Effect of Relative Density for Moderate Strain Rate and Low Confining Pressure for Frozen MFS

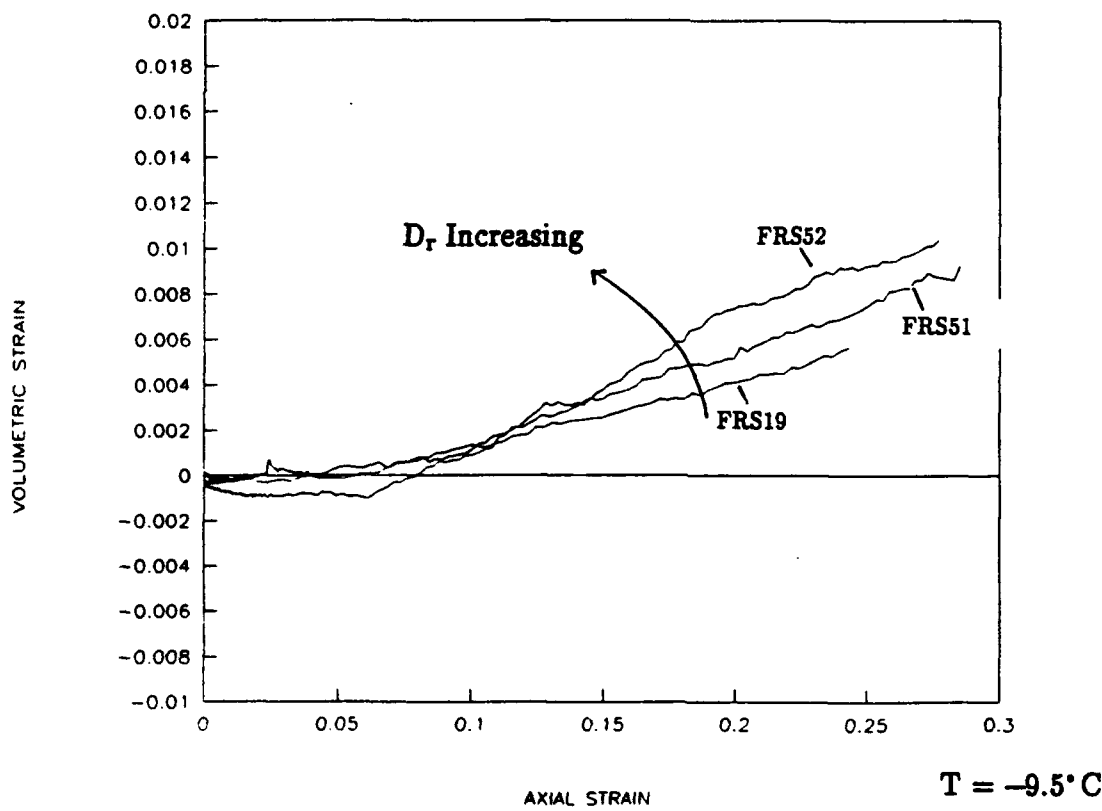
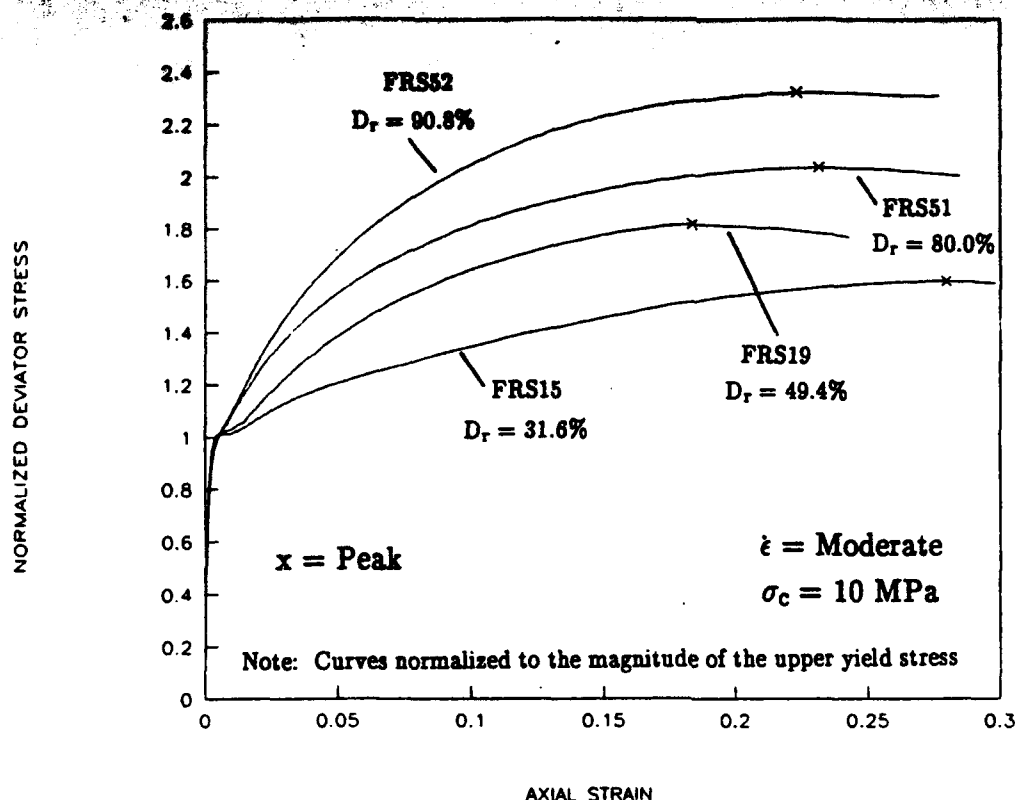


Figure 3.6(b):

Normalized Stress–Strain Curves Showing the Effect of Relative Density for Moderate Strain Rate and High Confining Pressure for Frozen MFS

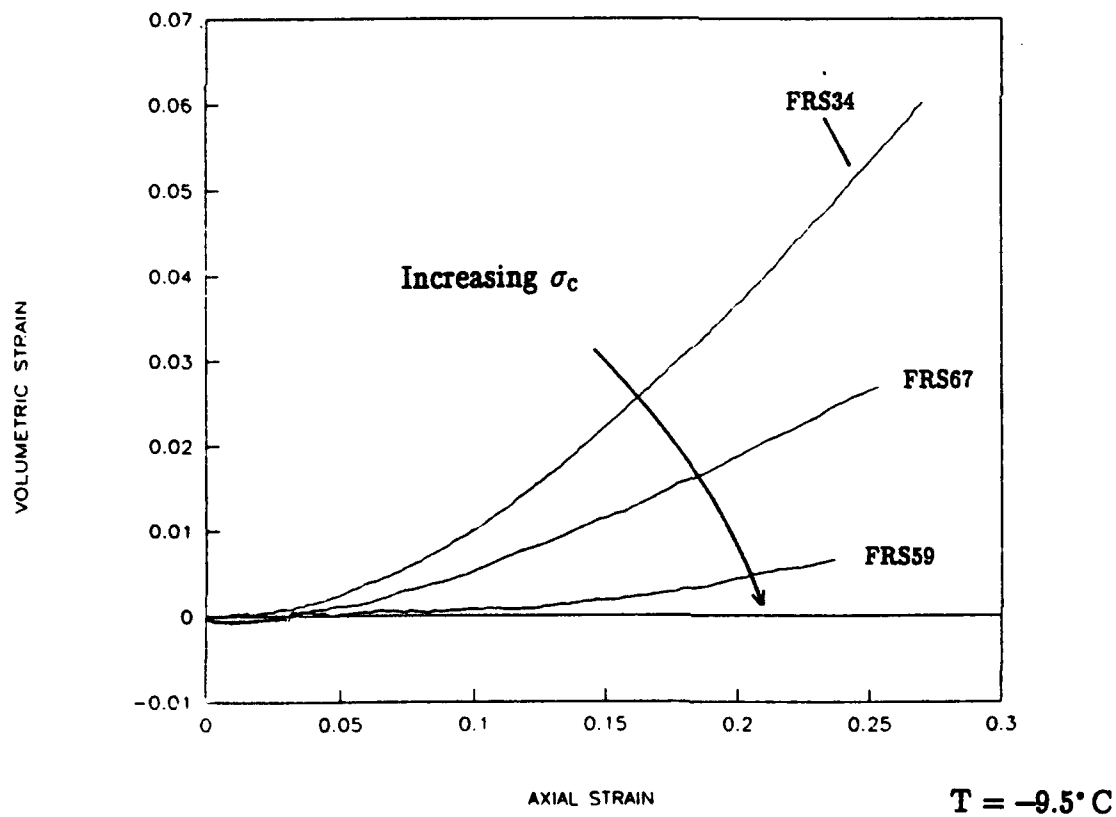
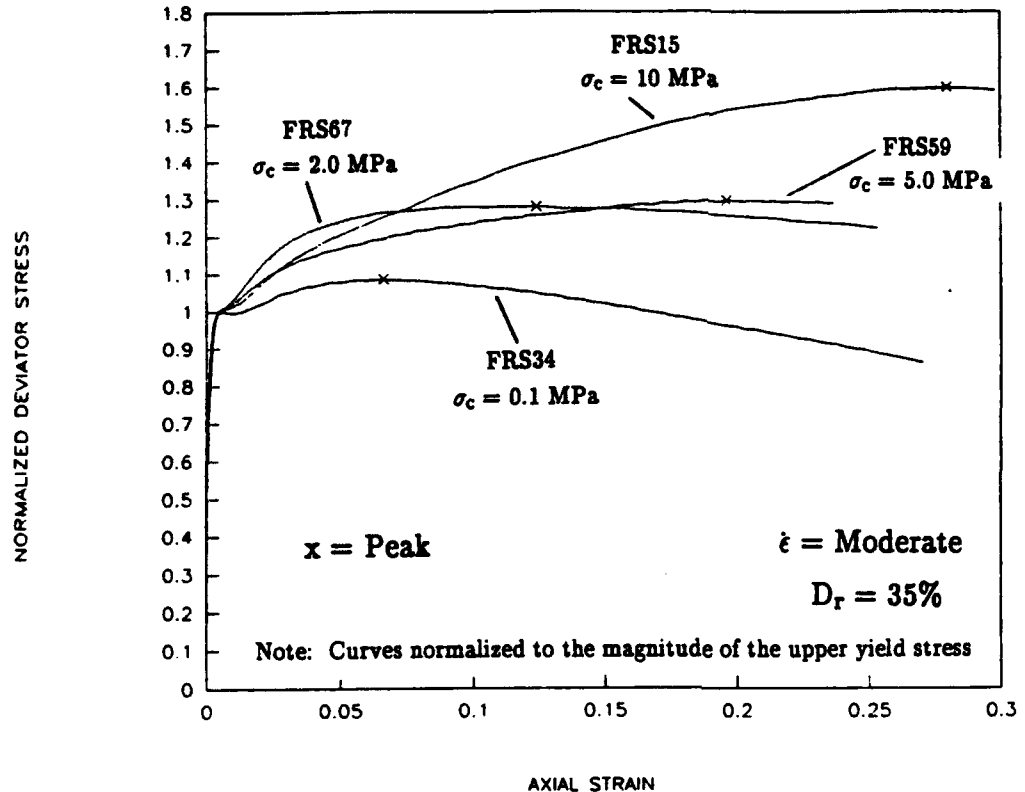


Figure 3.7(a):

Normalized Stress-Strain Curves Showing the Effect of Confining Pressure for Moderate Strain Rate and Low Relative Density for Frozen MFS

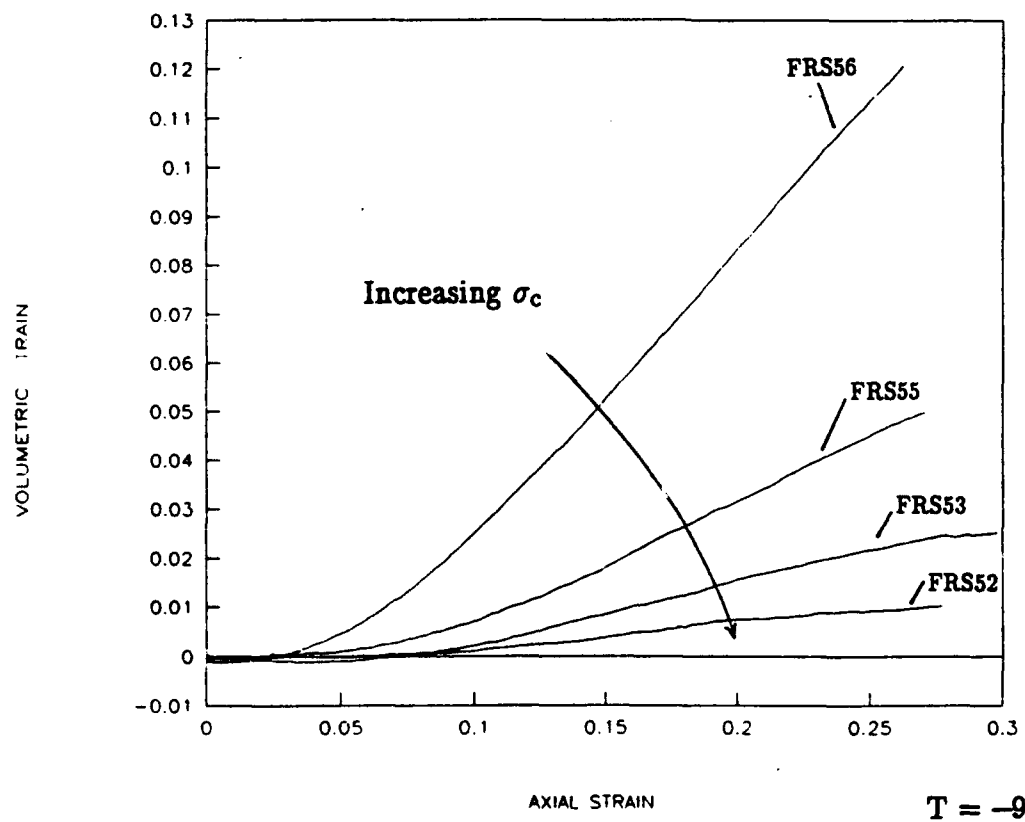
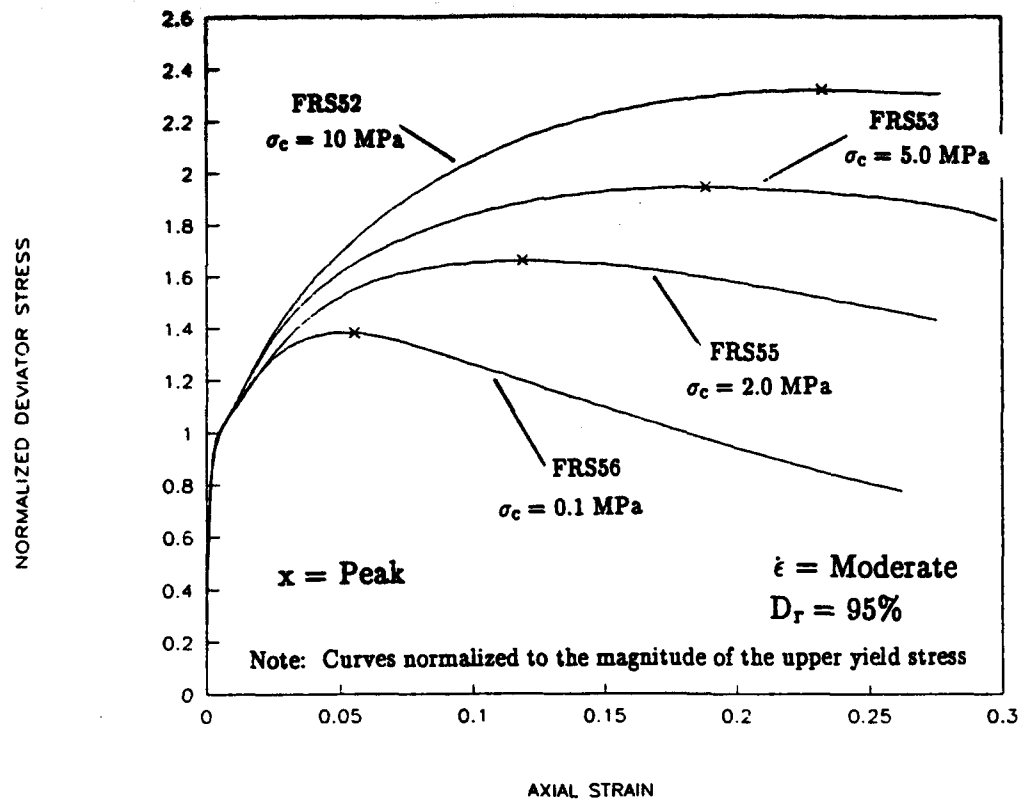


Figure 3.7(b):

Normalized Stress–Strain Curves Showing the Effect of Confining Pressure for Moderate Strain Rate and High Relative Density for Frozen MFS

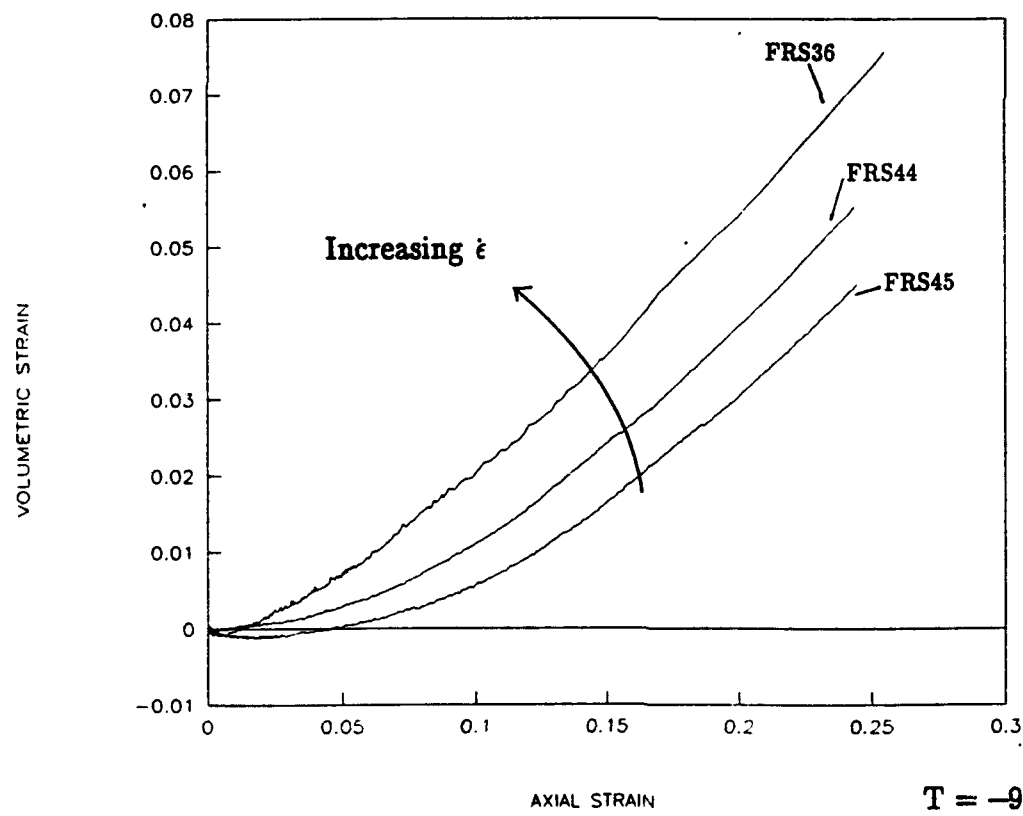
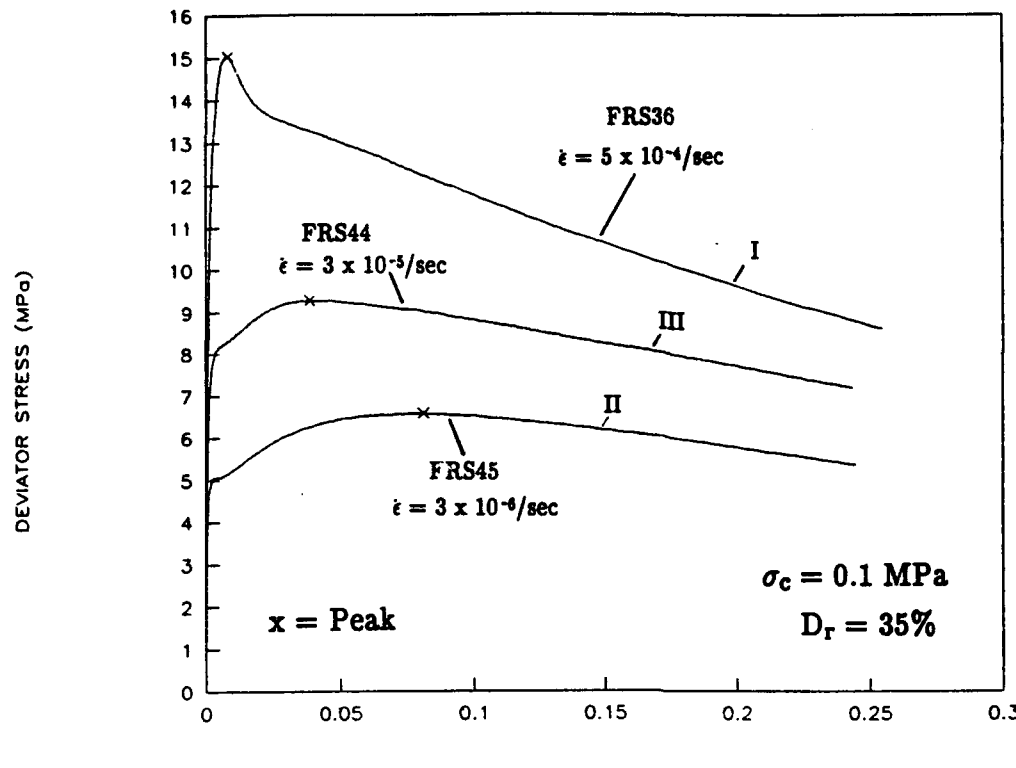


Figure 3.8(a): Stress-Strain Curves Showing the Effect of Strain Rate for Low Relative Density and Low Confining Pressure on Frozen MFS

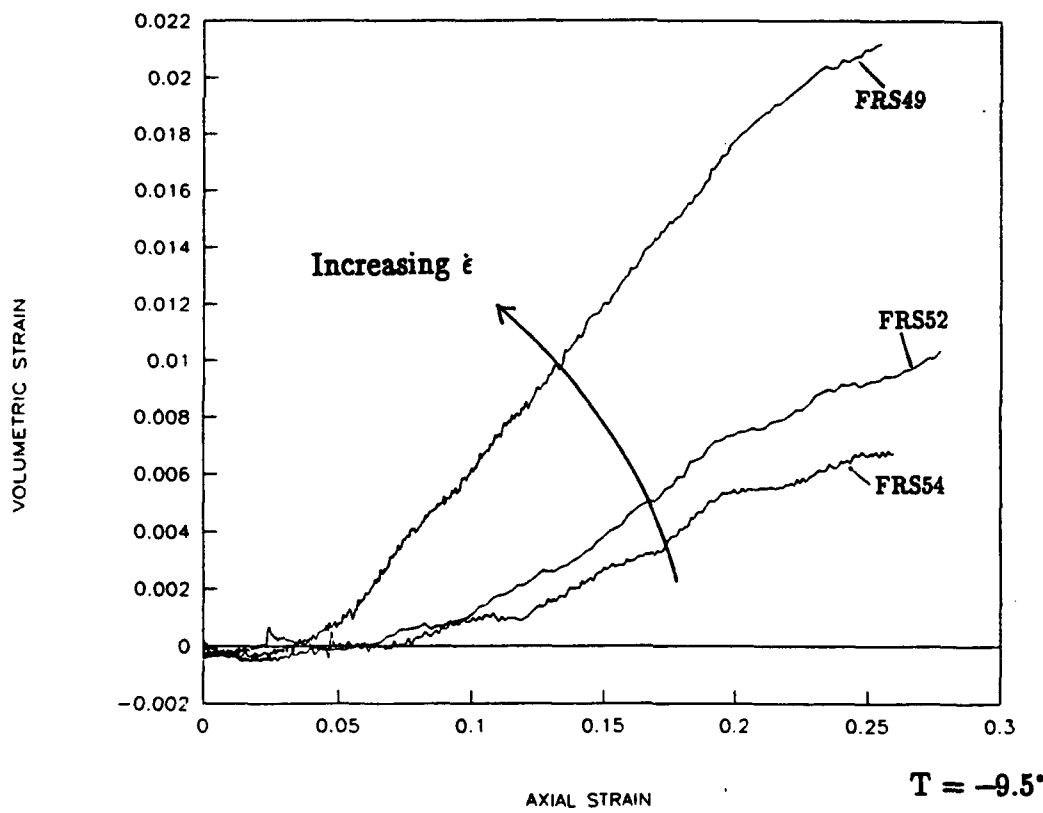
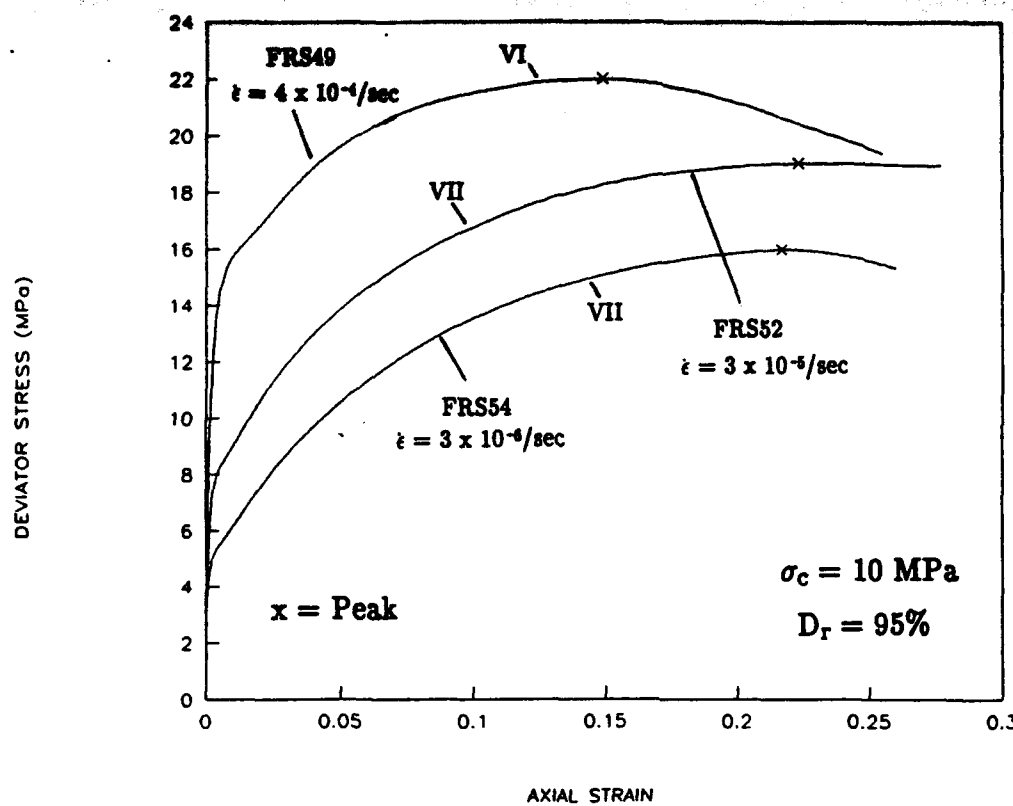


Figure 3.8(b):

Stress-Strain Curves Showing the Effect of Strain Rate for High Relative Density and High Confining Pressure on Frozen MFS

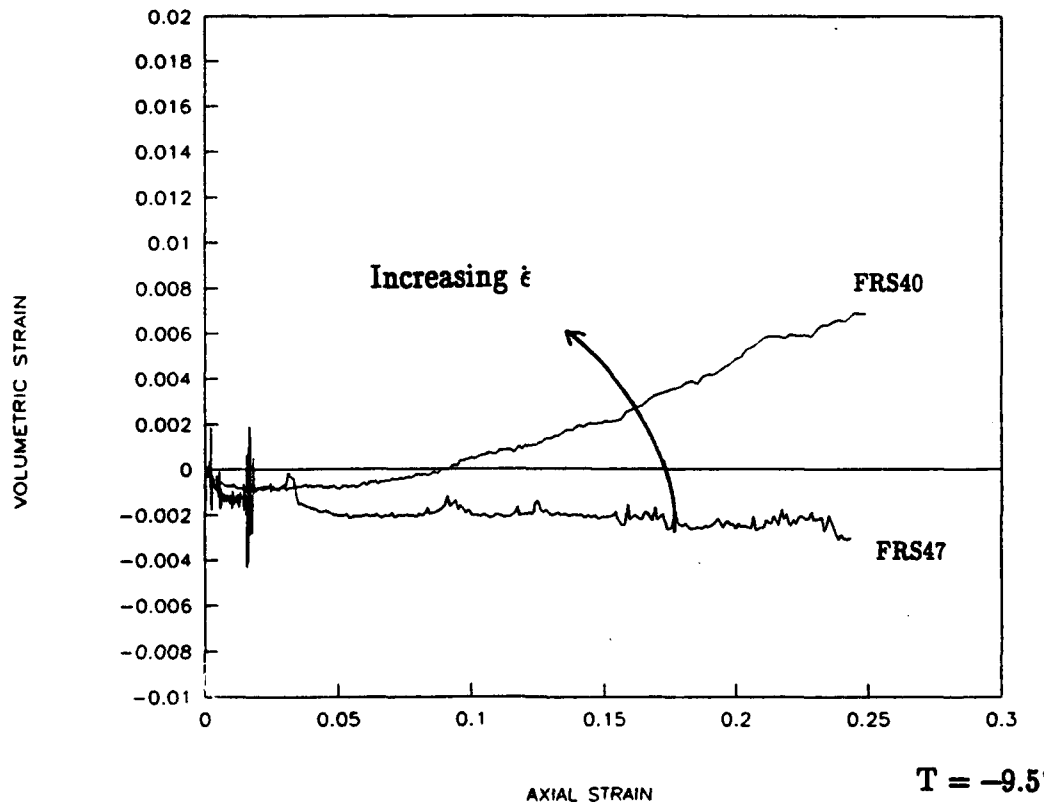
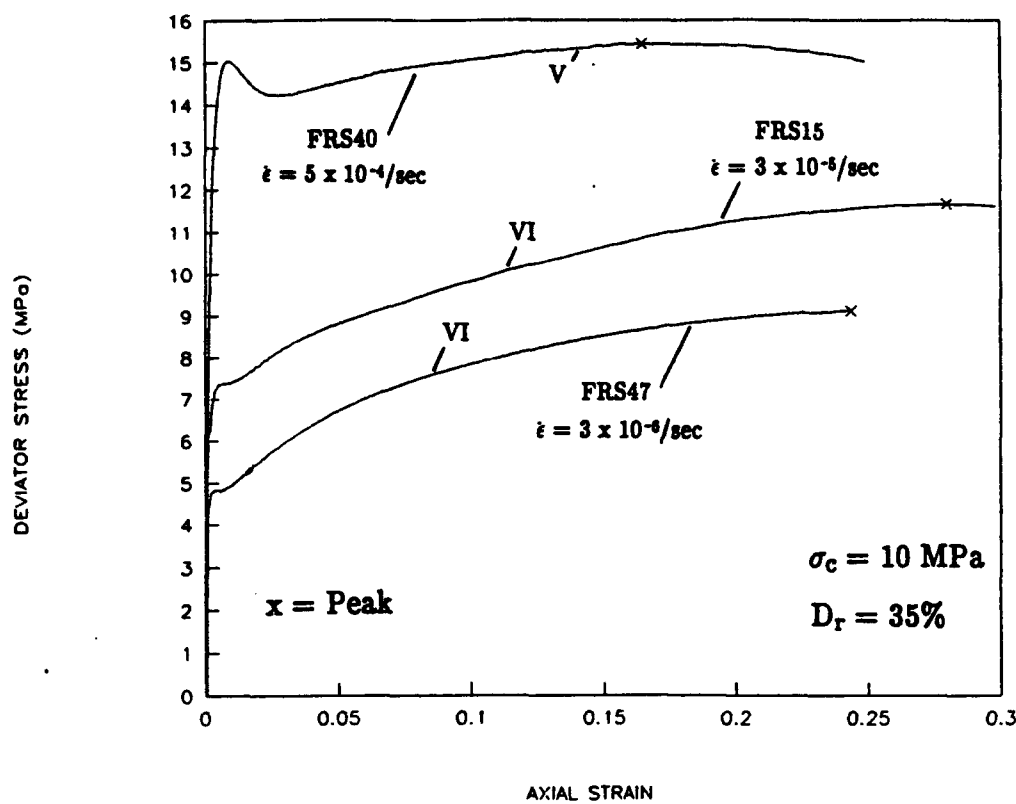
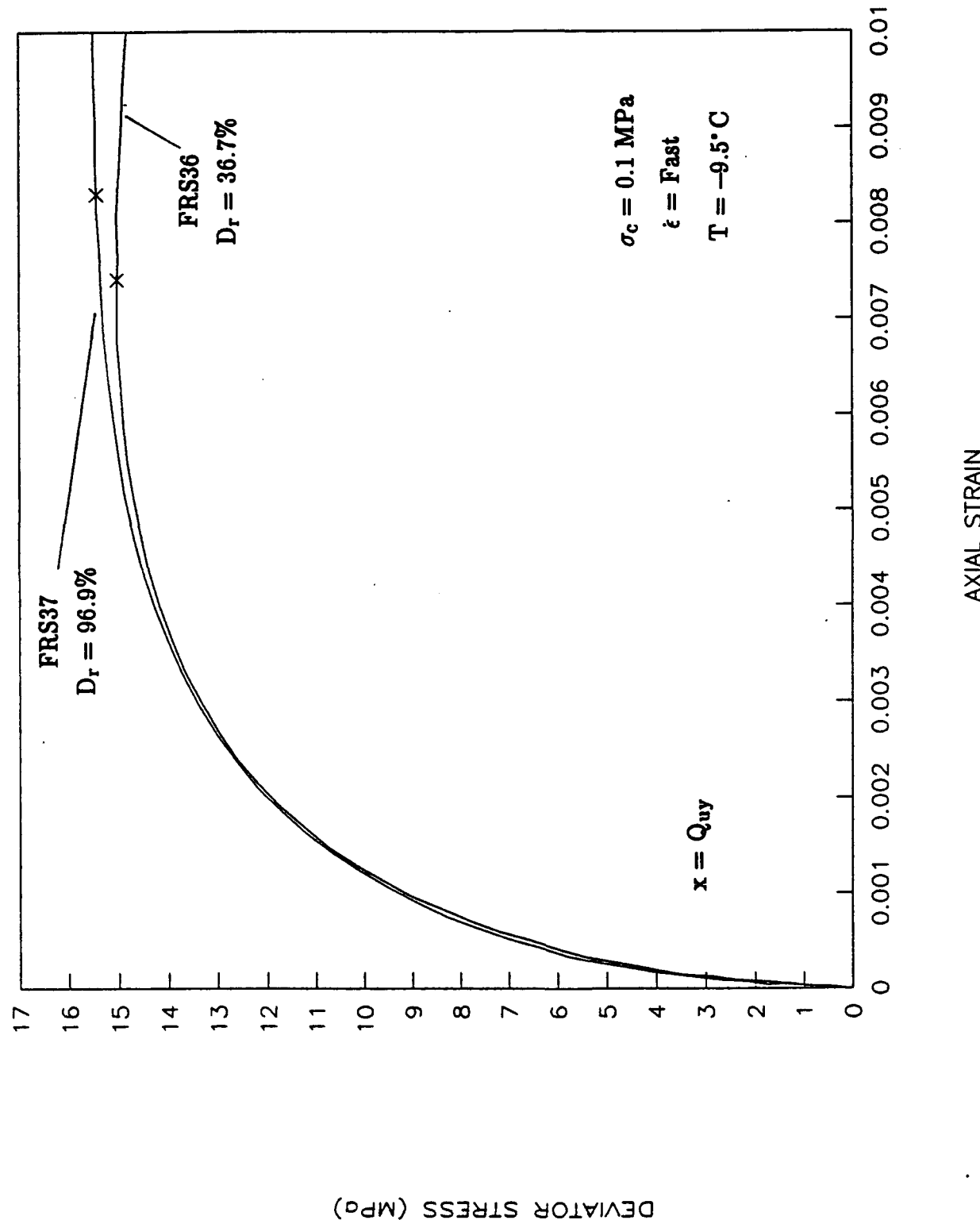


Figure 3.8(c): Stress-Strain Curves Showing the Effect of Strain Rate for Low Relative Density and High Confining Pressure on Frozen MFS



Stress-Strain Curves Showing Upper Yield Behavior of
Frozen MFS at Varying Relative Density

Figure 3.9(a):

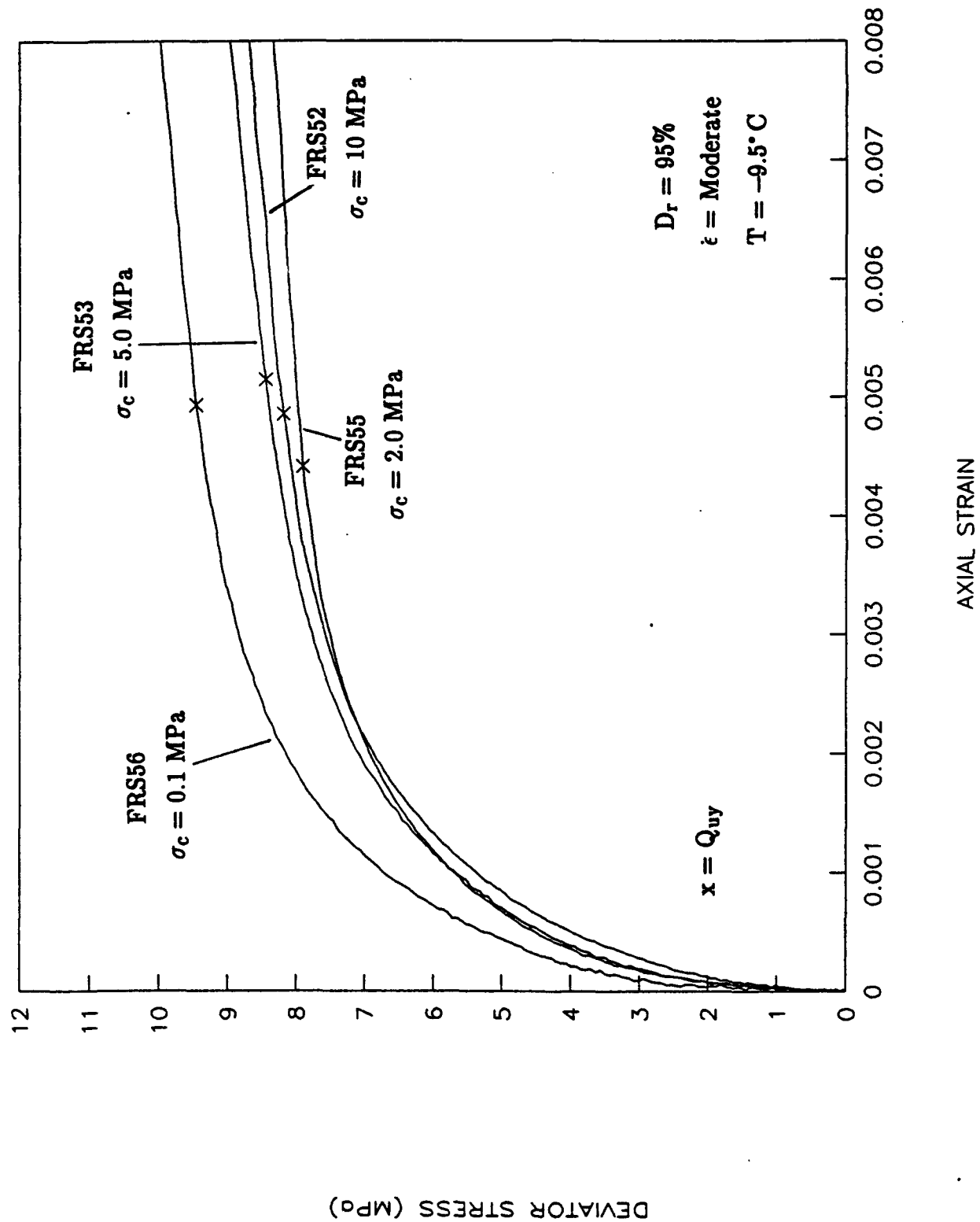
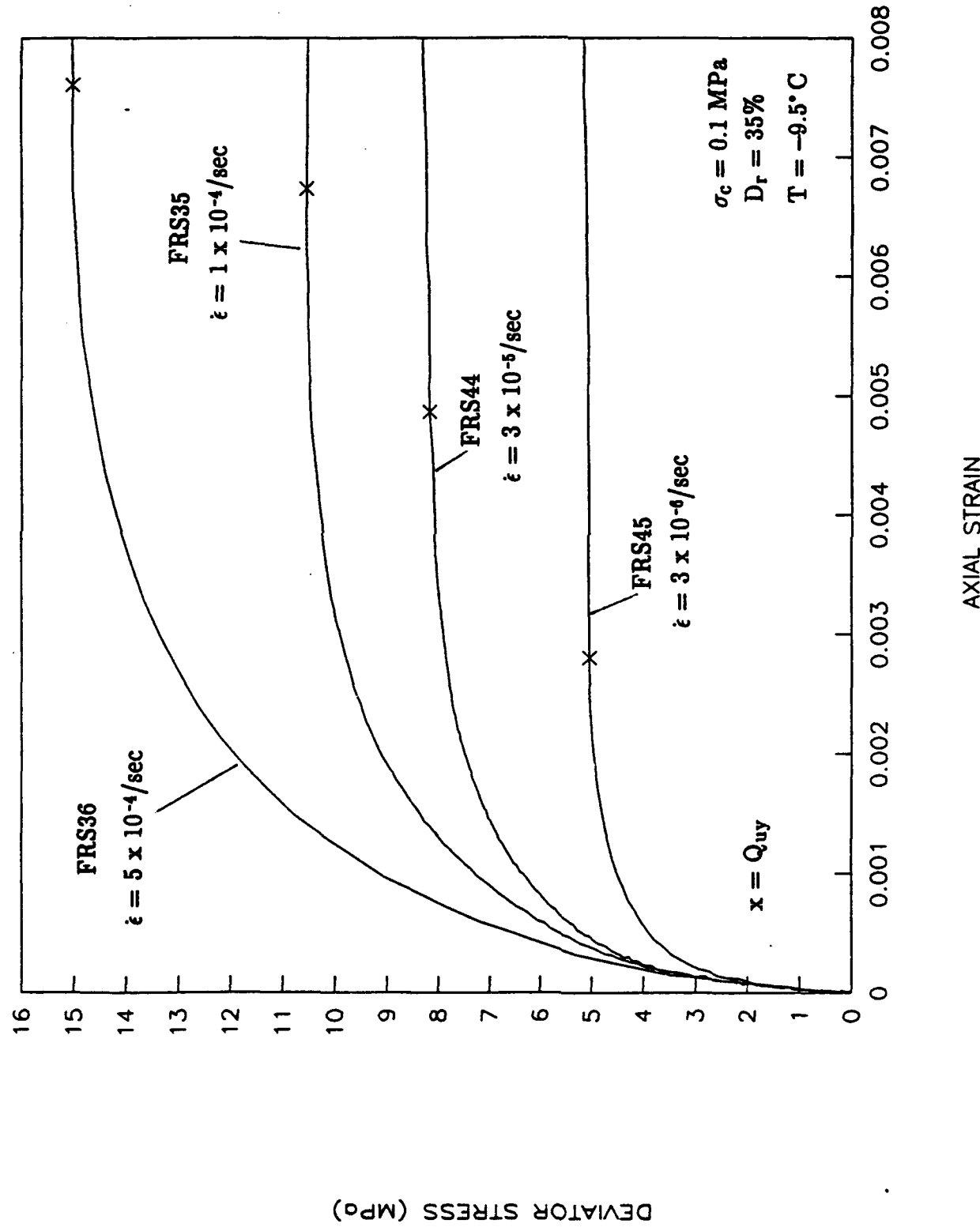


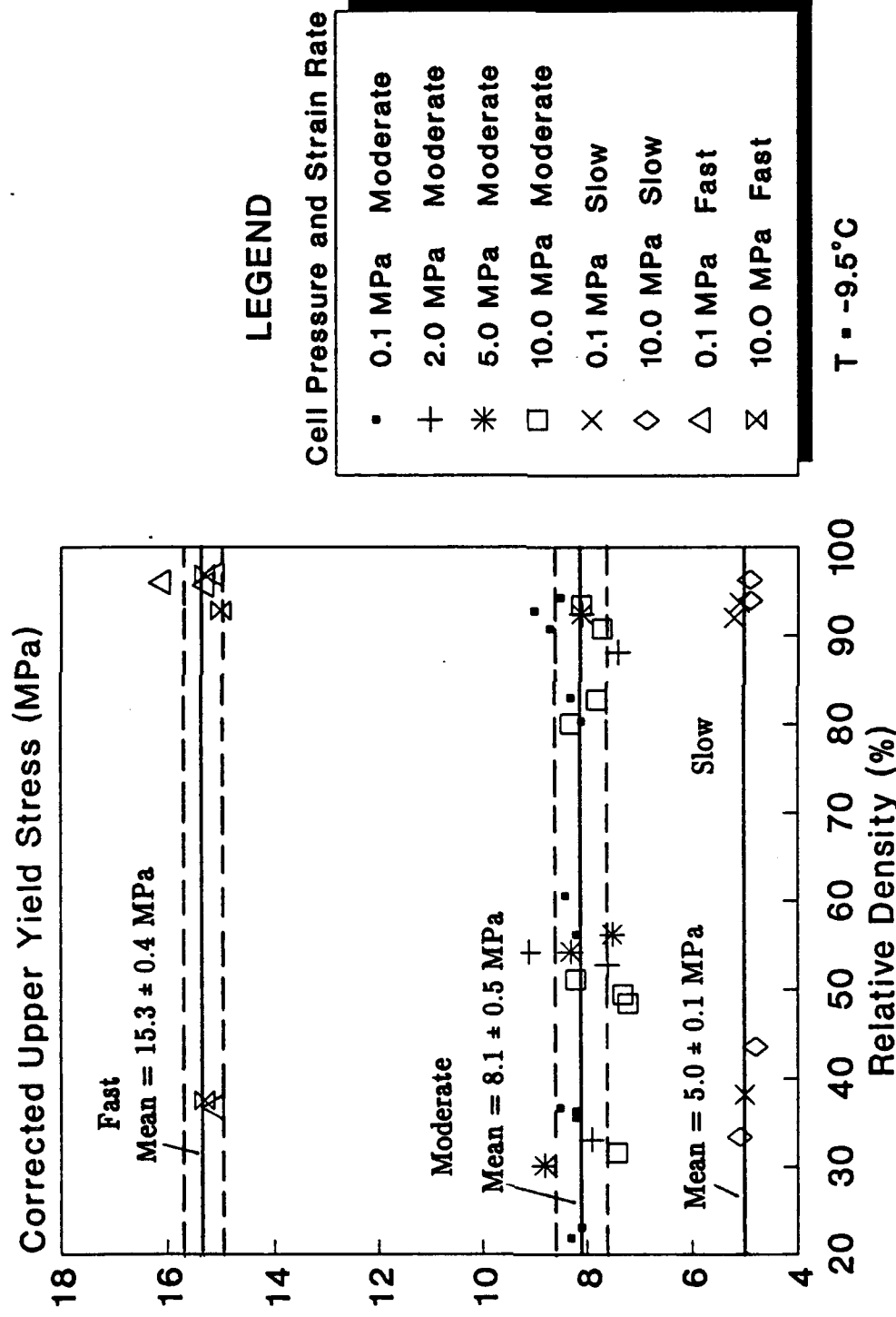
Figure 3.9(b): Stress-Strain Curves Showing Upper Yield Behavior of Frozen MFS at Varying Confining Pressure

77



Stress-Strain Curves Showing Upper Yield Behavior of
Frozen MFS at Varying Strain Rate

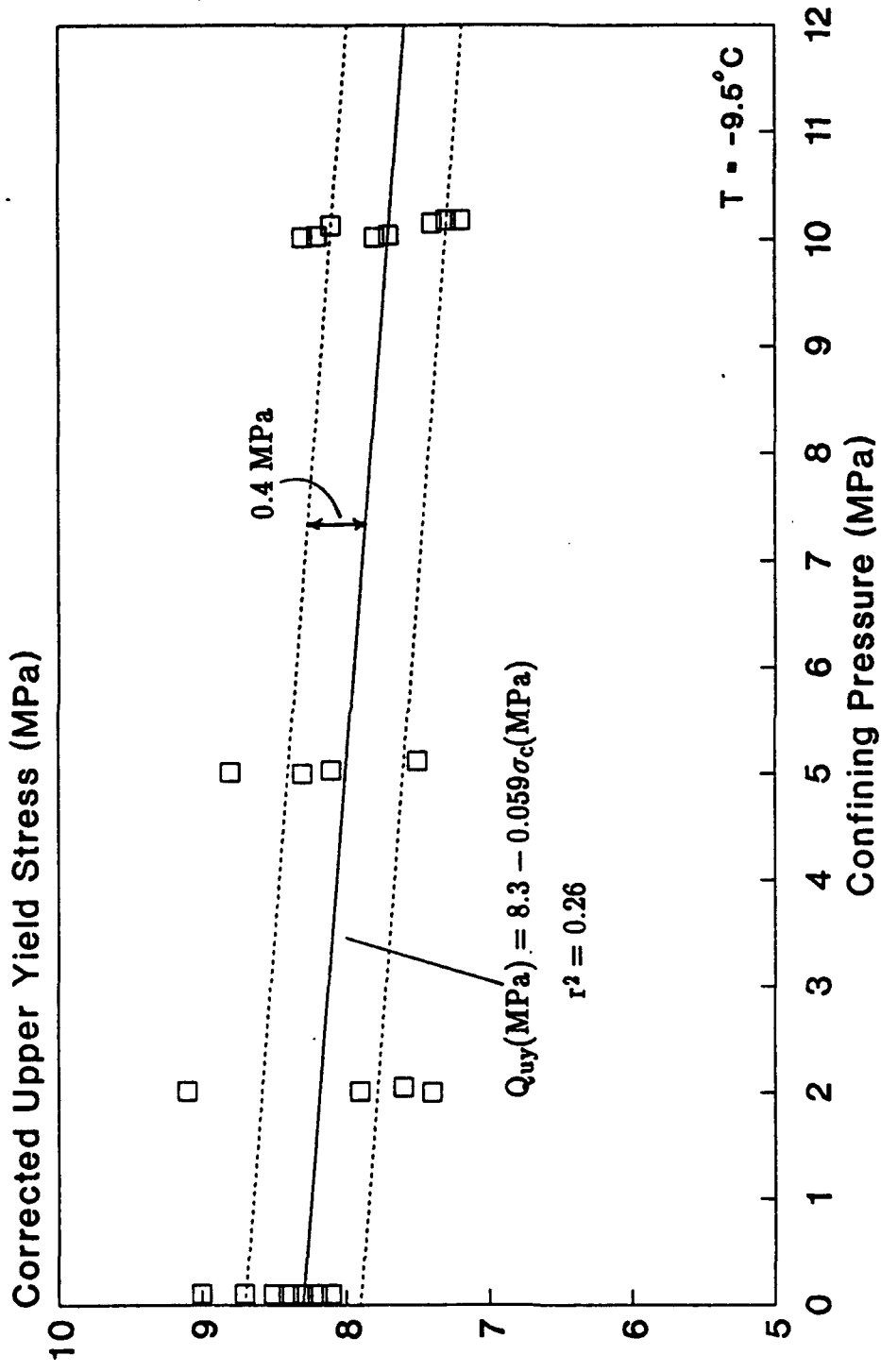
Figure 3.9(c):



MSP, gfpvp Stability, gfp ADCT's
Lub and Fric Ends

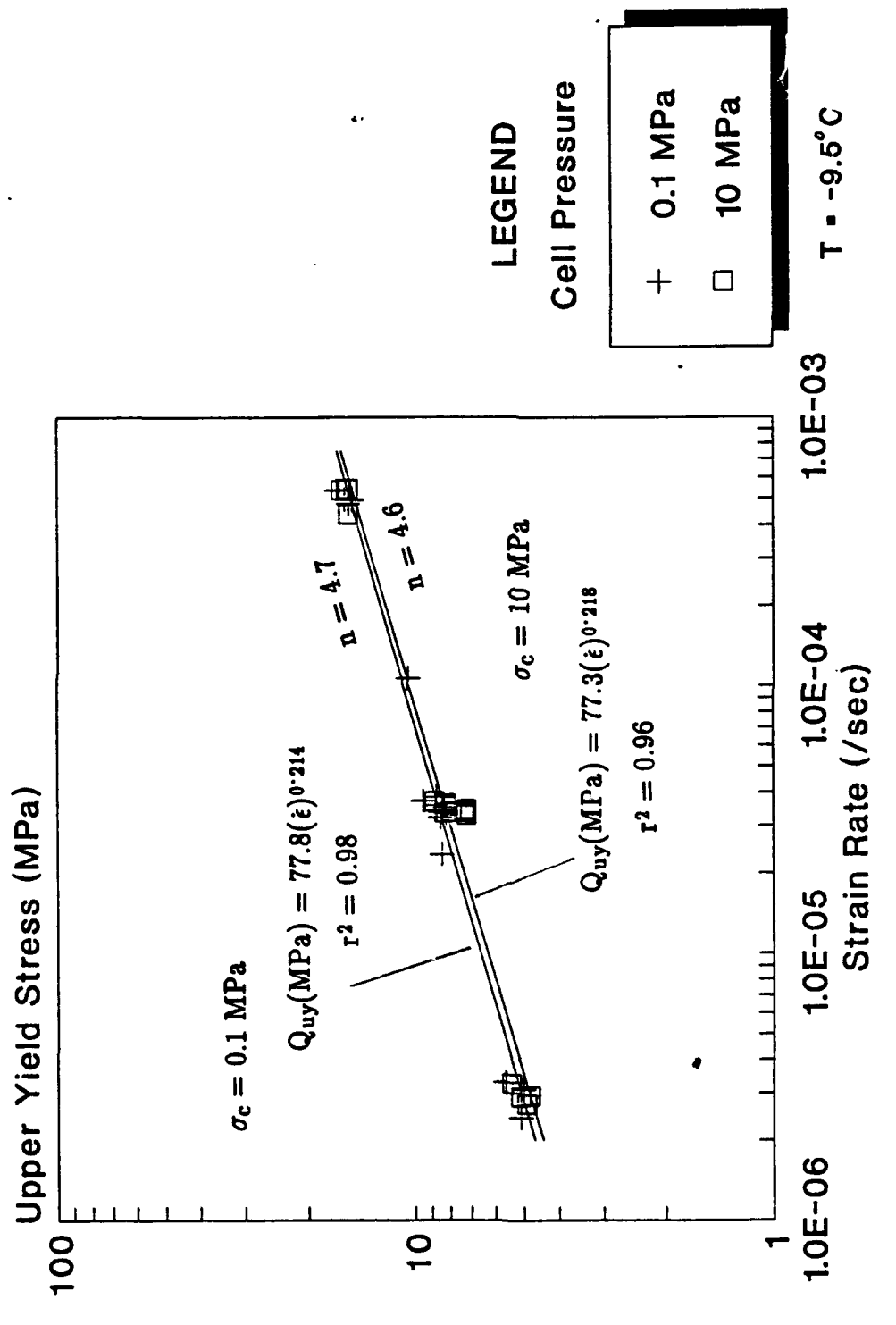
Corrected Upper Yield Stress Versus Relative Density
for Frozen MFs

Figure 3.10:



Moderate Strain Rate
MSP, gfpvp Stability, gfp ACDT's
Lub and Fric Ends

Figure 3.11:
Effect of Confining Pressure on Corrected Upper Yield Stress for Frozen MFS



MSP, gfpvp Stability, gfp ACDT's
Lub and Fric Ends

Effect of Strain Rate on Upper Yield Stress for Frozen
MFs

Figure 3.12:

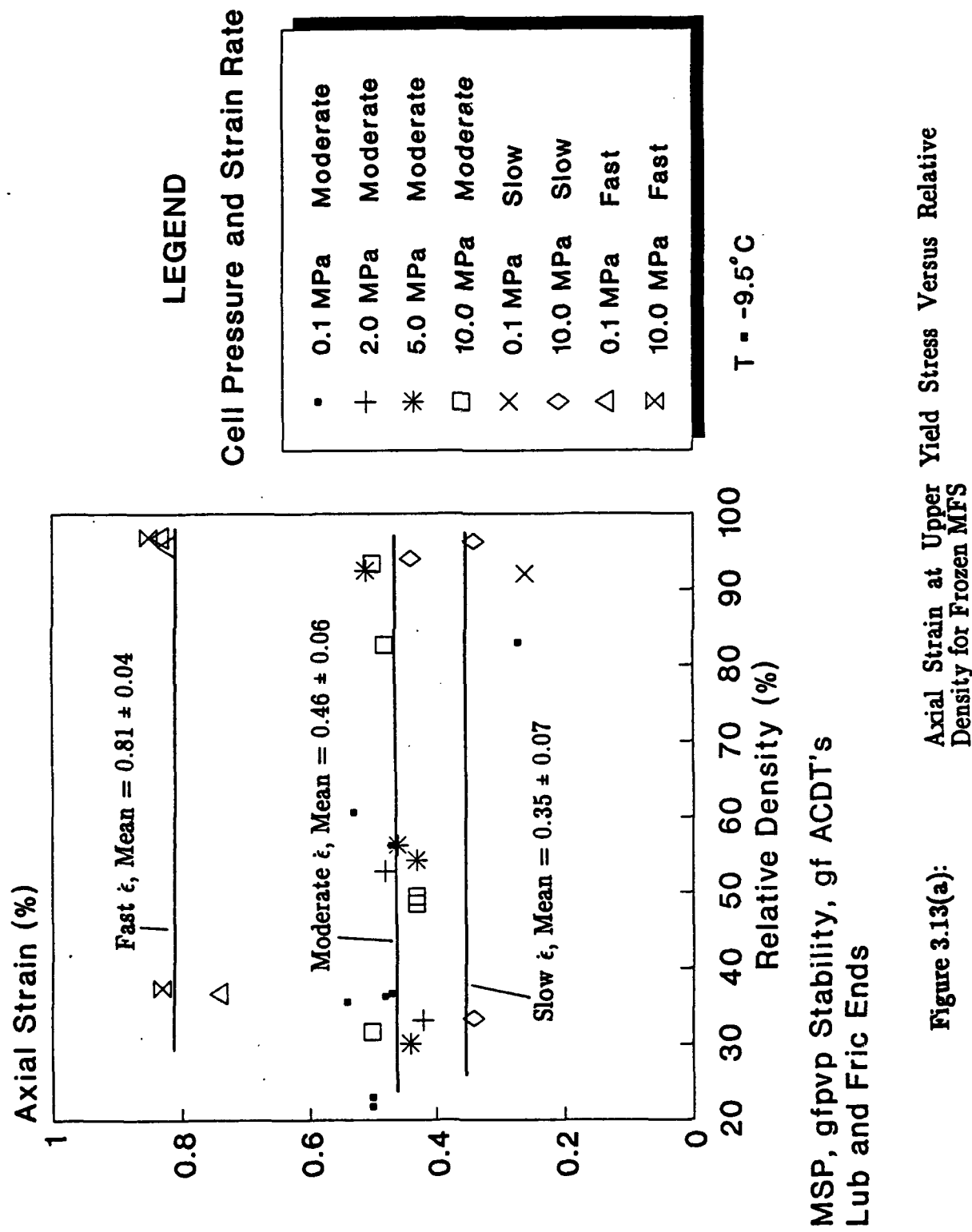
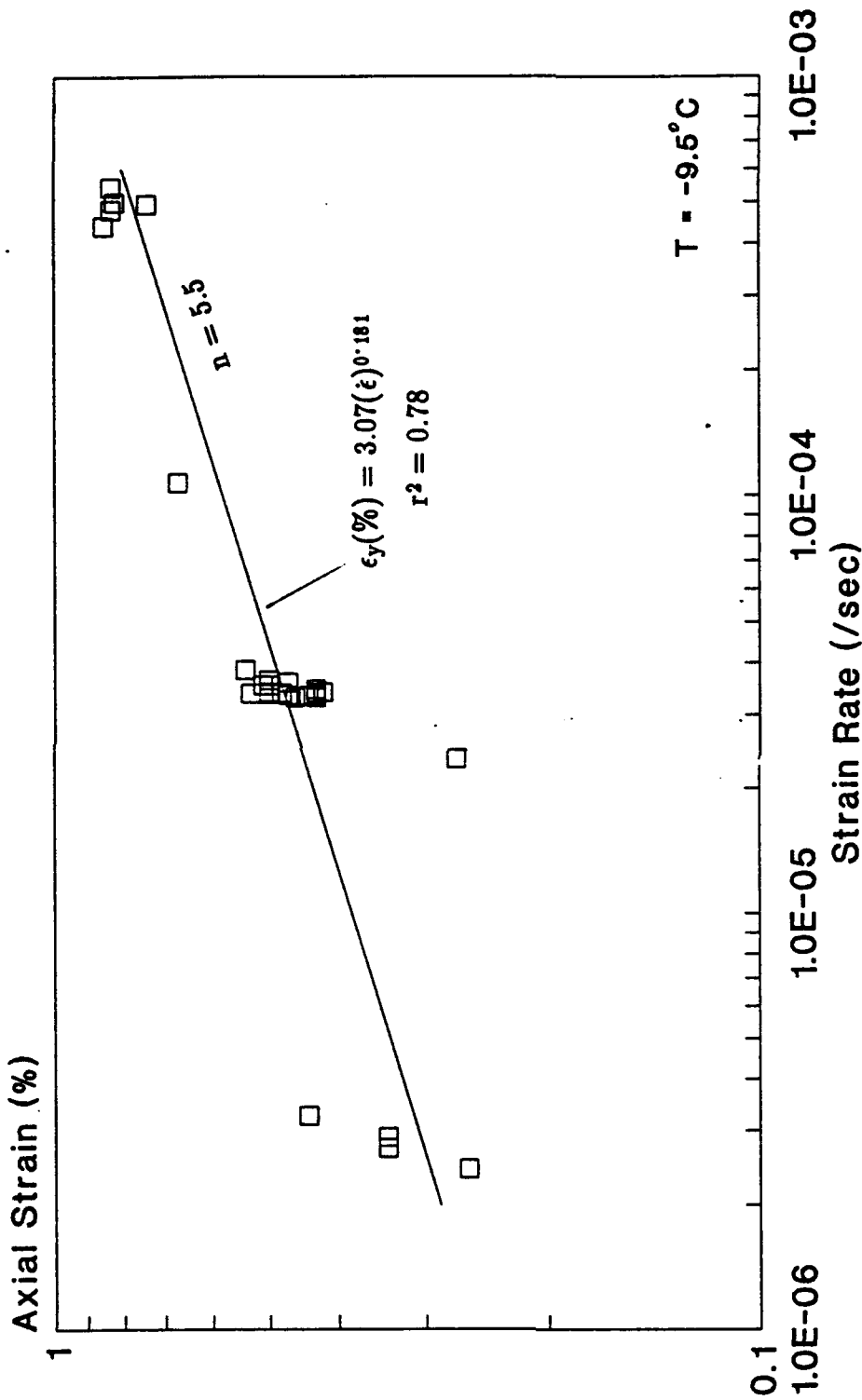


Figure 3.13(a):

Axial Strain at Upper Yield Stress Versus Relative Density for Frozen MFS



All Confining Pressures and Dr
MSP, gfpvp Stability, gf ACDT's
Lub and Fric Ends

Figure 3.13(b):

Effect of Strain Rate on the Axial Strain at the Upper Yield Stress for Frozen MFS

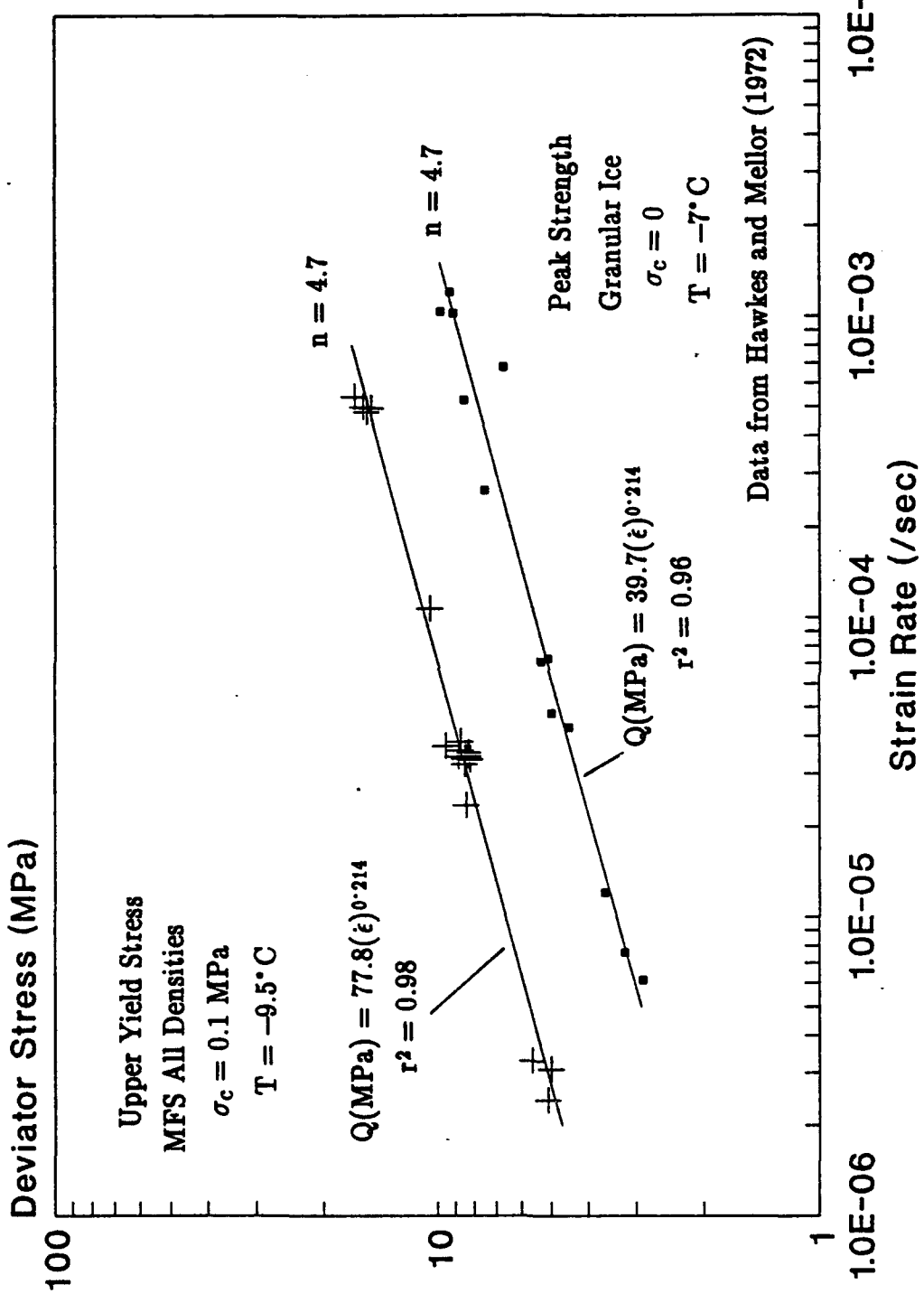


Figure 3.14: Comparison of Rate Sensitivity of Upper Yield Stress of Frozen MFS to that of Peak Strength of Polycrystalline Ice

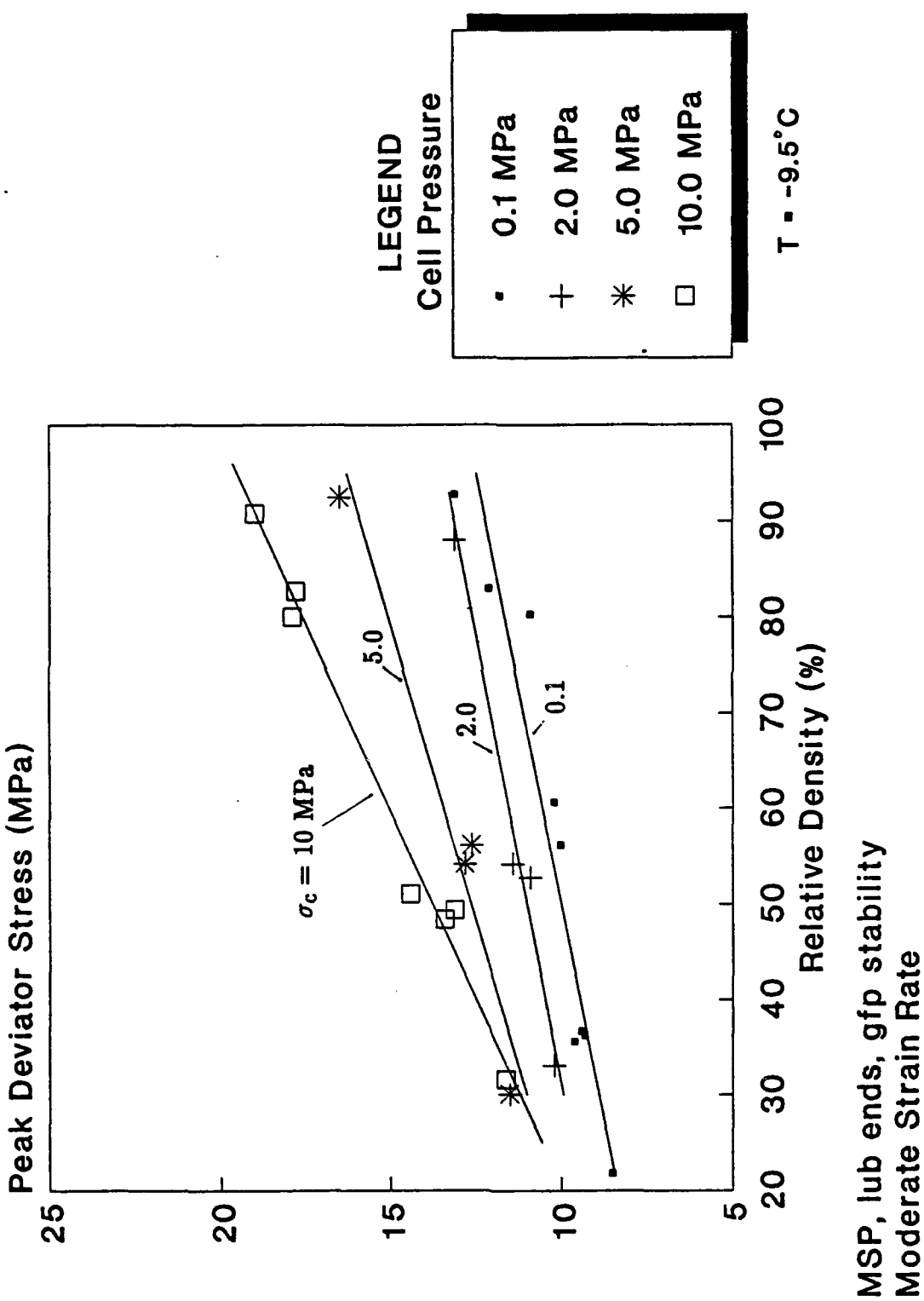
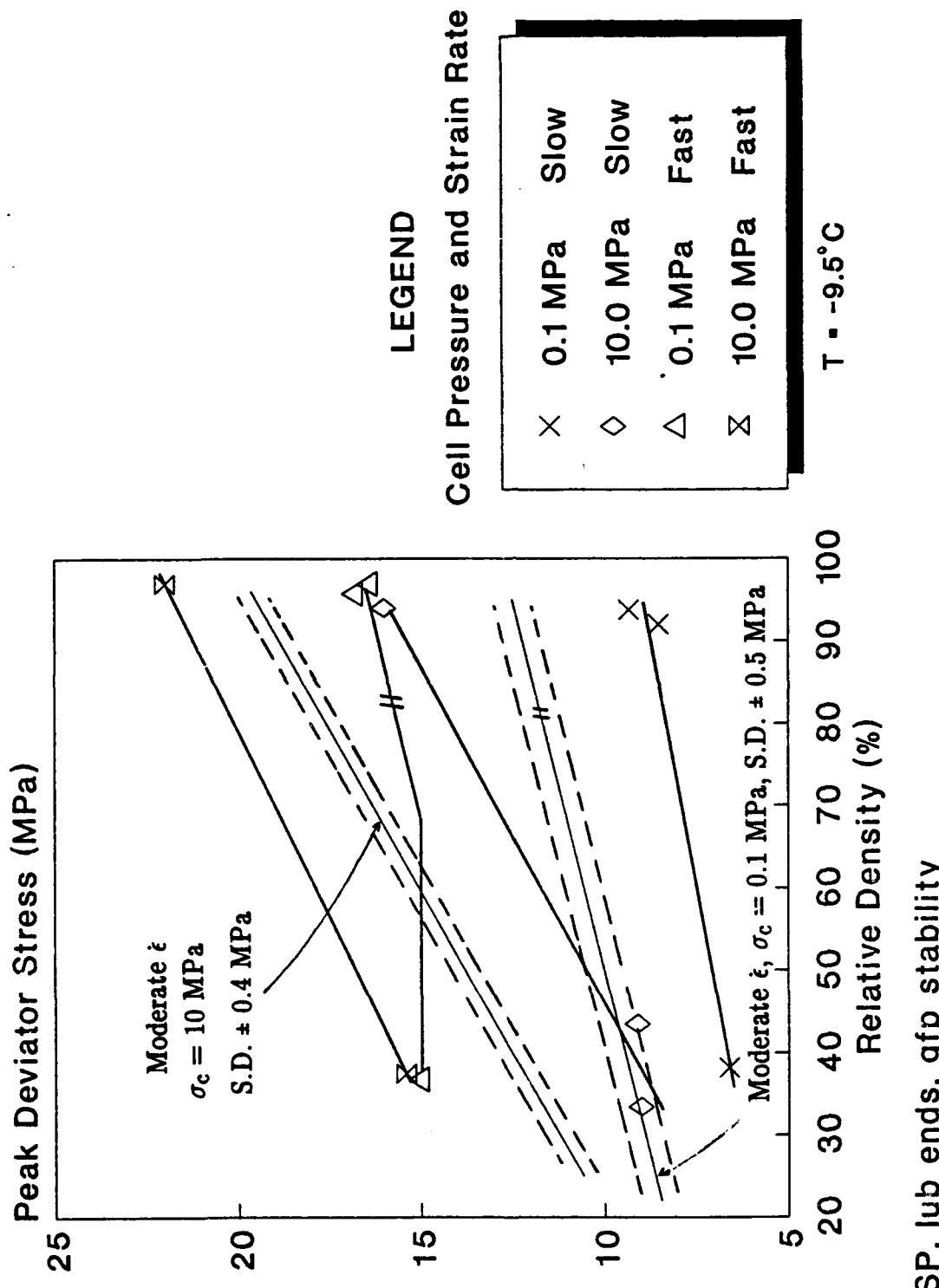


Figure 3.15(a):

Peak Deviator Stress Versus Relative Density at
Moderate Strain Rate for Frozen MFS



MSP, lub ends, gfp stability

Figure 3.15(b):
Peak Deviator Stress Versus Relative Density for Range
in Strain Rates and Confining Pressures for Frozen
MFS

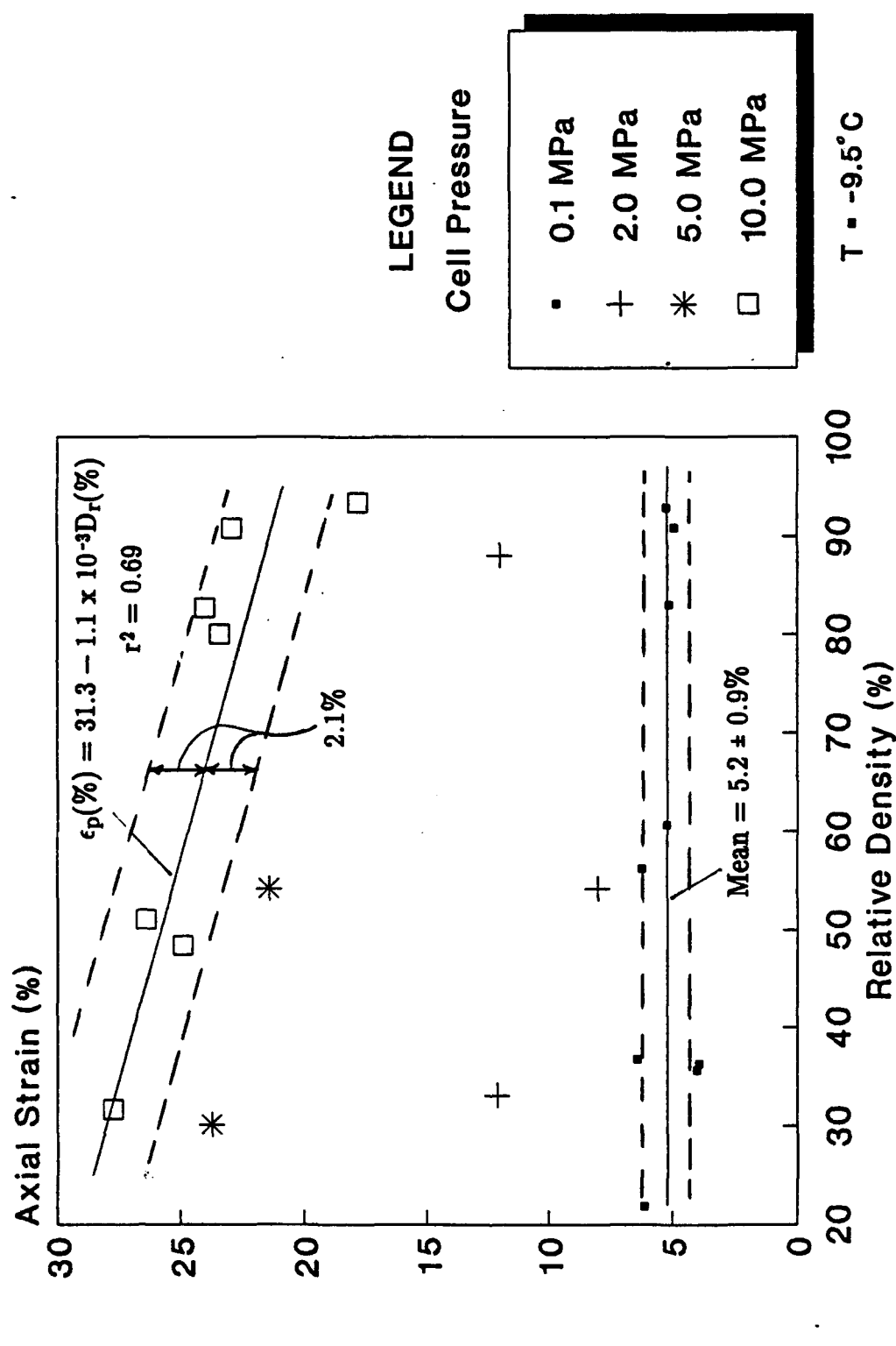


Figure 3.16(a): Axial Strain at Peak Deviator Stress Versus Relative Density for Moderate Strain Rate and Range in Confining Pressures for Frozen MFs

Figure 3.16(b):

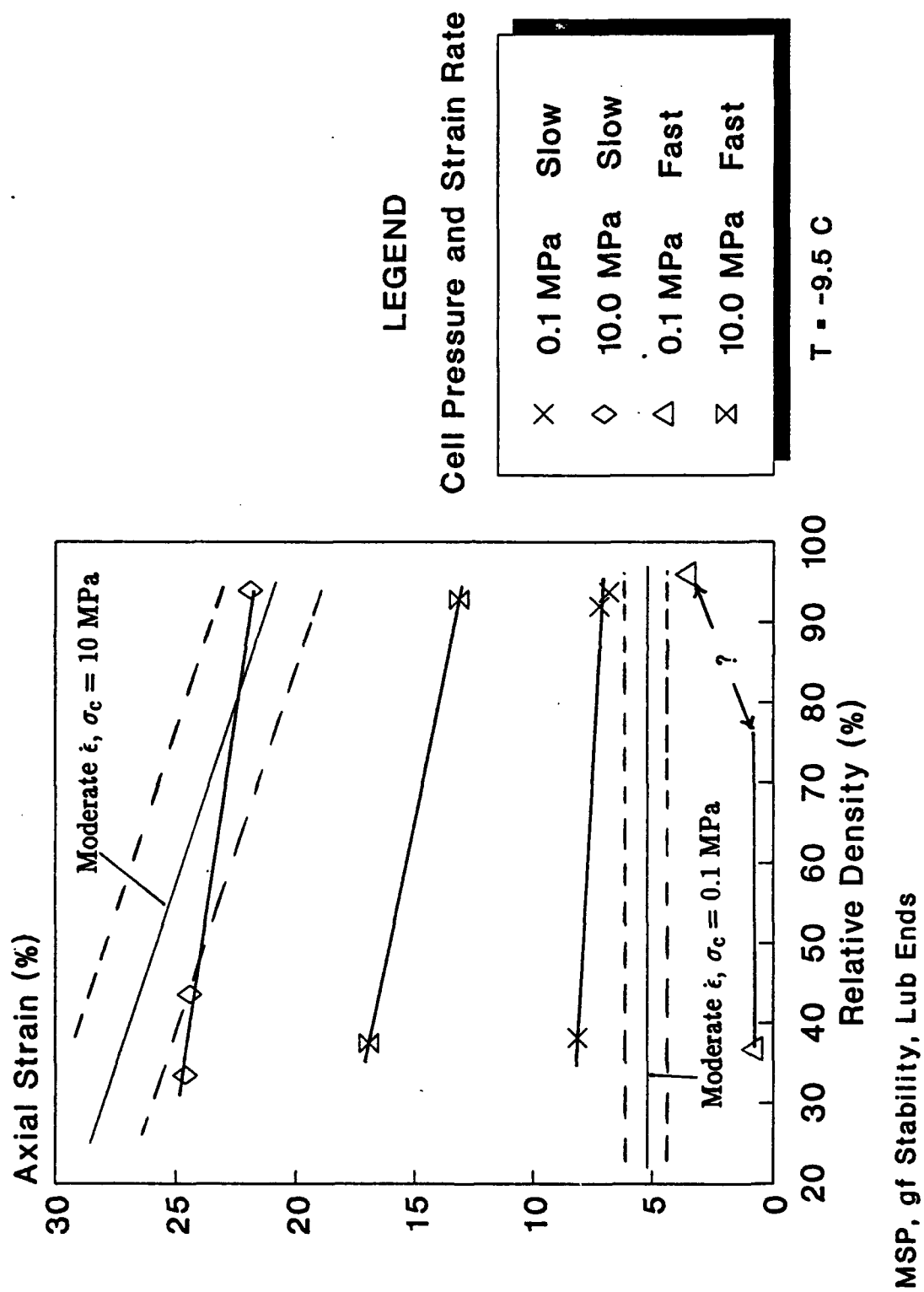
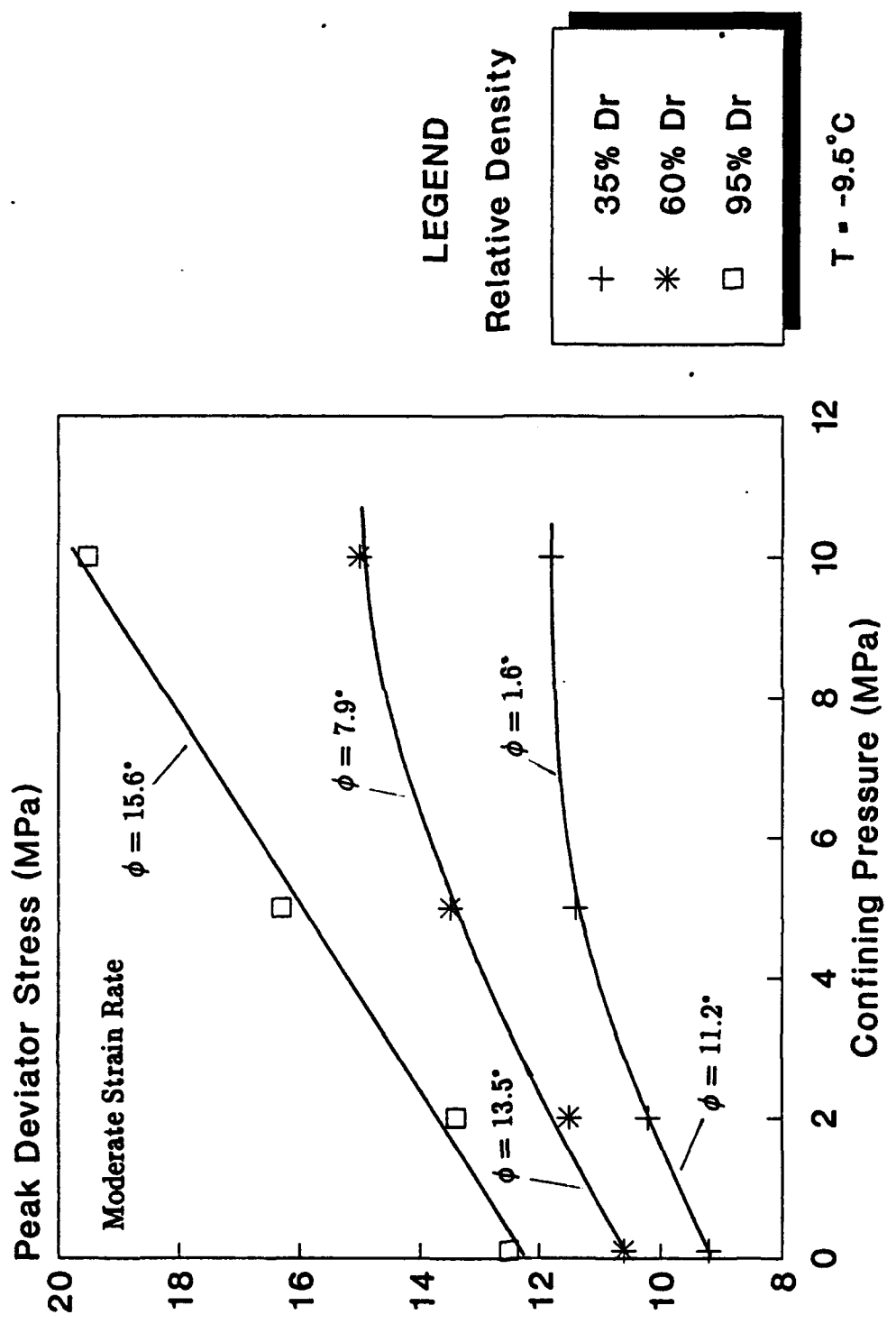


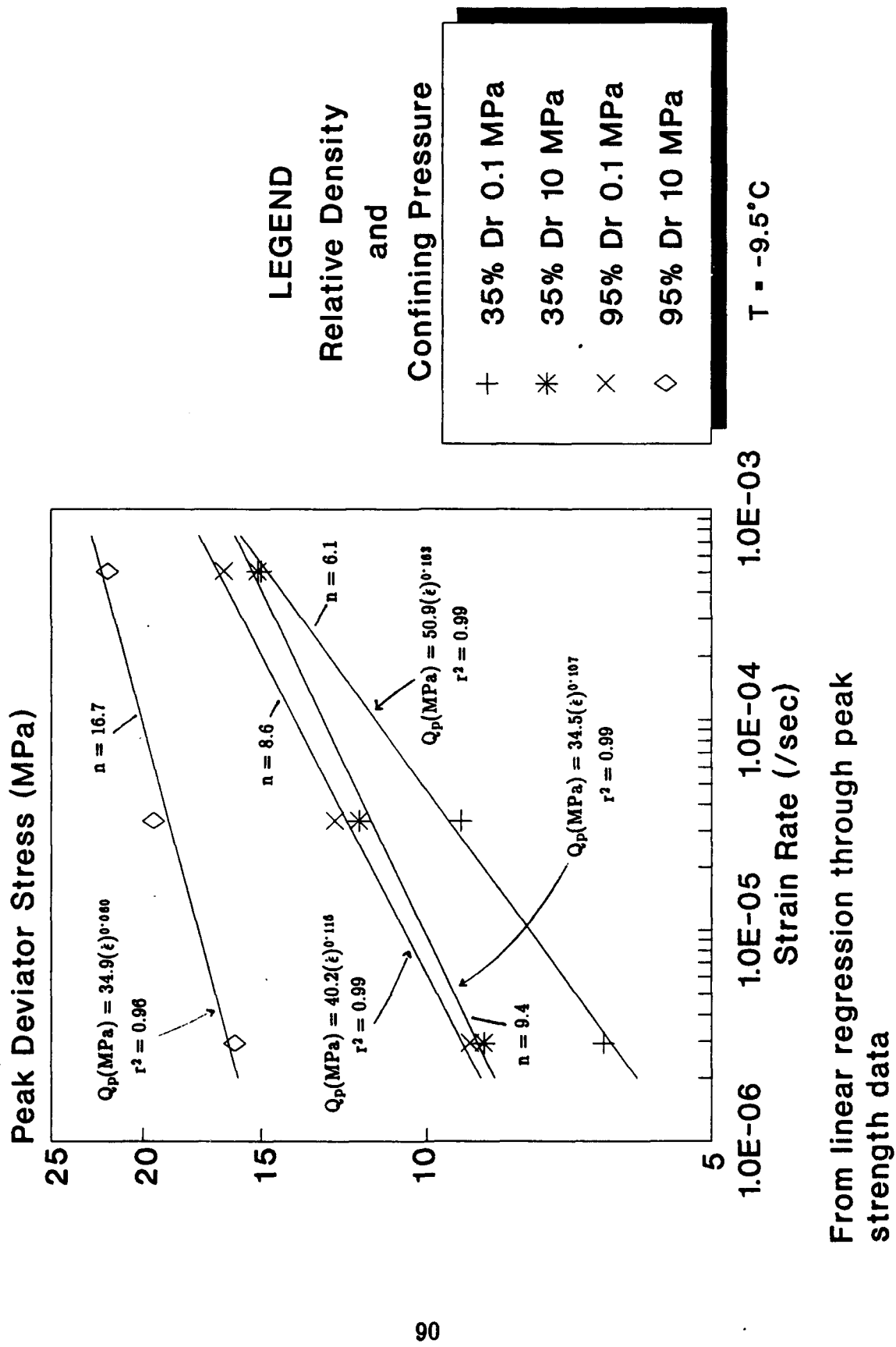
Figure 3.16(b):
Axial Strain at Peak Deviator Stress Versus Relative Density for Range in Strain Rates and Confining Pressures for Frozen MFS

Figure 3.16(b):



From linear regression through peak strength data

Figure 3.17: Effect of Confining Pressure on Peak Deviator Stress for Moderate Strain Rate for Frozen MFS



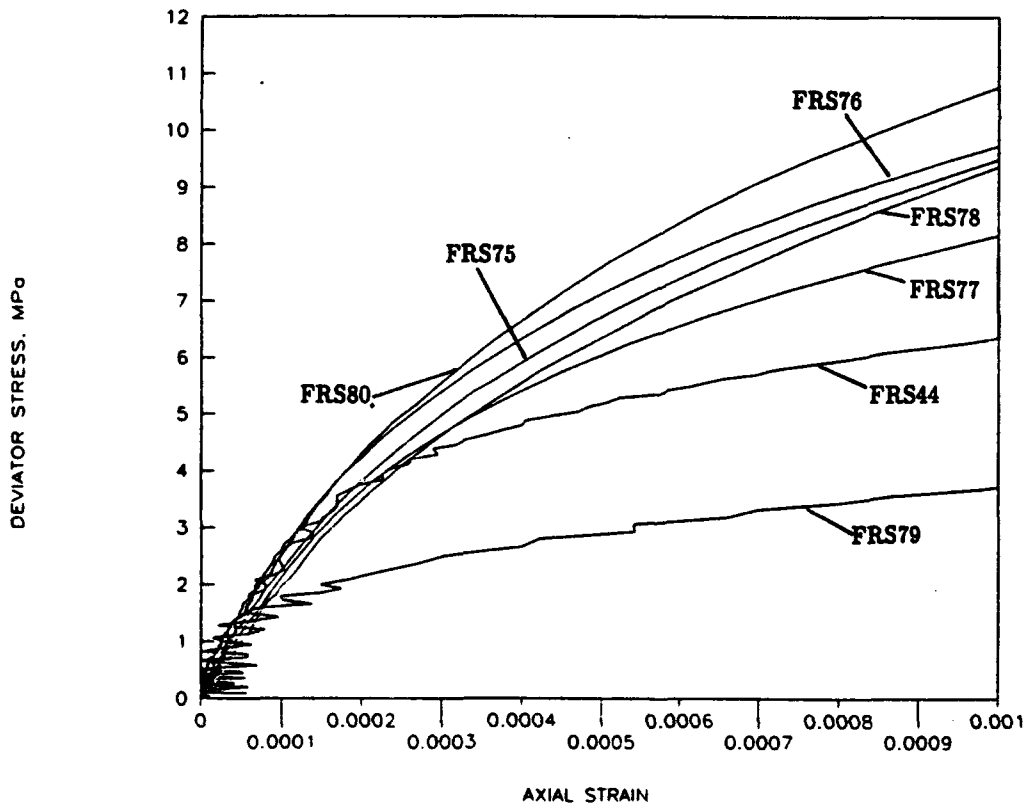
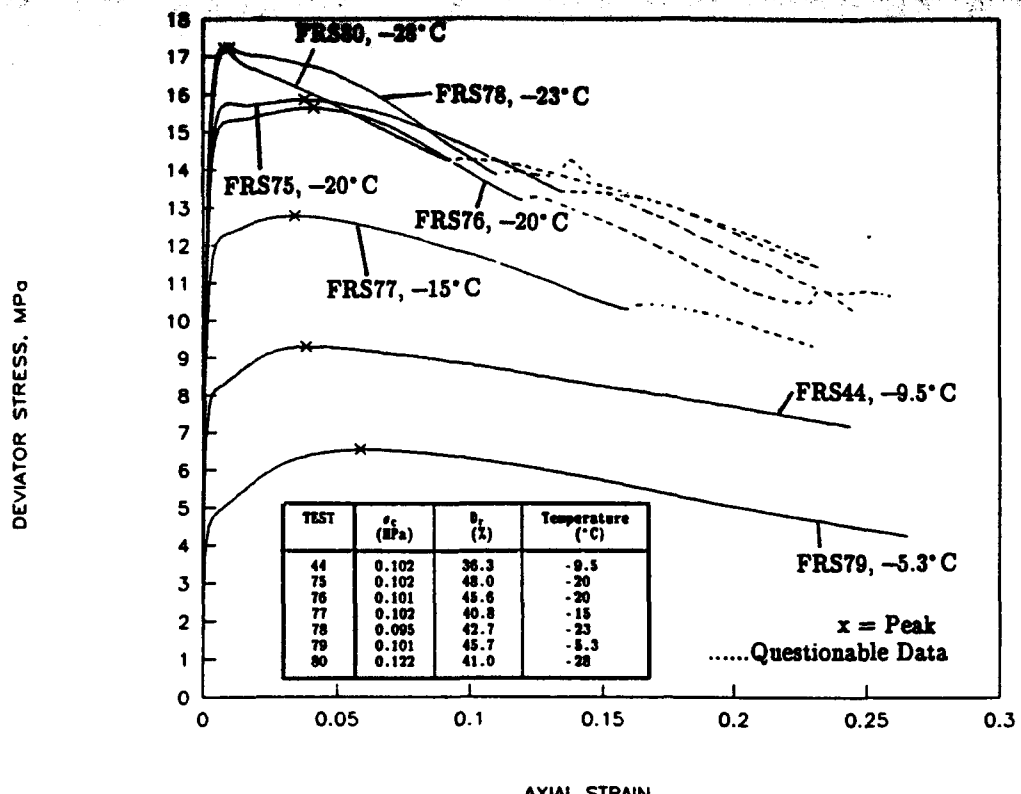
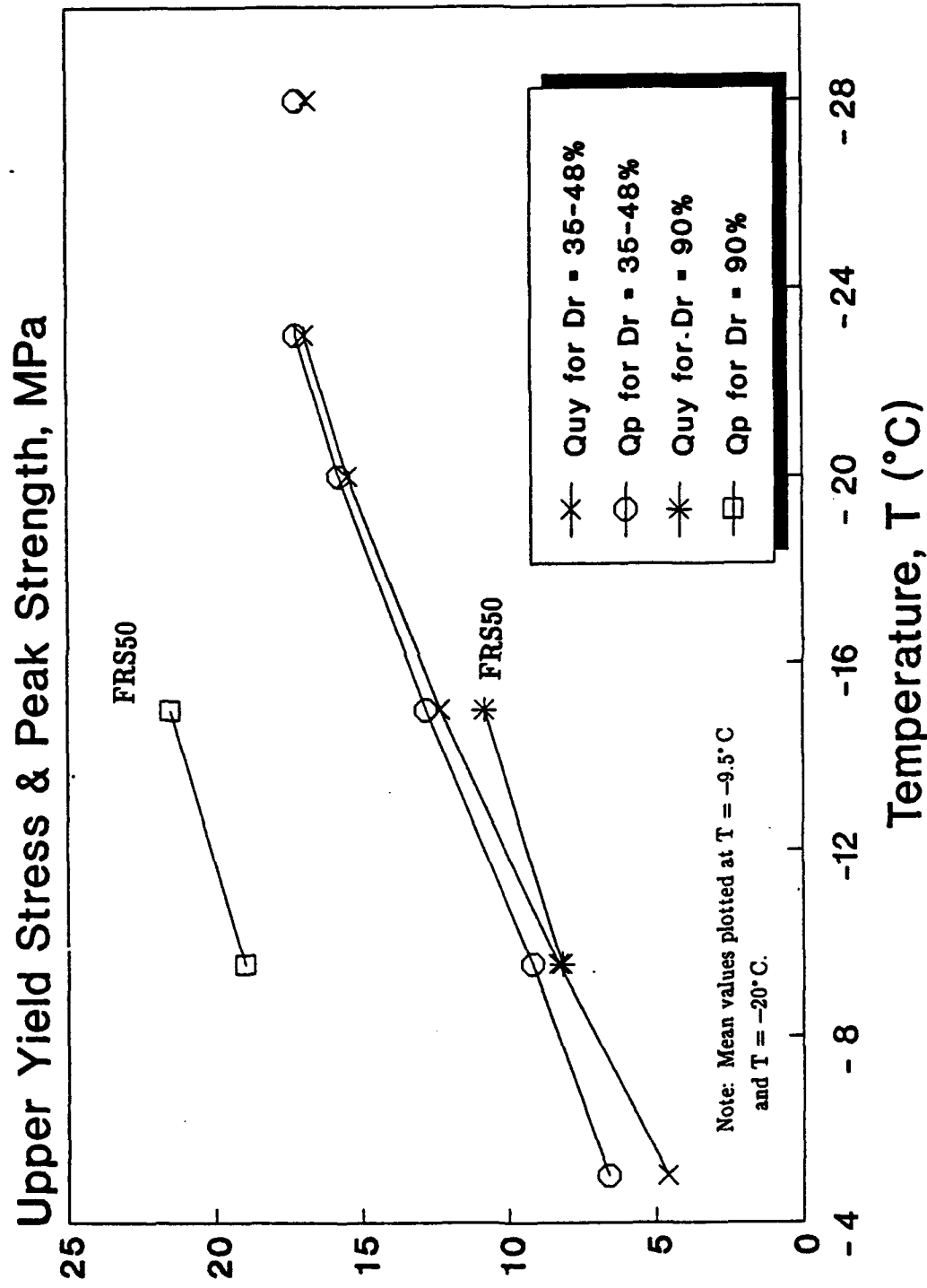


Figure 3.19:

Stress-Strain Curves Showing the Effect of Temperature at Moderate Strain Rate for Low Relative Density and Low Confining Pressure for Frozen MFS



Effect of Temperature on the Upper Yield Stress and Peak Strength of Frozen MFS at Moderate Strain Rate

Figure 3.20:

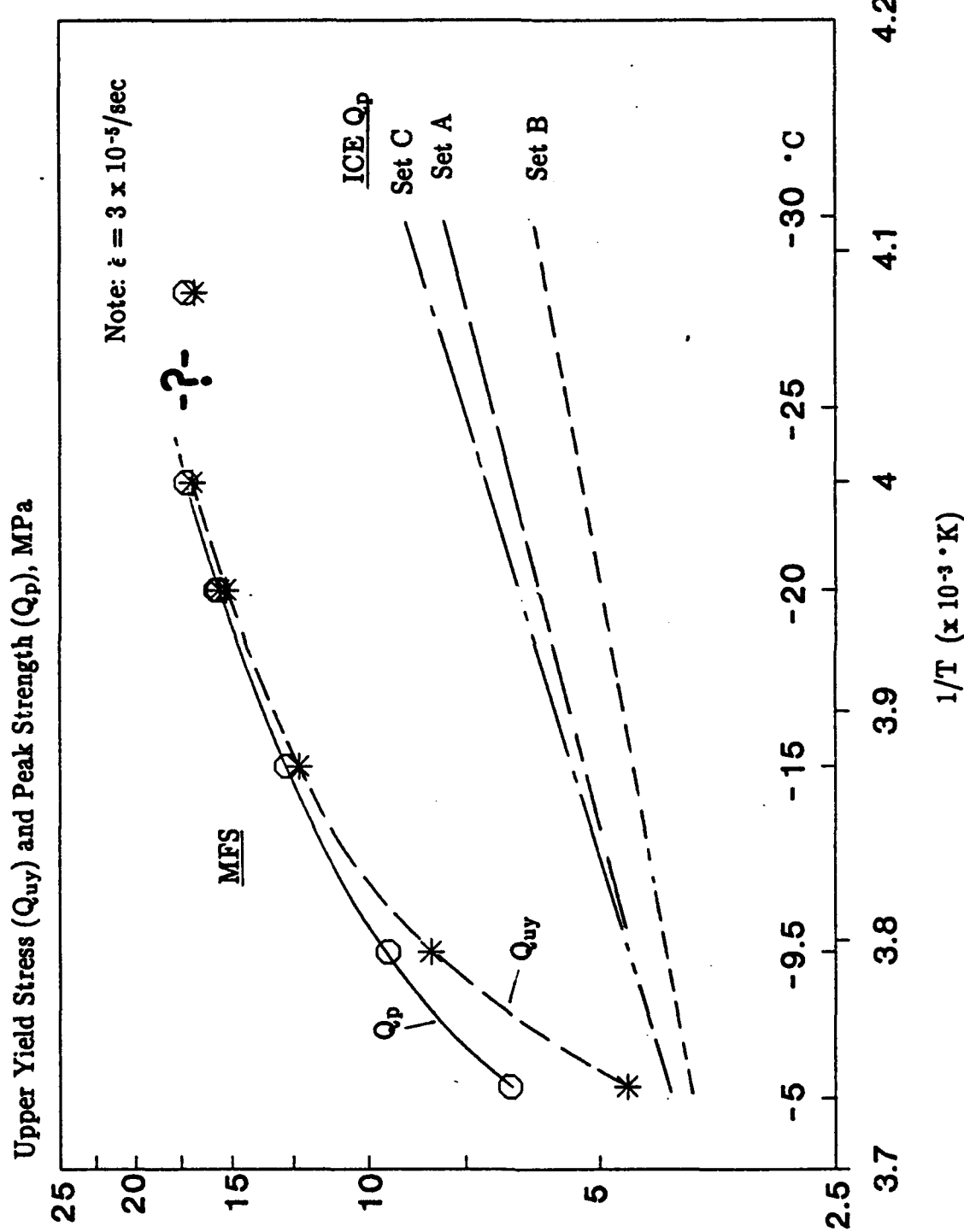


Figure 3.21: Comparison Between Measured Upper Yield Stress and Peak Strength of Frozen MFS and Calculated Peak Strength of Ice at Moderate Strain Rate

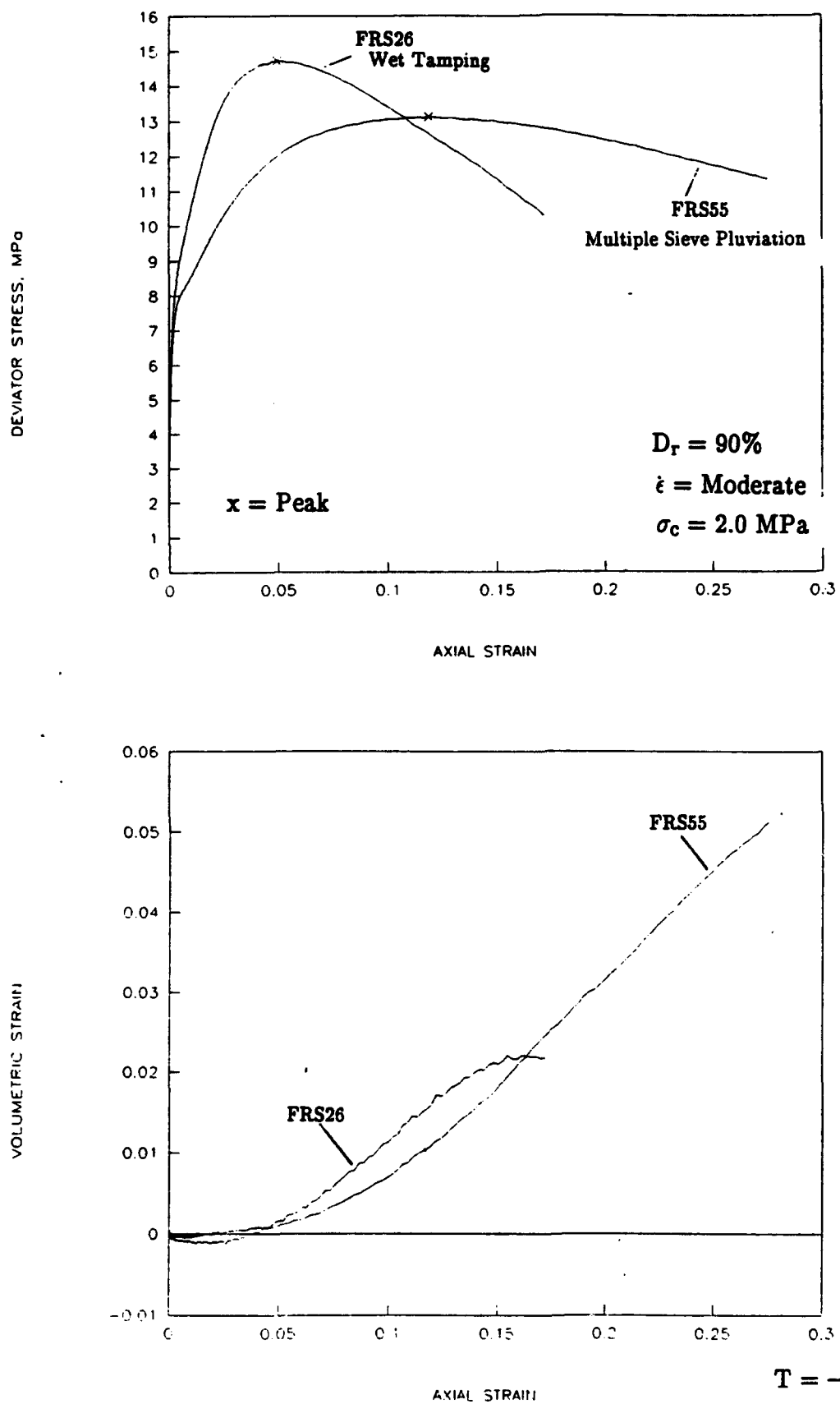


Figure 3.22:

Stress-Strain Curves to Show the Effect of Specimen Preparation Technique on Frozen MFS

4. BEHAVIOR OF UNFROZEN MANCHESTER FINE SAND IN TRIAXIAL COMPRESSION

4.1 SCOPE OF TESTING

The unfrozen Manchester Fine Sand (MFS) testing program consisted of isotropically (hydrostatically) consolidated-undrained (CIUC) and consolidated-drained (CIDC) triaxial compression tests. The majority of the tests (80%) were undrained. The program was performed in two series, Series A and Series B, as summarized in Table 4.1 and discussed below. Of the total 56 tests set-up, only 38 (68%) provide useful information for analysis. The reasons for the deletion of certain tests are also described. Specimen history and stress-strain data from the successful tests are tabulated in Appendix B.

4.1.1 Series A Tests

For Series A, 16 tests were set-up with a range in effective confining stresses (σ'_c) of 0.1, 1, 2, 4 and 5 MPa. All except one test were sheared under undrained conditions. Preshear relative densities (D_r) ranged from 14 to 106 percent. A nominal strain rate of 2.3×10^{-5} /second was used for all tests.

Of the 16 tests set-up, only six were successful. Several factors contributed to this low success rate. Some of the difficulties involved developing new experimental techniques, e.g., lubricated end platens, on-specimen axial strain measurements, internal axial load cell, high capacity pressure/volume control units, and specimen preparation techniques. The specimen preparation techniques for Series A tests included open-air raining of MFS into the mold (i.e., the specimen former as illustrated in Fig. 2.10), vibratory densification of rained specimens and "undercompaction" (a "wet tamping" method where the specimen is formed by compacting layers inside the mold, see R.S. Ladd 1974). None of these tests were prepared using multiple sieve pluviation. These preparation techniques created non-uniformities in the test specimens that lead to numerous erratic and questionable test

results. The most common anomalies in the testing results fell into two areas: 1) the axial load on the specimen would suddenly drop to near zero, which would coincide with a sudden jump in measured pore pressure; and 2) a predominant failure surface would develop prematurely in the specimen during shear, causing the measured pore pressures and axial stress to vary unpredictably during shear.

Additional problems encountered during Series A tests included:

- 1) Membrane breakage and/or leakage during consolidation or shearing;
- 2) Malfunction of the on-specimen ACDTs thereby losing small strain information;
- 3) Indeterminate volume changes during the (attempted) simultaneous increase of the cell and back pressure for overnight saturation. In some cases, the set-up effective stress was lost during this manually-controlled, pressure-up procedure.

Because of these problems, many specimens rarely reached the large strain region, i.e., 15 to 25% axial strain.

4.1.2 Series B Tests

Forty tests were performed in the second set of tests, Series B. All specimens for Series B were prepared using multiple sieve pluviation. It is believed that this one change in testing procedure was responsible for dramatically increasing the success rate for this series. Of the 40 tests performed (32 CIUC and 8 CIDC), 32 tests were successful. Preshear relative densities varied from 44 to 104% and effective confining pressures were 0.1, 2, 5 and 10 MPa, except for a test at 7.5 MPa and another at 11 MPa. Strain rates varied from 2.3×10^{-5} /sec. The Series B tests not only had a higher success rate than for Series A, but also reached higher strains (25%) with better stability than those in Series A. Hence, the analysis that follows is based largely on the results from the Series B tests.

4.2 UNDRAINED STRESS-STRAIN AND EFFECTIVE STRESS PATH BEHAVIOR

The majority of useful tests are CIUC tests (32 of the 38); therefore, the discussion will focus on the undrained behavior of MFS. Figure 4.1 presents a plot of $q_m = 0.5(\sigma_1 - \sigma_3)$ versus $p'_m = 0.5(\sigma'_1 + \sigma'_3)$, where q_m and p'_m correspond to conditions at the point of maximum obliquity, $R_{max} = (\sigma'_1/\sigma'_3)_{max}$. (Note: Fig. 4.1 also includes data from six CIDC tests.) Most of the undrained tests results have effective friction angles within a range of 32 to 37 degrees. The failure envelope has a noticeable curvature (concave downward), which is typical, e.g., as observed by Lee and Seed (1967) from drained triaxial compression tests on the Sacramento River Sand.

Figure 4.2 plots deviator stress and excess pore pressure versus strain for four CIUC tests at different effective confining pressures (0.1, 2, 5 and 10 MPa) on dense specimens having almost identical preshear void ratios ($e = 0.606 \pm 0.007$, $D_r = 91 \pm 2\%$). Test 22 ($\sigma'_c = 0.1$ MPa) exhibits a strong dilative response as indicated by the development of large negative pore pressures which strengthen the sand as straining continues. In contrast, test 23 ($\sigma'_c = 10$ MPa) exhibits a strong contractive response, i.e., development of large positive pore pressures. This behavior is typical of similiar comparisons at higher preshear void ratios (i.e., lower densities). Figure 4.3 presents the effective stress paths of these same four tests. The dilatancy-hardening response of test 22 causes its effective stress path to "climb up" the failure envelope and requires almost 20% strain to reach its peak strength. As the effective confining pressure increases, the stress paths move more to the left before climbing the failure envelope, until at 10 MPa the sand exhibits only contractive behavior. In fact, test 23 may have failed prematurely (this specimen had significant sliding at the top cap and the after-shear form was S-shaped).

Figure 4.4 shows the influence of preshear density on stress-strain behavior for three CIUC tests having an effective confining pressure of 2 MPa. As expected, the looser the specimen, the stronger is its contractive response during shear (generation of higher excess pore pressures) and the lower the undrained strength. This trend in behavior is

more readily seen from a plot of the effective stress paths in Fig. 4.5. The loosest specimen (test 39) has the most initial contraction and little strain hardening, whereas the densest specimen (test 7) shows the opposite.

4.3 BEHAVIOR IN TERMS OF STEADY STATE LINE AND STATE PARAMETER Ψ

Been and Jefferies (1985) introduced a concept that helps to unify the effects of density (D_r) and confining stress (σ'_c) on the behavior of sands. The state parameter Ψ is a measure of the physical condition (state) of a sand in terms of its initial void ratio and initial state of stress with respect to an ultimate or steady state condition. They proposed the use of the mean normal stress (i.e., the first invariant ($I_1 = \sigma'_{oct}$) of the stress tensor) as a suitable measure of the stress. I_1 is defined as $\frac{1}{3}(\sigma'_1 + \sigma'_2 + \sigma'_3)$.

Been and Jefferies (1985) assume that all specimens of a given sand tend to approach the same steady state irrespective of the initial state. They adopt the concept of "the Steady State of Deformation" as proposed by Poulos (1981) as the ultimate condition of the sand. They explain, however, that their concept of the state parameter Ψ "does not depend on the nature of the sand structure at the steady state. Rather it depends on there being a unique, repeatable particle arrangement at the steady state condition".

Figure 4.6 illustrates how the state parameter is defined. The ordinate is the void ratio and the abscissa is the mean normal stress (I_1) on a log scale. The Ψ parameter is defined as the vertical distance from the initial state to the Steady State Line (SSL) expressed in units of void ratio. A sand which has an initial state that plots above the SSL has a $+\Psi$ and one that plots below the SSL has a $-\Psi$. Been and Jefferies (1985 and 1986) report that many sands with the same Ψ exhibit the same general behavior (e.g., the same peak drained ϕ' for $-\Psi$ values and the same peak undrained strength ratio for $+\Psi$ values) regardless of the absolute magnitude of the D_r or σ'_c . Thus Ψ can apparently unify the effects of both D_r and σ'_c .

To define the Steady State Line, Been et al. (1991) state that tests must achieve a condition of constant volume (if drained) or constant pore pressure (if undrained) during continued shear deformations at *constant shear stress*. Based on this criterion and concentrating on the undrained test results, it was judged that 16 tests either reached or were near the SSL during shear. Where appropriate, the selected steady state condition is shown on the stress-strain curve and the effective stress path. Figure 4.7 plots the mean effective stress ($I_1 = \sigma'_{oct}$) versus void ratio for these tests. Appendix B presents tabulated results of the conditions at steady state for these tests. A Steady State Line with $\lambda = 0.253$ was determined using a linear regression analysis on this set of data ($r^2 = 0.95$) and is also shown in Fig. 4.7. It is important to note that the Steady State Line was developed from tests having both negative (moving from left of the line) and positive (moving from right of the line) Ψ -values as shown by the arrows in the figure.

The state parameter can be correlated to undrained shear parameters such as the A parameter at the peak strength (A_f) and the undrained strength ratio (q_f/σ'_c) as shown in Fig. 4.8 and 4.9, respectively. These indicate an excellent correlation for both A_f and q_f/σ'_c .

The concept and use of the SSL and Ψ parameter has experienced strong debate in the literature, e.g. see Been and Jefferies (1986). The writers agree that the choice of exactly where the steady state occurs can be subject to error. Whereas test 23 in Fig. 4.2 appears to have reached a steady state condition (before undergoing strain softening, probably due to cap slippage), tests 7 and 15 in that figure did not exhibit continued straining at constant shear stress (although the final points were selected). Likewise, the final points were selected for tests 11 and 39 in Fig. 4.4 even though the shear stress was still changing.

Other factors also influence evaluation of the SSL. These include determination (measurement) of the correct void ratio of a test, specimen non-uniformities (especially true for frictional end conditions) and grain crushing during shear which is applicable for

tests at higher confining or shear stresses. In addition, a large amount of strain is usually required to obtain a steady state condition in MFS; therefore, specimen stability on lubricated ends becomes a critical issue. However, in spite of these potential problems, the data in Fig. 4.7 are reasonably consistent, and the selected SSL gives an excellent correlation for A_f and q_f/σ'_c (Fig. 4.8 and 4.9). Nevertheless, some additional study of the undrained behavior of MFS is warranted.

4.4 DRAINED STRESS-STRAIN AND VOLUMETRIC BEHAVIOR

A study of the drained behavior of MFS was more recently initiated. Six successful tests were performed, all at constant $p' = 0.5(\sigma'_1 + \sigma'_3)$. Figure 4.10 shows preliminary stress and volumetric strain results of four tests at different effective confining stresses but with very similar preshear densities. The test at $\sigma'_c = 0.1$ MPa exhibits the most expansion (dilation) during shear. (Note: problems occurred after about 8% axial strain.) As the confinement increases, the strength increases and the tendency of the specimen to dilate decreases. Figure 4.11, which shows the stress paths for these tests, illustrates the curvature of the failure envelope with increasing stress.

One CIDC test (No. 37) meets Been et al. (1991) definition of steady state. The steady state condition of this test is plotted on Fig. 4.12 along with the SSL as defined by the CIUC tests on MFS. Although not conclusive, this CIDC "state point" appears to validate the use of one SSL for both drained and undrained MFS tests. However, more testing is necessary before a more definitive conclusion can be made.

**Table 4.1 Scope of Testing Program on Unfrozen Manchester Fine Sand
in Triaxial Compression**

SERIES A

15 Undrained Tests (CIUC) - 6 successful
1 Drained Test (CIDC) - 0 successful

SERIES B

32 Undrained Tests (CIUC) - 26 successful
8 Drained Tests (CIDC) - 6 successful

VARIABLES OF THE SUCCESSFUL TESTS

RANGE IN PRESHEAR RELATIVE DENSITY (%)	EFFECTIVE CONFINING PRESSURE (MPa)						
	0.1	2	4	5	7.5	10	11
10- 40	•						
40- 60	•	•	•				
60- 80		•		•		•	
80- 100	•	•		•	•	•	•

RANGE IN STRAIN RATES
 $\approx 2.3 \times 10^{-5}$ /sec to 3.7×10^{-5} /sec

SPECIMEN PREPARATION TECHNIQUES

Open Air Raining Vibratory Densification Under Compaction (Wet tamping) Multiple Sieve Pluviation] Series A
--	------------

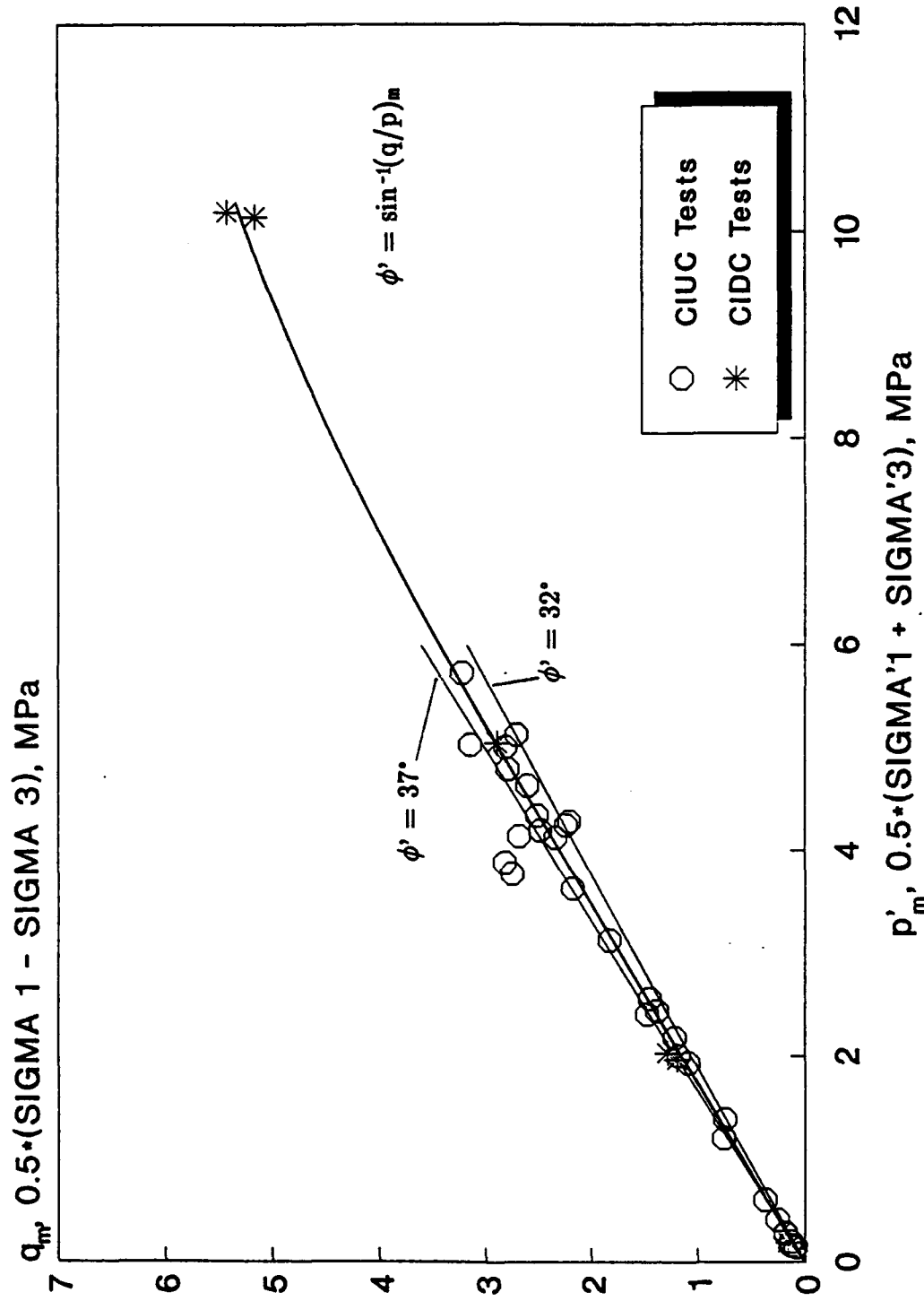
SPECIMEN END CONDITIONS

Silicone lubricant only

Rubber Membrane only

Rubber membrane and silicone lubricant

Rubber membrane and high vaccuum grease



Effective Stress Failure Envelope of MFS at Maximum Obliquity from Unfrozen Triaxial Compression Results

Figure 4.1:

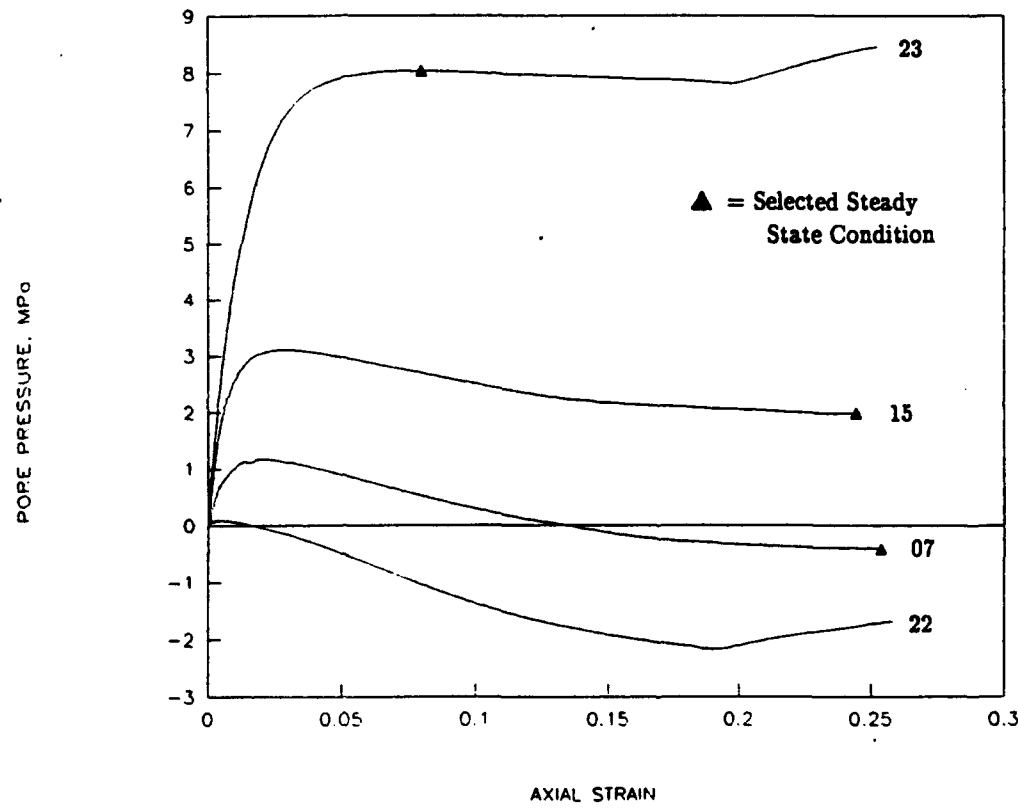
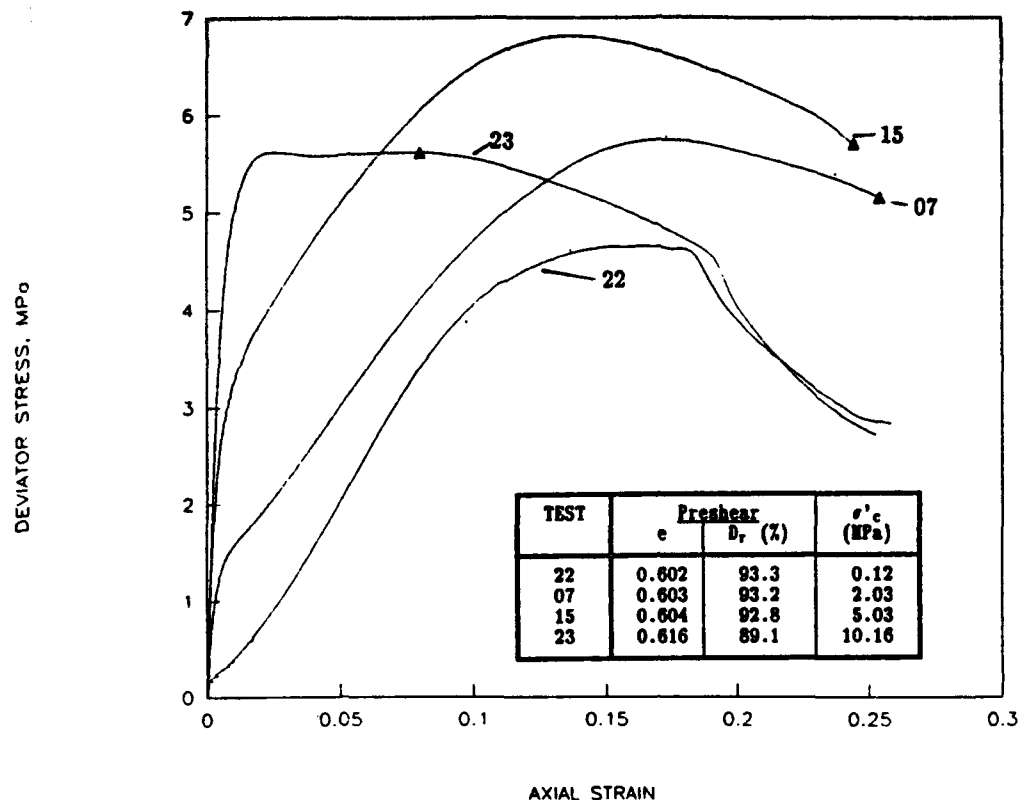
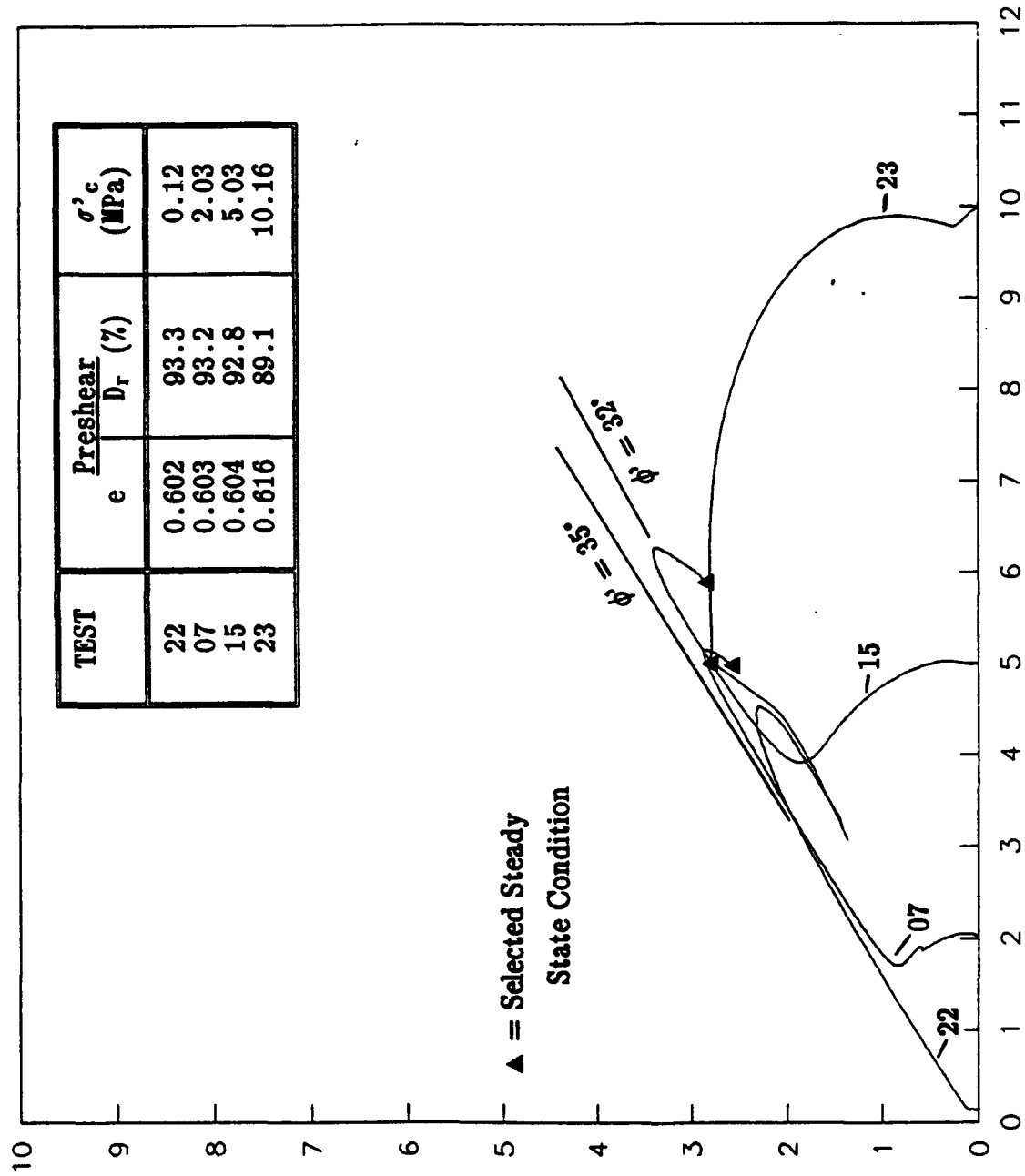


Figure 4.2: Effect of Confining Stress on Stress-Strain Behavior of Unfrozen Dense MFS from CIUC Tests



$p' \cdot (0.5 \cdot (\sigma_1 + \sigma_3))$, MPa

Effect of Confining Pressure on Effective Stress Paths of Unfrozen Dense MFS for CIUC Tests

Figure 4.3:

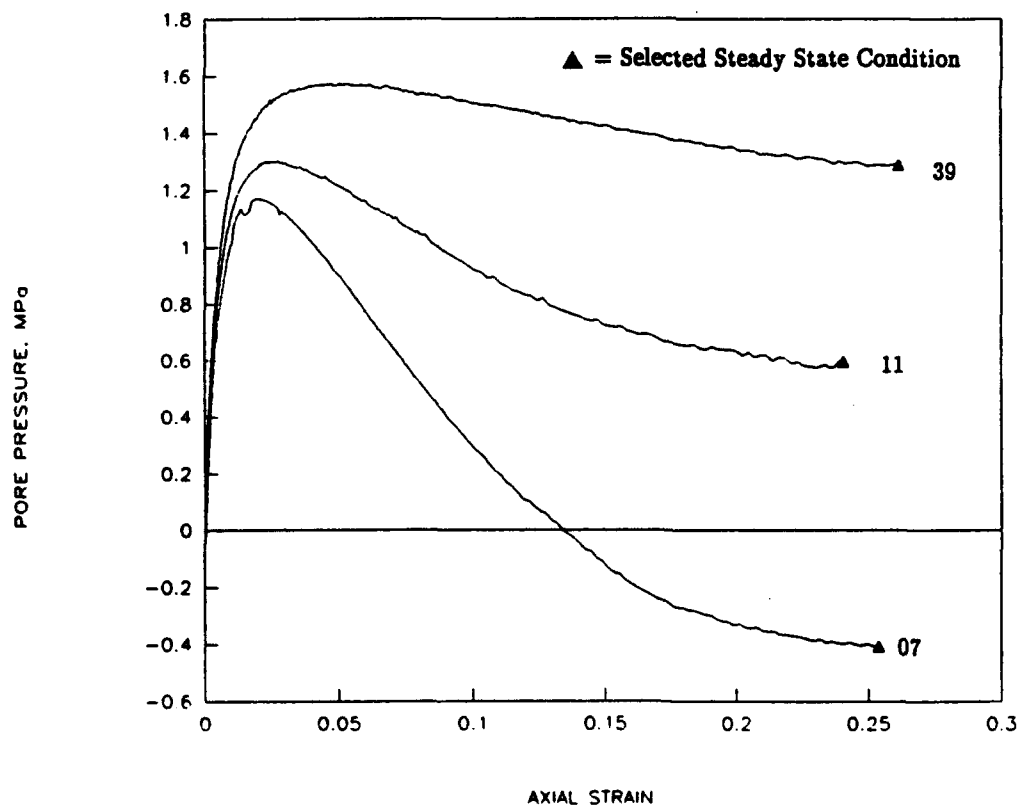
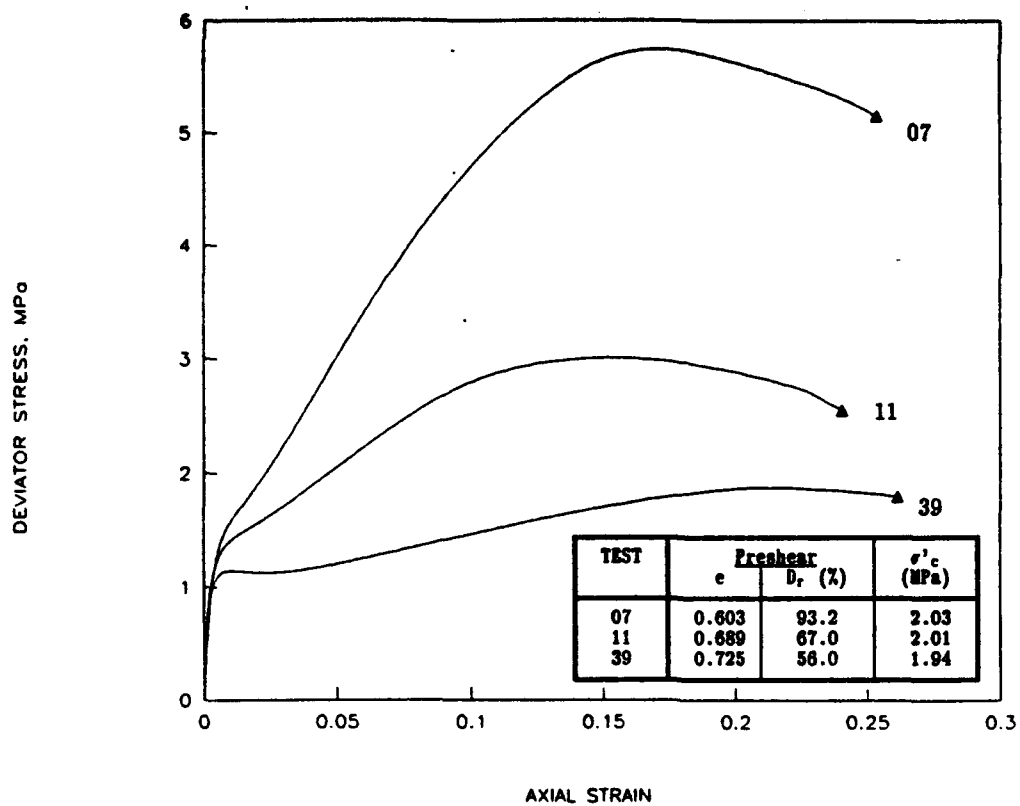
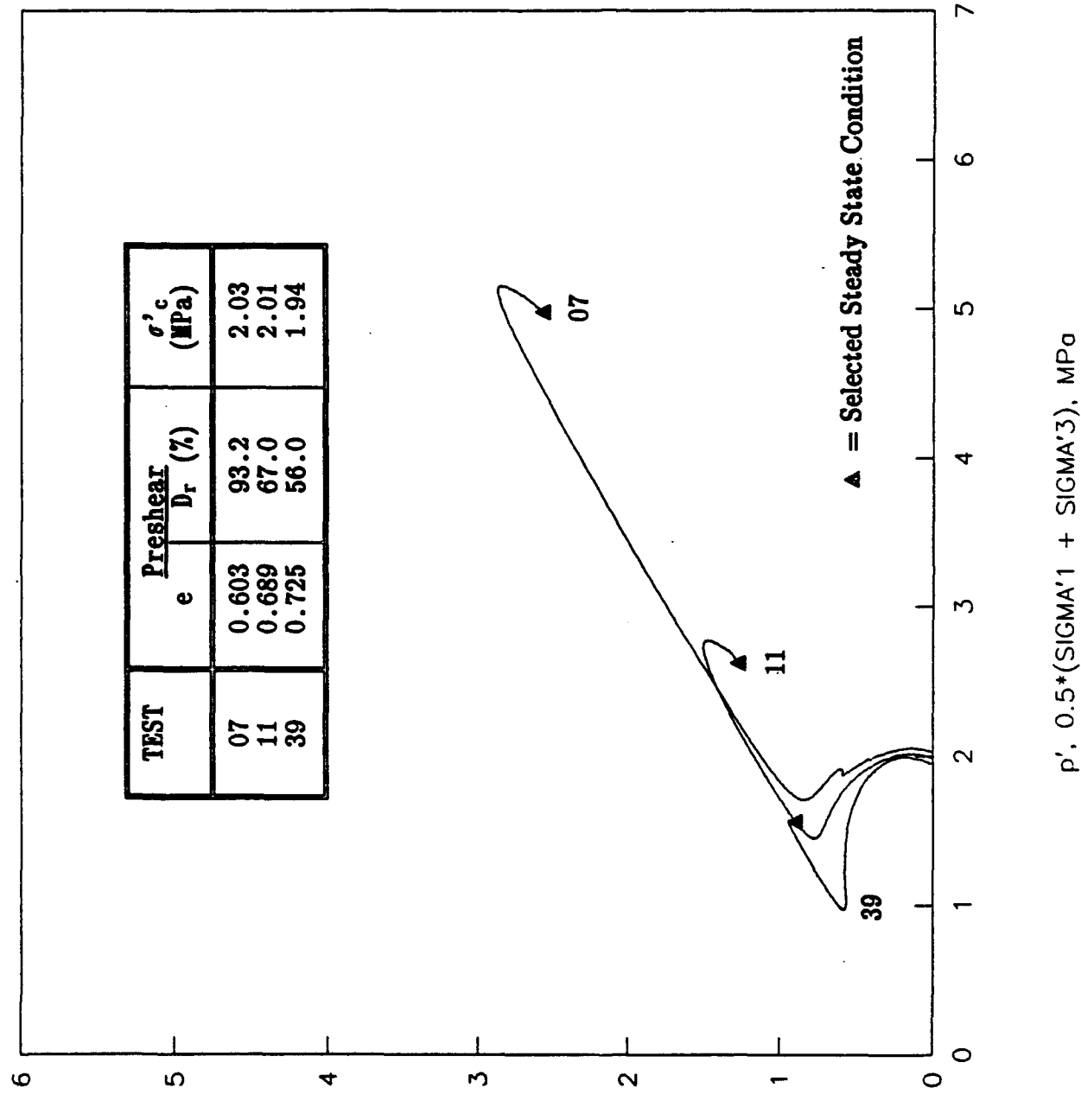


Figure 4.4:

Effect of Density on Stress-Strain Behavior of CIUC Tests on Unfrozen MFS with $\sigma'_{c} = 2.0$ MPa



$\sigma'_1, 0.5 * (\sigma'_1 + \sigma'_3), \text{ MPa}$

Effect of Density on Effective Stress Paths for CIUC Tests on Unfrozen MFS with $\sigma'_c = 2.0 \text{ MPa}$

Figure 4.5:

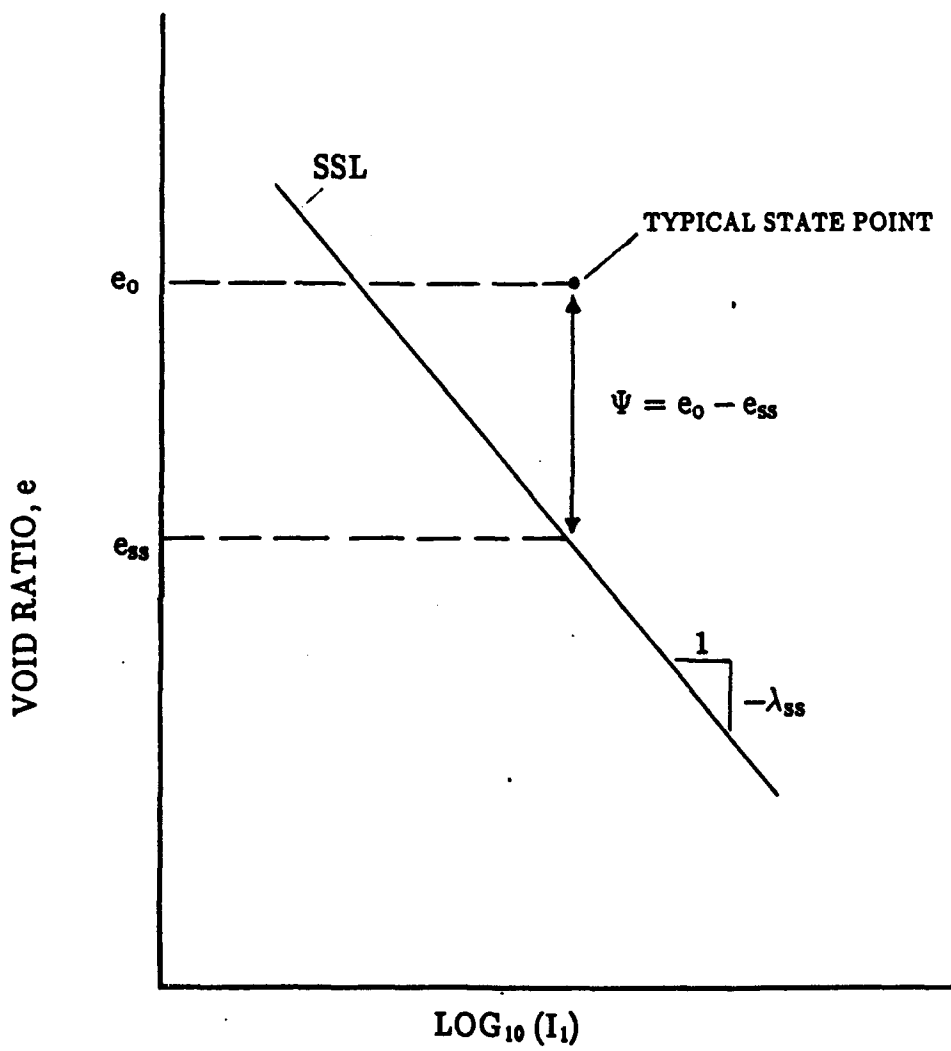


Figure 4.6: Definition of State Parameter, Ψ (after Been and Jefferies 1985)

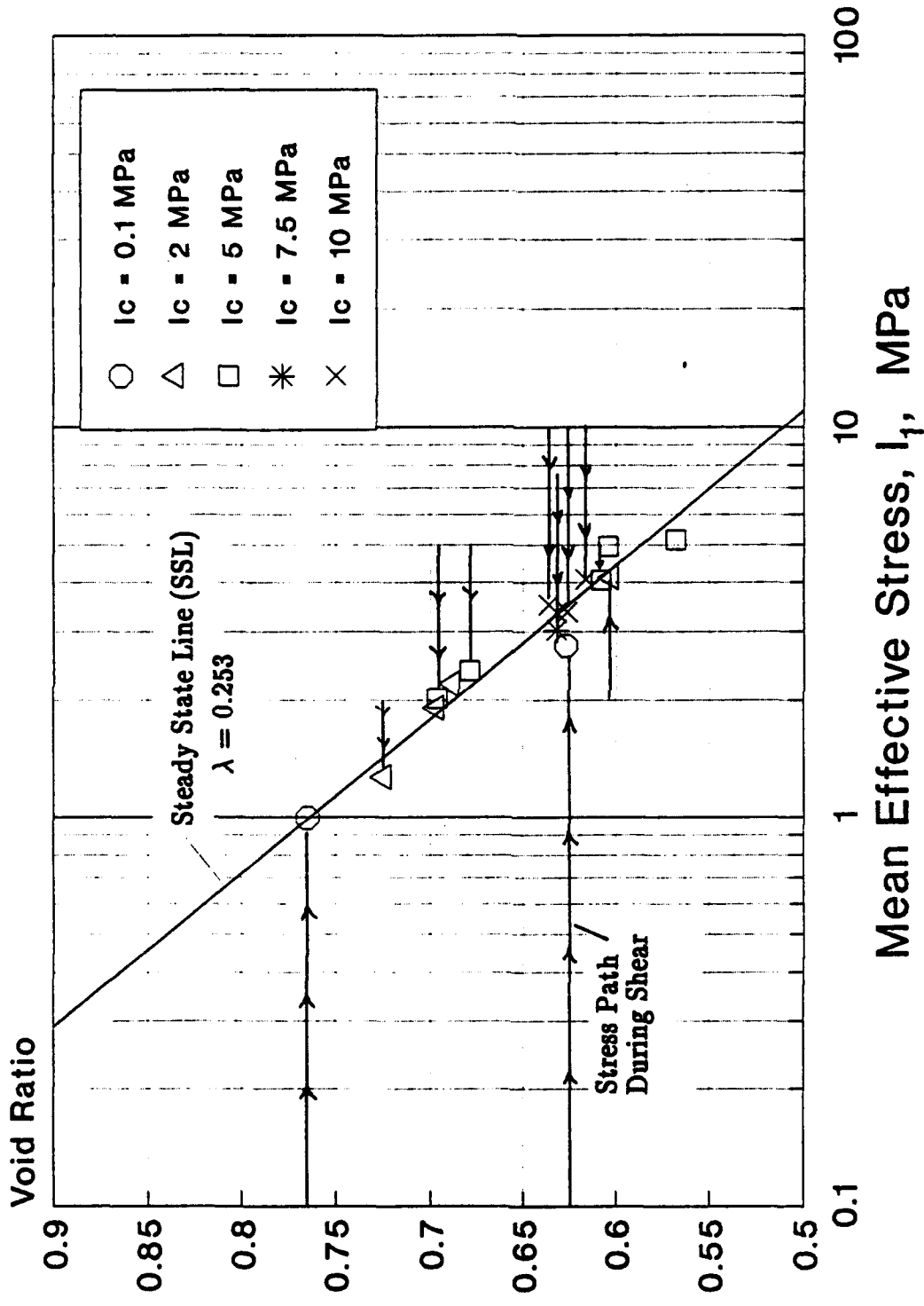


Figure 4.7:

Steady State Line for 16 CIUC Tests on Unfrozen MFS

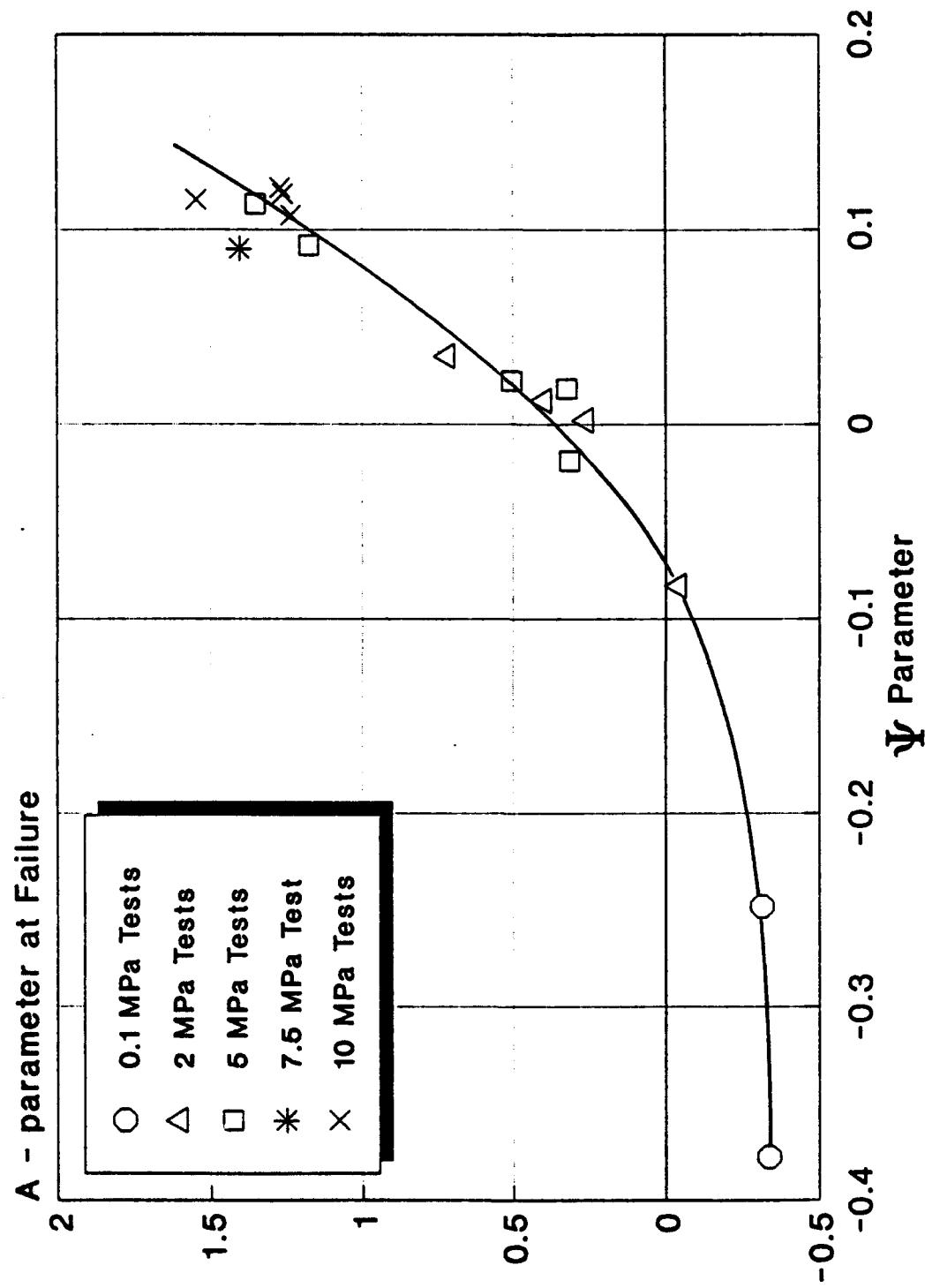


Figure 4.8:
A_f Versus Ψ Parameter from CIUC Tests on Unfrozen
MFS

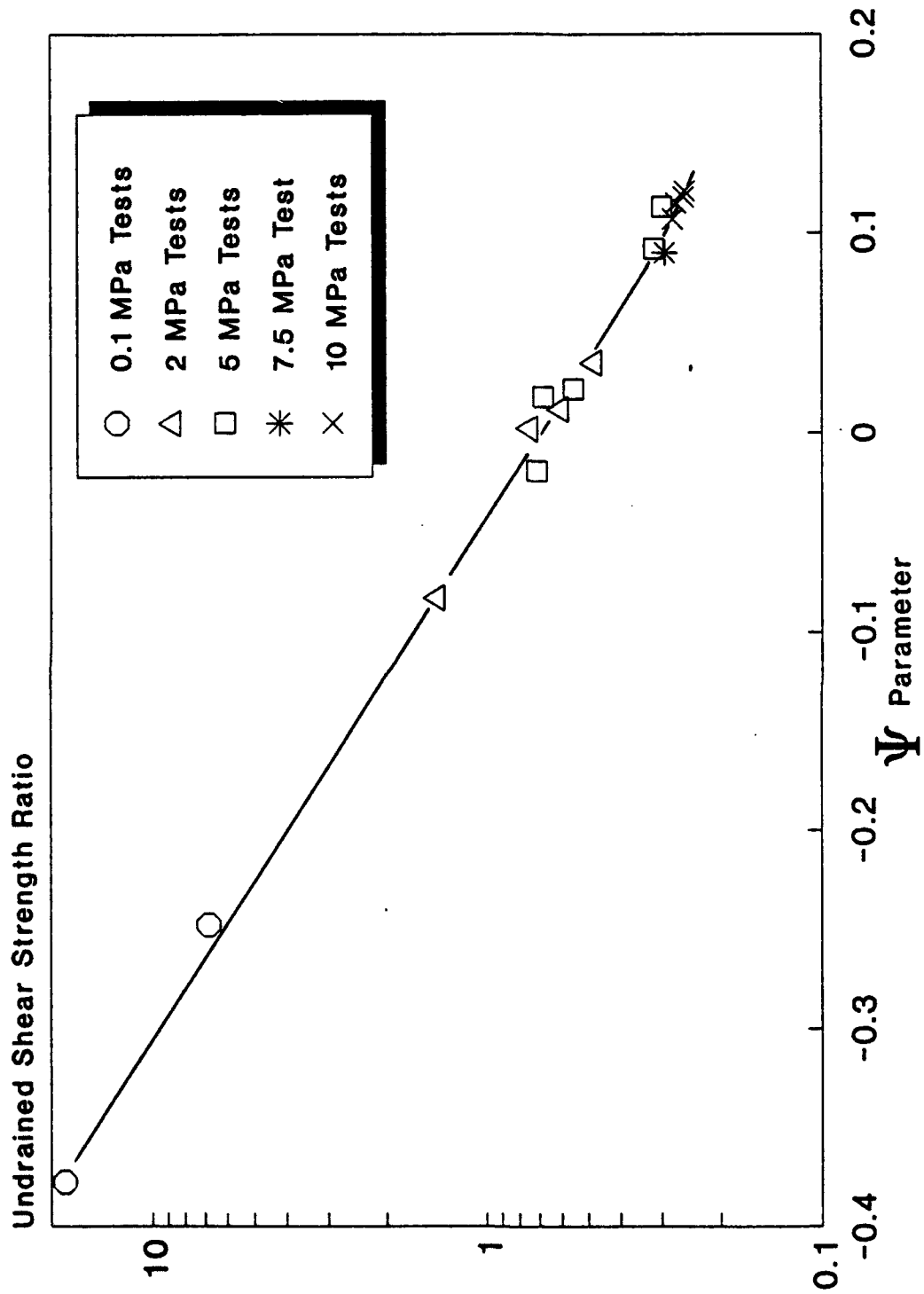


Figure 4.9:
Normalized Undrained Shear Ratio Versus Ψ Parameter
from CIUC Tests on Unfrozen MFS

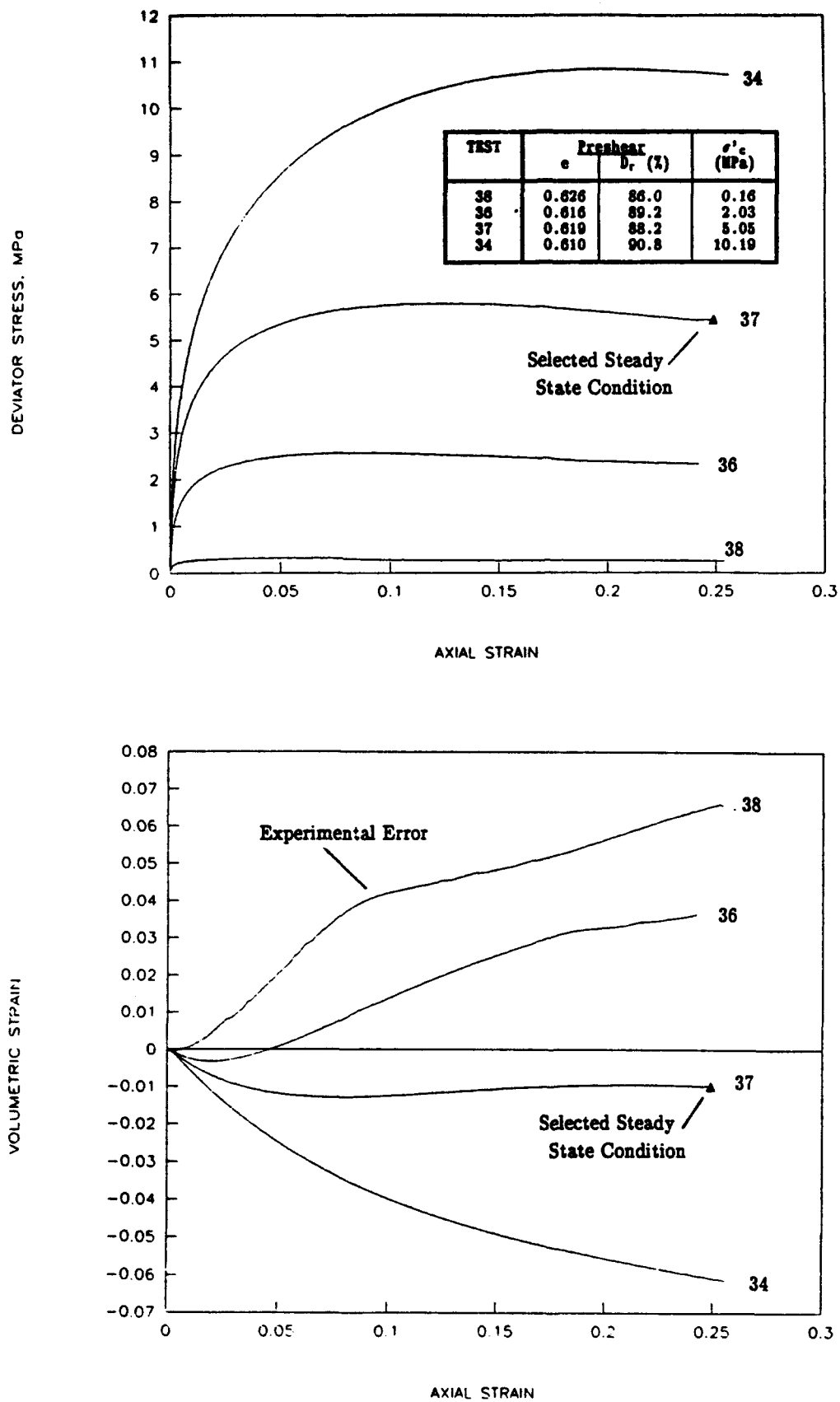
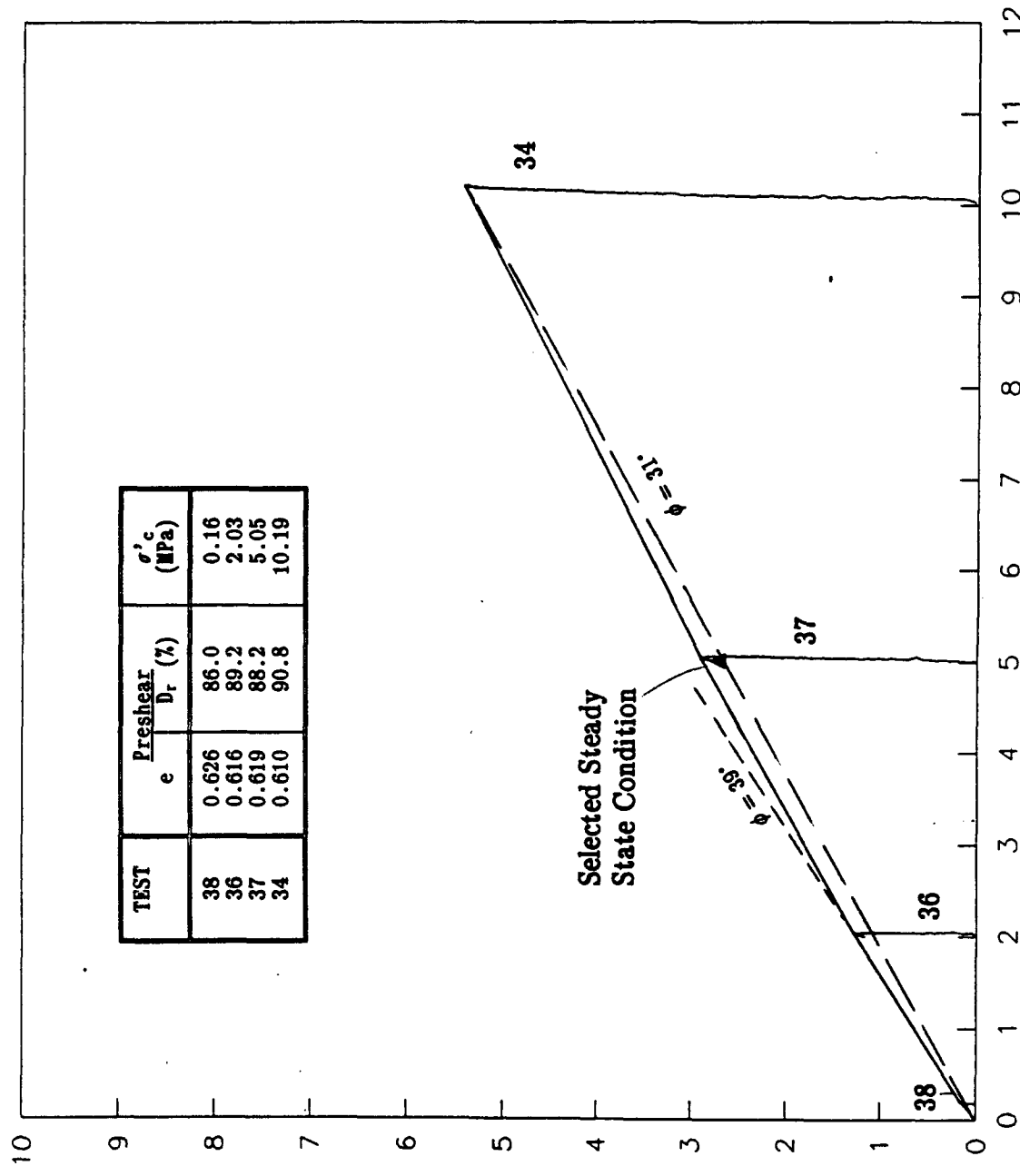


Figure 4.10: Stress–Strain and Volumetric Strain Response for CIDC Tests on Dense Unfrozen MFS



$p', 0.5*(\Sigma \sigma_1 + \Sigma \sigma_3)$, MPa

Effective Stress Paths of CIDC Test Results on Dense
Unfrozen MFS

Figure 4.11:

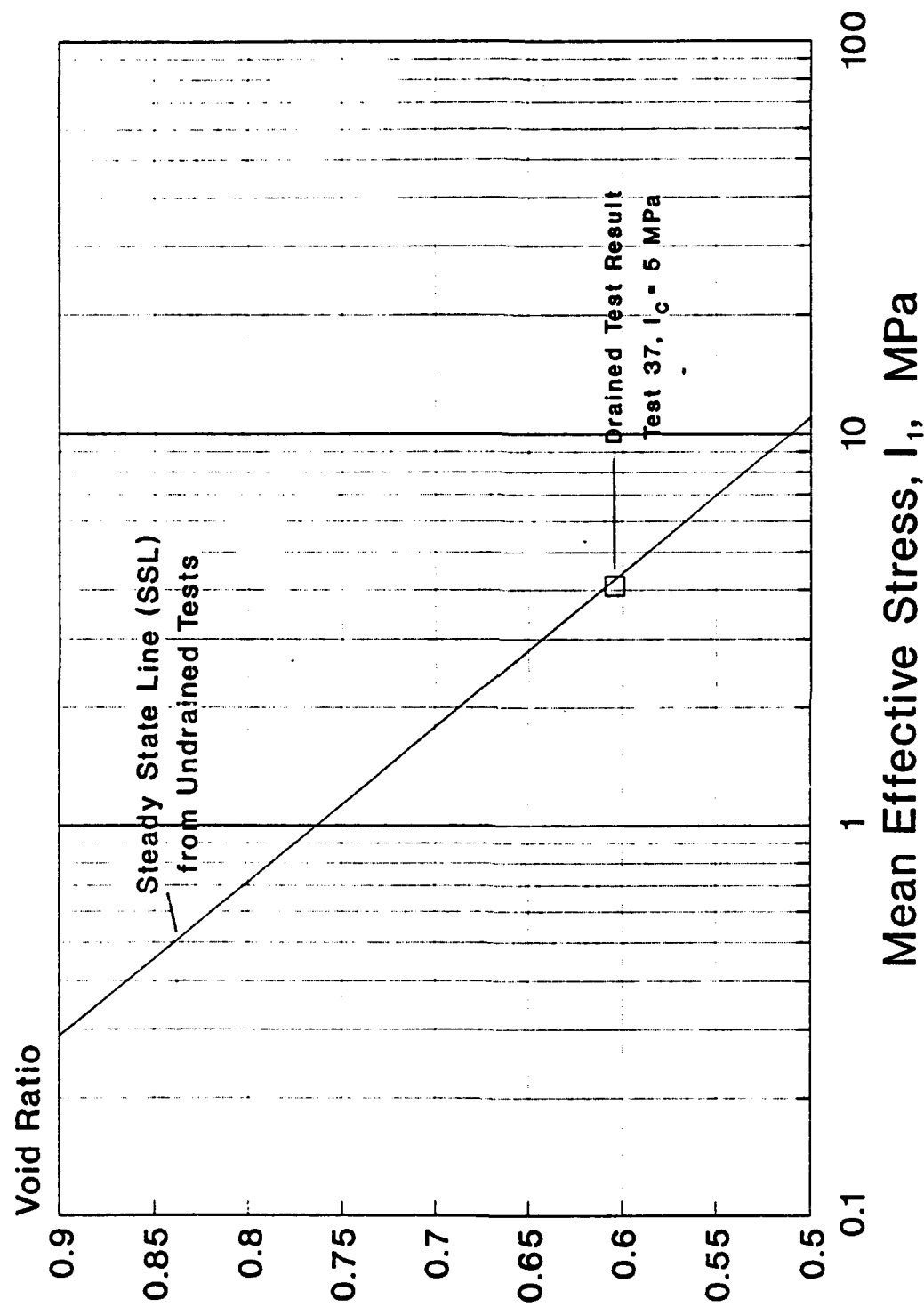


Figure 4.12:
Steady State Line and CIDC Test Result for Unfrozen
MFS

5. APPLICATION OF DILATANCY-HARDENING MODEL

5.1 LADANYI'S MODEL

Ladanyi (1985) developed a dilatancy-hardening theory to predict the strength of frozen dense sand and Ladanyi and Morel (1990) present experimental results to check the validity of the model. The basic concept assumes that the effective stress path followed by the soil skeleton in a frozen sand will be the same as that for unfrozen sand provided that: 1) both systems are subjected to the same strain path (axial loading at constant confining pressure and constant volume); and 2) the sand skeleton in both systems starts from the same "state" (density and effective stress). Unfrozen dense sand sheared undrained at low confinement (i.e., $-\Psi$) tends to dilate (expand in volume). This causes development of negative pore pressures that increase the effective stresses acting on the sand which results in increased frictional resistance. The dilatancy-hardening model makes the following assumptions (Ladanyi and Morel 1990):

- 1) All of the pore water in the sand is considered to be frozen.
- 2) The behavior of the sand is a function of the state parameter Ψ as introduced by Been and Jefferies (1985) and described in Section 4.
- 3) No consolidation occurs prior to shear, i.e., the tests are considered as "unconsolidated". The shear starts from a known density and confining pressure.
- 4) So long as the pore ice is continuous and unbroken during shear, the sand will behave as "undrained". When the pore ice fails, i.e., breaks up, the sand behaves as "drained". This breakup of the ice has been associated with axial strains of 1 to 2% in the literature.
- 5) As long as the test behaves undrained (i.e., before the pore ice becomes broken), the dilatancy-hardening principles established for unfrozen sand are also

applicable to frozen sand provided that proper account is made for the tensile strength of the pore ice matrix.

Before further description of the dilatancy-hardening model, the definition of the critical confining pressure, $\sigma'_{3\text{cr}}$, is needed. Seed and Lee (1967) and others have observed that if a dense sand is sheared in an undrained mode with no back pressure in a state where it exhibits a tendency to dilate, i.e., it has a large $-\Psi$ parameter, the pore water pressure decreases and the effective stresses increase on the sand skeleton until one of two conditions occurs. Either the pore water pressure reaches the "tensile strength" of water, i.e., it decreases sufficiently to cause cavitation, or the effective stresses increase until the "state point" reaches the Critical Void Ratio Line (CVRL) or alternatively, the Steady State Line (SSL). The transition confining pressure between these two condition is termed the critical confining pressure, $\sigma'_{3\text{cr}}$. Seed and Lee (1967) define the critical confining pressure as that confining pressure for a given preshear void ratio which results in no net volume change at the peak strength in a drained triaxial compression test on unfrozen sand (or no net change in pore pressure at failure for an undrained test). As used by Ladanyi et al., $\sigma'_{3\text{cr}}$ is the initial confining pressure that will result in no change in pore pressure at failure for undrained shear of unfrozen sand at a given initial density (or void ratio).

Although Ladanyi et al. presented stresses in the form $Q = (\sigma_1 - \sigma_3)$ and $\sigma_{\text{oct}} = \frac{1}{3}(\sigma_1 + \sigma_2 + \sigma_3)$, its application will be illustrated using the "MIT" format: $q = 0.5(\sigma_1 - \sigma_3)$ and $p = 0.5(\sigma_1 + \sigma_3)$ as represented by Fig. 5.1. Summarizing this figure, undrained shear of unfrozen sand starting from $P_3 = \sigma'_{3\text{cr}}$ will end up at point B. For frozen sand starting from the same $P_3 = \sigma'_{3\text{cr}}$, Ladanyi et al. add q_i (the shear strength of the ice matrix) and thereby obtain point C. To explain further, consider the strength of the unfrozen soil. Referring to Fig. 5.1, the effective stress envelope starts at the origin and has a slope equal to $K_f = (\sigma'_3/\sigma'_1)_{\text{at failure}}$. The cavitation domain is represented by a total stress failure envelope with an initial slope identical to the effective stress envelope, but translated to the left by an amount equal to the tensile strength of the pore fluid. The

transition point between the cavitating and noncavitating regimes occurs for a confining pressure of

where T is the tensile strength of the pore fluid ($T = T_w$ for water = 1 atm and $T = T_i$ for ice $>> 1$ atm). For a confining pressure greater than $\sigma'_{scr} - T$, the total stress envelope is horizontal with a value of $q = B$. The predicted strength of the soil skeleton in this region is therefore solely controlled by the magnitude of the σ'_{scr} and the effective friction angle ϕ' .

Since pore ice can support both tensile and shear stresses, Ladanyi proposed that the shear strength of the ice be added directly to the shear strength of the sand skeleton. Thus, the total stress line (TSL) for the frozen sand plus ice (FS + ice) is offset vertically by a distance equal to q_i above the TSL (FS) line.

Pertinent equations for predicting the shear strength (q_{FS}) of "relatively dense frozen sand" from Ladanyi's model are as follows.

Noncavitation Case

In this case, σ_3 is greater than or equal to $\sigma'_{3cr} - T_i$, where T_i = tensile strength of ice. The shear strength of the sand skeleton, q_{ss} , will equal $0.5 \sigma'_{3cr} (R_f - 1)$, where $R_f = (\sigma'_1 / \sigma'_3)_{\text{at failure}}$ (i.e., $1/K_f$). Therefore, the shear strength of frozen soil, q_{fs} , can be derived by adding the shear strength of the sand skeleton to the shear strength of the ice matrix

For this case, where the initial confining pressure is greater than or equal to P_1 in Fig. 5.1, the model predicts a constant strength; i.e., q_{FS} does not increase with increasing confinement.

Cavitation Case

Here, σ_3 is less than $\sigma'_{3cr} - T_i$; therefore, the shear strength of the sand skeleton is defined as $0.5 (\sigma_3 + T_i)(R_f - 1)$. The shear strength of frozen soil is now given by

If the initial confining pressure is less than P_1 , the model predicts that q_{ps} increases with increasing confinement. The slope of this total stress envelope equals K_f , the effective stress failure envelope of the sand skeleton.

5.2 APPLICATION OF LADANYI'S MODEL TO FROZEN MFS

As stated by Ladanyi and Morel (1990), "undrained tests with pore pressure measurements would have been more appropriate" than their use of consolidated-drained triaxial compression tests. Section 4 presented the results of triaxial compression tests characterizing the CIUC behavior of MFS as a function of density and consolidation (confining) pressure. Also presented was a Steady State Line (SSL) for MFS, thus allowing the measured undrained shear behavior to be evaluated in terms of the state parameter ψ .

Figure 4.8 plots $A_f [\Delta u / (\sigma_1 - \sigma_3)_f]$ versus ψ and shows that ψ equals -0.07 at $A_f = 0$; i.e., where there is no change in pore pressure at failure. Given this result, one can define a line representing the critical confining pressure σ'_{3cr} versus preshear void ratio by offsetting the SSL (presented in Figure 4.7) downward 0.07 along the void ratio axis. This line is presented in Fig. 5.2. As illustrated in the figure, for dense frozen MFS ($D_r = 95\%$), this gives $\sigma'_{3cr} = 2.37$ MPa.

Figure 5.3 compares predicted strengths from Ladanyi's model to measured upper yield stress (Q_{uy}) and peak strength (Q_p) data on frozen MFS at confining pressures of 0.1 and 10 MPa. Assumed ice properties for the predictions were $T_i = 2.0$ to 2.1 MPa (taken from Hawkes and Mellor 1972) and Q_i equal to those illustrated on Fig. 5.3 (taken from Jones 1982). Since T_i is very close to the critical pressure the strength of the sand skeleton was computed using Eq. 5.3 (cavitation case) for $\sigma_c = 0.1$ MPa and Eq. 5.2 (non cavitation case) for $\sigma_c = 10$ MPa. For low confinement ($\sigma_c = 0.1$ MPa) and $\sigma'_{scr} = 2.37$ MPa, $Q_{ss} = 4.74$ and 5.65 for $\phi' = 32^\circ$ and 35° , respectively. For high confinement ($\sigma_c = 10$ MPa), $Q_{ss} = 5.34$ and 6.38 MPa for $\phi' = 32^\circ$ and 35° , respectively. In Fig. 5.3,

the hatched zone is the calculated Q_{FS} for $\sigma_c = 0.1$ MPa with ice strengths taken from unconfined tests ($\sigma_c = 0$). Although Ladanyi et al. did not consider ice strengthening due to confinement, the shaded zone used higher ice strengths corresponding to $\sigma_c = 10$ MPa. The MFS upper yield stress and peak strength data for $D_r = 95\%$ are from Figs. 3.12 and 3.18, respectively.

Given the uncertainties in the ice properties, the predicted strengths at low confinement compare reasonably well with the measured peak strengths. However, there is a severe problem with "strain compatibility": the theory requires identical strain paths for the soil skeleton in both frozen and unfrozen states, and the pore ice cannot be broken. The frozen MFS failed at $\epsilon_p = 7\%$ to 4% (with increasing $\dot{\epsilon}$), whereas unfrozen sand requires more than 15% strain (test 22 in Fig. 4.2) and unconfined granular ice would probably fail at less than 1 or 2% .

Comparison at high confinement is less satisfactory, with measured peak strengths being much larger than predicted at slow and moderate strain rates, even after including higher values of Q_i for the ice matrix. But strain compatibility is better regarding the sand skeleton since frozen MFS failed at $\epsilon_p = 15\%$ to 23% [Fig. 3.8(b)].

5.3 DISCUSSION

Although the dilatancy-hardening model represents a significant advancement in trying to understand the physical mechanisms controlling the behavior of dense frozen sand, the results in Fig. 5.3 clearly show that detailed evaluation of the model requires experimental data covering a range of frozen soil conditions, plus data on undrained, unfrozen sand behavior. Major problems with the model appear to be:

- 1) Strain incompatibility between the sand skeleton in frozen and unfrozen states.
- 2) The assumption that the sand skeleton has identical effective stress behavior in frozen and unfrozen states. For example, the forces acting on sand particles will differ significantly when surrounded by ice rather than water (see below).

- 3) Estimates of properties for pore ice having grain sizes much smaller than tested.
- 4) Although Ladanyi and Morel (1990) imply that the theory applies to "unconsolidated" frozen sand, the magnitude of the effective stress initially acting on the soil skeleton presumably will affect frozen soil behavior. For example, the data in Fig. 4.2 show a much stiffer response for dense unfrozen sand with increasing consolidation (effective) stress even though all samples had the same initial density.

Section 2.3.4 of Andersen (1991) discusses item 2) in some detail. The following summarizes the main points. The mechanics of deformation in unfrozen sands that experience no particle crushing is governed by the magnitude and direction of the intergranular contact forces. These contact forces, when integrated over a large area, describe an equilibrium stress state in terms of both normal and shear stresses. In contrast to an unfrozen sand, a saturated frozen sand is a continuous medium (i.e., the pores contain an ice matrix that has a significant shear strength). This means that both the sand particles and pore ice participate actively in the stress transferring process. This results in significant differences between the types of forces that are carried by the sand skeleton.

In a frozen sand, the portion of the total applied stress that is transmitted by the sand skeleton via intergranular contact forces may not form an equilibrium stress state as is the case in unfrozen sands. This is illustrated qualitatively in Fig. 5.4. This figure is a two-dimensional free-body diagram of an individual sand particle in a frozen sand matrix. The particle is idealized as a five-sided polygon. One set of forces acting on this particle are due to the intergranular contacts with adjacent sand grains and these are depicted as solid vectors. Another set of forces acting on this particle are those transmitted across the ice-silicate interface, that may have both normal and shear components (Jellinek 1962). These are depicted as broken arrows. The writers recognize the inaccuracy associated with this schematic diagram in the assumption that the five intergranular forces are coplanar. In actuality, there are probably not even five particles in contact with an individual grain

considering all three dimensions. This presentation is only given to discuss the idea of particle equilibrium and the 2-D simplification is made for convenience.

Since ice can support shear stresses, this means that in general, neither the intergranular contact forces when considered separately, nor the ice-silicate interface forces when considered separately, will form an equilibrium force condition on the particle. But when these are considered jointly, and if the particle is not accelerating, the net resultant of all of the forces acting on the particle must be zero (neglecting the weight of the sand particle), i.e., the total forces must constitute an equilibrium condition.

Ice will creep even under extremely small shear stresses. This means that the magnitude of the forces transmitted across the ice-silicate interface are highly time dependent and the state of stress in the pore ice will eventually tend towards hydrostatic. When external stresses are initially applied to a frozen sand, a portion of that stress will be carried by the pore ice. Some fraction of these pore ice stresses must be transmitted across the ice-silicate interface. Over time, if the strain rate goes to zero, the shear stresses being carried by the ice matrix decrease towards zero and a hydrostatic state of stress will be approached in the pore ice. For this limiting condition, both the ice-silicate interface forces (now hydrostatic) and the intergranular contact forces, when considered separately, will each be in equilibrium and the state of stress determined from the intergranular contact forces will be similar to that in an unfrozen sand under the same total applied stresses. Such a condition may only apply under isotropic stresses after consolidation when the strain rate is very close to zero. In general however, under the action of external stresses, the strain rate does not go to zero and there will always be some shear stresses acting on the pore ice and hence the intergranular contact forces will not be in equilibrium when considered separately.

If the intergranular contact forces do not represent a state of equilibrium at the particle level, then integrating these forces over a large area will generate a state of stress that is also not in equilibrium. Thus, unless the intergranular contact forces are in

equilibrium, the state of stress determined from these will not be similar to the state of stress acting on the same sand skeleton in an unfrozen state. This means that it might be possible for a frozen sand to undergo a strain history which would be impossible for the same system in an unfrozen state (e.g., dilation of loose frozen sand at low confinement to less than $D_r = 0\%$). In the writers' opinion, this represents a significant difference between the mechanics of particle deformation in frozen sands as opposed to unfrozen sands.

ASSUMPTIONS

$$\sigma_{3\text{crit}} = 4 \text{ MPa}$$

$$\phi' = 32^\circ$$

$$\text{MIT } q_1 = T_1$$

$$T_1 = 2 \text{ MPa}$$

$$\sigma'_3 = 0.1 \text{ MPa}$$

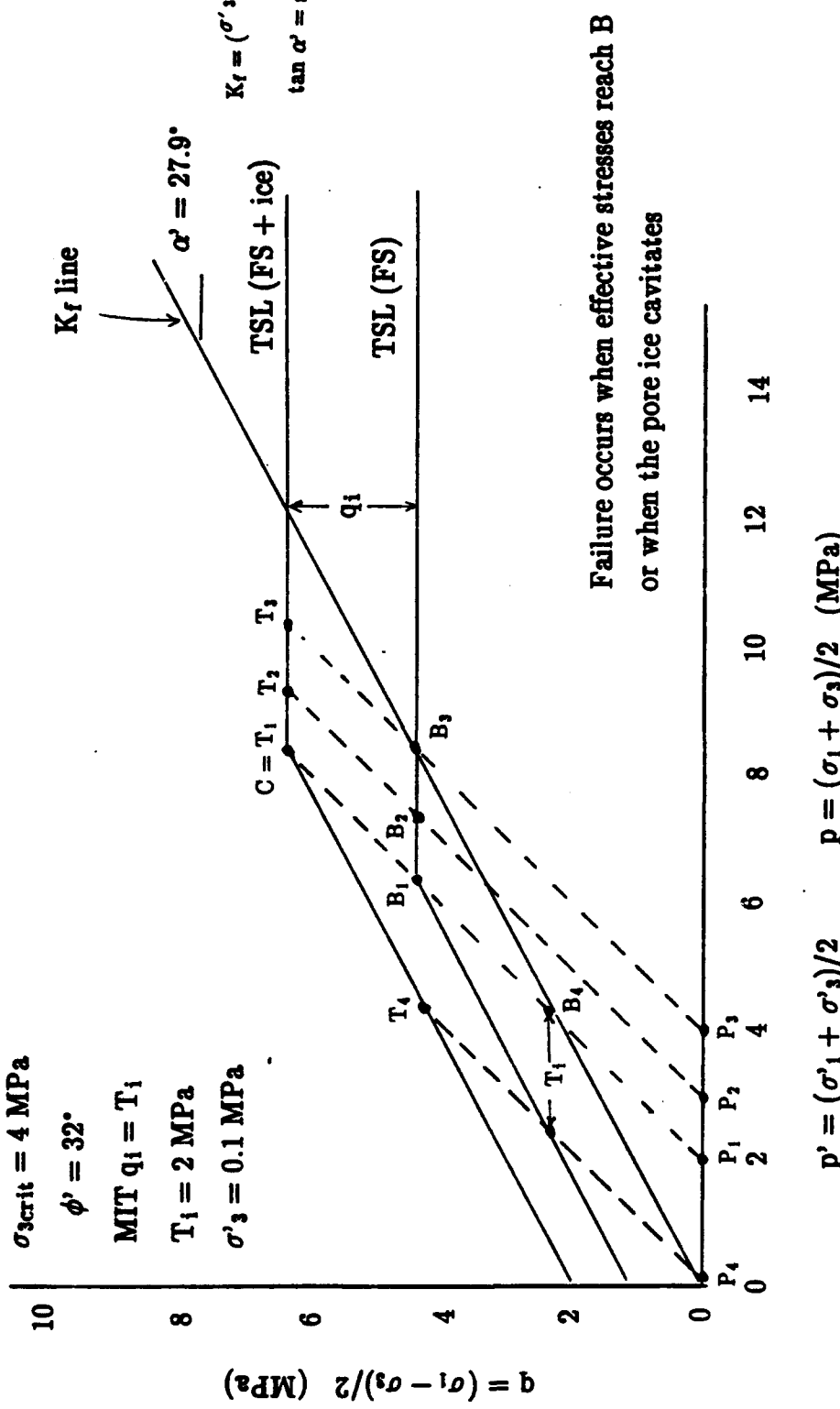


Figure 5.1:

MIT q-p Plot for Ladanyi's Dilatancy Hardening Model

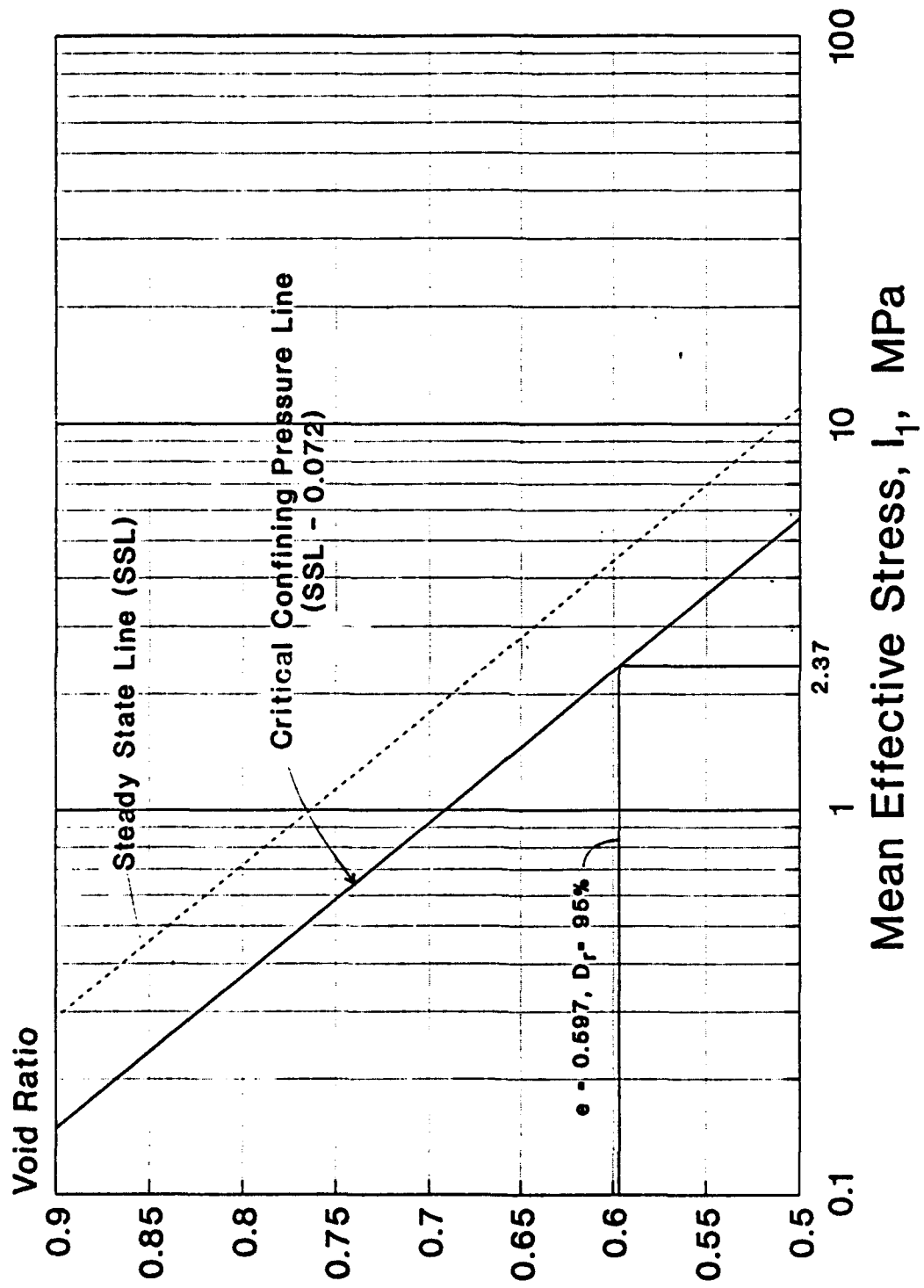
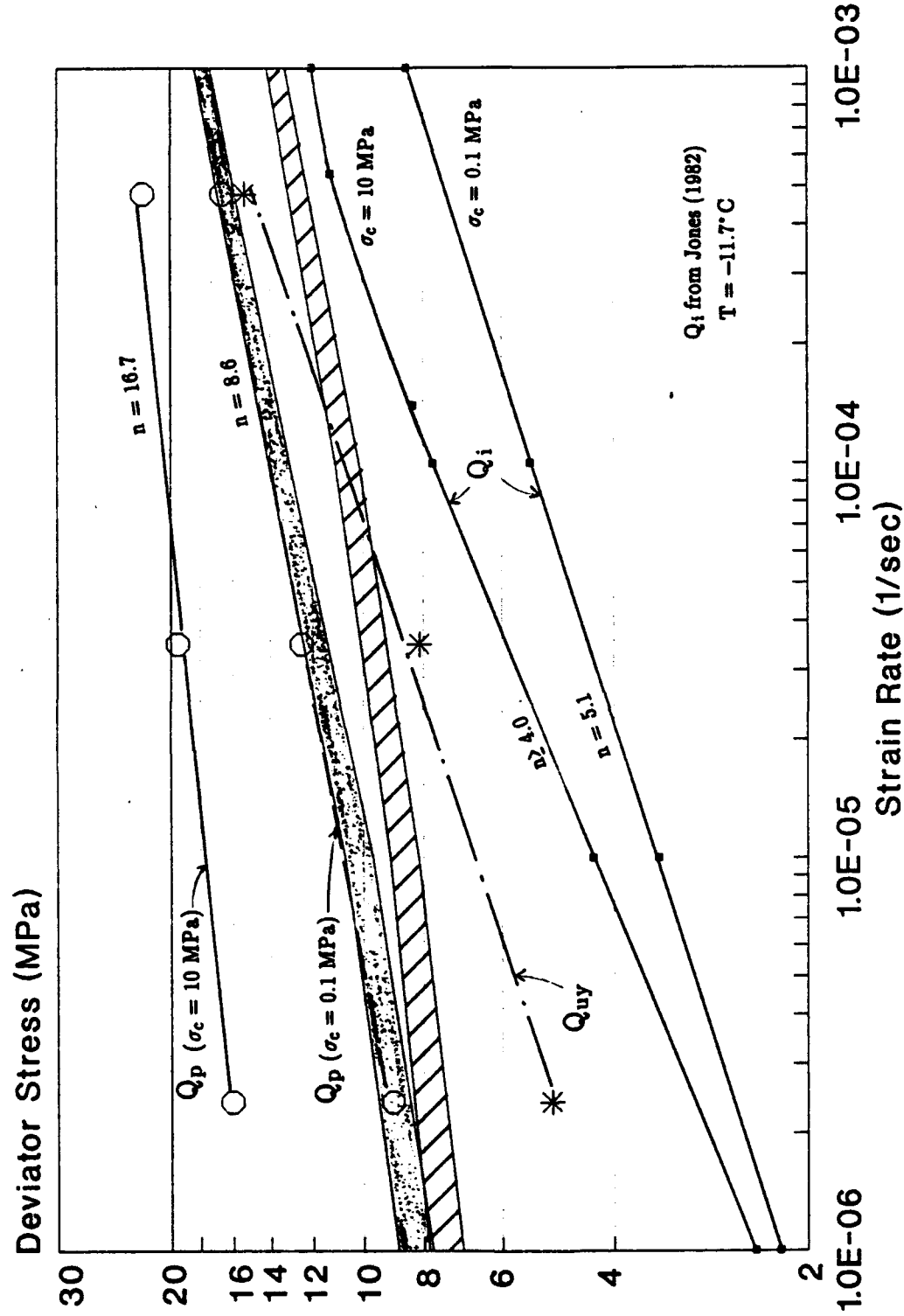
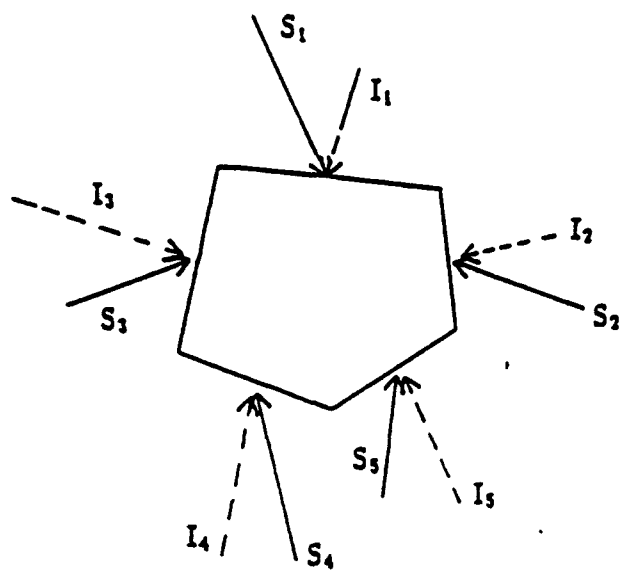


Figure 5.2:
Critical Confining Pressure Line of Unfrozen MFS from
CIUC Tests

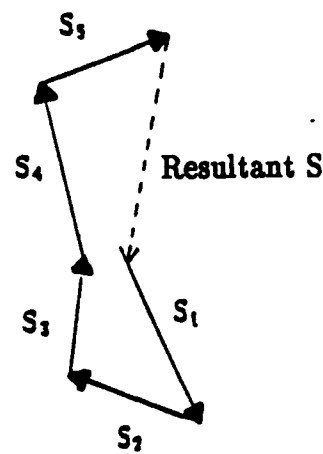


Application of Ladanyi's Model to Dense Frozen MFs
($D_r = 95\%$, $T = -9.5^\circ\text{C}$)

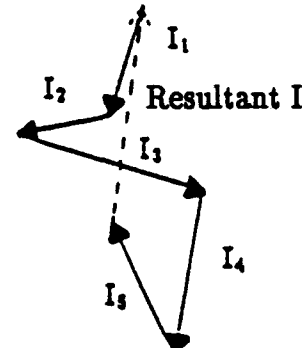
Figure 5.3:



FORCE POLYGONS



Sand Intergranular Contact Forces



Ice-Silicate Interface Forces

Figure 5.4:

Force Equilibrium of Sand Particle In Frozen Sand

6. SUMMARY, CONCLUSIONS AND RECOMMENDATIONS

6.1 SUMMARY AND CONCLUSIONS

Research Objectives

Development of rational constitutive relationships to model the time-dependent strength-deformation behavior of frozen sand for use in design practice involves three steps: 1) a complete characterization of the stress-strain-time behavior of frozen sand as a function of the relevant experimental variables (i.e., sand density, confining pressure, strain rate and temperature); 2) analysis of the results (often using deductive reasoning based on comparisons with the response of ice and unfrozen sand) to identify the physical mechanisms controlling behavior; and 3) the eventual use of principles from ice mechanics, soil mechanics, composite materials, etc. to develop physically based constitutive models. This research focused mainly on step 1) because an extensive literature review showed that this type of information had not been published for any frozen soil. The resulting experimental data set represents the most significant contribution of the research, although progress was also made on step 2).

Experimental Program

A high-pressure low-temperature triaxial testing system was developed in order to measure the stress-strain behavior of frozen Manchester Fine Sand (MFS) from very small (0.01%) to very large (25%) axial strains. This system incorporates internal force and temperature measurement, lubricated end platens, on-specimen axial strain measurement, pressure control to 10 MPa, temperature regulation to $\pm 0.35^{\circ}\text{C}$ and volumetric strain measurement to $\pm 0.2\%$. The "principal" testing program on frozen MFS evaluated the following variables for specimens sheared in triaxial compression at a temperature of $T = -9.5^{\circ}\text{C}$ (Table 3.1):

- Relative density (D_r) ranging from 20 to 100%;
- Confining pressures (σ_c) of 0.1, 2, 5 and 10 MPa;

- Axial strain rates ($\dot{\epsilon}$) of $3 \times 10^{-6}/\text{sec}$ (slow), $3 \times 10^{-5}/\text{sec}$ (moderate) and $4 \times 10^{-4}/\text{sec}$ (fast).

A "supplemental" program evaluated the influence of varying the temperature from -5 to -28°C for loose sand sheared at $\sigma_c = 0.1 \text{ MPa}$ and $\dot{\epsilon} = 3 \times 10^{-5}/\text{sec}$ (moderate rate).

A similar high-pressure triaxial testing system was developed to measure the stress-strain behavior of unfrozen MFS as a function of relative density and effective (consolidation) pressure. This program, which included 32 successful consolidated-undrained (CIUC) and 6 successful consolidated-drained (CIDC) triaxial compression tests (Table 4.1), was conducted for two reasons: 1) to compare the strength-deformation behavior of the same sand in frozen and unfrozen states; and 2) to obtain sand properties required for application of Ladanyi's (1985) dilatancy-hardening model that attempts to quantify the relative contributions of the frictional resistance of the soil skeleton and of the tensile and compressive strength of the ice matrix.

Most of the specimens used for both the frozen and unfrozen triaxial testing programs were prepared by multiple sieve pluviation (MSP), which produced very uniform sand specimens having a wide range of relative densities.

General Overview of Stress-Strain Behavior of Frozen MFS

The use of on-specimen axial strain measurements provided the first complete characterization of the stress-strain behavior of a frozen soil from very small to very large strains. This enabled determination of the following stress-strain parameters from plots of axial strain (ϵ_a) versus deviator stress ($Q = \sigma_1 - \sigma_3$) and volumetric strain ($\epsilon_v = \Delta v/v_0$), as illustrated in Fig. 3.1.

- 1) Definition of small strain behavior, such as values of Young's modulus (E) representing the initial slope of the stress-strain curve.
- 2) Values of the upper yield stress (Q_{uy}), which represents the knee of the stress-strain curve where very significant amounts of plastic deformation begin to occur.

- 3) The nature of the post upper yield behavior, i.e., the degree of strain hardening or strain softening after the knee. Most curves exhibited a distinct double yield behavior similar to that of fine-grained polycrystalline ice within the ductile to brittle transitional deformational regime.
- 4) Values of the peak stress (Q_p) and post peak behavior.
- 5) The volumetric behavior, including the rate of dilation = $d\epsilon_v/d\epsilon_a$.

The general shape of the stress-strain curves was classified into seven different types. These are shown in Fig. 3.2 which plots deviator stress divided by the upper yield stress (Q/Q_{uy}) for tests sheared at "low" and "high" confining pressures. The effects of changes in relative density, confining pressure, strain rate and temperature on stress-strain behavior are illustrated in Figs. 3.6, 3.7, 3.8 and 3.19.

Small Strain Behavior of Frozen MFS

The results in Fig. 3.3 show that the initial Young's modulus (E) equals 26.6 ± 4.5 MPa and is essentially independent of changes in density, confinement and strain rate. Section 3.5 also indicates that E does not vary with temperature. Section 3.3.2 shows that the initial modulus of frozen MFS can be reasonably predicted by treating the system as a composite material using Counto's (1964) model. In this isostrain model, the frozen sand was idealized as a cube of "stiff" sand grains embedded in a "soft" ice matrix.

Large Strain Behavior of Frozen MFS

The magnitude of the upper yield stress (Q_{uy}) is independent of sand density (Fig. 3.10) and decreases only slightly with confining pressure (Fig. 3.11). This suggests that Q_{uy} is not affected by the frictional characteristics of the sand skeleton. Although Q_{uy} is about double the unconfined peak strength of fine-grained polycrystalline ice at temperatures near -10°C , both systems exhibit similar sensitivities to strain rate (Fig. 3.14). This observation led to the suggestion in Section 3.4.2 that the physical mechanisms controlling the upper yield behavior of frozen MFS might be similar to those controlling the strength of ice. However, initial results from low-density, low-confinement, moderate

strain rate tests at varying temperatures show that the temperature sensitivity of frozen MFS is very different from that predicted for ice (Fig. 3.21). Thus the above hypothesis requires further experimental evaluation, such as proposed in Section 6.2.

The peak strength (Q_p) of frozen MFS is greatly affected by the frictional resistance of the sand skeleton, except for Type I curves wherein failure occurs at the upper yield stress. This $Q_p = Q_{uy}$ condition occurred for loose sand having low confinement and sheared either at a fast rate or at a low temperature. All other conditions (lower $\dot{\epsilon}$ or higher T, higher D_r , and/or higher σ_c) led to post yield strain hardening and failure at larger strains. Under these latter conditions, the peak strength for shearing at $T = -9.5^\circ C$ was shown to: 1) increase linearly with relative density, with the rate of increase becoming larger with confinement (Fig. 3.15); and 2) increase nonlinearly with confinement, with the rate being larger at higher density (Fig. 3.17). These strengthening effects are less rate sensitive than granular ice (Fig. 3.18) and presumably reflect a greater contribution of the frictional resistance of the sand skeleton to the peak strength. However, initial results from tests at varying temperature indicate that the temperature sensitivity of Q_p for frozen MFS is much greater than that for granular ice at temperatures ranging from $-5^\circ C$ to $-15^\circ C$ (Fig. 3.21).

Behavior of Unfrozen MFS

Section 4 presented stress-strain curves and effective stress paths from isotropically (hydrostatically) consolidated-undrained (CIUC) and consolidated-drained (CIDC) triaxial compression tests that illustrate the effects of changes in relative density and confining pressure on the behavior of unfrozen MFS. These data were used to define the location of the large strain Steady State Line (SSL) in void ratio-log stress space (Fig. 4.7) and then evaluated in terms of the state parameter Ψ (Fig. 4.6) proposed by Been and Jefferies (1985). This approach unified the combined effects of changes in density and confining pressure for CIUC tests as illustrated by plots of Ψ versus the pore pressure parameter at failure (Fig. 4.8) and undrained strength ratio (Fig. 4.9).

Application of Dilatancy-Hardening Model

Section 5 summarized the dilatancy-hardening model developed by Ladanyi (1985) to predict the strength of frozen dense sand in terms of the frictional resistance of the sand skeleton and of the tensile and compressive strength of the ice matrix. Application of this approach to frozen dense MFS required the determination of the critical confining pressure (σ'_{scr}), which was obtained from the Ψ versus A_f relationship at $A_f = 0$ to give $\sigma'_{scr} = 2.37$ MPa (Fig. 5.2). Figure 5.3 compared predicted and measured strengths at varying strain rates. At low confinement ($\sigma_c = 0.1$ MPa), the agreement is considered reasonable given the uncertainties in the assumed ice properties, but there is a severe problem with "strain compatibility" as discussed in Section 5.2. At high confinement ($\sigma_c = 10$ MPa), the measured Q_p is much larger than predicted at slow and moderate strain rates. Section 5.3 discussed other potential problems with the dilatancy-hardening model, with emphasis on how the ice matrix might affect the stress-strain behavior of the sand skeleton which is assumed in the model to be the same for frozen and unfrozen sand.

6.2 RECOMMENDATIONS

- 1) The results in Section 3.5 from the initial study of the effects of changing temperature on the behavior of frozen MFS indicate trends very different from those obtained for changing strain rate (both compared to their effects on ice behavior). This study should be extended to include a fairly comprehensive program of testing over a range of experimental conditions such as outlined in Table 3.2.
- 2) The undrained (constant volume) stress-strain data for *unfrozen* dense MFS in Fig. 4.2 show that increases in the preshear effective stress cause a very large increase in the stiffness of the sand skeleton. Such changes in stiffness presumably could have a very significant affect on the strength-deformation behavior of frozen sand at strains near and beyond the upper yield region. Consequently, tests should be conducted on sand that is frozen after application of the confining pressure,

rather than vice versa as has been done for all prior experimental programs on frozen soil. This will require a more complex freezing technique, but should simulate more closely actual in situ conditions for "deep" permafrost and for soil stabilization via artificial freezing. Such testing also might help to further evaluate Ladanyi's dilatancy-hardening model.

- 3) No information exists about the behavior of ice having very small grain sizes that presumably exist within most frozen sands. An investigation of the response of frozen spheres having large changes in the mean particle diameter (e.g., using glass beads) might prove useful. Likewise, changes in the particle surface (roughness and affinity for water) may shed light on behavior at the ice-silicate interface.
- 4) The modeling of frozen sand as a composite material deserves further study to determine if this approach can be extended to larger strain levels. The Discrete Element Method (DEC) also might be considered, although introduction of a "viscoelastic" matrix will certainly make such analyses highly complex compared to current capabilities.

7. REFERENCES

ASCE = American Society of Civil Engineers
CRREL= U.S. Army Cold Regions Research and Engineering Laboratory
IAHR = International Association for Hydraulics Research
JGE = Journal of Geotechnical Engineering
JGED = Journal of the Geotechnical Engineering Division
JSMFD= Journal of the Soil Mechanics and Foundations Division
SPE-AIME= American Institute of Mining, Metallurgical, and Petroleum Engineers

Alkire, B.D. and O.B. Andersland (1973), "The Effect of Confining Pressure on the Mechanical Properties of Sand-Ice Materials", Journal of Glaciology, Vol. 12, No. 66, pp. 469-481.

Andersen, G.R. (1991), "Physical Mechanisms Controlling the Strength and Deformation Behavior of Frozen Sand" Thesis submitted in partial fulfillment for Doctor of Science degree, Massachusetts Institute of Technology, 560p.

Ashby, M.F., and P. Duval (1985), "The Creep of Polycrystalline Ice", Cold Regions Science and Technology, Vol. 11, pp. 285-300.

Baker, T.H.W. and P.J. Kurfurst (1985), "Acoustic and Mechanical Properties of Frozen Sand", 4th International Symposium on Ground Freezing, Sapporo, pp. 227-234.

Been, K. and M.G. Jefferies (1985), "A State Parameter for Sands", Géotechnique, Vol. 35, No. 2, pp. 99-112.

Been, K. and M.G. Jefferies (1986), Discussion, "A State Parameter for Sands", Géotechnique, Vol. 36, No. 1, pp. 123-132.

Been, K., M.G. Jefferies and J. Hachey (1991), "The Critical State of Sands", Géotechnique, Vol. 41, No. 3, pp. 365-381.

Bourbonnais, J. and B. Ladanyi (1985), "The Mechanical Behavior of Frozen Sand Down to Cryogenic Temperatures", 4th International Symposium on Ground Freezing, Sapporo, pp. 235-244.

Bragg, R.A. and O.B. Andersland (1980), "Strain Rate, Temperature, and Sample Size Effects on Compression and Tensile Properties of Frozen Sand", 2nd International Symposium on Ground Freezing, Trondheim, pp. 34-47.

Chamberlain, E, C. Groves and R. Perham (1972), "The Mechanical Behavior of Frozen Earth Materials Under High Pressure Triaxial Test Conditions", Géotechnique, Vol. 22, No. 3, pp. 469-483.

Cole, D.M. (1987), "Strain-Rate and Grain-Size Effects in Ice", Journal of Glaciology, Vol. 33, No. 115, pp. 274-280.

Counto, U.J. (1964), "The Effect of the Elastic Modulus of the Aggregate on the Elastic Modulus, Creep and Creep Recovery of Concrete", Magazine of Concrete Research, Vol. 16, No. 48, pp. 129-138.

Glen, J.W. (1955), "The Creep of Polycrystalline Ice", Proceedings of the Royal Society of London, Series A, Vol. 228, pp. 519-538.

Goodman, M.A. (1975), "Mechanical Properties of Simulated Deep Permafrost", ASME, Journal of Engineering for Industry, Series B, Vol. 97, No. 5, pp. 417-425.

Goughnour, R.R. and O.B. Andersland (1968), "Mechanical Properties of a Sand-Ice System", JSMFD, ASCE, Vol. 94, No. SM4, pp. 923-950.

Hawkes, I. and M. Mellor (1972), "Deformation and Fracture of Ice Under Uniaxial Stress", Journal of Glaciology, Vol. 11, No. 61, pp. 103-131.

Jacka, T.H. (1984), "The Time and Strain Required for the Development of Minimum Strain-Rates in Ice", Cold Regions Science and Technology, Vol. 8, pp. 261-268.

Jellinek, H.H.G. (1962), "Ice Adhesion", Canadian Journal of Physics, Vol. 40, pp. 1294-1309.

Jones, S.J. (1982), "The Confined Compressive Strength of Polycrystalline Ice", Journal of Glaciology, Vol. 28, No. 98, pp. 171-177.

Jones, S.J. and V.R. Parameswaran (1983), "Deformation Behavior of Frozen Sand-Ice Materials Under Triaxial Compression", 4th International Conference on Permafrost, Fairbanks, pp. 560-565.

Ladanyi, B. (1985), "Stress Transfer Mechanism in Frozen Soils", Proceedings of the Tenth Canadian Congress of Applied Mechanics, University of Western Ontario, London.

Ladanyi, B. and J. Morel (1990), "Effect of Internal Confinement on Compression Strength of Frozen Sand", Canadian Geotechnical Journal, Vol. 27, pp. 8-18.

Ladd, C.C. and J.T. Germaine (1991) proposal to ARO, "Physical Mechanisms Controlling the Strength-Deformation Behavior of Frozen Sand: Part 2".

Ladd, R.S. (1974), "Specimen Preparation and Liquefaction of Sand", JGED, ASCE, Vol. 100, No. SM10, pp. 1180-1184.

Lee, K.L. and H.B. Seed (1967), "Drained Strength Characteristics of Sands", JSMFD, ASCE, Vol. 93, No. SM6, pp. 117-141.

Martin, R.T., J.M. Ting and C.C. Ladd (1981), "Creep Behavior of Frozen Sand Final Report Part 1", MIT Department of Civil Engineering, Research Report No. R81-19, 237p.

Miura, S. and S. Toke (1982), "A Sample Preparation Method and Its Effects on Static and Cyclic Deformation-Strength Properties of Sand", Soils and Foundations, Vol. 22, No. 1, pp. 61-77.

Poulos, S.J. (1981), "The Steady State of Deformation", JGED, ASCE, Vol. 107, No. GT5, pp. 553-562.

Rowe, P.W. (1962), "The stress-Dilatancy Relation for Static Equilibrium of an Assembly of Particles in Contact", Proceedings of the Royal Society of London, Series A, Vol. 269, pp. 500-527.

Seed, H.B. and I.K. Lee (1967), "Undrained Strength Characteristics of Cohesionless Soils", JSMFD, ASCE, Vol. 93, No. SM6, pp. 333-360

Sego, D.C., T. Schultz and R. Banasch (1982), "Strength and Deformation Behavior of Frozen Saline Sand", 3rd International Symposium on Ground Freezing, Hanover, pp. 11-17.

Shibata, T., T. Adachi, A. Yashima, T. Takahashi and I. Yoshioka, (1985), "Time-Dependence and Volumetric Change Characteristic of Frozen Sand Under Triaxial Stress Condition", 4th International Symposium on Ground Freezing, Sapporo, pp. 173-179.

Shyam Sunder, S. and M.S. Wu (1989), "A Differential Flow Model For Polycrystalline Ice", Cold Regions Science and Technology, Vol. 16, pp. 45-62.

Singh, S., H.B. Seed and C.K. Chan (1982), "Undisturbed Sampling of Saturated Sands by Freezing", JGED, ASCE, Vol. 108, No. GT2, pp. 247-264.

Sinha, N.K. (1989), "Elasticity of Natural Types of Polycrystalline Ice", Cold Regions Science and Technology, Vol. 17, pp. 127-135.

Ting, J.M., R.T. Martin and C.C. Ladd (1983), "Mechanisms of Strength for Frozen Sand", JGE, ASCE, Vol. 109, No. 10, pp. 1286-1302.

Yuanlin, Z., Z. Jiayi and S. Zhongyan (1988), "Uniaxial Compressive Strength of Frozen Medium Sand Under Constant Deformation Rates", 5th International Symposium on Ground Freezing", pp. 225-232.

**APPENDIX A: TABULATED DATA FROM TEST
PROGRAM ON FROZEN MFS**

Table A.1 Summary of Specimen Physical Properties (2 pages)

Table A.2 Measured Strength and Deformation Properties: Principal Program (2 pages)

Table A.3 Statistical Analysis of Small Strain Data: Principal Program

Table A.4 Summary of Small Strain Behavior: Principal Program

Table A.5 Statistical Analysis of Upper Yield Behavior: Principal Program

Table A.6 Summary of Upper Yield Behavior: Principal Program

Table A.7 Summary of Work Hardening Behavior: Principal Program

Table A.8 Summary of Peak Strength Behavior: Principal Program (2 pages)

Table A.9 Summary of Volumetric Behavior: Principal Program (4 pages)

Table A.10 Summary of Effect of Specimen Preparation Technique: Principal Program

Table A.11 Effect of Temperature on Stress-Strain Behavior

TABLE A.1 SUMMARY OF SPECIMEN PHYSICAL PROPERTIES (page 1/2)

Test Number	Date Frozen	Date Tested	Frozen Density (kg/m ³)	Dry Density (kg/m ³)	Dr (%)	Water Content (%)	Deg. of Sat. (%)	Total Length (cm)	Ice Cap Length (mm)	Method of Prep.	End Cond.
PRINCIPAL PROGRAM											
PRS 15	7/12/89	9/26/89	1894	1489	31.6	27.20	99.2	7.614	1.83	MSP	Ice
PRS 18	11/26/89	12/9/89	1922	1536	48.4	25.13	98.4	7.475	1.22	MSP	Ice
PRS 19	11/26/89	12/12/89	1926	1539	49.4	25.15	99.0	7.623	1.45	MSP	Ice
PRS 20	11/26/89	12/14/89	1982	1621	76.3	22.27	99.4	7.381	0.89	Tamp	Ice
PRS 21	11/26/89	12/19/89	1976	1615	74.4	22.35	98.9	7.522	1.45	Tamp	Ice
PRS 22	11/26/89	1/19/90	1987	1634	80.3	21.60	98.4	7.701	0.47	Tamp	Ice
PRS 23	1/22/90	1/30/90	1944	1559	56.2	24.70	100.2	7.614	1.37	MSP	Ice
PRS 24	1/22/90	2/2/90	2003	1668	90.5	20.08	96.5	7.539	1.63	Tamp	Ice
PRS 25	1/22/90	2/9/90	1936	1549	52.8	24.98	99.8	7.502	1.63	MSP	Ice
PRS 26	1/22/90	2/14/90	2016	1680	94.0	20.00	98.0	7.462	1.80	Tamp	Ice
PRS 27	1/22/90	2/17/90	2014	1668	90.5	20.74	99.7	7.397		Tamp	Grease
PRS 28	2/14/90	3/7/90	2035	1698	99.2	19.85	100.1	7.379		Tamp	Grease
PRS 29	2/14/90	3/10/90	1943	1559	56.2	24.63	99.9	7.411	1.65	MSP	Ice
PRS 30	3/28/90	4/2/90	1880	1463	21.8	28.50	100.0	7.346	1.60	MSP	Emery
PRS 31	3/28/90	4/6/90	1879	1466	23.0	28.17	99.3	7.142		MSP	Ice
PRS 32	4/9/90	4/23/90	1988	1634	80.3	21.66	98.7	7.304	1.65	MSP	Ice
PRS 33	4/9/90	4/27/90	1948	1572	60.6	23.92	99.0	7.278	1.88	MSP	Ice
PRS 34	3/28/90	5/8/90	1905	1503	36.7	26.75	99.7	7.087	1.57	MSP	Ice
PRS 35	4/9/90	5/23/90	1904	1502	36.3	26.76	99.6	7.000	1.60	MSP	Ice
PRS 36	4/9/90	5/28/90	1892	1503	36.7	25.88	96.4	7.534	1.93	MSP	Ice
PRS 37	5/22/90	5/31/90	2022	*	1690	96.9	19.64	97.8	7.416	2.01	MSP
PRS 38	5/22/90	6/4/90	2012	1681	94.3	19.69	96.6	7.463	1.80	MSP	Grease
PRS 39	5/22/90	6/7/90	2010	1676	92.8	19.93	97.0	7.169		MSP	Grease
PRS 40	5/30/90	6/13/90	1901	1505	37.4	26.31	98.3	7.595	2.03	MSP	Ice
PRS 41	5/30/90	6/15/90	2016	1687	96.0	19.86	98.4	7.357		MSP	Grease
PRS 42	6/7/90	6/19/90	2013	1669	90.8	20.14	98.4	7.291		MSP	Ice
PRS 43	6/7/90	6/22/90	1502	1678	93.4	20.14	98.4	7.327		MSP	Grease
PRS 44	6/14/90	6/27/90	1905	1687	96.0	19.86	98.4	7.581	2.41	MSP	Ice
PRS 45	6/14/90	7/2/90	1906	1507	38.1	26.48	99.3	7.553	2.03	MSP	Ice
PRS 46	6/18/90	7/6/90	2015	1673	92.0	20.44	99.0	7.644	2.41	MSP	Ice
PRS 47	6/18/90	7/12/90	1917	1522	43.5	25.95	99.5	7.497	2.01	MSP	Ice

* Based on final washed weight

TABLE A.1 SUMMARY OF SPECIMEN PHYSICAL PROPERTIES (page 2/2)

Test Name	Date Frozen	Date Tested	frozen Density (kg/m ³)	Dry Density (kg/m ³)	Dr (%)	Water Content (%)	Deg. of Sat. (%)	Total Length (cm)	Ice Cap Length (mm)	Method of Prep.	End Cond.
PRINCIPAL PROGRAM (cont.)											
FRS 48	6/18/90	7/12/90	2018	**1688	96.3	19.55	97.0	7.522	1.98	ISP	Ice
FRS 49	7/11/90	7/19/90	2023	1690	96.9	19.70	98.1	7.476	1.96	ISP	Ice
FRS 50	7/11/90	7/20/90	2017	1679	93.7	20.13	98.5	6.698	1.91	ISP	Ice
FRS 51	5/22/90	7/24/90	1982	1633	80.0	21.37	97.2	6.565	1.73	ISP	Ice
FRS 52	7/11/90	7/25/90	2007	1669	90.8	20.25	97.5	6.596	2.01	ISP	Ice
FRS 53	7/11/90	7/26/90	2016	1675	92.5	20.36	99.0	6.685	2.24	ISP	Ice
FRS 54	7/11/90	7/30/90	2016	1680	94.0	20.00	98.0	6.537	1.63	ISP	Ice
FRS 55	6/18/90	8/1/90	2006	1660	88.1	20.84	98.9	6.530	1.85	ISP	Ice
FRS 56	7/30/90	8/2/90	2015	1676	92.8	20.23	98.5	6.523	1.42	ISP	Ice
FRS 57	7/30/90	8/6/90	1904	1500	35.6	26.93	99.9	6.567	2.18	ISP	Ice
FRS 58	7/30/90	8/13/90	2018	1679	93.7	20.19	98.8	6.553	1.45	ISP	Ice
FRS 59	3/28/90	8/16/90	1891	1485	30.1	27.34	99.1	7.404	1.32	ISP	Ice
FRS 60	5/22/90	8/17/90	1938	1553	54.2	24.79	99.7	7.379	1.96	ISP	Ice
FRS 61	7/30/90	8/20/90	1896	1494	33.4	26.91	98.9	7.468	1.52	ISP	Ice
FRS 62	5/30/90	8/22/90	1938	1553	54.2	24.79	99.7	7.417	1.40	ISP	Ice
FRS 63	5/30/90	8/23/90	1929	1544	51.1	24.94	98.9	7.407	1.81	ISP	Ice
FRS 64	6/14/90	8/24/90	1994	1642	82.7	21.44	98.9	7.277	1.50	ISP	Ice
FRS 65	7/30/90	8/27/90	2020	**1686	95.7	19.81	98.0	7.343	1.91	ISP	Ice
FRS 66	5/30/90	8/29/90	1997	1643	83.0	21.55	99.6	7.353	1.56	ISP	Ice
FRS 67	8/28/90	9/4/90	1884	1493	33.1	26.19	96.1	7.291	1.30	ISP	Ice
NEW PROGRAM											
FRS 75	8/1/91	8/3/91	1920	1535	48.0	26.31	101.7	7.252	1.36	ISP	Ice
FRS 76	8/1/91	8/5/91	1908	1528	45.7	25.88	99.4	7.540	1.17	ISP	Ice
FRS 77	8/1/91	8/14/91	1893	1513	40.3	26.09	97.4	7.600	1.21	ISP	Ice
FRS 78	8/1/91	8/24/91	1892	1520	42.9	25.73	97.6	7.217	1.50	ISP	Ice
FRS 79	8/21/91	11/19/91	1847	1528	45.7	24.80	89.1	6.855	0.87	ISP	Ice
FRS 80	8/21/91	1/2/92	1882	1515	41.0	25.35	96.8	7.086	1.18	ISP	Ice

** Based on total weight from trimmings and pouring

TABLE A.2 MEASURED STRENGTH AND DEFORMATION PROPERTIES (page 1/2)

PRINCIPAL PROGRAM

ES (page 1/2)

FRS	D _f	σ _c ave MPa	INITIAL RESPONSE			PEAK STRENGTH			VOLUMETRIC BEHAVIOR			S* ε _f ε _f p vp					
			Strain Rate /sec	Q Y _i max Off x10 ⁻⁷	E GPa	Pro Y _i Lim MPa	Q _{off} MPa	Q _{cor} MPa	ε _a x10 ⁻³	q dε _a MPa	Q _p MPa	ε _a x10 ⁻³					
15	31.6	10.15	31	336	21.4	1.0	2.8	7.3	7.4	5.0	11.8	46	11.6	27.7	-	-	-
18	48.4	10.18	27	329	28.6	1.6	2.7	7.2	7.2	4.3	10.9	73	13.4	24.9	0	0	f
19	49.4	10.18	24	344	21.4	1.5	2.7	7.2	7.3	4.3	13.3	81	13.1	18.4	3	3	f
20	76.3	10.18	31	299	20.7	1.8	3.2	8.6	8.5	5.0	258	16.7	16.5	5	5	f	
21	74.4	10.18	27	311	20.0	1.7	3.0	8.2	8.2	5.2	213	15.9	14.8	4	4	f	
22	80.3	10.15	22	320	25.0	1.6	3.0	8.2	8.3	5.1	218	16.3	13.5	5	5	f	
23	56.2	5.12	19	330	23.1	1.9	3.1	7.4	7.5	4.6	10.4	81	12.6	17.6	4	4	f
24	90.5	5.12	19	303	33.3	1.7	3.2	8.9	8.9	5.4	282	15.8	9.0	12	12	f	
25	52.8	2.05	21	336	26.1	2.2	3.4	7.6	7.6	4.8	10.1	75	10.9	12.1	17	17	f
26	94.0	2.08	18	300	31.8	2.0	3.7	9.2	9.2	5.3	283	14.7	5.1	15	23	f	
27	90.5	2.07	15	348	33.3	2.1	3.8	9.0	8.9	5.3	278	15.0	5.7	11	31	f	
28	99.2	0.103	15	386	21.2	1.7	3.2	9.1	9.0	4.4	4.4	361	14.6	3.4	24	42	f
29	56.2	0.106	15	334	25.9	2.2	3.8	8.2	8.2	4.7	10.3	73	10.0	6.2	19	29	f
30	21.8	0.106	17	339	25.9	2.7	4.2	8.4	8.3	5.0	11.9	12	8.5	6.1	16	20	f
31	23.0	0.106	12	352	29.2	2.0	3.8	8.3	8.1	5.0	11.9	15	8.6	4.8	15	42	f
32	80.3	0.102	16	344	28.0	2.1	3.9	8.3	8.2	4.2	8.1	96	10.9	6.1	24	50	f
33	60.6	0.103	22	337	29.2	1.6	3.4	8.5	8.4	5.3	100	10.2	5.2	18	42	f	
34	36.7	0.102	24	358	23.5	3.1	4.9	8.7	8.5	4.7	12.2	31	9.4	6.4	13	33	f
35	36.3	0.101	53	1070	25.8	2.3	4.3	10.5	--	6.7	14.8	2	10.5	0.67	0	35	f
36	36.7	0.101	230	4950	25.0	3.0	5.2	15.0	15.1	7.4	18	-25	15.0	0.74	11	39	f
37	96.9	0.101	180	4790	30.3	2.6	5.1	15.4	15.1	8.3	14.4	54	16.4	3.9	28	60	f
38	94.3	0.101	14	322	41.2	2.5	4.1	8.5	8.5	4.4	4.4	138	11.6	5.2	25	47	f
39	92.8	10.11	260	5360	29.0	2.8	4.4	16.1	15.0	10.2	19.5	104	21.6	13.1	12	17	f
40	37.4	10.13	400	5420	25.7	2.4	4.7	15.0	15.3	8.3	20.0	14	15.4	16.9	4	4	f
41	96.0	0.102	16	342	25.9	2.8	4.2	8.8	8.7	5.0	5.0	158	12.4	4.9	23	64	f
42	93.4	10.13	19	362	25.0	1.5	3.1	8.2	8.1	5.0	5.0	185	18.8	17.8	8	8	f
43	90.8	0.102	16	342	25.9	2.8	4.2	8.8	8.7	5.0	5.0	158	12.4	4.9	23	64	f
44	36.3	0.102	17	336	25.7	2.3	4.1	8.2	8.2	4.8	8.4	53	9.3	3.9	10	36	f
45	38.1	0.102	1.6	30.9	28.6	1.8	3.0	5.0	5.0	2.8	6.7	46	6.6	8.1	12	33	f
46	92.0	0.101	1.3	24.3	40.0	2.0	3.3	5.1	5.2	2.6	2.6	100	8.5	7.2	34	57	f
47	43.5	10.03	1.9	29.2	20.0	1.8	2.7	4.8	4.8	3.6	7.9	54	9.1	24.4	0	0	f
48	96.3	10.04	2.0	27.2	25.0	1.6	2.7	4.9	4.9	3.4	119	13.0	13.0	13.0	0	0	f

TABLE A.2 MEASURED STRENGTH AND DEFORMATION PROPERTIES (page 2/2)

PMS Test #	D _r %	σ_c ave MPa	Strain Rate /sec $\dot{\epsilon}$ Y _i max Off $\times 10^7$	INITIAL RESPONSE			UPPER YIELD			STRAIN H/S			PEAK STRENGTH			VOLMETRIC BEHAVIOR			S* A*				
				E GPa	Y _i MPa	Pro Off	Q _{off} MPa	Y _i MPa	Q _{lim} MPa	Q _{cor} MPa	Q _{uy} MPa	ϵ_a $\times 10^{-3}$	$\frac{d\sigma}{d\epsilon_a}$ MPa	Q _p MPa	ϵ_a $\times 10^{-3}$	$\frac{d\sigma}{d\epsilon_a}$ MPa	ε _v $\times 10^{-3}$	bdi1 $\times 10^3$	ε _v $\times 10^{-3}$	bdi1 $\times 10^3$	ε _f p	ε _f vp	ε _f p
49	96.9	10.01	370	4380	24.3	2.0	4.3	15.4	15.3	8.5	8.5	112	22.0	15.0	11	11	28	18	p	g	g	g	
*50	93.7	10.03	18	212	28.0	1.9	3.3	10.8	--	5.4	5.4	177	21.5	23.2	10	10	27	14	f	p	f	p	
51	80.0	10.02	20	370	31.6	2.0	3.3	8.8	8.3	5.2	5.2	157	17.9	23.4	4	4	80	5	f	f	f	p	
52	90.8	10.04	27	355	20.7	1.8	2.8	8.2	7.7	4.8	4.8	158	19.0	22.9	6	6	56	7	f	p	f	p	
53	92.5	5.03	15	352	35.3	1.5	2.9	8.5	8.1	5.1	5.1	165	16.5	18.5	13	13	73	16	P	P	g	f	
54	94.0	10.04	3.1	32.5	26.3	1.7	2.8	5.4	4.9	4.4	4.4	142	16.0	21.9	4	4	64	5	g	g	g	g	
55	88.1	2.00	24	382	26.1	2.1	3.4	7.9	7.4	4.4	8.5	119	13.1	12.0	20	20	27	21	32	d	f	p	
56	92.8	0.101	12	371	46.7	2.7	3.8	9.5	9.0	4.9	4.9	154	13.1	5.2	26	26	61	25	84	f	f	p	
57	35.6	0.101	18	384	25.0	1.7	3.3	8.7	8.2	5.4	5.4	38	9.6	4.0	11	11	35	26	39	g	g	g	
58	93.7	0.100	0.7	32.9	14.3	0.9	1.8	5.6	5.1	4.9	4.9	128	9.3	6.8	34	34	67	40	83	g	g	g	
59	30.1	5.01	23	333	29.2	1.8	3.5	8.9	8.8	4.4	10.3	50	11.5	23.7	6	6	40	4	f	f	f	f	
60	54.2	2.01	20	339	31.8	2.0	3.5	9.2	9.1	4.3	4.3	92	11.4	8.0	14	14	22	23	28	1	g	g	
61	33.4	10.02	2.8	28.9	21.7	1.5	2.9	5.1	5.1	3.4	10.7	46	9.0	24.6	2	2	127	1	146	1	103	2	
62	54.2	5.00	19	335	25.9	2.0	3.4	8.3	8.3	4.3	9.1	85	12.8	21.4	6	6	126	4	f	f	f	f	
63	51.1	10.03	28	335	24.0	2.0	3.0	8.2	8.2	5.0	5.0	9.9	81	14.4	26.4	1	1	146	1	103	2	11	91
64	82.7	10.02	23	338	24.3	2.2	3.3	7.9	7.8	4.8	10.4	127	17.8	24.0	2	2	60	11	67	g	g	g	
65	95.7	0.102	290	4990	26.3	2.6	5.0	15.8	15.3	8.2	15.9	46	16.8	4.0	24	24	46	20	67	f	f	f	
66	83.0	0.102	18	235	35.6	3.0	4.3	8.4	8.3	2.7	2.7	185	12.1	5.1	21	21	69	10.2	12.1	12	15	30	
67	33.1	2.01	26	339	25.0	1.9	3.6	8.0	7.9	4.2	8.2	69	10.2	12.1	12	12	15	30	19	6	6	6	

* Test temperature ≈ -15°C

$\text{Yield Offset at } 10^{-4} \text{ Strain}$

Pro Lim = Proportional Limit

$\theta_{\text{corr}} = \text{Corrected Inner Yield Stress}$

ϵ_{cor} = corrected upper yield stress

EA 0011 = Axial Strain at 20%

ϵ_V = Stabilization factor

314 * *Journal of Health Politics*

**TABLE A.3 STATISTICAL ANALYSIS OF SMALL STRAIN DATA
PRINCIPAL PROGRAM**

STRESS-STRAIN QUANTITY	STRAIN RATE	CONFINING PRESSURE (MPa)	MEAN VALUE	STANDARD DEVIATION	# OF OBSERVATIONS	COMMENTS
Young's Modulus (GPa)	Slow	0.1 10.0	40 24.3	0 2.4	1 3	
	Moderate	0.1 2.0 5.0 10.0	27.5 28.7 28.4 23.0	3.6 3.6 5.2 2.7	8 4 4 8	
	Fast	0.1 10.0	27.2 25.0	2.3 0.7	3 2	
Proportional Limit (MPa)	Slow	0.1 10.0	2.0 1.6	0 0.1	1 3	
	Moderate	0.1 2.0 5.0 10.0	2.3 2.0 1.8 1.6	0.5 0.1 0.2 0.3	8 4 4 8	
	Fast	0.1 10.0	2.7 2.2	0.2 0.2	3 2	
Yield Offset Stress at 10^{-4} Strain (MPa)	Slow	0.1 10.0	3.3 2.8	0 0.1	1 3	
	Moderate	0.1 2.0 5.0 10.0	4.0 3.6 3.2 3.0	0.5 0.1 0.3 0.2	8 4 4 8	
	Fast	0.1 10.0	5.1 4.5	0.1 0.2	3 2	
Power Law Coefficient - $\sigma_c = 0.1 \text{ MPa} -$ $n = 15.6$ $r^2 = 0.19$						
Power Law Coefficient - $\sigma_c = 10.0 \text{ MPa} -$ $n = 17.8$ $r^2 = 0.18$						
Power Law Coefficient - $\sigma_c = 0.1 \text{ MPa} -$ $n = 11.2$ $r^2 = 0.63$						
Power Law Coefficient $\sigma_c = 10 \text{ MPa} -$ $n = 11.2$ $r^2 = 0.66$						

TABLE A.4

SUMMARY OF SMALL STRAIN BEHAVIOR
PRINCIPAL PROGRAM

PARAMETER	EFFECT OF INCREASING			
	RELATIVE DENSITY		CONFINING PRESSURE	
Young's Modulus	Trend	Not consistent	Decrease	None
	Figure	3.3	None	None
Proportional Limit	Empirical Equations	- All $\dot{\epsilon}$, σ_c and D - mean = 26.6 ± 4.5 GPa	- moderate strain rate- $E(\text{GPa}) = 28.5 - 0.454\sigma_c (\text{MPa})$ $r^2 = 0.22$	
	Trend	None	Decrease	Increase
Yield Offset Stress at 10 ⁻⁴ Strain	Empirical Equations	3.4 (a)	3.4 (b)	3.4 (c)
	Figure			
		- moderate strain rate- P.I. (MPa) = $2.3 - 0.067 \sigma_c (\text{MPa})$ $r^2 = 0.37$	- $\sigma_c = 0.1 \text{ MPa}$ $PL(\text{MPa}) = 5.33 (\dot{\epsilon})^{0.064}$ $r^2 = 0.19 (n=15.6)$	
			- $\sigma_c = 10 \text{ MPa}$ $PL(\text{MPa}) = 3.45 (\dot{\epsilon})^{0.056}$ $r^2 = 0.18 (n=17.9)$	
	Trend	None	Decrease	Increase
	Figure	3.5 (a)	3.5 (b)	3.5 (c)
		- Moderate strain rate- $Y_0(\text{MPa}) = 3.9 - 0.095\sigma_c (\text{MPa})$ $r^2 = 0.58$	- $\sigma_c = 0.1 \text{ MPa}$ $Y_0(\text{MPa}) = 13.0 (\dot{\epsilon})^{0.089}$ $r^2 = 0.63 (n=11.2)$	
			- $\sigma_c = 10 \text{ MPa}$ $Y_0(\text{MPa}) = 9.96 (\dot{\epsilon})^{0.089}$ $r^2 = 0.66 (n=11.2)$	

TABLE A.5 STATISTICAL ANALYSIS OF UPPER YIELD BEHAVIOR
PRINCIPAL PROGRAM

STRESS-STRAIN QUANTITY	STRAIN RATE	CONFINING PRESSURE (MPa)	MEAN VALUE (MPa)	STANDARD DEVIATION	# OF OBSERVATIONS	CONTENTS
Corrected Upper Yield Stress	Slow	0.1 10.0	5.1 4.9	0.1 0.13	3 4	-Over All Confining Pressures- mean = 5.0 ± 0.1 MPa
	Moderate	0.1 2.0 5.0 10.0	8.38 8.0 8.18 7.75	0.27 0.76 0.54 0.42	12 4 4 8	-Over All Confining Pressures- mean = 8.1 ± 0.5 MPa
	Fast	0.1 10.0	15.4 15.2	0.48 0.1	4 3	-Over All Confining Pressures- mean = 15.3 ± 0.3 MPa
	Slow	0.1 10.0	0.0026 0.0037	0 0.0005	1 3	-Over All Confining Pressures- mean = 0.0035 ± 0.0006
	Moderate	0.1 2.0 5.0 10.0	0.0047 0.0044 0.0046 0.0047	0.0008 0.0003 0.0003 0.0003	7 3 4 5	-Over All Confining Pressures- mean = 0.0046 ± 0.0006
	Fast	0.1 10.0	0.0080 0.0047	0.0004 0.0001	3 2	-Over All Confining Pressures- mean = 0.0081 ± 0.0004

TABLE A.6 SUMMARY OF UPPER YIELD BEHAVIOR
PRINCIPAL PROGRAM

PARAMETER	EFFECT OF INCREASING					
	RELATIVE DENSITY		CONFINING PRESSURE		STRAIN RATE	
Trend	None		Decrease (slight)		Increase	
Figure	3.9 (a)	3.10	3.9 (b)	3.11	3.9(c)	3.12 3.14
Upper Yield Stress	-Fast $\dot{\epsilon}$, all σ_c & D_r -mean = 15.3 \pm 0.4 MPa -Mod $\dot{\epsilon}$, all σ_c & D_r -mean = 8.1 \pm 0.5 MPa -Slow $\dot{\epsilon}$, all σ_c & D_r -mean = 5.0 \pm 0.1 MPa	-Moderate Strain Rate- -all D_r - $Q_{uy} (\text{MPa}) = 8.3 - 0.059\sigma_c (\text{MPa})$ $r^2 = 0.26$ SD = ± 0.44	- $\sigma_c = 0.1 \text{ MPa}$, all D_r - $Q_{uy} = 77.8 (\dot{\epsilon})^{0.214}$ $r^2 = 0.98$ (n = 4.7) - $\sigma_c = 10 \text{ MPa}$, all D_r - $Q_{uy} = 77.3 (\dot{\epsilon})^{0.218}$ $r^2 = 0.96$ (n = 4.6)			
Trend	None		None		Increase	
Figure	3.13 (a)		None		3.13(b)	
Axial Strain at Upper Yield Stress	-Fast $\dot{\epsilon}$, all σ_c & D_r -mean = 0.81 \pm 0.04% -Mod $\dot{\epsilon}$, all σ_c & D_r -mean = 0.46 \pm 0.06% -Slow $\dot{\epsilon}$, all σ_c & D_r -mean = 0.35 \pm 0.07%		-All σ_c and all D_r - $\epsilon_a (\%) = 0.307 (\dot{\epsilon})^{0.181}$ $r^2 = 0.78$ (n=5.5)			

TABLE A.7 SUMMARY OF WORK HARDENING BEHAVIOR
PRINCIPAL PROGRAM

PARAMETER	EFFECT OF INCREASING			
	RELATIVE DENSITY		CONFINING PRESSURE	STRAIN RATE
	Trend	Increase	Complex	Complex
Rate of Work Hardening	Figure	3.6 (a) 3.6 (b)	3.7 (a) 3.7 (b)	3.8 (a), (b) and (c)
Empirical Equations and Comments	-Moderate $\dot{\epsilon}$, All σ_c - $\frac{dq}{d\epsilon_a}(\text{MPa}) = 31.3 + 2.2Dr(\%)$ $r^2 = 0.91 \pm 15.4$	- For Moderate $\dot{\epsilon}$ - No Effect - For Slow and Fast $\dot{\epsilon}$ - Increase	- $\sigma_c = 0.1\text{MPa}$, $D_r = 95\%$ - Slow to mod. $\dot{\epsilon}$ -Increase Mod $\dot{\epsilon}$ to fast $\dot{\epsilon}$ -Decrease - $\sigma_c = 10\text{MPa}$, $D_r = 35\%$ - Slow to mod $\dot{\epsilon}$ -No change Mod to Fast $\dot{\epsilon}$ - Decrease	- $\sigma_c = 0.1\text{MPa}$, $D_r = 95\%$ - Slow to mod. $\dot{\epsilon}$ -Increase Mod $\dot{\epsilon}$ to fast $\dot{\epsilon}$ -Decrease - $\sigma_c = 10\text{MPa}$, $D_r = 35\%$ - Slow to mod $\dot{\epsilon}$ -No change Mod to Fast $\dot{\epsilon}$ - Decrease
Axial Strain at Beginning of Work Hardening	Trend	Decrease	Complex	Complex
	Empirical Equations	- $\sigma_c = 0.1$, mod $\dot{\epsilon}$ - $\epsilon_a(\%) = 1.43 - 1.32 \times 10^{-2}Dr(\%)$ $r^2 = 0.57$	- Slow and mod $\dot{\epsilon}$ - Increase - Fast $\dot{\epsilon}$ low D_r - Increase - Fast $\dot{\epsilon}$ high D_r - Decrease	- $D_r = 35\%$, $\sigma_c = 10\text{MPa}$ - Slow-mod. No change (within Scatter band) Mod- fast Increase . - $D_r = 95\%$, $\sigma_c = 10\text{MPa}$ - No Change (within Scatter band)

TABLE A.8 SUMMARY OF PEAK STRENGTH BEHAVIOR (page 1/2)
PRINCIPAL PROGRAM

PARAMETER	EFFECT OF INCREASING			
	RELATIVE DENSITY		CONFINING PRESSURE	STRAIN RATE
Peak Deviator Stress (Q_p)	Trend	Increase	Increase	Increase
Empirical Equations and Comments Figure 3.6(a)&(b), 3.15(a)&(b)	- Moderate $\dot{\epsilon}$ - $\sigma_c = 10 \text{ MPa}$ $Q_p (\text{MPa}) = 7.36 + 0.128 D_r (\%)$ $r^2 = 0.98$ $\sigma_c = 5 \text{ MPa}$	$D_r = 95\%$ Linear with $\phi_t = 15.6$	- Moderate $\dot{\epsilon}$ - $D_r = 35\%$, $\sigma_c = 0.1 \text{ MPa}$	3.8(a), (b)&(c), 3.18
	$Q_p (\text{MPa}) = 8.55 + 0.082 D_r (\%)$ $r^2 = 0.95$ $\sigma_c = 2 \text{ MPa}$	$D_r = 60\%$ Curved failure envelope ϕ_t from 13.5° to 7.9°	- $D_r = 35\%$, $\sigma_c = 10 \text{ MPa}$ $Q_p (\text{MPa}) = 34.5 (\dot{\epsilon})^{0.1069}$ $r^2 = 0.99$ (n=9.4)	
	$Q_p (\text{MPa}) = 8.35 + 0.053 D_r (\%)$ $r^2 = 0.98$ $\sigma_c = 0.1 \text{ MPa}$	$D_r = 35\%$ Curved failure envelope ϕ_t from 11.2° to 0°	- $D_r = 95\%$, $\sigma_c = 0.1 \text{ MPa}$ $Q_p (\text{MPa}) = 40.2 (\dot{\epsilon})^{0.116}$ $r^2 = 0.99$ (n=8.6)	
	$Q_p (\text{MPa}) = 4.98 + 0.042 D_r (\%)$ $r^2 = 0.93$ $\sigma_c = 10 \text{ MPa}$	$D_r = 35\%$	- $D_r = 95\%$, $\sigma_c = 10 \text{ MPa}$ $Q_p (\text{MPa}) = 34.9 (\dot{\epsilon})^{0.060}$ $r^2 = 0.96$ (n = 16.7)	
	$Q_p (\text{MPa}) = 4.40 + 0.122 D_r (\%)$ $r^2 = 0.98$	- Fast $\dot{\epsilon}$ - $\sigma_c = 0.1 \text{ MPa}$		
		Assume $Q_p = Q_u$ to 75% D_r thereafter same slope as moderate $\dot{\epsilon}$		
		$Q_p = 11.25 + 0.111 D_r (\%)$		

TABLE A.8 SUMMARY OF PEAK STRENGTH BEHAVIOR (page 2/2)
PRINCIPAL PROGRAM

PARAMETER	EFFECT OF INCREASING		
	RELATIVE DENSITY	CONFINING PRESSURE	STRAIN RATE
Axial Strain at Peak Deviator Stress	Trend Complex Figures 3.8(a)&(b), 3.16(a)&(b)	Increases 3.7 (a) & (b)	Complex 3.8 (a), (b) and (c)
Empirical Equations and Comments	- Mod $\dot{\epsilon}$, $\sigma_c = 0.1 \text{ MPa}$ No Effect $\epsilon_a = 5.2 \pm 0.9\%$	For all $\dot{\epsilon}$ and D_r	$\sigma_c = 0.1 \text{ MPa}$ Increase
	- Mod $\dot{\epsilon}$, $\sigma_c = 2.0 - 0.10 \text{ MPa}$ Slow $\dot{\epsilon}$ all σ_c and Fast $\dot{\epsilon}$, $\sigma_c = 10 \text{ MPa}$ Linear Decrease	$\sigma_c = 10 \text{ MPa}$ Slow to moderate $\dot{\epsilon}$ No effect (Slow data in or near scatter band of moderate data)	
	- Mod. $\dot{\epsilon}$, $\sigma_c = 10 \text{ MPa}$ - $\epsilon_a (\%) = 31.3 - 1.09 \times 10^{-3} D_r (\%)$ $r^2 = 0.69$	$\sigma_c = 10 \text{ MPa}$ Moderate to fast $\dot{\epsilon}$ Decrease for all D_r	
	- Fast $\dot{\epsilon}$, $\sigma_c = 0.1 \text{ MPa}$ - Increase		

TABLE A.9 SUMMARY OF VOLVETIC BEHAVIOR (page 1/4)
PRINCIPAL PROGRAM

PARAMETER	EFFECT OF INCREASING		
	RELATIVE DENSITY	CONFINING PRESSURE	STRAIN RATE
Rate of Dilation at Peak Strength	Trend Figure	Increase 3.6 (a) and (b)	Increase 3.8 (a), (b) and (c) Complex
Empirical Equations and Comments	- Moderate $\dot{\epsilon}$, $\sigma_c = 0.1 \text{ MPa}$ $\frac{d\epsilon_v}{d\dot{\epsilon}_a} = 0.07 + 1.9 \times 10^{-3} D_r (\%)$ $r^2 = 0.79$	- No effect (Slow and fast data within scatterband of moderate data) For All Strain Rates and relative densities	- $\sigma_c = 0.1 \text{ MPa}$, low D_r -No effect (Slow and fast data within scatterband of moderate data) - $\sigma_c = 0.1 \text{ MPa}$, high D_r -Slow to moderate Decrease Moderate to fast Little or no change
	- Moderate $\dot{\epsilon}$, $\sigma_c = 10 \text{ MPa}$ $\frac{d\epsilon_v}{d\dot{\epsilon}_a} = -0.04 + 1.1 \times 10^{-3} D_r (\%)$ $r^2 = 0.65$		- $\sigma_c = 10 \text{ MPa}$, all D_r -Slow to moderate No effect Moderate to fast Increase

TABLE A.9 SUMMARY OF VOLUMETRIC BEHAVIOR (page 2/4)
PRINCIPAL PROGRAM

PARAMETER	EFFECT OF INCREASING		
	RELATIVE DENSITY	CONFINING PRESSURE	STRAIN RATE
Maximum Rate of Dilatation	Trend Figure	Increase 3.6 (a) and (b)	Decrease 3.7 (a) and (b)
Empirical Equations and Comments	- Moderate $\dot{\epsilon}$ $\sigma_c = 0.1 \text{ MPa}$ $\frac{d\epsilon_v}{d\epsilon_a} = 0.16 + 4.5 \times 10^{-3} D_r (\%)$ $r^2 = 0.81$	For all D_r and $\dot{\epsilon}$ $\sigma_c = 2.0 \text{ MPa}$ $\frac{d\epsilon_v}{d\epsilon_a} = 0.08 + 2.2 \times 10^{-3} D_r (\%)$ $r^2 = 0.87$	- $\sigma_c = 0.1 \text{ MPa}$ all $\dot{\epsilon}$ - No effect (All data in or near scatterband of moderate strain rate) - $\sigma_c = 10 \text{ MPa}$ - Slow to moderate No effect Moderate to fast Increase

TABLE A.9 SUMMARY OF VOLUMETRIC BEHAVIOR (page 3/4)
PRINCIPAL PROGRAM

PARAMETER	EFFECT OF INCREASING		
	RELATIVE DENSITY	CONFINING PRESSURE	STRAIN RATE
Axial Strain at the Beginning of Dilation	Trend Figure	Complex 3.6 (a) and (b)	Increase Decrease 3.8 (a), (b) and (c)
	Empirical Equations and Comments	- $\sigma_c = 0.1$ MPa, all $\dot{\epsilon}$ - No effect Moderate $\dot{\epsilon}$ Mean = $1.9 \pm 0.6\%$	For all $\dot{\epsilon}$, and D_r Most noticeable at $\sigma_c = 0.1$ and high D_r

TABLE A.9 SUMMARY OF VOLUMETRIC BEHAVIOR (page 4/4)
PRINCIPAL PROGRAM

PARAMETER	EFFECT OF INCREASING		
	RELATIVE DENSITY	CONFINING PRESSURE	STRAIN RATE
Volumetric Strain at 20% Axial Strain	Increase Figure 3.6 (a) and (b)	Decrease 3.7 (a) and (b)	Increases 3.8 (a), (b) and (c)
Empirical Equations and Comments	Uniform over all $\dot{\epsilon}$ and σ_c $\epsilon_v(\%) = 1.5 + 7.0 \times 10^{-2} D_r (\%)$ $R^2 = 0.94$ $\sigma_c = 2.0 \text{ MPa}$ $\epsilon_v(\%) = 1.1 + 2.4 \times 10^{-2} D_r (\%)$ $R^2 = 0.75$	Uniform over all D_r and $\dot{\epsilon}$ $\sigma_c = 0.1 \text{ MPa}$ $\epsilon_v(\%) = -0.4 + 2.1 \times 10^{-2} D_r (\%)$ $R^2 = 0.84$ $\sigma_c = 10 \text{ MPa}$ $\epsilon_v(\%) = 0.3 + 0.97 \times 10^{-3} D_r (\%)$ $R^2 = 0.47$	- $\sigma_c = 0.1 \text{ MPa}$ low D_r -Slow to fast Increase - $\sigma_c = 0.1 \text{ MPa}$ high D_r -Slow to moderate No change Moderate to fast Increase - $\sigma_c = 10 \text{ MPa}$ -Slow to moderate No change Moderate to fast Increase

TABLE A.10
SUMMARY OF THE EFFECT OF SPECIMEN PREPARATION TECHNIQUE
PRINCIPAL PROGRAM

PRS Test #	D _r %	σ _c ave MPa	Prep Tech	STRAIN RATE /sec		INITIAL RESPONSE		UPPER YIELD		STRAIN H/S		PEAK STRENGTH		VOLUMETRIC BEHAVIOR		S* A*			
				Q	Y _i max	Pro Y _i	Lim Off	E ACDT x10 ⁷ GPa	Q _{uy} MPa	Q _{cor} MPa	ε _s x10 ³	dQ dε _s	Q _p MPa	ε _a x10 ³	Dilatation ε _a	peak max. x10 ²	bdi ₁ x10 ³	ε _v 20%	ε _f vp
20	76.3	10.18	WT	31	299	20.7	1.8	3.2	8.6	8.5	5.0	5.0	258	16.7	16.5	5	5	132	4
64	82.7	10.02	ISP	23	338	24.3	2.2	3.3	7.9	7.8	4.8	10.4	127	17.8	24.0	2	2	103	2
24	90.5	5.12	WT	19	303	33.3	1.7	3.2	8.9	8.9	5.4	5.4	282	15.8	9.0	12	12	55	15
53	92.5	5.03	ISP	15	352	35.3	1.5	2.9	8.5	8.1	5.1	5.1	165	16.5	18.5	13	13	73	16
26	94.0	2.08	WT	18	300	31.8	2.0	3.7	9.2	9.2	5.3	5.3	283	14.7	5.1	15	23	38	-
55	88.1	2.00	ISP	24	382	26.1	2.1	3.4	7.9	7.4	4.4	8.5	119	13.1	12.0	20	27	21	32

Note: All specimens tested with lubricated ends

TABLE A.11 EFFECT OF TEMPERATURE ON STRESS-STRAIN BEHAVIOR

FRS Test #	D _r %	σ _c ave MPa	TEMP °C	STRAIN RATE / sec	INITIAL RESPONSE		UPPER YIELD	STRAIN H/S	PEAK STRENGTH		VOLUMETRIC BEHAVIOR		S* A*						
					Q _i	Y _i Max	Pro Y _i Off	E	Lim Off	Q _{uy} MPa	Q _{cor} MPa	ε _a x10 ³	Q _p MPa	ε _a x10 ³					
PRINCIPAL PROGRAM																			
50	93.7	10.03	-15*	18	212	28.0	1.9	3.3	10.8	-	5.4	5.4	177	21.5	23.2	10	27	14	f
52	90.8	10.04	-9.5	27	355	20.7	1.8	2.8	8.2	7.7	4.8	4.8	158	19.0	22.9	6	6	56	f
NEW PROGRAM																			
75	48.0	0.101	-20	NA	368	27.5	1.2	4.6	15.8	15.6	8.9	20.3	10	15.9	3.4	NA	NA	p	f
76	45.7	0.101	-20	NA	355	29.2	1.3	5.1	15.3	15.3	8.9	11.5	14	15.6	4.1	NA	NA	p	f
77	40.3	0.102	-15	NA	349	24.1	1.2	4.6	12.3	12.3	9.0	9.2	32	12.8	3.6	NA	NA	f	g
78	42.9	0.095	-23	NA	369	19.6	1.7	5.2	17.2	16.9	9.6	9.6	21	17.2	1.0	NA	NA	vp	f
79	45.7	0.101	-5.3	NA	385	29.5	1.3	2.1	4.8	4.6	4.0	7.7	62	6.6	5.9	NA	NA	p	f
80	41.0	0.122	-28	NA	380	27.1	1.5	5.6	17.2	16.8	7.8	7.8	57	17.2	0.8	NA	NA	p	p

* Estimated temperature

NA - Not Available

See Table A.2 for explanations of notation

Also see Table A.2 for results of FRS34, 44 and 57
tested at T = -9.5°C, σ_c = 0.1 MPa and D_r ≈ 36%

**APPENDIX B: TABULATED DATA FROM TEST
PROGRAM ON UNFROZEN MFS**

Table B.1 Conditions at Maximum Obliquity and Peak Strength from Undrained (CIUC) Tests

Table B.2 Condition at Steady State from Undrained (CIUC) Tests

Table B.3 Condition at Maximum Obliquity = Peak Strength and at Steady State from Drained (CIDC) Tests

TABLE B.1 UNFROZEN MFS TEST RESULTS: UNDRAINED TESTS (CIVC)
Conditions at Maximum Obliquity and Peak Strength Page 1/2

Test Series	Test No.	Pre-shear Dr (%)	e	σ'_c (MPa)	ϵ_a (%)	Maximum q (MPa)	P' (MPa)	Obliquity ϕ' (deg)	ϵ_a (%)	Peak Strength A_f	P' (MPa)	ϕ' (deg)	q/σ'_c
SERIES A 0.1 MPa Tests	11	93.7	0.601	0.092	1.88	0.179	0.282	39.4	9.12	0.835	1.421	-0.30	9.06
	12	13.8	0.864	0.102	5.75	0.084	0.144	35.7	13.4	0.107	0.195	0.07	1.05
	13	47.0	0.755	0.103	3.00	0.124	0.196	39.2	13.5	0.353	0.627	-0.24	3.43
2.0 MPa Tests	117	80.8	0.643	1.890	12.7	1.373	2.443	34.2	14.6	1.475	2.630	-0.13	34.1
	220	40.7	0.775	1.939	14.1	0.741	1.380	32.5	25.4	0.854	1.632	0.68	31.6
4.0 MPa Test	223	56.2	0.724	4.077	16.0	1.207	2.180	33.6	21.9	1.282	2.347	1.17	33.1
SERIES B 0.1 MPa Tests	08	82.9	0.637	0.104	1.86	0.175	0.272	40.0	38.63	1.064	1.743	-0.27	37.6
	09	82.9	0.637	0.114	2.43	0.252	0.403	38.7	31.7	1.662	2.807	-0.31	36.3
	10	43.7	0.765	0.102	8.99	0.366	0.599	37.7	22.5	0.693	1.236	-0.32	34.1
	12	85.7	0.627	0.110	0.82	0.119	0.157	49.3	17.0	1.994	3.461	-0.34	35.2
	22	93.3	0.602	0.122	0.49	0.136	0.164	56.2	116.5	2.326	4.456	-0.43	31.5
	22	93.3	0.602	0.122	0.49								19.07
2.0 MPa Tests	06	64.4	0.697	2.035	11.3	1.080	1.930	34.0	18.3	1.231	2.283	0.40	32.6
	07	93.2	0.603	2.030	6.67	1.820	3.130	35.6	17.5	2.871	5.136	-0.04	34.0
	11	67.0	0.689	2.013	6.72	1.170	2.000	35.8	15.2	1.504	2.729	0.26	33.4
	39	56.0	0.725	1.937	10.6	0.749	1.200	38.6	21.7	0.938	1.566	0.72	36.8
5.0 MPa Tests	01	70.0	0.679	4.983	12.5	1.440	2.560	34.2	23.1	1.563	2.877	1.17	32.9
	02	103.8	0.568	5.005	6.81	2.790	4.790	35.6	16.8	3.532	6.340	0.31	33.9
	04	75.4	0.661	4.982	8.16	2.705	5.126	31.9	11.5	2.813	5.405	0.43	31.4
	05	91.5	0.608	5.010	8.01	2.603	4.630	34.2	11.0	2.753	5.004	0.50	33.4
													0.55

¹ Premature failure before reaching "true" peak.

² No ACDT measurements therefore values are approximate.

³ Represents end of test measurements. May not be "true" peak.

TABLE B.1 UNFROZEN MFS TEST RESULTS: UNDRAINED TESTS (CIUC)
Conditions at Maximum Obliquity and Peak Strength Page 2/2

Test Series	Test No.	Pre-shear D_r (%)	e	σ'_{c} (MPa)	ϵ_a (%)	Maximum Obliquity ϕ' (deg)	ϵ_a (%)	Peak Strength A_f	ϕ' (deg)	$q/\sigma' c$
SERIES B cont.										
5.0 MPa Tests	13	64.9	0.696	5.184	6.91	1.470	2.410	37.6	10.2	0.30
	14	92.3	0.605	5.006	6.98	2.510	4.340	35.3	12.2	0.56
	15	92.8	0.604	5.034	9.74	3.220	5.730	34.2	13.9	0.68
	19	69.9	0.679	5.049	9.43	2.200	4.280	30.9	12.7	0.47
7.5 MPa Test	28	84.3	0.632	7.484	10.2	2.171	3.632	36.7	12.1	0.29
10 MPa Tests	23	89.1	0.616	10.16	7.91	2.810	5.006	34.1	2.57	0.28
	24	86.0	0.626	9.937	10.3	2.678	4.140	40.3	13.3	0.27
	25	83.0	0.636	9.362	7.93	2.232	4.242	31.7	1.97	0.25
	26	84.3	0.632	9.910	8.43	2.330	4.124	34.4	2.18	0.25
	27	76.6	0.657	10.10	9.60	2.476	4.198	36.1	1.63	0.26
	30	91.9	0.607	10.03	8.32	2.747	3.777	46.7	1.53	0.28
	40	101.6	0.575	9.961	13.3	3.145	5.027	38.7	17.9	0.32
11 MPa Test	29	97.0	0.590	10.99	7.82	2.816	3.885	46.5	1.71	0.27

TABLE B.2 UNFROZEN MFS TEST RESULTS: UNDRAINED TESTS (CIUC)
Conditions at Steady State

Test Series	Test No.	D_r (%)	Pre-Shear e	I_c (MPa)	ϵ_a (%)	q (MPa)	p' (MPa)	I_{ss} (MPa)	ϕ' (deg)	A_f	ϕ' (deg)	$q/\sigma'c$ (peak)
SERIES B 0.1 MPa Tests	10	43.7	0.765	0.102	25.3	0.648	1.209	0.994	-0.248	-0.32	32.4	6.79
	12	85.7	0.627	0.110	24.3	1.796	3.353	2.754	-0.378	-0.34	32.4	18.13
2.0 MPa Tests	06	64.4	0.697	2.035	25.6	1.142	2.291	1.909	0.012	0.40	29.9	0.60
	07	93.2	0.603	2.030	25.4	2.574	4.979	4.119	-0.083	-0.04	31.1	1.41
5.0 MPa Tests	11	67.0	0.689	2.013	24.1	1.276	2.619	2.194	0.002	0.06	29.2	0.75
	39	56.0	0.725	1.948	25.7	0.905	1.568	1.264	0.035	0.72	35.3	0.48
7.5 MPa Test	01	70.0	0.679	4.983	25.2	1.553	2.888	2.371	0.092	1.17	32.5	0.31
	02	103.8	0.568	5.005	23.0	3.314	6.253	5.148	-0.019	0.31	32.0	0.71
10 MPa Tests	05	91.5	0.608	5.010	21.5	2.347	4.835	4.053	0.022	0.50	29.0	0.55
	13	64.9	0.696	5.184	22.8	1.286	2.444	2.015	0.113	1.35	31.7	0.30
	15	92.8	0.604	5.034	24.4	2.850	5.901	4.951	0.018	0.32	28.9	0.68
	28	84.3	0.632	7.529	16.3	2.153	3.737	3.019	0.090	1.40	35.2	0.29
	23	89.1	0.616	10.16	8.03	2.805	5.006	4.070	0.107	1.23	34.1	0.28
	24	86.0	0.626	9.937	14.2	2.726	4.262	3.358	0.115	1.54	39.8	0.27
	25	83.0	0.636	9.362	9.21	2.217	4.233	3.494	0.118	1.26	31.6	0.25
	26	84.3	0.632	9.921	8.43	2.171	4.124	3.347	0.121	1.27	34.4	0.25

TABLE B.3 UNFROZEN MFS TEST RESULTS: DRAINED TESTS (CIDC)

Conditions at Maximum Obliquity = Peak Strength

Test Series	Test No.	D_r (%)	Pre-shear		ϵ_a^s (%)	ϵ_y (%)	$\Delta\epsilon$	ϕ' (deg)
			e	σ_c (MPa)				
SERIES B								
0.1 MPa Test	38	86.0	0.626	0.160	5.79	0.157	0.189	2.54
2.0 MPa Tests	35	70.7	0.676	1.920	12.9	1.189	1.968	0.63
	36	89.2	0.616	1.997	9.75	1.279	2.032	1.30
5.0 MPa Test	37	88.2	0.619	4.969	13.3	2.895	5.046	-1.13
10 MPa Tests	33	86.6	0.624	10.03	19.3	5.158	10.14	-5.37
	34	90.8	0.610	9.978	19.6	5.419	10.19	-5.52

Conditions at Steady State

Test Series	Test No.	D_r (%)	Pre-shear		ϵ_a^s (%)	ϵ_y (%)	I_{ss}^s (MPa)	Φ	ϕ' (deg)
			e	I_c (MPa)					
SERIES B									
5.0 MPa Test	37	88.2	0.619	4.977	20.9	2.783	5.024	-0.95	4.097